Advanced thermal analysis and transport properties of stereocomplex polylactide

Nagihan Varol

Normandie Université

THESE

Pour obtenir le diplôme de doctorat

Spécialité : Physique

Préparée au sein de l'Université de Rouen Normandie

Analyse Thermique Avancée et Propriétés de Transport de Matériaux PolyLactide Stéréocomplexe

Présentée et soutenue par
Nagihan VAROL

Thèse soutenue publiquement le 26 Juin 2019 devant le jury composé de		
M. Eric DANTRAS	MCF HDR / Université Toulouse 3- Paul Sabatier	Rapporteur
Mme. Isabelle ROYAUD	Pr / Université de Lorraine	Rapporteur
M. Sébastien CHARLON	MCF / Institut Mines-Télécom Lille Douai	Examinateur
M. Loïc LE PLUART	Pr / Université de Caen	Examinateur
Mme. Kateryna FATYEYEVA	MCF HDR / PBS, Université de Rouen Normandie	Co-directeur de thèse
M. Eric DARGENT	Pr / GPM, Université de Rouen Normandie	Directeur de thèse

Thèse dirigée par Dr. Kateryna FATYEYEVA (laboratoire PBS UMR 6270) et Pr. Eric DARGENT (laboratoire GPM UMR 6634)

UNIVERSITÉ DE ROUEN NORMANDIE

ED PSIME

GPM Groupe de Physique des Matériaux

Normandie Université

PhD THESIS

In order to obtain the degree of Doctor of Philosophy in Science

Speciality: Physics

Submitted to the Faculty of Science- University of Rouen Normandie in partial fulfillment of the requirements for the degree

Advanced Thermal Analysis and Transport Properties of Stereocomplex PolyLactide

Presented and defended by
Nagihan VAROL

Defended on 26 June 2019 in front of the dissertation committee composed of		
M. Eric DANTRAS	MCF HDR / Université Toulouse 3- Paul Sabatier	Reviewer
Mme. Isabelle ROYAUD	Pr. / Université de Lorraine	Reviewer
M. Sébastien CHARLON	MCF / Institut Mines-Télécom Lille Douai	Examiner
M. Loïc LE PLUART	Pr / Université de Caen	Examiner
Mme. Kateryna FATYEYEVA	MCF HDR / PBS, Université de Rouen Normandie	Co-supervisor of thesis
M. Eric DARGENT	Pr. / GPM, Université de Rouen Normandie	Supervisor of thesis

Supervised by Dr. Kateryna FATYEYEVA (PBS UMR 6270) and Pr. Eric DARGENT (GPM UMR 6634)

UNIVERSITÉ DE ROUEN NORMANDIE

ED PSIME

GPM Groupe de Physique des Matériaux

Financial support: the Normandy Region and the Fonds European Regional Development (FEDER)

Laboratories: "Groupe Physique des Matériaux" (GPM – UMR CNRS 6634) and "Polymères Biopolymères Surfaces" (PBS – UMR CNRS 6270)

ACKNOWLEDGMENTS

First of all, I would like to express my gratitude to the jury's members who have accepted to review my work and for the fruitful discussion during the defense.

The "Région Normandie" and the "Fonds European Regional Development (FEDER)" are gratefully acknowledged for the financial support of this work. I also gratefully acknowledged the "Groupe de Physique des Matériaux GPM (EIRCAP team)" and the "Polymères Biopolymères Surfaces PBS (MPBM team)" for hosted me with their professional and friendly nature during the PhD project.

I address my sincere thanks to my PhD supervisors, Kateryna FATYEYEVA and Eric DARGENT for the chance they offered me to work in two laboratories as well as for their support, guidance, encouragement and patience throughout my PhD project.

I would like to give a special thanks to Allisson SAITER, Laurent DELBREILH, Nicolas DELPOUVE, Antonella ESPOSITO and Stéphane MARAIS for the valuable discussions which have enriched my scientific knowledge. I also would like to thank to Clément DEMAREST and Corinne CHAPPEY for their support and help during the measurements.

I would like to thank each person that I have met during my master and PhD study and who have contributed either by personal or professional way to this work: Clément DEMAREST, Laurent DELBREILH, Antonella ESPOSITO, Nicolas DELPOUVE, Allisson SAITER, Eric DARGENT, Jean GRENET, Eric DONTZOFF, Marie-Rose GARDA, Yoga Sugama SALIM, Rakibul ISLAM, Sélim ZAHOUR, Steven ARAUJO, Xavier MONNIER, Bidur RIJAL, J. Arturo SOTO PUENTE, Quentin VIEL, Benjamin SCHAMME, Aurélie BOURDET, Sareh MOGHADDAM MAHMOUDIAN, Bienvenu ATAWA, Clément FOSSE, Quentin LOZAY, Alexandre MORVAN, Blandine QUELENNEC, Corinne CHAPPEY, Nadège FOLLAIN, Louise HESPEL, Laurent LEBRUN, Stéphane MARAIS, Carole KARAKASYAN-DIA, Najat BTEICH, Ferhat SELLAMI, Edyta RYNKOWSKA, Bassidi DIAWARA, Naila BOU-HAIDAR, Julien BOUILLON, Xuelian LIU, Hajar FARAJ, Yevhenii PRYKHODKO, Mohamed JIZZINI, Yaroslav KOBZAR, Tarik ELLADJI, Anne MABIRE, Alex MEYE BIOGO. I wish the best and good luck for the next ones.

During my PhD journey, I gained a lot of friends. I also would like to thank to them who were not only colleagues but also amazing friends: Clément D. (my hero), Yoga (the prof), Rakibul (big boss), Steven (sir), Sélim (dear Sélim), Xavier (boss), Sareh and Aurélie (girls' power), Clément F. (Bradley, (you bad)), Quentin L. (Mr. hey with smile since M2), Edyta (canim sister-friend), Najat (my sweetheart and sister-friend), Naila (my dear sister-friend, take it easy girl), Imane (my dear and sister-friend), Bassidi (the king), Ferhat (Mr. milk lover), and of course Bouchra (cicim, my sister-friend) and Carole K. (dear sister), dream team: José, David, Florian and Clément (coffee boys).

I would like to give my sincere thanks to Jean-Marc SAITER and his wife for their hospitality and help for the life in France.

I would like to sincerely thank to Yoga and Rakibul for their family-like nature. You are my gained brothers and will always be in the family.

I would like to extend my special thanks to my dear Clément DEMAREST. I know it is not enough how much I thank to you. Thank you so much for being there always and in any condition. I appreciate your patience to deal with my stress and caprices (it is precious and it is not easy to find a friend like you). Thank you so much for your constant encouragement and support. You are my best gain during my PhD, I hope you would always be there.

Finally, my deepest gratitude goes to my parents (dad… I wish you could see this precious moment), my brothers and sister, my aunts and uncles for their immense emotional support, unconditional love, dedication and constant encouragement. My lovely brother Ömer, whatever I say will not be enough your efforts and support "merci beaucoup askitosum". They all are greatly involved in the achievement of this work and my life. I could not succeed this without you. Love you all…

À mon père …

Table of contents

List of figures

Chapter 1: STATE OF THE ART

Chapter 2: EXPERIMENTAL PART

Chapter 3: INFLUENCE OF ELABORATION METHODS ON STEREOCOMPLEXATION REACTION

Chapter 4: THE CHIRALITY IMPACT ON PRIMARY AND SECONDARY RELAXATIONS IN AMORPHOUS STEREOCOMPLEX PLA

Chapter 5: MICROSTRUCTURE IMPACT ON MECHANICAL AND BARRIER PROPERTIES OF STEREOCOMPLEX PLA

List of tables

Chapter 1: STATE OF THE ART

Chapter 3: INFLUENCE OF ELABORATION METHODS ON STEREOCOMPLEXATION REACTION

Chapter 4: THE CHIRALITY IMPACT ON PRIMARY AND SECONDARY RELAXATIONS IN AMORPHOUS STEREOCOMPLEX PLA

Chapter 5: MICROSTRUCTURE IMPACT ON MECHANICAL AND BARRIER PROPERTIES OF STEREOCOMPLEX PLA

General Introduction

Thermoplastics are currently main polymer materials used in the packaging, automotive, electronics, and medical applications. Due to the environmental context of the sustainable innovations, biobased and biodegradable polymers occupy an increasingly important place in the eco-design of materials [1]. The increase of sustainable concerns of the petroleum-based polymers results in a growing interest in the biopolymers, in particular poly(lactic acid) (PLA)-based materials [2]. Besides, PLA requires 25-55% less energy to be produced than petroleum-based polymers and researches show that this value can be further reduced to less than 10% in the future [3]. In addition, good thermal properties of PLA-based polymers increase the competition with the fossil-based polymers. Nevertheless, the functional properties of PLA-based materials should be improved in terms of their thermal, mechanical and barrier properties in order to correspond to food packaging requirements. For this purpose, many different strategies have been already applied; physical or chemical modifications (crosslinking), blending with other components, and addition of plasticizers or compatibilizers [4-7].

When the interactions between the polymers with the different tacticity predominate over those with the same tacticity, a stereoselective association takes place, which is called stereocomplexation or stereocomplex (sc) formation. Such association allows to form new polymer with enhanced physical properties compared to the parents' polymers. The presence of the chiral carbon in the skeletal chain of PLA yields two stereoregular enantiomers, i.e. poly(*L*-lactide) (PLLA) and poly(*D*-lactide) (PDLA). The mixture of homochiral PLLA and PDLA macromolecules leads to the formation of stereocomplex PLA (sc PLA) by the stereocomplexation reaction. Stereocomplexation improves PLA properties through increasing the crystallization ability and crosslinkings between enantiomers. Sc PLA attracts great attention for packaging industry as 2nd generation PLA due to the enhanced thermal and mechanical properties. Sc PLA has higher melting temperature ($T_{m,\ sc\ PLA}$ = 240 °C) compared to the homopolymers (PLLA and PDLA) and co-polymer (PL-DLA) ($T_{m,\ PLA}$ = 180 °C) [8, 9]. Furthermore, it has been reported that the stereocomplexation enhances the mechanical properties, i.e. increase in ultimate tensile strengths from 31 MPa for pure PLLA to 50 MPa for

sc PLA, and in elongation at break from 3.1 - 5.8% to 15 - 160% depending on the molecular weight of PLAs is observed [10-12].

Unlike racemic mixtures of small chiral molecules, in the case of a polymer, the length of macromolecular chains (molecular molar mass) will strongly influenced the mobility and the structural arrangement of the material. The numerous studies dealing with the sc PLA formation, its microstructure, and degradation have been carried out. Although many researchers focused their attention on the sc crystals species in order to understand the sc PLA properties [13, 14], the behavior of the amorphous phase and the transport properties of sc PLA is still enigmatic topic. Besides it is known that the barrier properties of PLA are still too low in the presence of moisture for the industrial packaging requirements. In order to overcome this problem the addition of lamellar nanofillers [15], the plasma surface treatment [16] or elaboration of polymer blends [17] were proposed in the literature.

In this work, the sc PLA films were elaborated by two methods, i.e. solution casting and extrusion process. Furthermore, the enhancement of the physical and transport properties of PLA-based materials was noted by stereocomplexation, i.e. without the additives, surface treatments, chemical modifications, or inorganic fillers. The transport properties of small molecules (H_2O, N_2, O_2 and CO_2) were linked with the molecular mobility over a wide range of temperatures (from room temperature to the glass transition temperature) in order to understand the role and evolution of the free volume. The aim of this work is to study new PLA-based material obtained from PLLA and PDLA by solution casting and extrusion with enhanced transport properties. The originality of this work bases on the complementarity of two approaches (physics and chemistry) for a better understanding and a broader vision of the properties of the amorphous phase and the evolution of the free volume in stereocomplex polymer which is not studied yet. We studied wholly amorphous and isotropic crystalized materials in order to generate more or less confined amorphous phases. This research work and results have been presented as follows:

- the state-of-art of stereocomplexation and properties of amorphous and semi-crystalline polymer materials is presented in the first chapter. The effective parameters on stereocomplexation are discussed with the elaborations methods.

The properties of the glassy-polymers are presented to exhibit different theories and concepts related to the glass transition phenomenon. This information allows us better understanding the molecular dynamics and relaxation phenomena of the glass-forming liquids and the glassy state;

- the second chapter presents the materials as well as instrumental techniques used in this work, namely calorimetric investigations, microstructure analysis and permeametric analysis;
- the influence of the elaboration methods on the stereocomplexation is developed in the third chapter. The selection procedure of the sc PLA sample elaboration is detailed. The effective parameters, i.e. solvent nature, proportion of homopolymers, elaboration conditions, were compared and discussed;
- the fourth chapter reports glass transition and molecular mobility of the homopolymers and wholly amorphous sc PLA. Fast scanning calorimetry (FSC) and dielectric relaxation spectroscopy (DRS) methods were combined to perform the kinetic study of the molecular dynamic. The aim of this investigation is to observe the influence of the tacticity on the molecular dynamics in the stereocomplex structure;
- the last chapter presents the transport properties of sc PLA in relation to the molecular mobility of the semi-crystalline and amorphous samples. The microstructure of sc PLA is also reported to highlight the structural influences on the barrier properties of sc PLA. Special attention has been given to the water permeability as a function of temperature.

This research thesis, financially supported by the Normandy Region and the Fonds European Regional Development (FEDER) under the frame of project “MAterials and CHIrality”, MACHI. It was carried out at the “Groupe Physique des Matériaux” (GPM – UMR CNRS 6634) and “Polymères Biopolymères Surfaces” (PBS – UMR CNRS 6270) from the University of Rouen Normandy.

References

1. Madhavan Nampoothiri, K.; Nair, N. R.; John, R. P. An overview of the recent developments in polylactide (PLA) research. *Bioresource Technology* **2010,** 101 (22), 8493-8501 DOI: https://doi.org/10.1016/j.biortech.2010.05.092.
2. Slager, J.; Domb, A. J. Biopolymer Stereocomplexes. *Advanced Drug Delivery Reviews* **2003,** 55, 549-583 DOI: http://dx.doi.org/10.1016/S0169-409X(03)00042-5
3. Rasal, R. M.; Janorkar, A. V.; Hirt, D. E. Poly(lactic acid) modifications. *Progress in Polymer Science* **2010,** 35 (3), 338-356 DOI: https://doi.org/10.1016/j.progpolymsci.2009.12.003.
4. Thellen, C.; Orroth, C.; Froio, D.; Ziegler, D.; Lucciarini, J.; Farrell, R.; D'Souza, N. A.; Ratto, J. A. Influence of montmorillonite layered silicate on plasticized poly(l-lactide) blown films. *Polymer* **2005,** 46 (25), 11716-11727 DOI: https://doi.org/10.1016/j.polymer.2005.09.057.
5. Rhim, J.-W.; Hong, S.-I.; Ha, C.-S. Tensile, water vapor barrier and antimicrobial properties of PLA/nanoclay composite films. *LWT - Food Science and Technology* **2009,** 42 (2), 612-617 DOI: https://doi.org/10.1016/j.lwt.2008.02.015.
6. Fortunati, E.; Peltzer, M.; Armentano, I.; Torre, L.; Jiménez, A.; Kenny, J. M. Effects of modified cellulose nanocrystals on the barrier and migration properties of PLA nano-biocomposites. *Carbohydrate Polymers* **2012,** 90 (2), 948-956 DOI: https://doi.org/10.1016/j.carbpol.2012.06.025.
7. Delpouve, N.; Stoclet, G.; Saiter, A.; Dargent, E.; Marais, S. Water Barrier Properties in Biaxially Drawn Poly(lactic acid) Films. *The Journal of Physical Chemistry B* **2012,** 116 (15), 4615-4625 DOI: 10.1021/jp211670g.
8. Furuhashi, Y.; Kimura, Y.; Yoshie, N.; Yamane, H. Higher-order structures and mechanical properties of stereocomplex-type poly(lactic acid) melt spun fibers. *Polymer* **2006,** 47 (16), 5965-5972 DOI: https://doi.org/10.1016/j.polymer.2006.06.001.
9. Yamane, H.; Sasai, K. Effect of the addition of poly(d-lactic acid) on the thermal property of poly(l-lactic acid). *Polymer* **2003,** 44 (8), 2569-2575 DOI: https://doi.org/10.1016/S0032-3861(03)00092-2.
10. Garlotta, D. A Literature Review of Poly(Lactic Acid). *Journal of Polymers and the Environment* **2001,** 9 (2), 63-84 DOI: 10.1023/a:1020200822435.
11. Hartmann, M. H., High Molecular Weight Polylactic Acid Polymers. In *Biopolymers from Renewable Resources*, Kaplan, D. L., Ed. Springer Berlin Heidelberg: Berlin, Heidelberg, 1998; pp 367-411.
12. Perego, G.; Cella, G. D.; Bastioli, C. Effect of molecular weight and crystallinity on poly(lactic acid) mechanical properties. *Journal of Applied Polymer Science* **1996,** 59 (1), 37-43 DOI: doi:10.1002/(SICI)1097-4628(19960103)59:1<37::AID-APP6>3.0.CO;2-N.
13. Tashiro, K.; Wang, H.; Kouno, N.; Koshobu, J.; Watanabe, K. Confirmation of the X-ray-Analyzed Heterogeneous Distribution of the PDLA and PLLA Chain Stems in the Crystal Lattice of Poly(lactic acid) Stereocomplex on the Basis of the Vibrational Circular Dichroism IR Spectral Measurement. *Macromolecules* **2017,** 50 (20), 8066-8071 DOI: 10.1021/acs.macromol.7b01573.
14. Tashiro, K.; Kouno, N.; Wang, H.; Tsuji, H. Crystal Structure of Poly(lactic acid) Stereocomplex: Random Packing Model of PDLA and PLLA Chains As Studied by X-ray Diffraction Analysis. *Macromolecules* **2017,** 50 (20), 8048-8065 DOI: 10.1021/acs.macromol.7b01468.
15. Tenn, N.; Follain, N.; Soulestin, J.; Crétois, R.; Bourbigot, S.; Marais, S. Effect of Nanoclay Hydration on Barrier Properties of PLA/Montmorillonite Based Nanocomposites. *The Journal of Physical Chemistry C* **2013,** 117 (23), 12117-12135 DOI: 10.1021/jp401546t.
16. Tenn, N.; Follain, N.; Fatyeyeva, K.; Poncin-Epaillard, F.; Labrugere, C.; Marais, S. Impact of hydrophobic plasma treatments on the barrier properties of poly(lactic acid) films. *RSC Advances* **2014,** 4 (11), 5626-5637 DOI: 10.1039/C3RA45323E.
17. Messin, T.; Follain, N.; Guinault, A.; Sollogoub, C.; Gaucher, V.; Delpouve, N.; Marais, S. Structure and Barrier Properties of Multinanolayered Biodegradable PLA/PBSA Films: Confinement Effect via Forced Assembly Coextrusion. *ACS Applied Materials & Interfaces* **2017,** 9 (34), 29101-29112 DOI: 10.1021/acsami.7b08404.

CHAPTER 1. STATE OF THE ART

In this chapter the bibliographical research related to PLA-based materials is presented. The different parameters affecting PLA stereocomplexation, its diverse properties have been summarized. The scientific basics and concepts that can be applied were briefly explained and discussed. Besides the scientific concepts, the history of poly(lactide)-based materials and their importance were presented to define the innovation of this work.

1.1 Chirality and Stereoisomers

The concepts of chirality and stereoisomerism offer a great importance to understand the physical and theoretical reasons behind the formation and structures of numerous molecules. A non-superimposable set of two molecules that are mirror image to one another is known as chiral molecules [1] (Fig 1.1). The chiral compounds share the same atomic shape but they are different in structural arrangements; such example of chiral compounds is lactides.

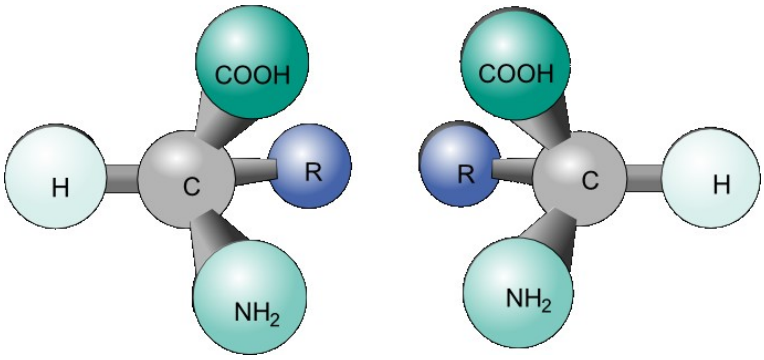

Figure 1. 1. Two enantiomers of a tetrahedral complex [1].

The isomers of chiral compounds are called stereoisomers. In contrast to the well-known constitutional isomerism, which develops isotopic compounds simply by different atomic connectivity, stereoisomerism generally maintains equal atomic connections and orders building blocks as well as has the same number of atoms and elements. Spatial arrangement of atoms concerns how different atomic particles and molecules are situated in the space around the carbon chains. In this sense, the spatial arrangement of a polymer chain will be different if one of the atoms in the polymer chain is shifted even by one degree in any three-dimensional directions. This opens up a broad possibility formation of different molecules, each with their unique placement of atoms in the three-dimensional space [2].

1.2 Lactides

Lactides are produced by the depolymerization of poly(lactides) under reduced pressure to give a mixture of *L*-lactide, *D*-lactide and/or *meso*-lactide isomers (Fig 1.2) [3]. The different percentages of the obtained isomers depends on the lactic acid isomer feedstock, temperature and catalyst.

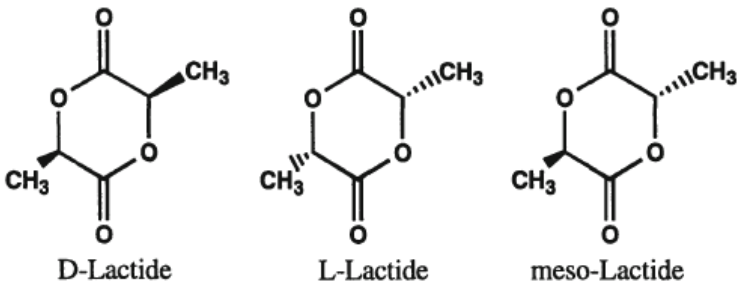

Figure 1. 2. Chemical structures of *L*-lactide, *D*-lactide and *meso*- or *LD*-lactide isomers [3].

1.3 Poly(lactide)

Due to environmental concern, the development of biosourced and biodegradable packaging materials has attracted great interest to replace petroleum-based plastic packaging materials. PLA is one of the mostly used biodegradable thermoplastic aliphatic polyester derived from renewable bio-resources [4, 5]. It is used in many applications from biomedical devices and tissue engineering to packaging due to its excellent biocompatibility and sustainability [6, 7]. In particular, PLA is used in food packaging application due to its numerous advantages:

- it can be obtained from renewable bio-sources
- it provides significant energy savings
- it is recyclable and compostable
- it is useful to improve farm economies
- the physical and mechanical properties can be tunable through the polymer architecture, i.e. grafted homopolymers by graphene oxide [8] and star-shaped isomers [9].

Many studies showed that PLA is an economically feasible material to use as a packaging polymer. However, PLA is a very brittle material and the toughness in its raw state is insufficient to resist a high level of impact strength [10]. The thermal and mechanical stability of PLA limits its wide applications that still need higher stress levels and higher barrier properties. In addition, the low crystallization rate of PLA causes low heat distortion temperatures (HDT) [7, 11]. Therefore, there are still so many challenges for the full applications in utilizing neat PLA-based materials. Many solutions have been developed to improve the property deficiency of PLA, including plasticization, copolymerization and melt

blending with flexible polymers [12]. Such modifications enhance PLA's elongation at break and reduce brittleness. However, the stiffness of the blended materials is also an important property for the applications. Therefore, the new production strategy is developed without compromising the stiffness and tensile strength to enhance the thermal and mechanical stability of neat PLA in a broad temperature range.

1.3.1 Chain structure and production of PLA

PLA is the simplest hydroxyl acid with a chiral (or an asymmetric) carbon atom and it exists in two optically active configurations, the *L*- (+) and *D*- (-) isomers which are presented in Fig 1.3. The basic configurational unit of PLA can be manufactured by carbohydrate fermentation (as shown in Fig 1.4) or chemical synthesis (as shown in Fig 1.5).

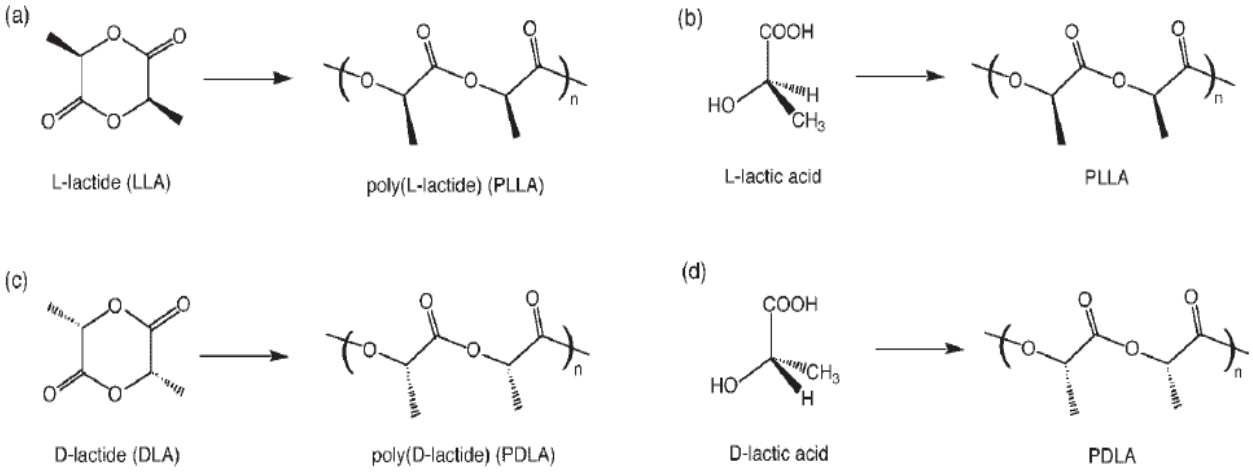

Figure 1. 3. Synthesis and molecular structures of PLLA [(a) and (b)] and PDLA [(c) and (d)] [13].

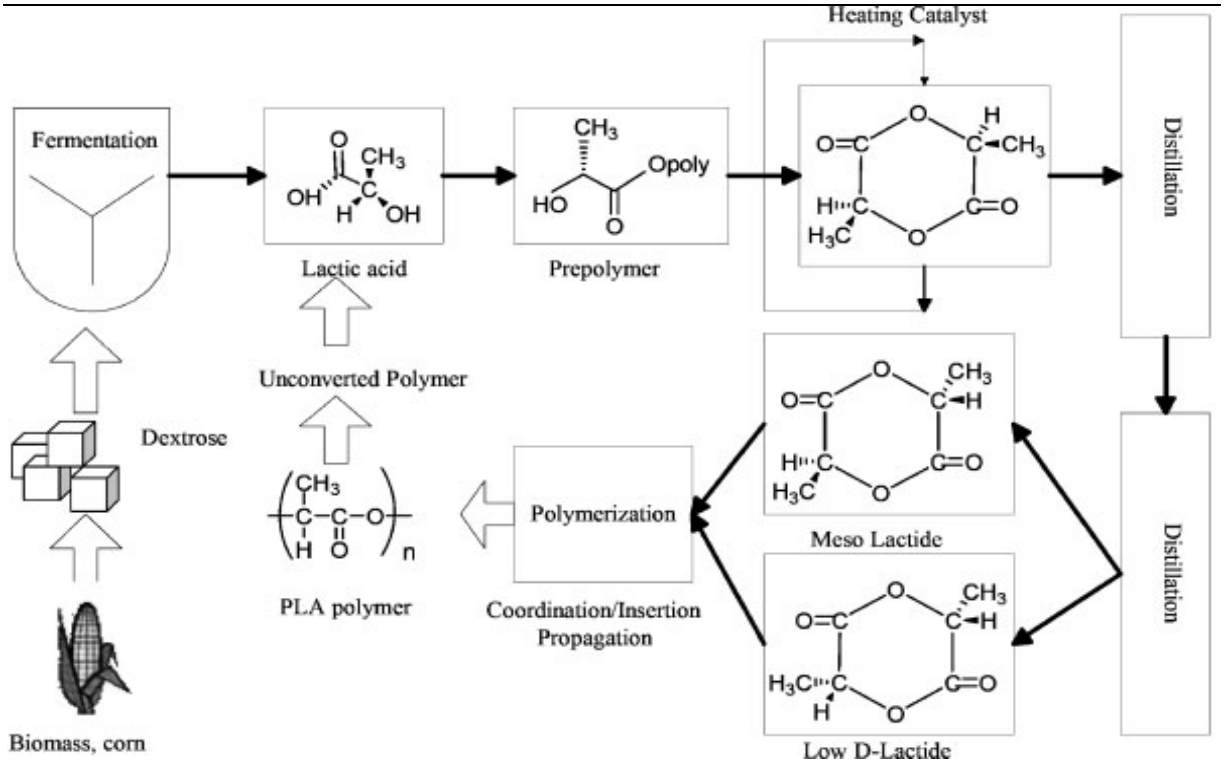

Figure 1. 4. Schematic illustration of the production of PLA, image was adopted from Gruber et al. [14].

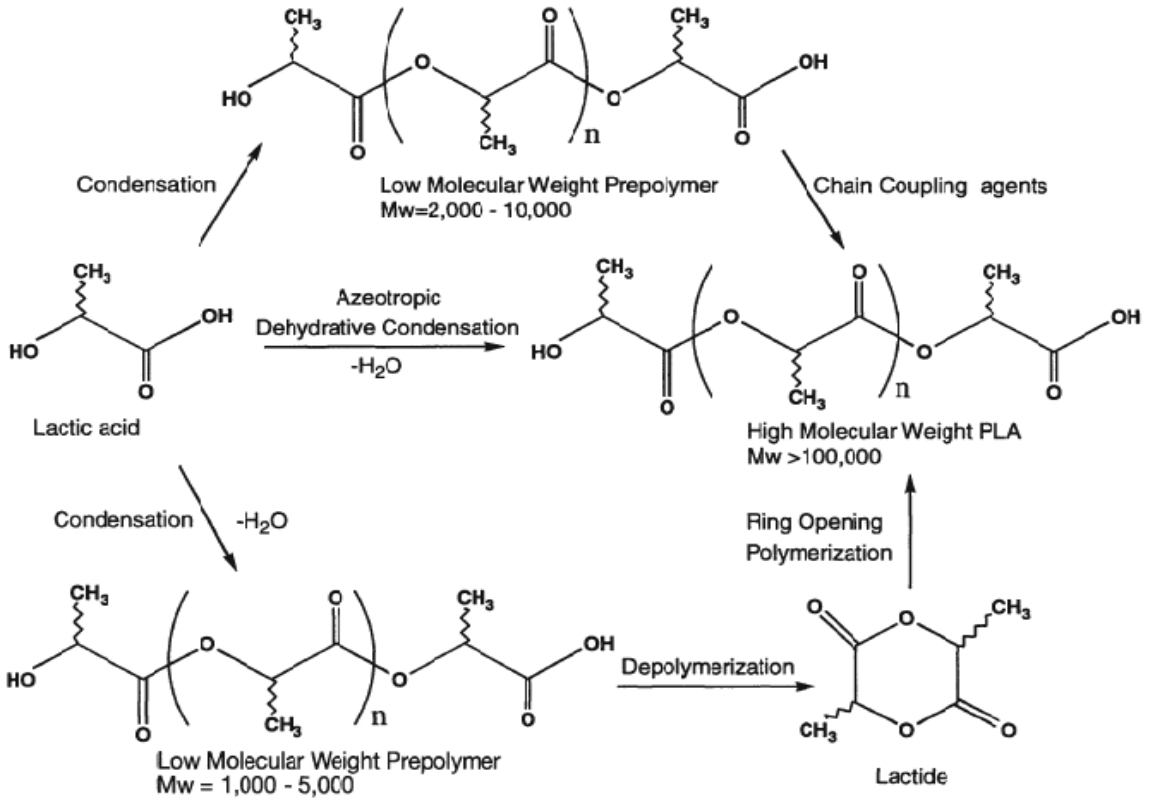

Figure 1. 5. Schematic illustration of chemical synthesis of low and high molecular weight PLA, image was adopted from Hartmann et al.[3].

1.3.2 Crystal structures of PLA

Different crystal structures of PLA have been reported according to the crystal formation and the crystallization conditions. The well-known α crystals obtained in conventional melt and solution crystallization conditions were first reported by De Santis and Kovacs [15], then further investigated in a numerous studies [16-18]. Zhang et al. [19] noted based on Wide Angle X-ray Diffraction (WAXD) and Infrared (IR) spectroscopy, the slightly different α' crystals of PLA crystalized below 120 °C. The chain conformation and crystal structure of α' form is similar to α form, but α' form has a less ordered chain packing. It is proposed that pure α' crystals are formed at crystallization temperatures below 100 °C, whereas crystallization between 100 °C and 120 °C leads to the coexistence of α' and α crystal structure [20, 21]. A β form, firstly reported by Eling et al. [22], is created by stretching the α form at high draw-ratio and high temperature, i.e. during hot-drawing of melt or solution spun fibers [22, 23]. Melting temperature of the β crystals is about 10 °C lower compared to the α crystal, attesting that β form is thermally less stable [23]**.** Then, Puiggali et al. [18] suggested that β form crystal is a frustrated structure with a trigonal cell containing three chains which are randomly oriented up and down. A more ordered crystal formation called γ was also reported by Cartier et al. [24]. In the γ form, which was obtained by epitaxial crystallization of PLA on hexamethyl benzene, two chains are oriented antiparallel in the crystal cell.

1.4 Stereocomplexation

Besides the homocrystallization of PLLA and PDLA, these two enantiomeric chains can co-crystallize together and form a stereocomplex crystals [25]**.** In contrast to PLLA or PDLA homocrystals, the stereocomplex crystal cell contains one PLLA and one PDLA chain. Well-known examples of stereocomplexation for enantiomeric polymers and for polymers with different tacticity were reported by Pauling and Corey in 1953 [26] and by Fox et al. in 1958 [27], respectively. Since a novel stereocomplex interaction between two chiral polymers was discovered, a third group of polymer complexes are obtained based on hydrophobic or van der Waals interactions. Stereocomplex formation between enantiomeric polymers leads to achieve better physical and mechanical properties than those of pure components.

Interestingly, melting temperature of the stereocomplex is about 50 °C higher than that of PLA homocrystals. In virtue of the different tacticity of PLA isomers, i.e. PLLA and PDLA, the improved interactions between the isomers with different tacticity are governed by stereocomplexation. Due to the different tacticities, a stereoselective association takes place through the stereocomplexation reaction. The presence of chiral carbon in the skeletal chain of PLA yields two stereoregular enantiomers (PLLA and PDLA) that allows forming the stereocomplex PLA (sc PLA) by stereocomplexation, as depicted in Fig 1.6. Stereocomplexation can be obtained by the attracting complementary interactions result from a hydrogen bonding [28]. *L*-lactide and *D*-lactide units can maintain the two helical chains with the opposite configuration together through the multicenter hydrogen bonding interactions, between —CH_3····O=C< and ≡CH····O=C< [29-31]. These improvements arise from a peculiar strong interaction between *L*- and *D*-lactide enantiomers, thus opening a new way of preparing innovative materials.

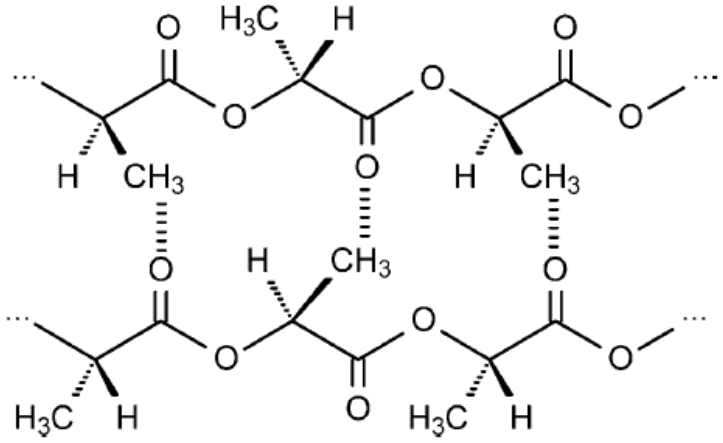

Figure 1. 6. Chain structure of sc PLA obtained from the linear poly(*L*-lactide) and poly(*D*-lactide) [32].

1.5 Stereocomplex PLA: structure and detection

1.5.1 Structure of stereocomplex PLA

Since sc PLA was discovered, Ikada et al. [25] noted that sc PLA has different X-ray diffraction pattern from homopolymers crystals; however, the stereocomplex crystal structure was not determined quantitatively. De Santis and Kovacs [15] reported a right-handed helical conformation of PDLA chain, structurally based on the left-handed helical

conformation of PLLA chain; therefore, they proposed van der Waals forces such as dipole-dipole interactions as the origin of the stereocomplexation (as shown in Fig 1.7).

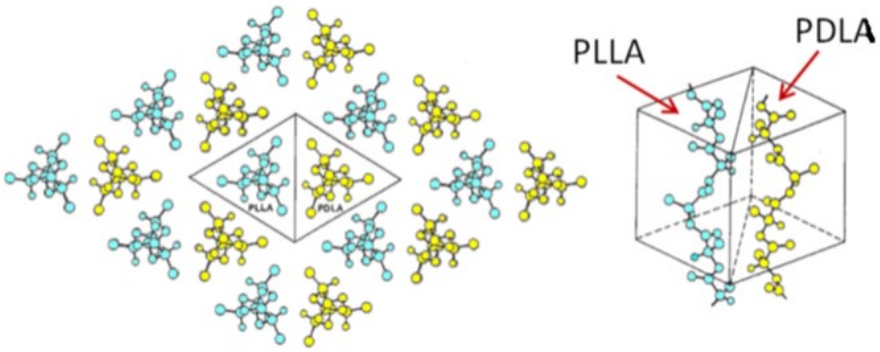

Figure 1. 7. Schematic illustration of the crystal structure of stereocomplex PLA [13].

Based on X-ray measurements and energy calculations, the crystalline structure of sc PLA was investigated in details. The stereocomplex crystals were discovered to be triclinic and trigonal unit cells with dimensions of a = 0.916 and 1.50 nm, b = 0.916 and 1.50 nm, and c = 0.870 and 0.87 nm, with the angles α = 109.2° and 90°, β = 109.2° and 90°, and γ = 109.8° and 120°, respectively [33, 34]. Properties of the different types of PLA crystal form are summarized in Table 1.1. The values of density are calculated based on the reported cell parameters and the number of monomers in each unit cell.

Crystal Type	Crystal system	Chain conformation	Cell parameters						$\rho_{theoretical}$ (g/cm^3)
			a (nm)	b (nm)	c (nm)	α (°)	β (°)	γ (°)	
α [15]	Pseudo-orthorhombic	10_3 helical	1.07	0.65	2.78	90	90	90	1.25
α [17]	Orthorhombic	10_3 helical	1.05	0.61	2.88	90	90	90	1.30
β [23]	Orthorhombic	3_1 helical	1.03	1.82	0.90	90	90	90	1.28
β [18]	Trigonal	3_1 helical	1.05	1.05	0.88	90	90	120	1.28
γ [24]	Orthorhombic	3_1 helical	0.99	0.63	0.88	90	90	90	1.31
sc [33]	Triclinic	3_1 helical	0.92	0.92	0.87	109.2	109.2	109.8	1.27
sc [34]	Trigonal	3_1 helical	1.50	1.50	0.87	90	90	120	1.27

Table 1. 1. Crystallographic parameters of different types of PLA crystals.

In addition, Cartier et al. [34] and Tsuji et al. [35] suggested that chains' conformation is 3_1 helix, and each unit cell involves a PLLA and a PDLA chain with the same number of *L*- and

D- units. Therefore, stereocomplex crystals have more extended chains compared to PLLA α crystals, in which chains are composed of 10_3 helices.

1.5.2 Detection of stereocomplex PLA

Sc PLA was detected mostly by X-ray diffraction and DSC analysis due to the different patterns and melting temperature from the homopolymers; thus the presence and fraction of sc crystals in the obtained new material can be easily evaluated.

1.5.2.1 X-ray diffraction

Since sc PLA has different XRD pattern compared to homopolymers, it can be detected without altering the thermal history of polymers. He et al. [36] and Ikada et al. [25] reported diffraction peaks for sc PLA appearing at 2θ around 12, 21 and 24° while PLA homocrystals diffraction peaks appear at 2θ equal to 15, 16, 18.5 and 22.5° (Fig 1.8). The quantitative analysis can also be done to evaluate the amount of stereocomplex present in the blends by XRD [35]. Wide Angle X-ray Scattering (WAXS) intensity curves (Fig 1.8A) of PLLA/PDLA blends were obtained by cooled from 175°C by 5°C/min with different shear rates (a) $0s^{-1}$ (b) $50s^{-1}$ (c) $100s^{-1}$ (d) $178s^{-1}$ with the temperature interval of 5°C.

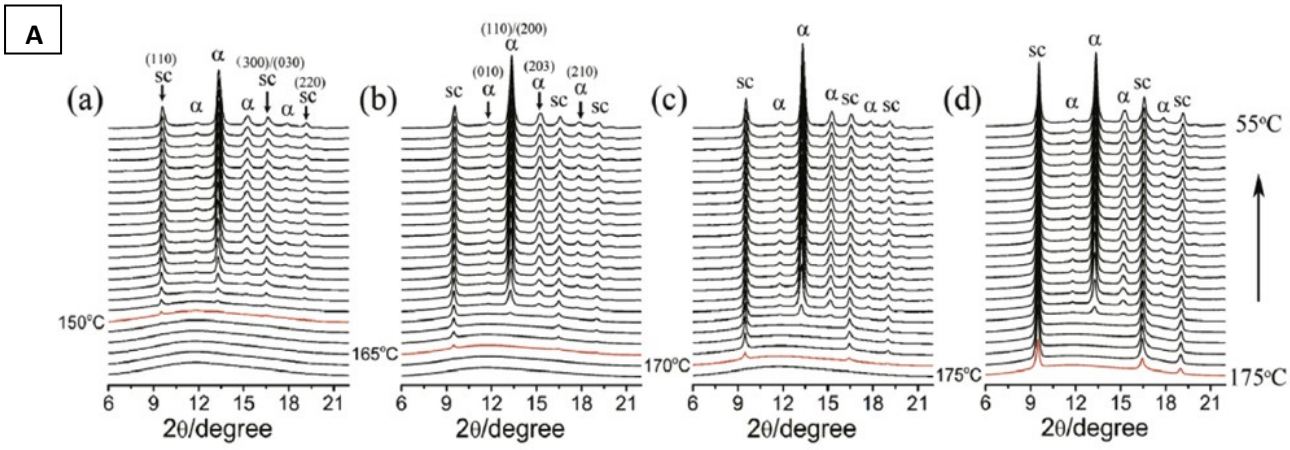

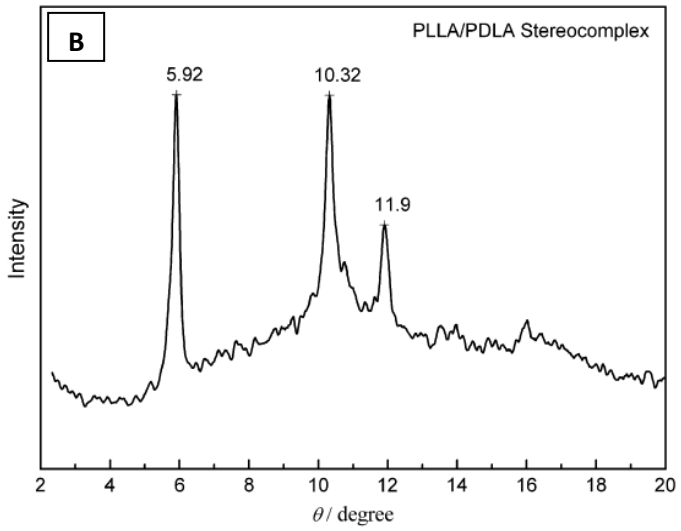

Figure 1. 8. Typical (A) WAXS [37] and (B) XRD spectra [36] of PLLA (α) and sc PLA (sc) registered with the radiation wavelength λ = 1.24 and 1.54 Å, respectively.

1.5.2.2 DSC analysis

The blends of PLLA and PDLA can form stereocomplex crystals which have a melting temperature about 50 °C higher than those of PLLA and PDLA homocrystals [25]. Due to the higher melting and crystallization temperature, the existence and amount of stereocomplex crystals in the blends can be simply evaluated by DSC analysis (Fig 1.9).

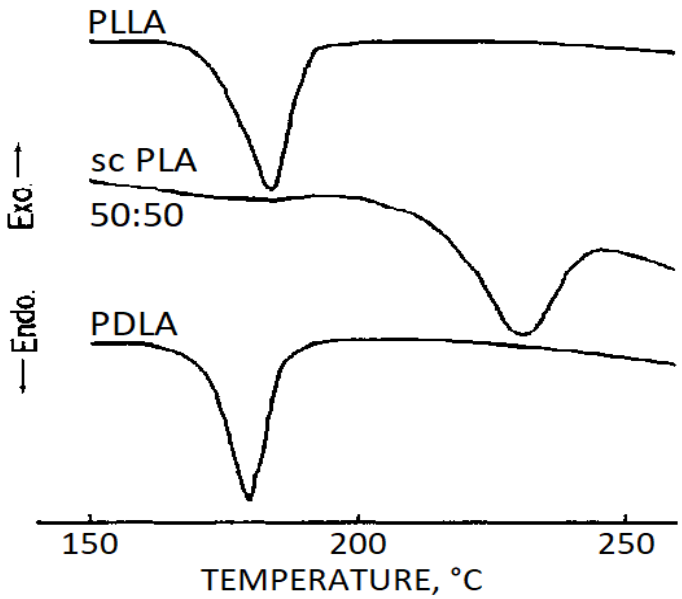

Figure 1. 9. Typical DSC curves of homopolymers and sc PLA [25].

1.5.2.3 Other techniques

The other methods have also been proposed to detect the presence of stereocomplex in the blends. Such techniques include microscopies and spectroscopies. The former (i.e. scanning electron microscopy (SEM), polarized optical microscopy (POM), transmission electron microscopy (TEM) and atomic force microscopy (AFM)) are generally used to reveal the information about surface morphology, crystals formation as well as crystallization kinetics; while the latter (i.e. Fourier-transform infrared spectroscopy (FTIR), Raman spectroscopy and nuclear magnetic resonance spectroscopy (NMR)) reveal information about the hydrogen bonding in stereocomplex polymers. For instance, there is a new absorption peak at 908 cm^{-1} in the FTIR spectra of sc PLA due to the hydrogen bonding as compared to homopolymers as shown in Fig 1.10 [38]. The hydrogen bonds undergo rearrangement between CH_3 group and C=O group and cause a conformational adjustment in the C-O-C backbone (shown in Fig 1.6). In addition, the 10_3 helix chain conformation (α crystals) at 923 cm^{-1} disappears after stereocomplexation.

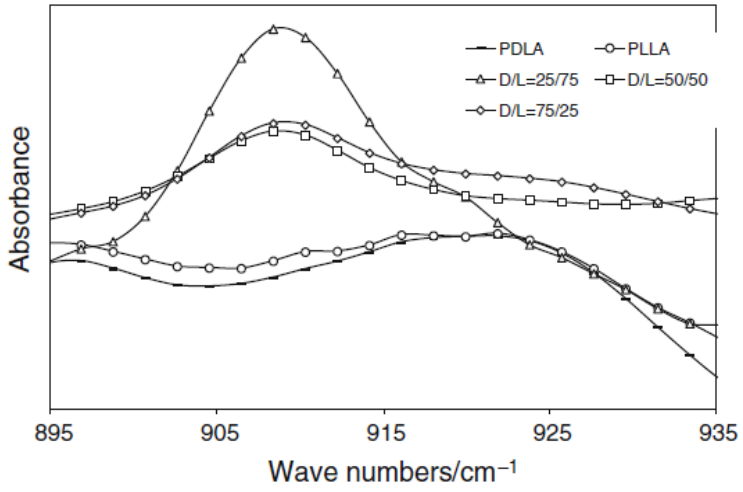

Figure 1. 10. FTIR spectra of homopolymers and sc PLA (e.g. D/L=25/75 corresponds to 25:75 (w/w) ratio of PDLA and PLLA) [38].

1.6 Influence of the different parameters on stereocomplexation

In the racemic mixture of PLLA and PDLA, there is a competition between homocrystallization and stereocomplexation. Several parameters that could influence this competition are follows [25, 33, 37, 39-47]:

- blending ratio of two homopolymers, PLLA and PDLA [25, 48-50]
- molecular weight of two homopolymers [49-51]
- optical purity of the two isomeric polymers [41, 52]
- temperature and time after blending of two homopolymers in solutions [42, 49, 50, 52]
- the solvents utilized for polymer casting [49, 51]
- the structure of co-monomer units and length of the lactide unit sequences in copolymers [53-57].

The most common conditions of blending to form stereocomplex crystallites without homocrystallites include: equimolar mixture of low *MW L*- and *D*-lactide homopolymers [25, 42, 49-52].

1.6.1 Blending ratio of homopolymers

Ikada et al. [25] has reported that the optimum blending ratio for homopolymers is 50:50 at which only stereocomplex is formed. When deviating from equimolar ratio of PLLA and PDLA, the formation of homocrystals is obvious through the appearance of melting peak at 180 °C. As for the equimolar blend, there is only melting of sc-crystals at 230 °C, as shown in Fig 1.11.

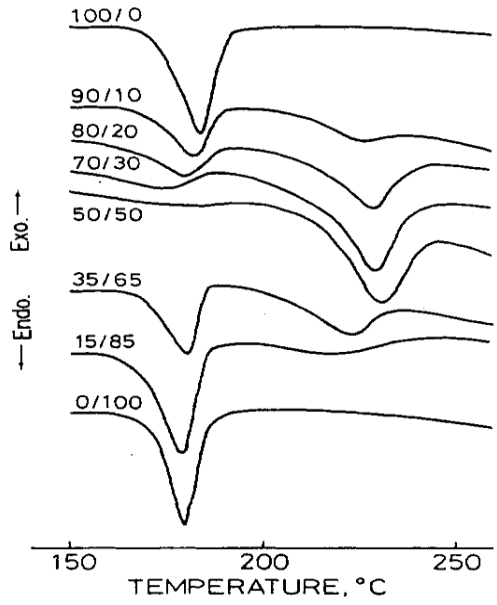

Figure 1. 11. Melting thermograms of polymer blends of PLLA and PDLA in different ratio [25].

In addition, Tsuji et al. [51, 58] indicated that the melting peaks of both homocrystals and stereocomplex were observed when PDLA fraction (X_D) was between 0.1 to 0.3 and 0.7 to 0.9, while the pure stereocomplex was detected for X_D between 0.4 and 0.6 with maximum of the melting enthalpy (ΔH_m) at X_D = 0.5. The only homocrystallization occurred near X_D = 0 and 1. According to the obtained stereocomplex crystalline structure in which PLLA and PDLA chains are paired in each units with the equilateral triangles structure, it is reported that equimolar blending ratio is the optimum condition for yielding formation of stereocomplex crystals.

1.6.2 Molecular weight of homopolymers

The work of Ikada et al. [51, 58] and Tsuji et al. [42, 48] demonstrated that the molecular weight of isomers affects the extent of homocrystallization and stereocomplex formation. In their work, not only the impact of the molecular weight of homopolymers was investigated but also different elaboration methods were compared in order to understand the competition between stereocomplex and homocrystals formation. The investigation was carried out by using different viscosity average molecular weight (M_v) PLLA and fixed PDLA in a 50:50 ratio of PLLA:PDLA. As shown in Fig 1.12, stereocomplex crystals were obtained over a wide range of M_v. Stereocomplexation was preferentially obtained when low molecular weight polymer (approximately below 40 kDa) was used in the film casting process. With increasing molecular weight, the formation of stereocomplex decreases while the homocrystals formation increases. When the polymer was prepared by precipitation accompanied by stirring, stereocomplex crystals formation was obtained regardless molecular weight variations, as shown in Fig 1.12. It can be deduced that the chain mobility in the samples prepared by precipitation is higher compared to the samples prepared by solution casting. However, if the precipitation was carried out in high concentration (5g/dL) and/or without stirring, the stereocomplex crystals failed to form. Instead, only homocrystals were obtained [51, 58].

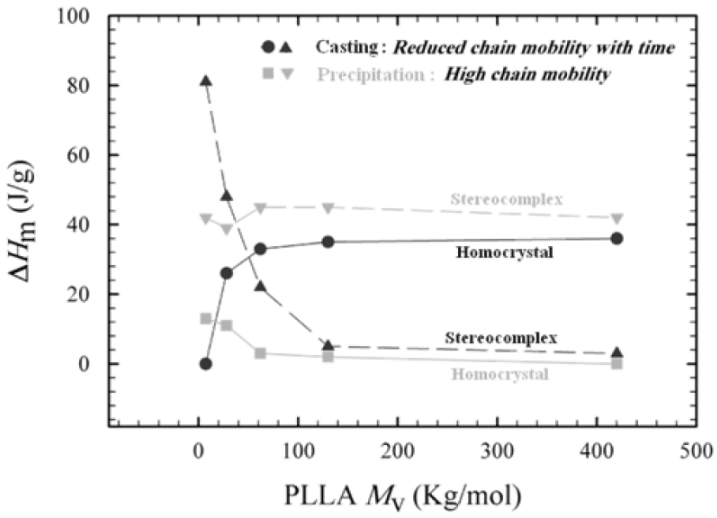

Figure 1. 12. Competitive stereocomplexation and homocrystallization in solution casting and precipitation methods [51, 58].

Fig 1.13 shows the effect of blending method as the function of M_v. Tsuji and Ikada [42] revealed that the stereocomplexation occurred rapidly (e.g. from 90 J/g in 10 kDa polymer prepared by solution casting to 70 J/g when the M_v is approaching 100 kDa) while homocrystallization required longer induction time (e.g. the ΔH_m increases only after 100 kDa).

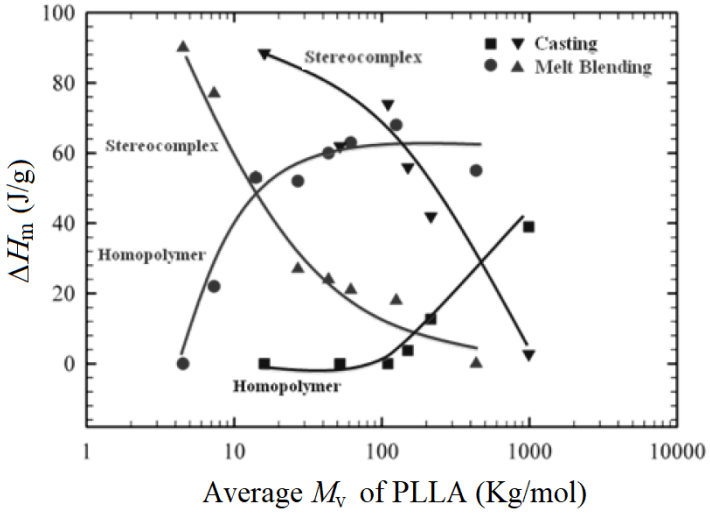

Figure 1. 13. Competitive stereocomplexation and homocrystallization in solution casting and melt blending as the function of M_v of homopolymer isomers [42, 48].

1.6.3 Chain structure of the components

The influence of chain structure on the homocrystallization and stereocomplex formation was investigated by comparing linear and branched PLAs in the racemic mixtures [39]. It was reported that the enhanced nucleation process occurred in the blends due to the branched chain structure. The impact of branched structure was confirmed by reducing cold crystallization temperature (from 140 °C in linear structure down to 111 °C), increasing spherulite density, different growth rate of branched PLAs and different internal morphology during stereocomplexation. In addition, Tsuji and Ikada [59] reported the influence of optical purity on the stereocomplexation of PLLA and PDLA (50:50 ratio) prepared by solution casting. POM micrographs demonstrated that no spherulitic structure was observed for non-blended polymers with optical purity less than 76%. The spherulite density increases with decreasing isothermal crystallization temperature (from 0.2 number/mm^2 at T_c = 140 °C to 1200 number/mm^2 at T_c = 100 °C in the same 98% optical purity PLLA) as well as at higher optical purity (i.e. from 36 number/mm^2 in 76% optical purity PLLA to 1200 number/mm^2 in 98% optical purity PLLA measured at T_c = 100 °C). Furthermore, blended films had higher spherulite density (4200-9700 number/mm^2 at T_c = 100 °C) at any optical purity and crystallization temperature compare to non-blended ones. DSC results depicted that increasing optical purity reduced the cold crystallization temperature and increased melting temperature. No homocrystallization and melting peaks were observed for optical purity less than 90%, and a melting peak corresponded to the stereocomplex crystal was monitored around 230 °C.

Brochu et al. [52] investigated the impact of composition and overall enantiomeric excess on the morphology of sc PLA. The samples were elaborated by solution casting and slow solvent evaporation. The ΔH_m of stereocomplex crystals increases with increasing PDLA content, with the maximum value at 50:50 ratio of 100% pure PLLA and 100% pure PDLA isothermally crystallized at 104 °C. Such result can be explained by the prohibition of homocrystals formation in the presence of stereocomplexation. For the blend films that contain 100% pure PLLA and 80% pure PDLA isothermally crystallized at 115 °C, the maximum ΔH_m for the stereocomplex crystals was achieved at 35:65 (PLLA:PDLA) blend ratio; while for homocrystals can be observed up to 30:70 ratio of PLLA:PDLA. Furthermore, the amount of homocrystals in the blend of 100% and 80% pure PLLA and PDLA, respectively, is similar to the

blend that contains entirely 100% pure homopolymers. On the contrary, the amount of stereocomplex crystals in the blend films containing 100% pure PLLA and 80% pure PDLA was less than that in the blends with 100% pure isomers. Such a consequence can be attributed to two facts: (1) a decline in the stereocomplexation rates due to the *L*- units in 80% optically pure PDLA chain, and (2) higher molecular weight of 80% optically pure PDLA samples as compared to the 100% pure isomers (higher molecular weight ensures slower chain diffusion to form stereocomplex crystals).

1.7 Barrier properties of PLA-based material

Transport property is one of the most important parameters in food packaging industry. The mostly used polymers should be in the form of non-porous films with high barrier property and selectivity. Permeants (H_2O and gases: N_2, O_2 and CO_2) pass through the polymer films when there is a pressure or activity difference between the opposite film interfaces. Permeation through non-porous polymer films is described by "solution-diffusion" mechanism [60-62]. Based on this mechanism, permeation is a complex process involving different sequence of events:

1) absorption of the permeant into the film at its interface applied to the higher pressure or activity
2) molecular diffusion of the permeant in and through the film
3) desorption and release of the permeant from the film at the opposite interface exposed to the lower pressure or activity.

Due to environmental concerns, the transport properties of traditional PLAs were widely investigated for packaging applications [63-68]. However to our best knowledge, the barrier properties of sc PLA is not well investigated. Tsuji and Tsuruno [69] proposed the influence of crystallinity degree and crystal types on the water vapor permeability (WVP) of PLAs. They prepared pure PLLA and PDLA films with homocrystals and PLLA/PDLA blends with only stereocomplex crystals as the crystalline species. Isothermal crystallization process was applied to the elaborated films in order to obtain films with different crystallinity degree and pure crystals. It was shown that the WVP of studied polymers decreases (barrier properties improves) with increasing degree of crystallinity. Water vapor transmission of homopolymers

became slower (permeability coefficient *P* decreased from 2.29 to 1.15 Barrer) with prolong isothermal crystallization time at 140 °C. In the case of sc PLA, the water vapor transmission is faster (*P* increases from 1.00 to 1.81 Barrer) when the sample is isothermally crystallized at higher T_c (ranging from 205 °C to 255 °C). To sum up, the *P* value of sc films is 14-23% lower than that of pure PLLA and PDLA films depending on the degree of crystallinity (Fig 1.14).

Nevertheless, there is no sufficient information about the impact of stereocomplexation on the barrier properties of PLA-based materials, especially towards water and gases (N_2, O_2 and CO_2). In literature, elaborated PLLA/PDLA films were thermally treated after elaboration to increase the purity of crystalline species and degree of crystallinity. Therefore, during this thesis the barrier properties of sc PLA film are studied (cf. Chapter 5). It has been widely accepted that the permeants transport through the "free volume" in amorphous phase disregard of its crystalline structure [70]. Therefore, the next section focuses on the amorphous phase through glass transition concept.

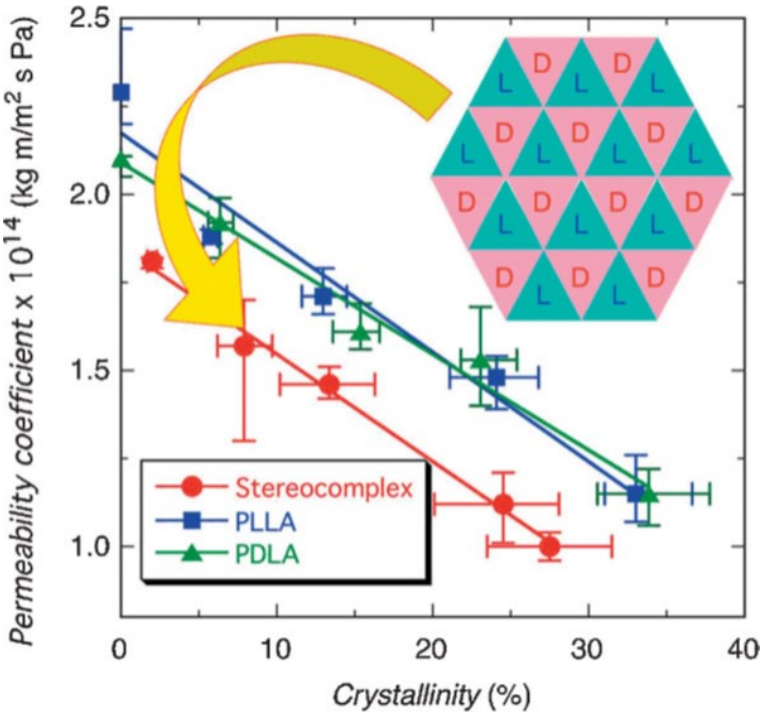

Figure 1. 14. The water vapor permeability coefficient (*P*) dependence on crystallinity degree [69].

1.8 Theory of the glass transition and its phenomenological aspects

The concept of the glass formation and the glass transition temperature (T_g) is detailed with theoretical models to describe the molecular mobility related to the glass transition.

1.8.1 Glasses and the concept of T_g

Glasses are defined as disordered materials, including all solids having a non-crystalline atomic-scale structure. The glasses indicate a transition when heated up to the liquid state. A liquid can form glasses in numerous ways if the applied cooling rate is enough to prevent crystallization of the material [71]. Glasses include different materials display different chemical nature; i.e. oxides [72], chalcogenides [73-75], ionic liquids [76, 77], and polymers [78-80]. The glass transition is a transition from metastable equilibrium (liquid-like state) to the glassy state. Meanwhile glass-forming liquid is cooled down rapidly, its viscosity η increases and reaches a value approximately 10^{13} Poise at a relaxation time close to 100s [81]. The temperature at which the viscosity is reached, is called T_g. The dynamic phenomenon associated to the T_g, so called the α-relaxation, has been widely used to investigate different polymer glass-forming liquids. Most commonly used theories and models are free-volume approach [82, 83], thermodynamic models [84], Adam and Gibbs theory [85], mode coupling theory [86], and coupling model [87]. The glass transition affects different dynamic quantities and thermodynamic parameters such as the viscosity, the heat capacity and the relaxation time which is the required time to recover equilibrium after an external perturbation [88]. Therefore, the T_g can be measured by different experimental techniques, such as dilatometry measurements and differential scanning calorimetry (DSC) measurements. In Fig 1.15 a typical curve shows the evolution of volume, the enthalpy and entropy of a glass-forming liquids as a function of temperature. Once the melting temperature T_m is reached, the thermodynamic properties of crystals turn into liquid state species. The molecules are extremely mobile at and above the equilibrium temperature. If the glass-forming liquid is able to crystalize, the thermodynamic properties of the crystalline state can quietly increase towards to higher temperature (path of the purple line). In this case, the entropy of the equilibrium liquid (S_{liquid}) would be equal to the entropy of the crystal ($S_{crystal}$) at a temperature, so called Kauzmann's temperature (T_K). T_K is inaccessible and can only be determined by extrapolation, so this situation is referred to the Kauzmann's paradox [89-91].

If the liquids were cooled down by sufficient cooling rate to avoid crystallization, the system will reach in a metastable state, so called the liquid-like state (cooling path on wine-red line). Meanwhile the temperature decreases along with the mobility of the molecules to reach the temperature where the liquid state seems to be frozen, the T_g is reached resulting in a discontinuity in the evaluation of the thermodynamic properties. Therefore, the T_g is also commonly defined as the intersection of the liquid and the glassy lines of the thermodynamic properties [92, 93].

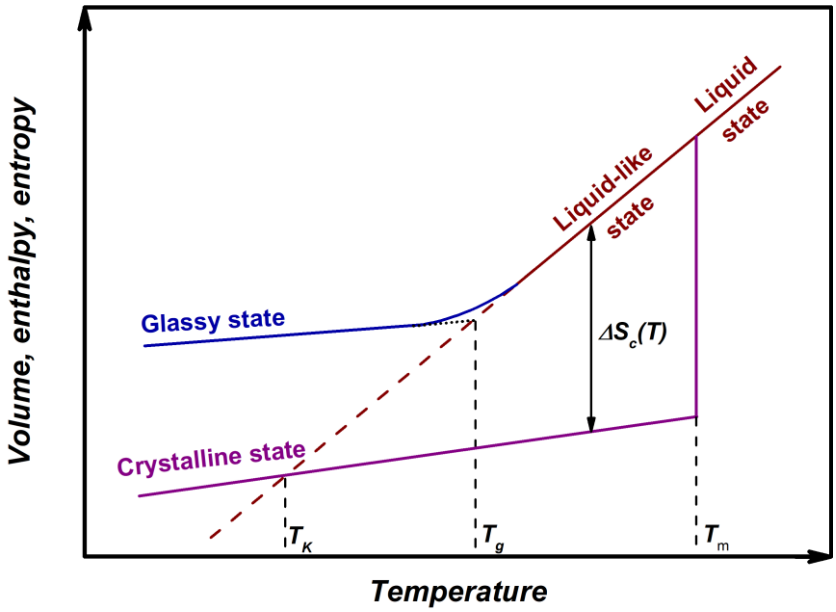

Figure 1. 15. Schematic representation of the thermodynamic properties of a glass-forming liquid as a function of temperature. Wine-red dotted line corresponds to the thermodynamic equilibrium. T_K: Kauzmann's temperature, T_g: glass transition temperature, T_m: melting temperature, ΔS_c: configurational entropy $\Delta S_c = S_{liquid} - S_{crystal}$.

The glass transition kinetic is demonstrated by the dependence of the T_g on the cooling rate [94-96]. The faster cooling rate the higher T_g value and the slower cooling rate the lower T_g value, as depicted in Fig 1.16. Thus, the T_g is not intrinsic temperature because of the dependency on the cooling rate. The cooling rate is defined by the first derivative of the temperature T by time t:

$$\beta_c = \frac{dT}{dt} \tag{1.1}$$

By estimating the cooling as the series of temperature steps, the eq 1.1 can be expressed as the time *t* taken towards each temperature *T*:

$$\Delta t = \frac{\Delta T}{\beta_c} \tag{1.2}$$

Hereby, higher cooling rate resulting in a shorter time between each *T*. Such result allows us to define the idea of relaxation time τ, which is required time by the system to reach the equilibrium after external perturbations. Therefore, the liquid falls out equilibrium when Δ*t* at each *T* is smaller than τ.

$\Delta t >> \tau \rightarrow$ liquid and liquid like state

$\Delta t \approx \tau \rightarrow$ glass transition

$\Delta t << \tau \rightarrow$ glass

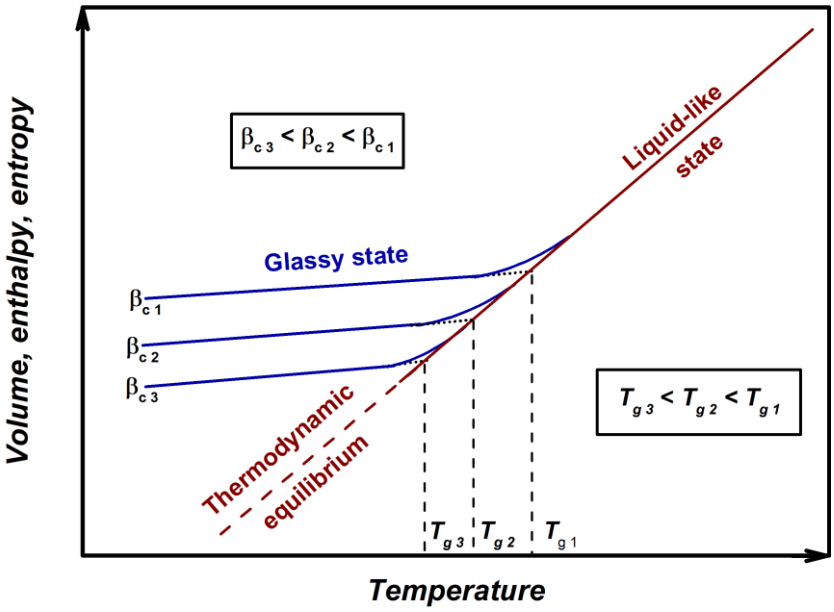

Figure 1. 16. Schematic illustration of the temperature dependence of the thermodynamic properties of a glass-forming system for three different cooling rates β_c. T_{g1}, T_{g2} and T_{g3} are the temperatures correspond to the glasses obtained at different cooling rates β_{c1}, β_{c2}, β_{c3}, respectively, where $\beta_{c3} < \beta_{c2} < \beta_{c1}$.

High cooling rate prevents the possibility of the rearrangement of molecules (cooling rate > relaxation rate), so the molecules can be frozen rapidly. This fact can explain high speed

cooling rate resulting in a higher T_g. The glass transition phenomenon can be explained as a discontinuity in the assessment of the enthalpy *H* (shown in Fig 1.15). The T_g will cause a step in the heat capacity plot as a function of temperature and can be estimated by the middle temperature of the occurring variations as shown in Fig 1.17.

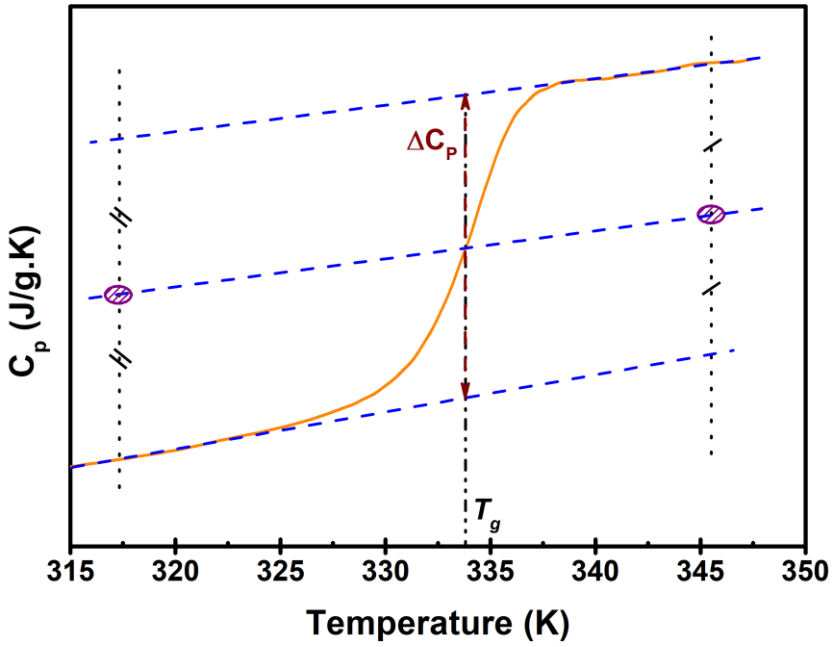

Figure 1. 17. Temperature dependence of the specific heat capacity of PLLA sample obtained by DSC measurement. The glass transition temperature is determined at the middle point.

The fundamental of glass transition is always a point of debate due to its complexity that includes the equilibrium, thermodynamic and kinetic factors related to the nature of the material. The physical properties of the materials, particularly in the case of amorphous polymers, drastically change at T_g. Therefore, any physical characteristics (i.e. chain flexibility, stiffness including steric hindrance, polarity, branching) and/or any other impacts (i.e. crystallization, crosslinking) that affect the chain mobility can also influence the value of T_g.

1.8.2 Theoretical approaches of the glass transition

Recently, various theories and models have been developed to explain the fundamental nature of glass transition in the glass-forming systems. Unfortunately, there is no generally accepted theoretical approach that can successfully describe all phenomena of

the glass transition. Nevertheless, theories based on the thermodynamic and kinetic aspects used in this work are briefly introduced.

1.8.2.1 Free volume model

The free volume theory proposed by Turnbull and Cohen [82] and Doolittle [97] was based on the following assumptions:

- free volume is continuously redistributed without any expense of local free energy for this redistribution, and
- molecular mobility is associated with movement of atoms or molecules into voids of approximately equal or greater size than that of molecular dimensions.

Motions of the molecules, resulting the redistribution of the free volume V_f, can be defined as the difference between the total specific volume V and an occupied volume V_0, i.e. $V_f = V - V_0$. The relation between viscosity and free volume was developed by Doolittle as follows [97]:

$$\ln \eta = \ln A + \frac{B(V-V_f)}{V_f} \tag{1.3}$$

in which η corresponds to viscosity, A and B are the fitting parameters, V is the total specific volume and V_f is the free volume. The average free volume is $v_f = V_f / N$, where N is the number of molecules. The fundamental assumption from Cohen and Turnbull [83] is based on the linear temperature dependency of average free volume (Eq 1.4). They proposed that redistribution of the free volume in viscous liquids takes place without any charge of the local energy. Thus, molecular motion is associated to the mobility of space which has a sufficient large volume to retain a molecule towards the redistribution of free volume.

$$V_f(T) = \alpha_T \overline{V_m}(T - T_0) \tag{1.4}$$

where T_0 is the temperature at which the average free volume is zero, α_T is the thermal expansion coefficient and $\overline{V_m}$ is the mean molecular volume. According to this hypothesis, the free volume model predicts that while the temperature approaches T_0, v_f evanesces, so then the molecular diffusion is stopped. When the contraction occurs, the packing density increases causing a reduced free volume and molecular mobility with the decrease in temperature.

Furthermore, these translational diffusive motions freeze at the glass transition. As a consequence, the free volume approach can be used to clarify strong temperature dependence of relaxation mechanisms like the segmental (α) relaxation or viscosity.

1.8.2.2 The Adam-Gibbs's model: configurational entropy

The configurational entropy S_c was proposed by Adam and Gibbs [85] based on reduction of the relaxation time with decreasing temperature towards the glass transition. The relaxation process of glass-forming liquids takes place by cooperative rearrangements of the molecular groups. Such a motion is only possible if the given number of neighboring molecular groups are dependently in motion. In other words, the rearrangements above energy barriers of molecular units must be "cooperative", involving a number of repeating units that necessarily increases with decreasing temperature. In addition, the systems can be divided into independent and equivalent regions, so called "cooperative rearranging region" (CRR). CRR is defined as the smallest region that can be exposed a new configuration without any essential simultaneous configurational change. The segmental relaxation is based on the rearrangement of the molecules in the CRRs.

1.8.2.3 The concept of cooperativity

Based on the Adam and Gibbs's assumptions, the system can be divided into *N*-independent and equivalent subsystems obtained by *z* molecules; also, *n* of these regions are assumed to be in the thermodynamic state which leads to cooperative rearrangements. The isothermal-isobaric partition function of the system can be defined as [85]:

$$\Delta(z,P,T) = \sum_{E,V} w(z,E,V) \exp\left(-\frac{E}{k_B T}\right) \exp(-\frac{PV}{k_B T}) \quad (1.5)$$

in which *w* is the degeneracy of energy level *E* and volume *V* of the subsystems, and k_B is the Boltzmann constant. If eq 1.5 is limited to the values of *E* and *V*, the fraction (*f*) of CRRs which involving transitions can then be estimated relatively [84]. The probability of cooperative transition *W* (*T*) with *z* molecules, which is proportional to the *f* of CRR, can be expressed as:

$$w\,(T) = A \exp(-\frac{z\Delta\mu}{k_B T}) \quad (1.6)$$

where *A* is a frequency factor which is negligibly dependent on temperature, and Δμ is the difference between the chemical potential of the molecules in cooperative region and the molecules in the non-cooperative region. While the relaxation time τ is related to the transition probability and the relaxation is proportional to the size of CRR region, the temperature dependence of relaxation time in a glass-forming liquid (approaching glass transition) is then expressed as:

$$\tau\,(T) = \tau_0 \exp\left(\frac{C}{TS_c}\right) \tag{1.7}$$

where τ_0 and *C* are constants, S_c corresponds to molar configurational entropy of the macroscopic sample. Although this equation depicts the relation between relaxation time and the configurational entropy, the configurational entropy is not experimentally accessible. Therefore, S_c (*T*) can be linked to the change in the heat capacity $\Delta C_P \sim 1/T$ resulting $S_c(T) \sim (T - T_0) / TT_0$ by using thermodynamic considerations.

1.9 Relaxation phenomena and molecular dynamics

Different molecular motions exist below and above the glass transition temperature in glass-forming systems. The type of polymer relaxation processes depends on the size of the segments that are related to the molecular movements. These movements can be separated in two main motions:

- the movement of long chain segments, and
- the local movement of group of molecules in the chain segment, so called "localized motion".

Deceleration of the molecular movements in glass-forming liquids broadens the relaxation time or frequency interval, and the time shifts to longer interval at T_g. The information about the dynamics of these motions can be obtained by measuring the dielectric responses of the sample; i.e. the complex dielectric function (ε*) or the complex conductivity (σ*). The corresponding response of a time dependent dielectric function ε(*t*) to outer alternating electric field E (*t*) is called a relaxation (Fig 1.18). The relaxation function is measured as the response to external perturbation based on time or frequency. The

characteristic relaxation time τ and/or the relaxation rate $\nu \sim 1/\tau$ of these motions are measured as a function of temperature by dielectric spectroscopy technique [98]. Therefore, the glass transition temperature is conventionally determined on the basis of the time scale, in which the structural relaxation (α-relaxation) time τ_α reaches 100s.

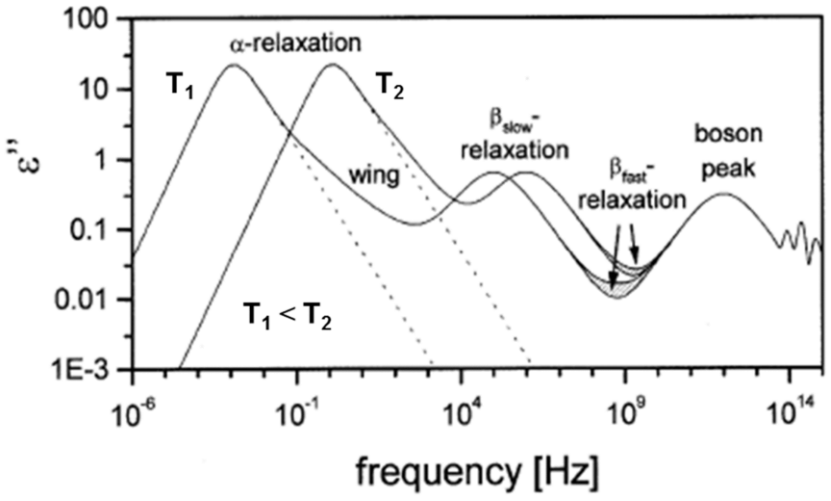

Figure 1. 18. Schematic illustration of dielectric loss spectra in the frequency range 10^{-6} – 10^{15} Hz at temperatures T_1 and T_2 [99]. The dotted lines correspond to the slope at high frequency flank of α-relaxation peaks.

The characteristic dielectric loss spectra in broad range of frequency at two different temperatures are represented in Fig 1.18, where different relaxation processes in glass-forming systems are depicted. A slow process called α-relaxation (primary relaxation) is generally observed at low frequency range. It is well known that many glass-forming systems show a β-relaxation and/or an inflection at the high frequency side of α-relaxation, usually called wing [100, 101]. The secondary process named β-relaxation or β_{slow} is associated with intramolecular fluctuation and can be observed at higher frequency range. The β-relaxation processes can be attributed to the internal change of the molecular conformation, i.e. a molecular side group motion in a polymer. Some other responses can be observed in the higher frequency range like a peak called boson peak, which corresponds to the vibrational properties of the systems. The α-relaxation is associated with the segmental movements and is based on the atrophied diffusion of conformational changes as like gauche-trans transition throughout the polymer chain [98]. Such a conformational changes influence the bond length

and the bond angles, thus increases the probability of a neighboring movements that undergoes a cooperative motions. Therefore, the α-relaxation is a cooperative phenomenon that can be defined as a conformational rearrangement in the amorphous domain which can take place without affecting rearrangements in the surrounding. The cooperative character of the α-relaxation is described by the size of the cooperative rearranging region (CRR) in the Adam and Gibbs approach [85]. The cooperative molecular motion occurs around the crossover temperature T_c, and the CRR size increases with decreasing the temperature to the glass transition temperature. Such an increase in the CRR size is linked to the evident characteristics of the relaxation dynamics around the glass transition, i.e. the non-Arrhenius dependence of the α-relaxation time τ [98].

1.9.1 The non-Arrhenius temperature dependence

Although several work proposed the numerous theories, findings and understanding the universal features of relaxation phenomena in glassy systems are challenging [102, 103]. The study of the dynamics of glass-forming liquids is attractive topic to find an explanation of the Arrhenius to non-Arrhenius temperature dependence of the α-relaxation time τ (or viscosity η) of the glassy polymers while approaching the glass transition temperature. The temperature dependence of the relaxation dynamics can be studied by differential scanning calorimetry (DSC), modulated temperature DSC (MT-DSC), fast scanning calorimetry (FSC), dielectric relaxation spectroscopy (DRS). These techniques allow us to investigate this temperature dependency as schematically demonstrated in Fig 1. 19.

The liquids at very high temperature exhibit Arrhenius temperature dependence, which can be explained by an Arrhenius law:

$$\tau(T) = \tau_\infty \exp\left(\frac{E_a}{k_B T}\right) \tag{1.8}$$

where τ_∞ is the relaxation time at infinite temperature, E_a is the activation energy required for molecular motions and k_B is the Boltzmann constant (k_B = 1.38 × 10^{23} J.K^{-1}). At higher temperature, molecular motions occur with the coupling of α- and β- relaxations.

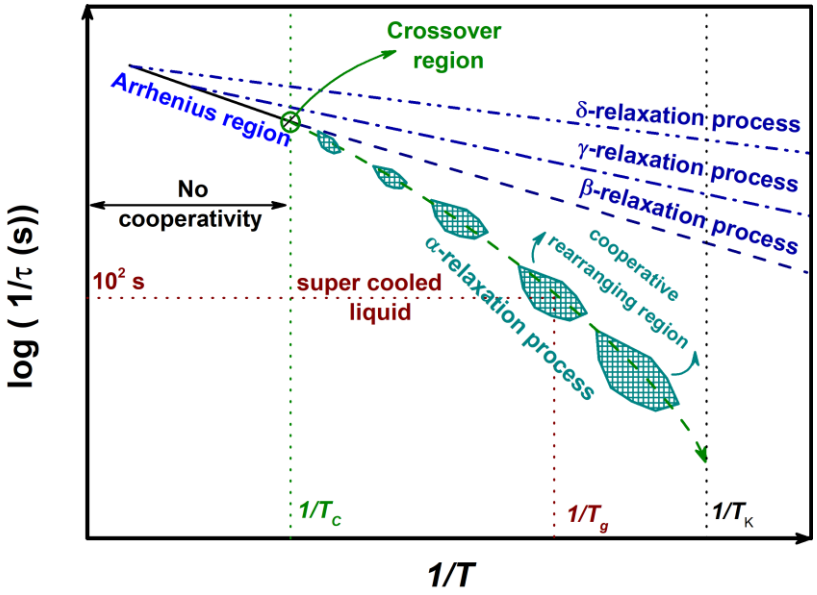

Figure 1. 19. Schematic illustration of the temperature dependence of the relaxation (α, β, γ, and δ) processes in a glass-forming liquid during cooling. The cross-over temperature (T_c), is the temperature at which the α- and β- processes combine each other. The Arrhenius-like behavior is depicted at high temperature. T_g and T_K are the glass transition and Kauzmann's temperature, respectively.

However, when the temperature is decreased to the crossover temperature T_c, these relaxation processes can be separated. The β-relaxation can be still explained by an Arrhenius behavior, the α-relaxation becomes cooperative motions, and can be described by the Adam and Gibbs theory. The temperature decrease of the α-relaxation between T_c and T_K exhibits the non-Arrhenius behavior (also called super-Arrhenius behavior) which can be explained by the empirical Vogel-Fulcher-Tamman (VFT) equation [104-106] as follows:

$$\tau(T) = \tau_0 \exp\left(\frac{D_T T_0}{T - T_V}\right) \quad (1.9)$$

where τ_0 is the relaxation time at infinite temperature, D_T is the strength parameter related to the fragility, and T_V is the characteristic temperature below T_g, so called the Vogel temperature. In addition to the α-relaxation processes, the CRR size is increased by decreasing temperature from T_c to T_K. The VFT law can explain the temperature dependence of the relaxation time of glass-forming liquids up to T_C. However, Ngai [107] presented that the most of the glass-forming systems, in particular polymer systems, have two differentiated temperature dependence of the relaxation processes at the crossover point. Therefore, two

VFT equations are required for good fitting of relaxation data in the temperature range from T_c to T_g. Furthermore, the temperature dependence of the α-relaxation has been studied by using derivative method that proposed by Stickel et al. [108] confirming the presence of the crossover regions. Stickel et al. defined the association of the VFT law in glass-forming liquids with the linearity of the correlation function Φ_T as a function of T. The Stickel's plot indicates the Φ_T versus $1/T$ whereas $\Phi_T = [\mathrm{d} \log_{10} \tau / \mathrm{d} (1/T)]^{-1/2}$. The non-Arrhenius temperature dependence of the α-relaxation time has been extensively investigated to classify the glass-forming liquids based on their relaxation time around T_g. The evaluation from Arrhenius to non-Arrhenius behavior was proposed in the terms of "fragility" to define the degree of the deviation from the Arrhenius dependence [109-111]. Fragility m is used to estimate the dynamic properties and movements of a glass-forming liquids when temperature approaches the glass transition. It shows the steepness of the temperature variations of viscosity η or relaxation time τ approaching T_g, and is expressed as follows:

$$m = \left[\frac{d(\log \tau)}{d\left({}^{T_g}/_{T}\right)}\right]_{T = T_g} \tag{1.10}$$

where m is the fragility index, T is the temperature, T_g is the glass transition temperature and τ is the relaxation time. The value of m gives information about the categories "strong" or "fragile". The systems which show a strong Arrhenius temperature dependence of τ (Arrhenius behavior) are called "strong". Meanwhile, the systems which present a severely non-Arrhenius temperature dependence of τ_α (non-Arrhenius or VFT behavior) with steep variations are known as "fragile". The m value is usually between $16 \leq m \leq 200$. The higher value of m indicates the more fragile systems which show deviation from strong systems, as shown by Angell's plot in Fig 1.20.

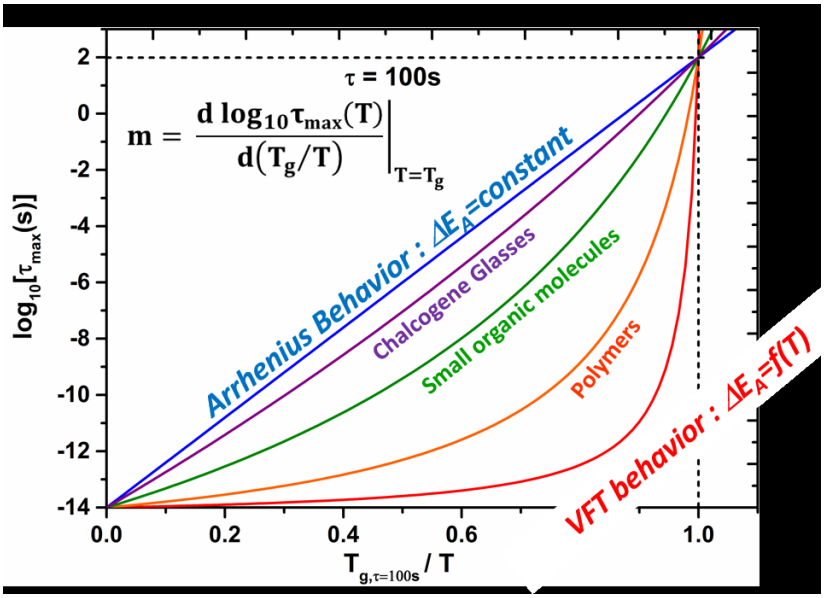

Figure 1. 20. Angell's plot presenting the variations of τ as a function of the normalized temperature $T_{g,\,\tau=100\,s}$ / T from Arrhenius to non-Arrhenius behavior.

1.9.2 The non-exponential behavior

Due to the molecular movements at equilibrium, a simple linear exponential function *exp* (-*t*/τ) is not sufficient to explain the isothermal time dependence of the α-relaxation in liquids. Such behavior can be observed by the time or frequency dependence of the equilibrium liquids measurements, i.e. mechanical [112], dielectric [113] and light scattering [114]. The relaxation or correlation function monitored generally slower decays than the exponential function, so this behavior represents "non-exponential" behavior. The same molecular movements are associated with the structural recovery, therefore the time dependence of the structural relaxation function under non-equilibrium conditions is called also "non-exponential". After long relaxation time, the systems relax completely and the correlation function decay approaches to zero, this corresponds to the α-relaxation of the system. Furthermore, due to the decrease in temperature, the α-relaxation process decelerates and becomes non-exponential near the glass transition. On the other hand, the configurational entropy theory showed that each CRR has unique relaxation time. Therefore, the correlation function in a broad distribution of relaxation time τ is well and simply expressed by a stretched exponential function Φ, so called Kohlraush-Williams-Watt (KWW) function [115, 116]:

$$\Phi\,(t) = exp\left[-\left(\frac{t}{\tau_{KWW}}\right)^{\beta_{KWW}}\right] \tag{1.11}$$

where β_{KWW} is the stretch exponent ($0 \leq \beta_{KWW} \leq 1$) corresponds to the distribution of the relaxation time, τ_{KWW} is the relaxation time. β_{KWW} is inversely proportional to the distribution of relaxation time as when β_{KWW} is near to 0, the distribution is very broad. In addition, when β_{KWW} is close to 1, the time distribution can be characterized by a simple exponential so called Debye relaxation that is observed in liquids above the melting point. Debye relaxation was firstly reported in 1863 to explain the mechanical creep in glassy fibers [115] and was then studied by Williams and Watts in 1970 to investigate dielectric relaxation in polymer systems [116]. The KWW law can be used for different physical and mathematical calculations of models based on distribution of relaxation times to complex correlated processes.

1.10 Dynamic heterogeneity and cooperative movements

There are some important concepts that have been universally accepted and in which the experimental results are linked to the investigation of vitrification and its dynamics. The most well-known studies are the notions of cooperativity and the spatially heterogeneous dynamics, named “dynamic heterogeneity”. The concept of the dynamic heterogeneity is applied to find an answer for why there are severe variations of experimental parameters like relaxation time and viscosity of glass-forming liquids towards glass transition [117-119]. Ediger [118] proposed that the dynamic heterogeneity may be expressed by the different regions (few nanometers away from each other) in a liquid including sub-ensembles of particles that show momentarily increased or diminished mobility relative to the average mobility. If these particles have higher mobility than the average, they are defined as “mobile” or “fast” particles. Those particles with lower mobility are considered to be “immobile” or “slow” particles. Dynamic heterogeneity in the glass-forming liquids is not static as it improves over time. The notion of dynamic heterogeneity exudes the dynamically correlated movements of the particles in the regions. Therefore, molecular cooperativity associated with the glass transition is intimately related to the dynamic heterogeneity [120-124]. Indirect methods, i.e. multipoint dynamic susceptibility function [125-127] and thermodynamic methods based on the fluctuation-dissipation theory [123, 128], are currently used for understanding the dynamic heterogeneity. These approaches lead to estimate the length scale at T_g that is

approximately from 1 nm to 4 nm for different glass-forming liquids [129]. It has been found that the dynamics of the glass-forming liquids is dynamically heterogeneous towards the calorimetric glass transition temperature T_g. The discovery of the dynamical heterogeneity well defines the deviation from the exponential behavior of the glass-forming systems responses. Furthermore, the variations in the temperature dependence of transitional or rotational diffusion in the systems approaching to the glass transition can be also defined by the dynamic heterogeneity existence. Thus, the approaches have been focused on the notion of the heterogeneous dynamics of the α-relaxation processes in the liquid-like state for better understanding the nature of the molecular mechanisms associated to the glass transition. Therefore, the majority of the research groups focus on the length scale of dynamic heterogeneity and the cooperativity as a function of time and temperature for polymer glass-forming liquids. Two independent models are mostly used to estimate the length scale. One model was proposed by Berthier et el. [125] on the basis of the higher order correlation function, the other one was reported by Donth [130] based on the fluctuation dissipation theory.

1.10.1 Length scale from four-point dynamic susceptibility function

Since the α-relaxation exhibits both super-Arrhenius and non-exponential behavior towards the glass transition temperature, the existence of the length scale associated to the coexistence of molecules with essentially different relaxation time is still widely investigated. Dynamical heterogeneity is spatially organized into fast and slow regions with a typical size. To define the quantity in dynamics, the two-point correlation function is used [125] and is generally expressed by the KWW (a stretched exponential) function to define the α-relaxation in glass-forming systems. However, the two-correlation function cannot individuate the homogenous and heterogeneous movements in one region of a glass-forming liquids. Therefore, higher order correlation function “four-point dynamic susceptibility” of the density fluctuation is used to investigate the behavior and magnitude of the dynamically correlated molecules in glass-forming liquids (i.e. repeating units in the case of polymers). Four-point dynamic susceptibility corresponds to the spatial correlation of localized particles, as the evident location is associated to the correlated motion of the particles occupied by neighboring particles [131, 132]. When two-point correlation function involves the variables

at two times for the dynamics description, the four-point correlation function expresses the spatial and temporal fluctuation of dynamic heterogeneity [120]. Therefore, the four-point susceptibility χ_4 (t) is estimated by the integration of the probability of a similar event that occurs at a distance r at the same time interval t (C_4 (r, t)) as [133]:

$$\chi_4(t) = \int C_4\,(r,t)dr \tag{1.12}$$

where χ_4 (t) corresponds to the maximum value at the relaxation time τ_α of glass-forming liquids. Interactions between regimes play a role on a longer time scale, then these regimes are separated in early and late regimes due to the elasticity theory. Later then, because of the approach and departure from the plateau of the four-point susceptibility function, the relaxation time τ_α is reached, and χ_4 (t) presents a peak with a maximum, which is proportional to the volume where correlation movements occur. The number of correlated molecules $N_{COOR,\,4}$ in an average relaxation time τ_α can be estimated as [120, 122, 125]:

$$N_{COOR,4} = max_t\,\{X_4\,(t)\} \tag{1.13}$$

Due to the impossibility of an experimental measurements of χ_4 (t), Berthier et al. [125] proposed a new model to estimate a typical length scale of the dynamic heterogeneity on the basis of the temperature dependence. They modified the four-point susceptibility function to the three-point dynamic susceptibility χ_T (t) which is experimentally accessible [125]. The χ_T (t) exhibits a peak at $t \sim \tau_\alpha$ from which the number of molecules N_C, whose dynamics on the time scale of the α-relaxation are correlated, can be estimated [134]:

$$N_C = \frac{N_A}{m_0}\frac{k_B}{\Delta C_P}\,T^2 \max(\chi_T(t))^2 \text{ , or } N_C = \frac{N_A}{m_0}\frac{k_B}{\Delta C_P}\,T^2 \max\left(\frac{\delta\varepsilon}{\delta T}\right)^2 \tag{1.14}$$

where N_C is the number of the dynamically correlated segments (repeating units in polymers), m_0 is the molecular weight of the repeating units, N_A is the Avogadro's number, ΔC_P is the variation in heat capacity between liquid and glassy states, k_B is the Boltzmann constant, and ε is the dielectric relaxation function. When the dielectric relaxation function shows a Kohlrausch form with a stretch exponent, the number of dynamically correlated units can be estimated by a simpler form or by eq. 1.14 as Capaccioli et al. proposed [135]:

$$N_C = \frac{N_A}{m_0}\frac{k_B}{\Delta C_P}\left(\frac{\beta_K}{e}\right)^2\left(\frac{dln\,\tau_\alpha}{dln\,T}\right)^2 \quad (1.15)$$

where ΔC_P is the variation in heat capacity between liquid and glassy states, m_0 is the molecular weight of the repeating units, N_A is the Avogadro's number, k_B is the Boltzmann constant, β_K is the stretch parameter, e is the Euler's number and τ_α is the relaxation time of α-process. As consequence, N_C increases with decreasing temperature and increase of τ_α as a function of temperature T and relaxation time τ_α, respectively.

In this work, the number of dynamically correlated systems is calculated using eq. 1.15. Different parameters in eq. 1.15 can be usually exported from the results of two experimental techniques that are DRS and MT-DSC.

1.10.2 Length scale from temperature fluctuation: Donth's approach

Donth proposed a simple method based on the temperature fluctuation in subsystems (CRR) in order to calculate the length scale at the calorimetric glass transition [129, 136]. As explained in the Adam-Gibbs's theory, the CRRs are definable independent subsystems that demonstrate thermodynamic fluctuations [85]. Therefore, CRR represents an independent relaxation from the rest of the system over its own relaxation time τ as well as own glass transition T_α. In addition, the dispersion in relaxation time can be linked to the distribution of T_α between these subsystems. Therefore, an average dynamic glass transition $<T_\alpha>$ of all subsystems can be defined as the conventional calorimetric glass transition temperature T_g. The density ρ, the temperature T, the entropy S and the energy E of the subsystems can be different in each equal sub-volume of the glass-forming liquids. The thermodynamic fluctuations were limited to slow degree freedom of the α-relaxation and the width of the relaxation times of α-processes [137]. Therefore, a characteristic length of glass transition can be estimated from experimental data.

Donth assumed that each CRR has partial structural entities with own frequency and local free volume that fluctuate during time as frequency is the function of the partial free volume. CRR is divided into the equivalent partial systems which are considered as statically independent but cooperatively associated by free volume redistribution. Therefore, Donth considered that the partial functions for each entities are independent and cooperative

movements are caused by the distribution of the partial free volume. Moreover, these partial subsystems can be investigated by its frequency and free volume and involved populations that are linked to a temperature. Then, an average temperature fluctuation δT confirmed in a CRR between the different populations.

The independent and equivalent free volume is thermodynamically in the metastable equilibrium where the fluctuation in variables can be defined by Gaussian fitting. The energy fluctuation is dependent on the isochoric heat capacity ($J.K^{-1}$), the freedom degree of the α-relaxation processes and vibrational motion associated with glass below T_g [138]. Therefore, the relation between the average T_g and the thermal heat capacity can be defined as:

$$\left(\delta T_g\right)^2 = k_B T_g^2 \frac{\Delta C_V}{C'_{V,\alpha}} \tag{1.16}$$

and/or

$$\frac{\Delta C_V}{C'_{V,\alpha}} \approx \Delta\left(\frac{1}{C_V}\right) = \frac{1}{C_{V,glass}} - \frac{1}{C_{V,liquid}} \tag{1.17}$$

By assuming that the variation of $1/C_P$ is identical with that of $1/C_V$, then:

$$\left(\delta T_g\right)^2 = k_B T_g^2 \Delta\left(\frac{1}{C_P}\right) \tag{1.18}$$

can be expressed. To calculate a length scale of cooperativity, the heat capacity $C'_{P,\alpha}$ ($J.K^{-1}$) can be modified in terms of the specific heat capacity in unit of $J\ g^{-1}\ K^{-1}$ as follows:

$$C'_{P,\alpha} = C_{P,\alpha}\ \rho\ V_\alpha \tag{1.19}$$

in which $C_{P,\alpha} = C_{P,\,T>Tg} - C_{P,\,T<Tg}$ is the change in the specific heat capacity step at the glass transition. Thus, the characteristic length scale of the glass transition ξ_α and the volume can be expressed as:

$$\xi_\alpha = \sqrt[3]{V_\alpha} = \sqrt[3]{\frac{\Delta C_P^{-1}\ k_B\ T_\alpha^2}{\rho\ (\delta T)^2}} \tag{1.20}$$

where ΔC_P^{-1} is the variation in the inverse of the isobaric heat capacity for liquid and glass at the dynamic glass transition temperature T_α, k_B is the Boltzmann constant, ρ is the density at T_α and δT is the temperature fluctuation in a CRR at T_α.

Correspondingly, the number of structural units in a CRR (N_α) can be estimated as:

$$N_\alpha = \frac{N_A k_B T_\alpha^2 \Delta C_P^{-1}}{m_0 (\delta T)^2} \quad (1.21)$$

where N_A is the Avogadro's number and m_0 is the molar mass of repeating unit.

The parameters of the Donth's approach, T_α, δT and ΔC_P^{-1} can be exported from calorimetric techniques such as DSC and MT-DSC. The cooperativity length ξ_α at the glass transition estimated by Donth's approach for glassy polymers is usually in the range of 1-3.6 nm [139-142].

1.10.3 The cooperativity size in a wide temperature and frequency range

The classical Donth's model proposed the CRR size estimation in only narrow temperature and frequency range close to the calorimetric T_g. However, the combination of two experimental techniques (MT-DSC and DRS) allow us to estimate the cooperativity length in a broad temperature and frequency range [142, 143]. There are several common and complementary notions of the glass transition used in these two techniques:

- the dynamic glass transition can be monitored by applying a periodic perturbation to the sample, i.e. a modulated temperature ramp in MT-DSC and a periodic electric field in DRS. Therefore, such techniques allow us to measure the complex quantities of the heat capacity C_P^* by MT-DSC and the dielectric permittivity ε^* by DRS involving real (C_P' and ε') and imaginary (C_P'' and ε'') parts, respectively;
- due to the linear response theory, both real and imaginary quantities can be directly compared;
- in case of MT-DSC, the dynamic glass transition can be estimated by a heat capacity step ΔC_P in the real part, while the relaxation peak can be observed in the imaginary part;

- in case of DRS, the dynamic glass transition can be determined from the dielectric strength $\Delta\varepsilon$, and a peak of ε" in the imaginary part.

Therefore, both ΔC_P and $\Delta\varepsilon$ correspond to the amorphous phase species at the dynamic glass transition temperature. So, the glass forming liquids exhibit a relaxation time distribution function at each temperature step. As the consequence, the temperature fluctuation δT is associated to the standard deviation σ_T of the Gaussian peak function, so the average temperature fluctuation δT can be obtained from the imaginary part C_P'' (T) of complex heat capacity as well as from the imaginary part ε'' (T) of the complex dielectric permittivity. In DRS analysis, the dynamic glass transition T_α is determined from the maximum of the peak in DRS spectra. The parameters of the Donth's approach, T_α, δT and ΔC_P^{-1} can be obtained by these two techniques and combined to extend Donth's approach to calculate the temperature dependence of the CRR size as well as the cooperativity degree N_α in a wide temperature range (from Eq 1.20 and 1.21, respectively).

1.11 Structural relaxation of glassy polymers

Besides the Arrhenius and non-Arrhenius temperature dependences of the α-relaxation process in glass-forming liquids, the structural relaxation takes place when the temperature approaches the glass transition temperature and below.

1.11.1 Physical aging concept

Even though the glassy form seems to be "frozen" on the measurement scale below glass transition temperature, a molecular mobility still exists [92, 93]. Therefore, when the glass-forming liquids are held below their respective glass transition temperature, so called physical aging (the structural relaxation) will occur. Such a structural relaxation is the convergent evolution of the thermodynamic properties towards equilibrium [93]. Such thermodynamic properties towards equilibrium are associated with a free volume hole diffusion towards surfaces which could be the external ones of the system or the internal ones in the low density region obtained by controlled cooling rate [144-146]. Thus, investigation of structural relaxation in the terms of physical aging gives information about molecular motions/dynamics.

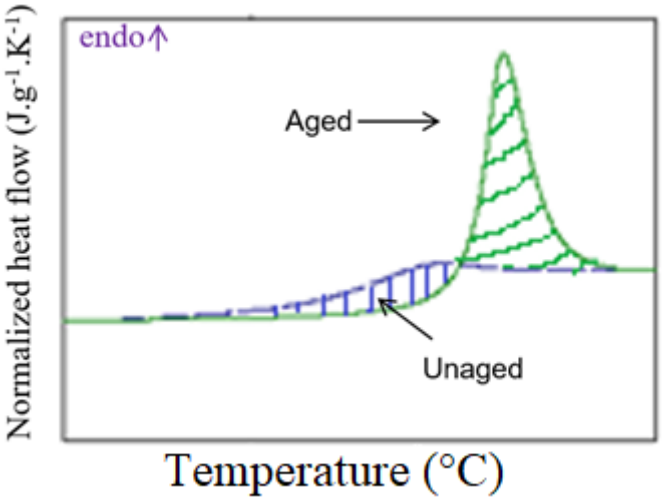

Figure 1. 21. Illustration of the heat flows of a glass-forming liquids during physical aging. Green area corresponds to superimposed peak at T_g (aged sample), blue area corresponds to unaged sample.

The physical aging can be studied by calorimetric investigations. When glass is held isothermally below the glass transition temperature, the following heating curve will exhibit a peak superimposed to the glass transition as shown in Fig 1.21. Such a peak is related to the enthalpy recovery of a glass forming liquids and gives an information about the excess of the energy released during physical aging. Enthalpy recovery of a glass that aged at a temperature T_{ag} for an aging time t_{ag} is calculated by the integration of the variations between the measure of aged and rejuvenated sample by following equation [147]:

$$\Delta H\left(T_{ag}, t_{ag}\right) = \int_{T_1}^{T_2} [C_P^a(T) - C_P^r(T)].dT \quad (1.22)$$

where C_P^a (T) and C_P^r (T) are the heat capacity of the aged and rejuvenated (unaged) sample, and T_1 and T_2 are the optional temperatures below and above the glass transition temperature, respectively. It is considered that equilibrium is reached for an infinite aging time. Therefore, the expected total enthalpy loss ΔH_∞ can be extrapolated from the equilibrium depending on the aging temperature T_{ag} and the glass transition temperature T_g, as well as the heat capacity step ΔC_P of the sample, as expresses by follows:

$$\Delta H_\infty = \Delta C_P\left(T_g - T_{ag}\right) \quad (1.23)$$

1.11.2 The fictive temperature concept

Due to the kinetics related with the glass transition temperature and devitrification upon heating, T_g can be measured by the concept of the fictive temperature T_f. The fictive temperature is thermodynamically defined as the crossover point of the enthalpies of the glassy and the liquid-like state at non-equilibrium process. This concept has been reported by Tool et Eicitlin in 1931 [148]. The kinetics of the structural relaxation can be also investigated by measuring the fictive temperature as a function of aging time. The fictive temperature concept is also used to examine the cooling rate dependence of the glass transition in order to understand the nature of glass-forming liquids. The kinetic impact of the cooling rate can be observed upon subsequent heating from the glassy state to liquid-like state. When a glass is obtained at β_{c1} and then it is heated at the same rate ($|\beta_{c1}| = \beta_{h1}$), the enthalpy recovery will occur on the same line at the liquid-like state. However, if a glass is formed at β_{c2} ($\beta_{c2} << \beta_{c1}$), the glass transition temperature will decrease. Then, a glass is heated at β_{h1} ($\beta_{h1} >> \beta_c$), the enthalpy recovery exhibits a peak superimposed on the glass transition upon heating. The fictive temperature T_f can be measured from calorimetric measurements, i.e. DSC and FSC by the Moynihan's equation [149]:

$$\int_{T_1}^{T_f}\left(C_{P,liquid} - C_{P,glass}\right).dT = \int_{T_1}^{T_2}\left(C_P - C_{P,glass}\right).dT \qquad (1.24)$$

where T_1 and T_2 are the optional temperatures above and below the glass transition, respectively; C_P is the heat capacity of the sample at constant pressure, $C_{P,\,liquid}$ and $C_{P,\,glass}$ are the extrapolated liquid and glassy heat capacity lines of the sample, respectively.

Background history of PLA-based materials and related theoretical approaches have been presented in this chapter. Existing literature focused its attention to the crystalline structure of sc PLA with very little emphasis on the amorphous phase. With this in mind, we established our objectives to understand the structural-property relationship of sc PLA. In Chapter 2 detailed experimental set-ups are presented in order to achieve the mentioned objectives. The effect of two different elaboration techniques on the sc PLA formation was first investigated (Chapter 3). Following this, we investigated the impact of tacticity/chirality on the amorphous species of sc PLA (Chapter 4). And lastly, the glass transition property in terms

of free volume concept (molecular mobility) was linked to the transport property of sc PLA as compared to that of homopolymers and commercial PLA (Chapter 5).

References

1. Pagni, R. Modern Physical Organic Chemistry (Eric V. Anslyn and Dennis A. Dougherty). *Journal of Chemical Education* **2006,** 83 (3), 387 DOI: 10.1021/ed083p387.
2. Hicks, J. M., *Chirality: Physical Chemistry*. American Chemical Society: 2002; Vol. 810, p 372.
3. Hartmann, M. H., High Molecular Weight Polylactic Acid Polymers. In *Biopolymers from Renewable Resources*, Kaplan, D. L., Ed. Springer Berlin Heidelberg: Berlin, Heidelberg, 1998; pp 367-411.
4. Pan, P.; Inoue, Y. Polymorphism and isomorphism in biodegradable polyesters. *Progress in Polymer Science* **2009,** 34 (7), 605-640 DOI: https://doi.org/10.1016/j.progpolymsci.2009.01.003.
5. Guoming, L.; Xiuqin, Z.; Dujin, W. Tailoring Crystallization: Towards High-Performance Poly(lactic acid). *Advanced Materials* **2014,** 26 (40), 6905-6911 DOI: doi:10.1002/adma.201305413.
6. Hiroharu, A.; Shogo, I.; Kai, K.; Mitsuru, A. Catechin-Modified Polylactide Stereocomplex at Chain End Improved Antibiobacterial Property. *Macromolecular Bioscience* **2016,** 16 (5), 694-704 DOI: doi:10.1002/mabi.201500398.
7. Gupta, B.; Revagade, N.; Hilborn, J. Poly(lactic acid) fiber: An overview. *Progress in Polymer Science* **2007,** 32 (4), 455-482 DOI: https://doi.org/10.1016/j.progpolymsci.2007.01.005.
8. Sun, Y.; He, C. Synthesis and Stereocomplex Crystallization of Poly(lactide)–Graphene Oxide Nanocomposites. *ACS Macro Letters* **2012,** 1 (6), 709-713 DOI: 10.1021/mz300131u.
9. Isono, T.; Kondo, Y.; Otsuka, I.; Nishiyama, Y.; Borsali, R.; Kakuchi, T.; Satoh, T. Synthesis and Stereocomplex Formation of Star-Shaped Stereoblock Polylactides Consisting of Poly(l-lactide) and Poly(d-lactide) Arms. *Macromolecules* **2013,** 46 (21), 8509-8518 DOI: 10.1021/ma401375x.
10. Gao, C.; Yu, L.; Liu, H.; Chen, L. Development of self-reinforced polymer composites. *Progress in Polymer Science* **2012,** 37 (6), 767-780 DOI: https://doi.org/10.1016/j.progpolymsci.2011.09.005.
11. Raquez, J.-M.; Habibi, Y.; Murariu, M.; Dubois, P. Polylactide (PLA)-based nanocomposites. *Progress in Polymer Science* **2013,** 38 (10), 1504-1542 DOI: https://doi.org/10.1016/j.progpolymsci.2013.05.014.
12. Suming, Y.; Ting, T. L.; Weng, W. T.; Pui, K. W.; Chaobin, H. Rubber toughening of poly(lactic acid): Effect of stereocomplex formation at the rubber-matrix interface. *Journal of Applied Polymer Science* **2013,** 128 (4), 2541-2547 DOI: doi:10.1002/app.38568.
13. Tsuji, H. Poly(lactide) Stereocomplexes: Formation, Structure, Properties, Degradation, and Applications. *Macromolecular Bioscience* **2005,** 5 (7), 569-597 DOI: doi:10.1002/mabi.200500062.
14. Gruber, P. R.; Hall, E. S.; Kolstad, J. H.; Iwen, M. L.; Benson, R. D.; Borchardt, R. L. US Pantent 5142023. 1992.
15. De Santis, P.; Kovacs, A. J. Molecular conformation of poly(S-lactic acid). *Biopolymers* **1968,** 6 (3), 299-306 DOI: doi:10.1002/bip.1968.360060305.
16. Kalb, B.; Pennings, A. J. General crystallization behaviour of poly(l-lactic acid). *Polymer* **1980,** 21 (6), 607-612 DOI: https://doi.org/10.1016/0032-3861(80)90315-8.
17. Kobayashi, J.; Asahi, T.; Ichiki, M.; Oikawa, A.; Suzuki, H.; Watanabe, T.; Fukada, E.; Shikinami, Y. Structural and optical properties of poly lactic acids. *Journal of Applied Physics* **1995,** 77 (7), 2957-2973 DOI: 10.1063/1.358712.
18. Puiggali, J.; Ikada, Y.; Tsuji, H.; Cartier, L.; Okihara, T.; Lotz, B. The frustrated structure of poly(l-lactide). *Polymer* **2000,** 41 (25), 8921-8930 DOI: https://doi.org/10.1016/S0032-3861(00)00235-4.
19. Zhang, J.; Duan, Y.; Sato, H.; Tsuji, H.; Noda, I.; Yan, S.; Ozaki, Y. Crystal Modifications and Thermal Behavior of Poly(l-lactic acid) Revealed by Infrared Spectroscopy. *Macromolecules* **2005,** 38 (19), 8012-8021 DOI: 10.1021/ma051232r.
20. Kawai, T.; Rahman, N.; Matsuba, G.; Nishida, K.; Kanaya, T.; Nakano, M.; Okamoto, H.; Kawada, J.; Usuki, A.; Honma, N.; Nakajima, K.; Matsuda, M. Crystallization and Melting Behavior of Poly (l-lactic Acid). *Macromolecules* **2007,** 40 (26), 9463-9469 DOI: 10.1021/ma070082c.

21. Zhang, J.; Tashiro, K.; Tsuji, H.; Domb, A. J. Disorder-to-Order Phase Transition and Multiple Melting Behavior of Poly(l-lactide) Investigated by Simultaneous Measurements of WAXD and DSC. *Macromolecules* **2008,** 41 (4), 1352-1357 DOI: 10.1021/ma0706071.
22. Eling, B.; Gogolewski, S.; Pennings, A. J. Biodegradable materials of poly(l-lactic acid): 1. Melt-spun and solution-spun fibres. *Polymer* **1982,** 23 (11), 1587-1593 DOI: https://doi.org/10.1016/0032-3861(82)90176-8.
23. Hoogsteen, W.; Postema, A. R.; Pennings, A. J.; Ten Brinke, G.; Zugenmaier, P. Crystal structure, conformation and morphology of solution-spun poly(L-lactide) fibers. *Macromolecules* **1990,** 23 (2), 634-642 DOI: 10.1021/ma00204a041.
24. Cartier, L.; Okihara, T.; Ikada, Y.; Tsuji, H.; Puiggali, J.; Lotz, B. Epitaxial crystallization and crystalline polymorphism of polylactides. *Polymer* **2000,** 41 (25), 8909-8919 DOI: https://doi.org/10.1016/S0032-3861(00)00234-2.
25. Ikada, Y.; Jamshidi, K.; Tsuji, H.; Hyon, S. H. Stereocomplex formation between enantiomeric poly(lactides). *Macromolecules* **1987,** 20 (4), 904-906 DOI: 10.1021/ma00170a034.
26. Pauling, L.; Corey, R. B. Two Rippled-Sheet Configurations of Polypeptide Chains, and a Note about the Pleated Sheets. *Proceedings of the National Academy of Sciences of the United States of America* **1953,** 39 (4), 253-256.
27. Fox, T. G.; Garrett, B. S.; Goode, W. E.; Gratch, S.; Kincaid, J. F.; Spell, A.; Stroupe, J. D. Crystalline polymers of methyl methacrylate. *Journal of the American Chemical Society* **1958,** 80 (7), 1768-1769 DOI: 10.1021/ja01540a068.
28. Slager, J.; Domb, A. J. Biopolymer Stereocomplexes. *Advanced Drug Delivery Reviews* **2003,** 55, 549-583 DOI: http://dx.doi.org/10.1016/S0169-409X(03)00042-5
29. Hideto, T.; Tomohiko, T. Crystallization Behavior of Stereo Diblock Poly(Lactide)s with Relatively Short Poly(D-Lactide) Segment from Partially Melted State. *Macromolecular Materials and Engineering* **2014,** 299 (9), 1089-1105 DOI: doi:10.1002/mame.201400002.
30. Yuzuru, S.; Hideto, T. Stereocomplex Crystallization Behavior and Physical Properties of Linear 1-Arm, 2-Arm, and Branched 4-Arm Poly(L-lactide)/Poly(D-lactide) Blends: Effects of Chain Directional Change and Branching. *Macromolecular Chemistry and Physics* **2013,** 214 (7), 776-786 DOI: doi:10.1002/macp.201200657.
31. Tsuji, H.; Hosokawa, M.; Sakamoto, Y. Ternary Stereocomplex Formation of One l-Configured and Two d-Configured Optically Active Polyesters, Poly(l-2-hydroxybutanoic acid), Poly(d-2-hydroxybutanoic acid), and Poly(d-lactic acid). *ACS Macro Letters* **2012,** 1 (6), 687-691 DOI: 10.1021/mz300155f.
32. Biela, T.; Duda, A.; Penczek, S. Enhanced Melt Stability of Star-Shaped Stereocomplexes As Compared with Linear Stereocomplexes. *Macromolecules* **2006,** 39 (11), 3710-3713 DOI: 10.1021/ma060264r.
33. Okihara, T.; Tsuji, M.; Kawaguchi, A.; Katayama, K.-I.; Tsuji, H.; Hyon, S.-H.; Ikada, Y. Crystal structure of stereocomplex of poly(L-lactide) and poly(D-lactide). *Journal of Macromolecular Science, Part B* **1991,** 30 (1-2), 119-140 DOI: 10.1080/00222349108245788.
34. Cartier, L.; Okihara, T.; Lotz, B. Triangular Polymer Single Crystals: Stereocomplexes, Twins, and Frustrated Structures. *Macromolecules* **1997,** 30 (20), 6313-6322 DOI: 10.1021/ma9707998.
35. Tsuji, H.; Horii, F.; Nakagawa, M.; Ikada, Y.; Odani, H.; Kitamaru, R. Stereocomplex formation between enantiomeric poly(lactic acid)s. 7. Phase structure of the stereocomplex crystallized from a dilute acetonitrile solution as studied by high-resolution solid-state carbon-13 NMR spectroscopy. *Macromolecules* **1992,** 25 (16), 4114-4118 DOI: 10.1021/ma00042a011.
36. He, Y.; Xu, Y.; Wei, J.; Fan, Z.; Li, S. Unique crystallization behavior of poly(l-lactide)/poly(d-lactide) stereocomplex depending on initial melt states. *Polymer* **2008,** 49 (26), 5670-5675 DOI: https://doi.org/10.1016/j.polymer.2008.10.028.
37. Song, Y.; Zhang, X.; Yin, Y.; de Vos, S.; Wang, R.; Joziasse, C. A. P.; Liu, G.; Wang, D. Enhancement of stereocomplex formation in poly(l-lactide)/poly(d-lactide) mixture by shear. *Polymer* **2015,** 72, 185-192 DOI: https://doi.org/10.1016/j.polymer.2015.07.023.

38. Ahmed, J.; Varshney, S. K.; Janvier, F. Rheological and thermal properties of stereocomplexed polylactide films. *Journal of Thermal Analysis and Calorimetry* **2014,** 115 (3), 2053-2061 DOI: 10.1007/s10973-013-3234-9.
39. Nouri, S.; Dubois, C.; Lafleur, P. G. Homocrystal and stereocomplex formation behavior of polylactides with different branched structures. *Polymer* **2015,** 67, 227-239 DOI: https://doi.org/10.1016/j.polymer.2015.04.065.
40. Woo, E. M.; Chang, L. Crystallization and morphology of stereocomplexes in nonequimolar mixtures of poly(l-lactic acid) with excess poly(d-lactic acid). *Polymer* **2011,** 52 (26), 6080-6089 DOI: https://doi.org/10.1016/j.polymer.2011.11.002.
41. Tsuji, H.; Ikada, Y. Stereocomplex formation between enantiomeric poly(lactic acid)s. 6. Binary blends from copolymers. *Macromolecules* **1992,** 25 (21), 5719-5723 DOI: 10.1021/ma00047a024.
42. Tsuji, H.; Ikada, Y. Stereocomplex formation between enantiomeric poly(lactic acids). 9. Stereocomplexation from the melt. *Macromolecules* **1993,** 26 (25), 6918-6926 DOI: 10.1021/ma00077a032.
43. Tsuji, H.; Tezuka, Y. Stereocomplex Formation between Enantiomeric Poly(lactic acid)s. 12. Spherulite Growth of Low-Molecular-Weight Poly(lactic acid)s from the Melt. *Biomacromolecules* **2004,** 5 (4), 1181-1186 DOI: 10.1021/bm049835i.
44. Brizzolara, D.; Cantow, H.-J.; Diederichs, K.; Keller, E.; Domb, A. J. Mechanism of the Stereocomplex Formation between Enantiomeric Poly(lactide)s. *Macromolecules* **1996,** 29 (1), 191-197 DOI: 10.1021/ma951144e.
45. Na, B.; Zhu, J.; Lv, R.; Ju, Y.; Tian, R.; Chen, B. Stereocomplex Formation in Enantiomeric Polylactides by Melting Recrystallization of Homocrystals: Crystallization Kinetics and Crystal Morphology. *Macromolecules* **2014,** 47 (1), 347-352 DOI: 10.1021/ma402405c.
46. Purnama, P.; Jung, Y.; Kim, S. H. Stereocomplexation of Poly(l-lactide) and Random Copolymer Poly(d-lactide-co-ε-caprolactone) To Enhance Melt Stability. *Macromolecules* **2012,** 45 (9), 4012-4014 DOI: 10.1021/ma202814c.
47. Sun, J.; Yu, H.; Zhuang, X.; Chen, X.; Jing, X. Crystallization Behavior of Asymmetric PLLA/PDLA Blends. *The Journal of Physical Chemistry B* **2011,** 115 (12), 2864-2869 DOI: 10.1021/jp111894m.
48. Tsuji, H.; Ikada, Y. Stereocomplex formation between enantiomeric poly(lactic acid)s. XI. Mechanical properties and morphology of solution-cast films. *Polymer* **1999,** 40 (24), 6699-6708 DOI: https://doi.org/10.1016/S0032-3861(99)00004-X.
49. Tsuji, H.; Horii, F.; Hyon, S. H.; Ikada, Y. Stereocomplex formation between enantiomeric poly(lactic acid)s. 2. Stereocomplex formation in concentrated solutions. *Macromolecules* **1991,** 24 (10), 2719-2724 DOI: 10.1021/ma00010a013.
50. Tsuji, H.; Hyon, S. H.; Ikada, Y. Stereocomplex formation between enantiomeric poly(lactic acids). 5. Calorimetric and morphological studies on the stereocomplex formed in acetonitrile solution. *Macromolecules* **1992,** 25 (11), 2940-2946 DOI: 10.1021/ma00037a024.
51. Tsuji, H.; Hyon, S. H.; Ikada, Y. Stereocomplex formation between enantiomeric poly(lactic acid)s. 3. Calorimetric studies on blend films cast from dilute solution. *Macromolecules* **1991,** 24 (20), 5651-5656 DOI: 10.1021/ma00020a026.
52. Brochu, S.; Prud'homme, R. E.; Barakat, I.; Jerome, R. Stereocomplexation and Morphology of Polylactides. *Macromolecules* **1995,** 28 (15), 5230-5239 DOI: 10.1021/ma00119a010.
53. Yui, N.; Dijkstra, P. J.; Feijen, J. Stereo block copolymers of L- and D-lactides. *Die Makromolekulare Chemie* **1990,** 191 (3), 481-488 DOI: doi:10.1002/macp.1990.021910303.
54. Tsuji, H.; Ikada, Y. Stereocomplex formation between enantiomeric poly(lactic acid)s. X. Binary blends from poly(D-lactide-CO-glycolide) and poly(L-lactide-CO-glycolide). *Journal of Applied Polymer Science* **1994,** 53 (8), 1061-1071 DOI: doi:10.1002/app.1994.070530808.
55. Spinu, M.; Jackson, C.; Keating, M. Y.; Gardner, K. H. Material Design in Poly(Lactic Acid) Systems: Block Copolymers, Star Homo- and Copolymers, and Stereocomplexes. *Journal of Macromolecular Science, Part A* **1996,** 33 (10), 1497-1530 DOI: 10.1080/10601329608014922.
56. Stevels, W. M.; Ankone, M. J. K.; Dijkstra, P. J.; Feijen, J., A flexible and highly efficient catalyst system for the ring-opening polymerization of lactones. 1996.

57. Wisniewski, M.; Borgne, A. L.; Spassky, N. Synthesis and properties of (D)- and (L)-lactide stereocopolymers using the system achiral Schiff's base/aluminium methoxide as initiator. *Macromolecular Chemistry and Physics* **1997,** 198 (4), 1227-1238 DOI: doi:10.1002/macp.1997.021980424.
58. Tsuji, H.; Hyon, S. H.; Ikada, Y. Stereocomplex formation between enantiomeric poly(lactic acid)s. 4. Differential scanning calorimetric studies on precipitates from mixed solutions of poly(D-lactic acid) and poly(L-lactic acid). *Macromolecules* **1991,** 24 (20), 5657-5662 DOI: 10.1021/ma00020a027.
59. Tsuji, H.; Ikada, Y. Crystallization from the melt of poly(lactide)s with different optical purities and their blends. *Macromolecular Chemistry and Physics* **1996,** 197 (10), 3483-3499 DOI: doi:10.1002/macp.1996.021971033.
60. Barrer, R. M.; Rideal, E. K. Permeation, diffusion and solution of gases in organic polymers. *Transactions of the Faraday Society* **1939,** 35 (0), 628-643 DOI: 10.1039/TF9393500628.
61. Hopfenberg, H. B., *Permeability of Plastic Films and Coatings To Gases, Vapors, and Liquids*. Springer, Boston, MA: Springer-Verlag US 1974; Vol. 6.
62. Stern, S. A.; Frisch, H. L. The Selective Permeation of Gases Through Polymers. *Annual Review of Materials Science* **1981,** 11 (1), 523-550 DOI: 10.1146/annurev.ms.11.080181.002515.
63. Shogren, R. Water vapor permeability of biodegradable polymers. *J Environ Polym Degr* **1997,** 5 (2), 91-95 DOI: https://doi.org/10.1007/BF02763592.
64. Lim, L. T.; Auras, R.; Rubino, M. Processing technologies for poly(lactic acid). *Progress in Polymer Science* **2008,** 33 (8), 820-852 DOI: https://doi.org/10.1016/j.progpolymsci.2008.05.004.
65. Drieskens, M.; Peeters, R.; Mullens, J.; Franco, D.; Lemstra, P. J.; Hristova-Bogaerds, D. G. Structure versus properties relationship of poly(lactic acid). I. Effect of crystallinity on barrier properties. *Journal of Polymer Science Part B: Polymer Physics* **2009,** 47 (22), 2247-2258 DOI: doi:10.1002/polb.21822.
66. Auras, R. A.; Harte, B.; Selke, S.; Hernandez, R. Mechanical, Physical, and Barrier Properties of Poly(Lactide) Films. *Journal of Plastic Film & Sheeting* **2003,** 19 (2), 123-135 DOI: 10.1177/8756087903039702.
67. Auras, R.; Harte, B.; Selke, S. An Overview of Polylactides as Packaging Materials. *Macromolecular Bioscience* **2004,** 4 (9), 835-864 DOI: doi:10.1002/mabi.200400043.
68. Cocca, M.; Lorenzo, M. L. D.; Malinconico, M.; Frezza, V. Influence of crystal polymorphism on mechanical and barrier properties of poly(l-lactic acid). *European Polymer Journal* **2011,** 47 (5), 1073-1080 DOI: https://doi.org/10.1016/j.eurpolymj.2011.02.009.
69. Tsuji, H.; Tsuruno, T. Water Vapor Permeability of Poly(L-lactide)/Poly(D-lactide) Stereocomplexes. *Macromolecular Materials and Engineering* **2010,** 295 (8), 709-715 DOI: doi:10.1002/mame.201000071.
70. Delpouve, N.; Stoclet, G.; Saiter, A.; Dargent, E.; Marais, S. Water Barrier Properties in Biaxially Drawn Poly(lactic acid) Films. *The Journal of Physical Chemistry B* **2012,** 116 (15), 4615-4625 DOI: 10.1021/jp211670g.
71. Angell, C. A. Formation of Glasses from Liquids and Biopolymers. *Science* **1995,** 267 (5206), 1924-1935 DOI: 10.1126/science.267.5206.1924.
72. Dislich, H. New Routes to Multicomponent Oxide Glasses. *Angewandte Chemie International Edition in English* **1971,** 10 (6), 363-370 DOI: doi:10.1002/anie.197103631.
73. Kozdras, A.; Golovchak, R.; Shpotyuk, O.; Szymura, S.; Saiter, A.; Saiter, J.-M. Light-assisted physical aging in chalcogenide glasses: Dependence on the wavelength of incident photons. *Journal of Materials Research* **2011,** 26 (18), 2420-2427 DOI: 10.1557/jmr.2011.264.
74. Chebli, K.; Saiter, J. M.; Grenet, J.; Hamou, A.; Saffarini, G. Strong-fragile glass forming liquid concept applied to GeTe chalcogenide glasses. *Physica B: Condensed Matter* **2001,** 304 (1), 228-236 DOI: https://doi.org/10.1016/S0921-4526(01)00501-4.
75. Tatsumisago, M.; Halfpap, B. L.; Green, J. L.; Lindsay, S. M.; Angell, C. A. Fragility of Ge-As-Se glass-forming liquids in relation to rigidity percolation, and the Kauzmann paradox. *Physical Review Letters* **1990,** 64 (13), 1549-1552 DOI: 10.1103/PhysRevLett.64.1549.

76. Xu, W.; Cooper, E. I.; Angell, C. A. Ionic Liquids: Ion Mobilities, Glass Temperatures, and Fragilities. *The Journal of Physical Chemistry B* **2003,** 107 (25), 6170-6178 DOI: 10.1021/jp0275894.
77. Wilkes, J. S. A short history of ionic liquids—from molten salts to neoteric solvents. *Green Chemistry* **2002,** 4 (2), 73-80 DOI: 10.1039/B110838G.
78. Saiter, A.; Devallencourt, C.; Saiter, J. M.; Grenet, J. Thermodynamically "strong" and kinetically "fragile" polymeric glass exemplified by melamine formaldehyde resins. *European Polymer Journal* **2001,** 37 (6), 1083-1090 DOI: https://doi.org/10.1016/S0014-3057(00)00242-1.
79. Schönhals, A.; Goering, H.; Schick, C.; Frick, B.; Zorn, R. Glass transition of polymers confined to nanoporous glasses. *Colloid and Polymer Science* **2004,** 282 (8), 882-891 DOI: 10.1007/s00396-004-1106-3.
80. Priestley, R. D.; Ellison, C. J.; Broadbelt, L. J.; Torkelson, J. M. Structural Relaxation of Polymer Glasses at Surfaces, Interfaces, and In Between. *Science* **2005,** 309 (5733), 456-459 DOI: 10.1126/science.1112217.
81. Ediger, M. D.; Angell, C. A.; Nagel, S. R. Supercooled Liquids and Glasses. *The Journal of Physical Chemistry* **1996,** 100 (31), 13200-13212 DOI: 10.1021/jp953538d.
82. Turnbull, D.; Cohen, M. H. Free-Volume Model of the Amorphous Phase: Glass Transition. *The Journal of Chemical Physics* **1961,** 34 (1), 120-125 DOI: 10.1063/1.1731549.
83. Cohen, M. H.; Turnbull, D. Molecular Transport in Liquids and Glasses. *The Journal of Chemical Physics* **1959,** 31 (5), 1164-1169 DOI: 10.1063/1.1730566.
84. Gibbs, J. H.; DiMarzio, E. A. Nature of the Glass Transition and the Glassy State. *The Journal of Chemical Physics* **1958,** 28 (3), 373-383 DOI: 10.1063/1.1744141.
85. Adam, G.; Gibbs, J. H. On the Temperature Dependence of Cooperative Relaxation Properties in Glass-Forming Liquids. *The Journal of Chemical Physics* **1965,** 43 (1), 139-146 DOI: 10.1063/1.1696442.
86. Götze, W., *Complex Dynamics of Glass-Forming Liquids: A Mode-Coupling Theory*. OUP Oxford: 2008.
87. Ngai, K. L.; Tsang, K. Y. Similarity of relaxation in supercooled liquids and interacting arrays of oscillators. *Physical Review E* **1999,** 60 (4), 4511-4517 DOI: 10.1103/PhysRevE.60.4511.
88. Debenedetti, P. G.; Stillinger, F. H. Supercooled liquids and the glass transition. *Nature* **2001,** 410, DOI: 10.1038/35065704.
89. Stillinger, F. H.; Debenedetti, P. G.; Truskett, T. M. The Kauzmann Paradox Revisited. *The Journal of Physical Chemistry B* **2001,** 105 (47), 11809-11816 DOI: 10.1021/jp011840i.
90. Speedy, R. J. Kauzmann's paradox and the glass transition. *Biophysical Chemistry* **2003,** 105 (2), 411-420 DOI: https://doi.org/10.1016/S0301-4622(03)00105-4.
91. Stillinger, F. H.; Debenedetti, P. G. Phase transitions, Kauzmann curves, and inverse melting. *Biophysical Chemistry* **2003,** 105 (2), 211-220 DOI: https://doi.org/10.1016/S0301-4622(03)00089-9.
92. Debenedetti, P. G.; Truskett, T. M.; Lewis, C. P.; Stillinger, F. H., Theory of supercooled liquids and glasses: Energy landscape and statistical geometry perspectives. In *Advances in Chemical Engineering*, Academic Press: 2001; Vol. 28, pp 21-79.
93. Struik, L. C. E. Physical aging in plastics and other glassy materials. *Polymer Engineering & Science* **1977,** 17 (3), 165-173 DOI: doi:10.1002/pen.760170305.
94. Moynihan, C. T.; Easteal, A. J.; De Bolt, M. A.; Tucker, J. Dependence of the Fictive Temperature of Glass on Cooling Rate. *Journal of the American Ceramic Society* **1976,** 59 (1-2), 12-16 DOI: 10.1111/j.1151-2916.1976.tb09376.x.
95. Gao, S.; Simon, S. L. Measurement of the limiting fictive temperature over five decades of cooling and heating rates. *Thermochimica Acta* **2015,** 603, 123-127 DOI: https://doi.org/10.1016/j.tca.2014.08.019.
96. Weyer, S.; Huth, H.; Schick, C. Application of an extended Tool–Narayanaswamy–Moynihan model.Part 2. Frequency and cooling rate dependence of glass transition from temperature modulated DSC. *Polymer* **2005,** 46 (26), 12240-12246 DOI: https://doi.org/10.1016/j.polymer.2005.10.097.
97. Doolittle, A. K. Studies in Newtonian Flow. II. The Dependence of the Viscosity of Liquids on Free-Space. *Journal of Applied Physics* **1951,** 22 (12), 1471-1475 DOI: 10.1063/1.1699894.

98. Kremer F, S. A., *Broadband dielectric spectroscopy*. New York: Springer, 2003.
99. Kremer, F. Dielectric spectroscopy – yesterday, today and tomorrow. *Journal of Non-Crystalline Solids* **2002,** 305 (1), 1-9 DOI: https://doi.org/10.1016/S0022-3093(02)01083-9.
100. Richert, R.; Blumen, A., Disordered Systems and Relaxation. In *Disorder Effects on Relaxational Processes: Glasses, Polymers, Proteins*, Richert, R., Blumen, A., Eds. Springer Berlin Heidelberg: Berlin, Heidelberg, 1994; pp 1-7.
101. Schneider, U.; Brand, R.; Lunkenheimer, P.; Loidl, A. Excess Wing in the Dielectric Loss of Glass Formers: A Johari-Goldstein beta relaxation? *Physical Review Letters* **2000,** 84 (24), 5560-5563 DOI: 10.1103/PhysRevLett.84.5560.
102. Ngai, K. L.; Prevosto, D.; Capaccioli, S.; Roland, C. M. Guides to solving the glass transition problem. *Journal of Physics: Condensed Matter* **2008,** 20 (24), 244125.
103. Martinez-Garcia, J. C.; Martinez-Garcia, J.; Rzoska, S. J.; Hulliger, J. The new insight into dynamic crossover in glass forming liquids from the apparent enthalpy analysis. *The Journal of Chemical Physics* **2012,** 137 (6), 064501 DOI: 10.1063/1.4739750.
104. Cyrot, M. A possible origin for the Vogel-Fulcher law. *Physics Letters A* **1981,** 83 (6), 275-278 DOI: https://doi.org/10.1016/0375-9601(81)90982-8.
105. Fulcher, G. S. ANALYSIS OF RECENT MEASUREMENTS OF THE VISCOSITY OF GLASSES. *Journal of the American Ceramic Society* **1925,** 8 (6), 339-355 DOI: doi:10.1111/j.1151-2916.1925.tb16731.x.
106. Tammann, V. G.; Hesse, W. Die Abhängigkeit der Viscosität von der Temperatur bie unterkühlten Flüssigkeiten. *Zeitschrift für anorganische und allgemeine Chemie* **1926,** 156 (1), 245-257 DOI: doi:10.1002/zaac.19261560121.
107. Ngai, K. L., *Relaxation and Diffusion in Complex Systems*. Springer Science+Business Media, LLC 2011: Springer, New York, NY, 2011.
108. Stickel, F.; Fischer, E. W.; Richert, R. Dynamics of glass-forming liquids. I. Temperature-derivative analysis of dielectric relaxation data. *The Journal of Chemical Physics* **1995,** 102 (15), 6251-6257 DOI: 10.1063/1.469071.
109. Angell, C. A. Spectroscopy simulation and scattering, and the medium range order problem in glass. *Journal of Non-Crystalline Solids* **1985,** 73 (1), 1-17 DOI: https://doi.org/10.1016/0022-3093(85)90334-5.
110. Wright, G. B.; Ngai, K. L.; United, S.; Naval Research, L., *Relaxations in complex systems*. U.S. G.P.O ; available from National Technical Information Services: Washington, D.C. : Springfield, VA, 1985; p ix, 345 p.
111. Böhmer, R.; Ngai, K. L.; Angell, C. A.; Plazek, D. J. Nonexponential relaxations in strong and fragile glass formers. *The Journal of Chemical Physics* **1993,** 99 (5), 4201-4209 DOI: 10.1063/1.466117.
112. Mandanicia, A.; Shi, X.; McKenna, G. B.; Cutroni, M. Slow dynamics of supercooled m-toluidine investigated by mechanical spectroscopy. *The Journal of Chemical Physics* **2005,** 122 (11), 114501 DOI: 10.1063/1.1856919.
113. Corezzi, S.; Campani, E.; Rolla, P. A.; Capaccioli, S.; Fioretto, D. Changes in the dynamics of supercooled systems revealed by dielectric spectroscopy. *The Journal of Chemical Physics* **1999,** 111 (20), 9343-9351 DOI: 10.1063/1.479847.
114. Mallamace, F.; Corsaro, C.; Leone, N.; Villari, V.; Micali, N.; Chen, S.-H. On the ergodicity of supercooled molecular glass-forming liquids at the dynamical arrest: the o-terphenyl case. *Scientific Reports* **2014,** 4, 3747 DOI: 10.1038/srep03747.
115. Kohlrausch, F. Ueber die elastische Nachwirkung bei der Torsion. *Annalen der Physik* **1863,** 195 (7), 337-368 DOI: doi:10.1002/andp.18631950702.
116. Williams, G.; Watts, D. C. Non-symmetrical dielectric relaxation behaviour arising from a simple empirical decay function. *Transactions of the Faraday Society* **1970,** 66 (0), 80-85 DOI: 10.1039/TF9706600080.
117. Garrahan, J. P. Dynamic heterogeneity comes to life. *Proceedings of the National Academy of Sciences* **2011,** 108 (12), 4701.
118. Ediger, M. D. Spatially Heterogeneous Dynamics in Supercooled Liquids. *Annual Review of Physical Chemistry* **2000,** 51 (1), 99-128 DOI: 10.1146/annurev.physchem.51.1.99.

119. Ranko, R. Heterogeneous dynamics in liquids: fluctuations in space and time. *Journal of Physics: Condensed Matter* **2002,** 14 (23), R703.
120. Berthier, L. Trend: Dynamic Heterogeneity in Amorphous Materials. *Physics 4* **2011,** 42, DOI: 10.1103/Physics.4.42

121. Ediger, M. D.; Harrowell, P. Perspective: Supercooled liquids and glasses. *The Journal of Chemical Physics* **2012,** 137 (8), 080901 DOI: 10.1063/1.4747326.
122. Dalle-Ferrier, C.; Thibierge, C.; Alba-Simionesco, C.; Berthier, L.; Biroli, G.; Bouchaud, J. P.; Ladieu, F.; L'Hôte, D.; Tarjus, G. Spatial correlations in the dynamics of glassforming liquids: Experimental determination of their temperature dependence. *Physical Review E* **2007,** 76 (4), 041510 DOI: 10.1103/PhysRevE.76.041510.
123. Hempel, E.; Hempel, G.; Hensel, A.; Schick, C.; Donth, E. Characteristic Length of Dynamic Glass Transition near Tg for a Wide Assortment of Glass-Forming Substances. *The Journal of Physical Chemistry B* **2000,** 104 (11), 2460-2466 DOI: 10.1021/jp991153f.
124. Hong, L.; Gujrati, P. D.; Novikov, V. N.; Sokolov, A. P. Molecular cooperativity in the dynamics of glass-forming systems: A new insight. *The Journal of Chemical Physics* **2009,** 131 (19), 194511 DOI: 10.1063/1.3266508.
125. Berthier, L.; Biroli, G.; Bouchaud, J.-P.; Cipelletti, L.; Masri, D. E.; L'Hôte, D.; Ladieu, F.; Pierno, M. Direct Experimental Evidence of a Growing Length Scale Accompanying the Glass Transition. *Science* **2005,** 310 (5755), 1797-1800 DOI: 10.1126/science.1120714.
126. Karmakar, S.; Dasgupta, C.; Sastry, S. Growing Length Scales and Their Relation to Timescales in Glass-Forming Liquids. *Annual Review of Condensed Matter Physics* **2014,** 5 (1), 255-284 DOI: 10.1146/annurev-conmatphys-031113-133848.
127. Fragiadakis, D.; Casalini, R.; Roland, C. M. Density Scaling and Dynamic Correlations in Viscous Liquids. *The Journal of Physical Chemistry B* **2009,** 113 (40), 13134-13137 DOI: 10.1021/jp907553b.
128. Donth, E. Dynamic or configurational approach to the glass transition? *Journal of Non-Crystalline Solids* **2002,** 307-310, 364-375 DOI: https://doi.org/10.1016/S0022-3093(02)01497-7.
129. Donth, E. Phenomenological treatment of dynamic glass transition heterogeneity. *Acta Polymerica* **1999,** 50 (7), 240-251 DOI: doi:10.1002/(SICI)1521-4044(19990701)50:7<240::AID-APOL240>3.0.CO;2-H.
130. Donth, E. Characteristic length of the glass transition. *Journal of Polymer Science Part B: Polymer Physics* **1996,** 34 (17), 2881-2892 DOI: doi:10.1002/(SICI)1099-0488(199612)34:17<2881::AID-POLB3>3.0.CO;2-U.
131. Dasgupta, C.; Indrani, A. V.; Sriram, R.; Phani, M. K. Is There a Growing Correlation Length near the Glass Transition? *EPL (Europhysics Letters)* **1991,** 15 (4).
132. Donati, C.; Franz, S.; Glotzer, S. C.; Parisi, G. Theory of non-linear susceptibility and correlation length in glasses and liquids. *Journal of Non-Crystalline Solids* **2002,** 307-310, 215-224 DOI: https://doi.org/10.1016/S0022-3093(02)01461-8.
133. Berthier, L. Finite-Size Scaling Analysis of the Glass Transition. *Physical Review Letters* **2003,** 91 (5), 055701 DOI: 10.1103/PhysRevLett.91.055701.
134. Fragiadakis, D.; Casalini, R.; Bogoslovov, R. B.; Robertson, C. G.; Roland, C. M. Dynamic Heterogeneity and Density Scaling in 1,4-Polyisoprene. *Macromolecules* **2011,** 44 (5), 1149-1155 DOI: 10.1021/ma102795w.
135. Capaccioli, S.; Ruocco, G.; Zamponi, F. Dynamically Correlated Regions and Configurational Entropy in Supercooled Liquids. *The Journal of Physical Chemistry B* **2008,** 112 (34), 10652-10658 DOI: 10.1021/jp802097u.
136. Donth, E. The size of cooperatively rearranging regions at the glass transition. *Journal of Non-Crystalline Solids* **1982,** 53 (3), 325-330 DOI: https://doi.org/10.1016/0022-3093(82)90089-8.
137. Garwe, F.; Schönhals, A.; Lockwenz, H.; Beiner, M.; Schröter, K.; Donth, E. Influence of Cooperative α Dynamics on Local β Relaxation during the Development of the Dynamic Glass Transition in Poly(n-alkyl methacrylate)s. *Macromolecules* **1996,** 29 (1), 247-253 DOI: 10.1021/ma9506142.

138. Bellac, M. L.; Mortessagne, F.; Batrouni, G. G., *Equilibrium and Non-equilibrium Statistical Thermodynamics*. Cambridge University Press: 2004.

139. Bouthegourd, E.; Esposito, A.; Lourdin, D.; Saiter, A.; Saiter, J. M. Size of the cooperative rearranging regions vs. fragility in complex glassy systems: Influence of the structure and the molecular interactions. *Physica B: Condensed Matter* **2013,** 425, 83-89 DOI: https://doi.org/10.1016/j.physb.2013.05.029.

140. Delpouve, N.; Delbreilh, L.; Stoclet, G.; Saiter, A.; Dargent, E. Structural Dependence of the Molecular Mobility in the Amorphous Fractions of Polylactide. *Macromolecules* **2014,** 47 (15), 5186-5197 DOI: 10.1021/ma500839p.

141. Lixon, C.; Delpouve, N.; Saiter, A.; Dargent, E.; Grohens, Y. Evidence of Cooperative Rearranging Region size anisotropy for drawn PET. *European Polymer Journal* **2008,** 44 (11), 3377-3384 DOI: https://doi.org/10.1016/j.eurpolymj.2008.08.001.

142. Saiter, A.; Prevosto, D.; Passaglia, E.; Couderc, H.; Delbreilh, L.; Saiter, J. M. Cooperativity length scale in nanocomposites: Interfacial and confinement effects. *Physical Review E* **2013,** 88 (4), 042605 DOI: 10.1103/PhysRevE.88.042605.

143. Saiter, A.; Delbreilh, L.; Couderc, H.; Arabeche, K.; Schönhals, A.; Saiter, J. M. Temperature dependence of the characteristic length scale for glassy dynamics: Combination of dielectric and specific heat spectroscopy. *Physical Review E* **2010,** 81 (4), 041805 DOI: 10.1103/PhysRevE.81.041805.

144. Cangialosi, D.; Wübbenhorst, M.; Groenewold, J.; Mendes, E.; Schut, H.; van Veen, A.; Picken, S. J. Physical aging of polycarbonate far below the glass transition temperature: Evidence for the diffusion mechanism. *Physical Review B* **2004,** 70 (22), 224213.

145. Huang, Y.; Paul, D. R. Physical aging of thin glassy polymer films monitored by gas permeability. *Polymer* **2004,** 45 (25), 8377-8393 DOI: https://doi.org/10.1016/j.polymer.2004.10.019.

146. Huang, Y.; Paul, D. R. Physical Aging of Thin Glassy Polymer Films Monitored by Optical Properties. *Macromolecules* **2006,** 39 (4), 1554-1559 DOI: 10.1021/ma050533y.

147. Hodge, I. M. Enthalpy relaxation and recovery in amorphous materials. *Journal of Non-Crystalline Solids* **1994,** 169 (3), 211-266 DOI: https://doi.org/10.1016/0022-3093(94)90321-2.

148. Tool, A. Q.; Eicitlin, C. G. VARIATIONS CAUSED IN THE HEATING CURVES OF GLASS BY HEAT TREATMENT1. *Journal of the American Ceramic Society* **1931,** 14 (4), 276-308 DOI: doi:10.1111/j.1151-2916.1931.tb16602.x.

149. Moynihan, C. T.; Macedo, P. B.; Montrose, C. J.; Gupta, P. K.; DeBolt, M. A.; Dill, J. F.; Dom, B. E.; Drake, P. W.; Easteal, A. J.; Elterman, P. B.; Moeller, R. P.; Sasabe, H.; Wilder, J. A. Structural relaxation in vitreous materials. *Annals of the New York Academy of Sciences* **1976,** 279 (1), 15-35 DOI: doi:10.1111/j.1749-6632.1976.tb39688.x.

CHAPTER 2. EXPERIMENTAL PART

This chapter presents the detailed description of experimental techniques (calorimetric investigations, microstructure analysis and permeametric analysis) used in this thesis in order to analyze the elaborated samples. Experimental set-ups and protocols applied during the analysis were briefly described.

2.1 Materials

PLLA and PDLA were chosen due to the presence of chiral carbon in the skeletal chain of PLA that yields to two stereoregular isomers, PLLA and PDLA. The mixture of these homopolymers by the stereocomplexation reaction allows obtaining a new structure, so called sc PLA. In this work, homopolymers of poly(L-lactide) (PLLA) and poly(D-lactide) (PDLA), and stereocomplex poly(lactide) (sc PLA) were studied (Fig 2.1).

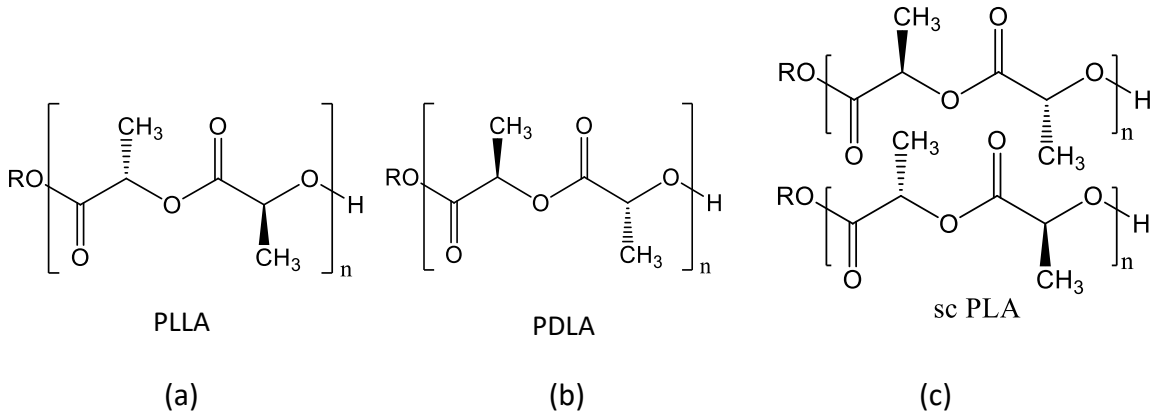

Figure 2. 1. Repeating units of (a) PLLA, (b) PDLA, and (c) sc PLA.

2.1.1 Homopolymers

PLLA pellets (NaturePlast Injection grade, France) have the density of 1.25 g/cm^3. The content of the *D*- isomers is negligible. The melting temperature T_m is between 170 °C and 180 °C. The number-average and weight-average molecular weight measured by Gel Permeation Chromatography (GPC) are M_n = 53 kDa and M_w = 97 kDa, respectively.

PDLA pellets (NaturePlast PDLA 002, France) have the density of 1.25 g/cm^3 with the content of the *L*-isomer less than 0.5%. The melting temperature T_m of PDLA is about 175 °C. The number-average and weight-average molecular weight measured by GPC are M_n = 56 kDa and M_w = 99 kDa, respectively. The molar mass of repeating unit (Fig 2.1 (a) and (b)) is m_0 = 72 g/mol. Both PLLA and PDLA homopolymers were dried at T = 55 °C during 3 days before using.

2.1.1.1 Preparation of amorphous homopolymers

After a study of the thermal stability by thermogravimetric analysis (TGA) (the degradation temperature T_d = 270-400 °C), the dried PLLA and PDLA pellets were thermo-

molded at 1 bar and 180 °C between hot plates during 5 min by using a manual hydraulic press ATLAS^{TM} SPECAC. The temperature was selected above the melting temperature T_m (ranging from 160 °C to 175 °C [1, 2]) and below the equilibrium melting temperature T_m^0 of PLAs (ranging from 199 °C to 207 °C [3]). The films samples were then rapidly quenched in liquid nitrogen and then dried at 60 °C for 24 h. The thickness of the obtained PLLA and PDLA films was 150 - 250 µm.

2.1.1.2 Preparation of semicrystalline homopolymers

Semi-crystalline PLLA and PDLA films were obtained by solution casting. Chloroform (99.8% purity) was used as a solvent. Dried pellets were dissolved in chloroform with the concentration of 3 g/dL at T_{amb} = 24 ± 1 °C under vigorous stirring during 1h. The prepared solution was poured onto glass Petri dish to obtain free standing films. The solvent evaporation was carried under the fume-hood at ambient temperature (T = 24 ± 1 °C) for 48h, and the samples were further dried in oven at 120 °C for 12h to remove the solvent completely. The overall preparation process for amorphous and semicrystalline homopolymers is summarized in Fig 2.2.

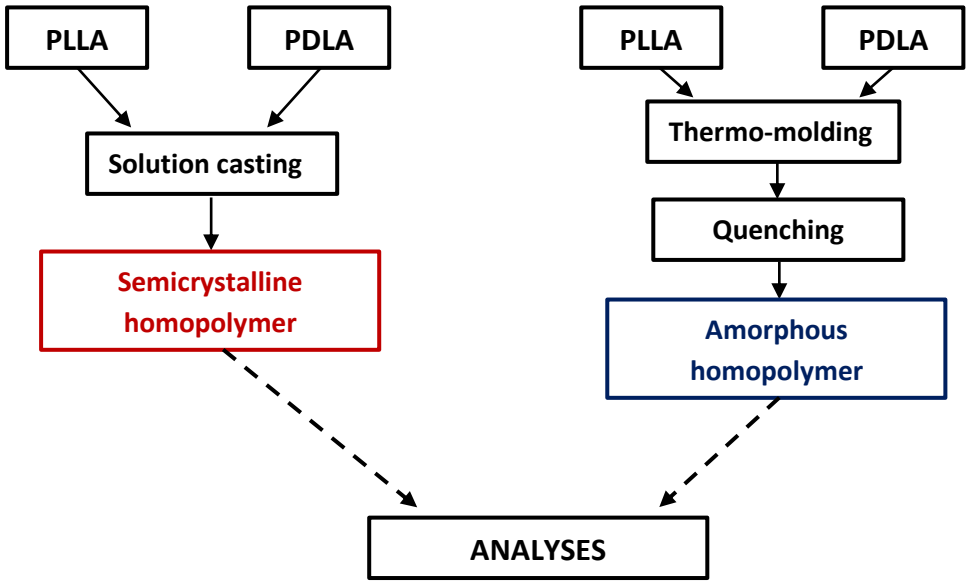

Figure 2. 2. Schematic illustration of homopolymer film preparation.

2.1.2 Stereocomplex poly(lactide) (sc PLA)

In order to study the influence of elaboration method on the film properties, stereocomplex poly(lactide) (sc PLA) was obtained by two elaboration methods, i.e. solution casting and extrusion process.

2.1.2.1 Solution casting

Sc PLA (also referred as PLLA/PDLA films in some Figures) was prepared by solution casting using chloroform (99.8% purity) as a solvent. In our work, only the influence of solution concentration and PLLA:PDLA ratio was investigated. In order to study the influence of homopolymer concentration on the stereocomplex formation, the solutions with different polymer concentrations (namely 1, 2 and 3 g/dL) were prepared. In this case, the ratio of PLLA:PDLA was maintained constant at 50:50 (w/w). In order to study the impact of homopolymers ratio on stereocomplexation, the solutions with different ratios of PLLA:PDLA were prepared: 50:50, 60:40, 70:30, 75:25, 90:10 and 95:05 ratio of PLLA:PDLA for the concentration of 3 g/dL (this concentration was chosen after careful analysis of the XRD patterns that will be discussed later in Chapter 3). Dried PLLA and PDLA pellets were dissolved in chloroform separately at 24 ± 1 °C. Then, PLLA and PDLA solutions were mixed together under vigorous stirring for additional 1h. The prepared solution was poured onto glass Petri dish (as shown in Fig 2.3). Solvent evaporation was carried out in the fume-hood ($T \approx 20$ °C) for 48h and then additional drying took place in convection oven (T = 120 °C) for 12h. The obtained free-standing films had the thickness of ~ 150 µm.

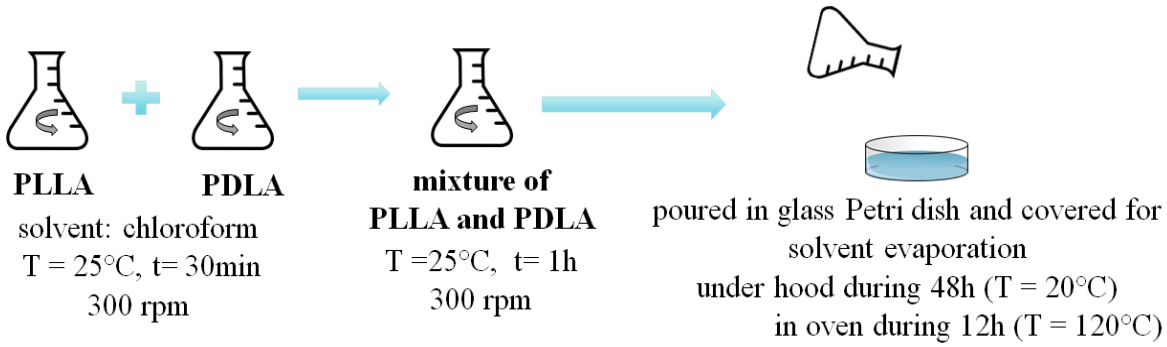

Figure 2. 3. Schematic illustration of the solvent casting process.

2.1.2.2 Quenching

PLLA/PDLA films elaborated by solution casting were thermo-molded at 230 °C and 1 bar between two hot plates during 5 min by using a manual hydraulic press ATLAS™ SPECAC. The temperature was selected close to the equilibrium melting temperature T_m^0 of 235 °C for sc PLA crystals [4]. The samples were then quickly quenched in liquid nitrogen to obtain amorphous films. The thickness of the obtained films was remained 150 ± 20 µm.

2.1.2.3 Extrusion

Blend of sc PLA was prepared by twin screw mixing. PLLA and PDLA pellets were mixed with the ratio of 50:50 (w/w) for extrusion process. The influence of extrusion temperature (T_{ext}) and mixing time (t_{ext}) on the stereocomplexation of PLA was investigated. In order to investigate the temperature dependence of extrusion, sc PLA was extruded at T_{ext} = 180, 190, 200, 210, and 220 °C during t_{ext} = 30 min with a rotation of 40 rpm. The impact of time was observed by comparing the extruded samples at different time (t_{ext} = 15 min and 30 min) at a fixed temperature (T_{ext} = 220 °C). The homogeneity of mixing was taken into account by the feeding amount of mixer because of its capacity. The amount of feeding was fixed as 6 g of polymers (m_{PLLA} = m_{PDLA} = 3 g). Fig 2.4 illustrates the overall process for the sc PLA elaboration.

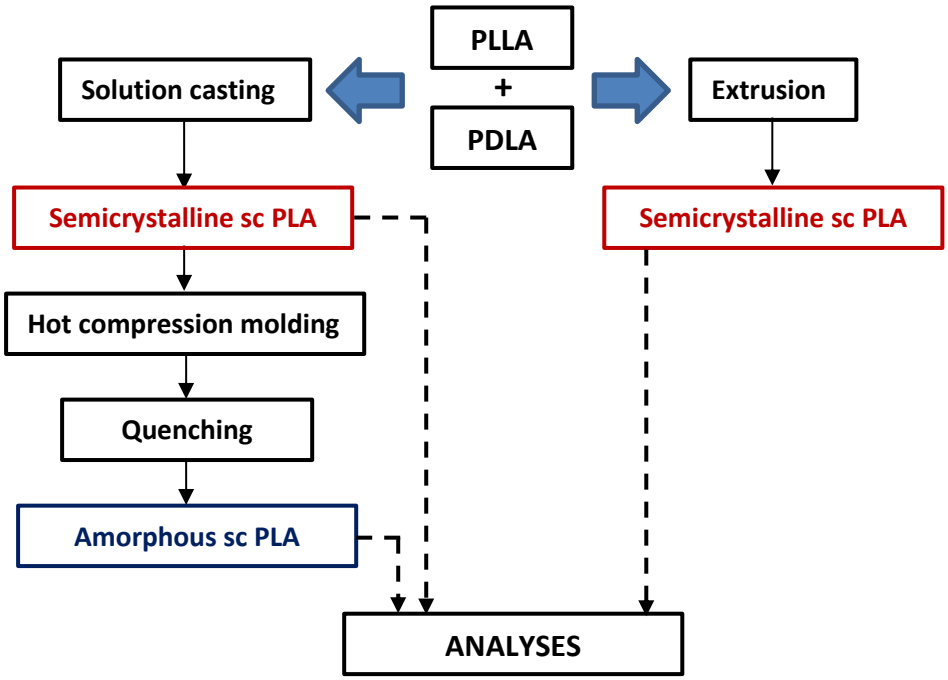

Figure 2. 4. Schematic illustration of the PLLA/PDLA sample preparation.

2.2 Instrumentation and methods

The influence of stereocomplexation on the microstructure and the material properties was studied by the microstructure and morphology analysis. In addition, calorimetric investigations were performed in order to understand the fundamentals of short- and/or long-range molecular mobility.

2.2.1 Thermogravimetric analysis (TGA)

TGA is a kind of thermal analysis in which the sample weight loss is measured either as a function of increasing temperature, or isothermally as a function of time, under nitrogen, helium, air, other gas, or vacuum. It provides information about different chemical phenomena such as thermal decomposition and physical phenomena including phase transitions, absorption and desorption [5]. It is a beneficial technique for the study of polymer materials, including thermoplastics, thermosets, elastomers, composites, fibers, and coating [6-8]. In this work, the measurements were performed by TGA Discovery (TA Instrument) (shown in Fig. 2.5) to determine the degradation temperature of the samples.

(a) (b)

Figure 2. 5. Images of (a) sample pan place and (b) balance in the furnace of TGA Discovery.

The samples were placed in the pan (Fig.2.5. a) with the mass around 5 mg and measurements were carried out from 30 °C to 600 °C with a heating rate of 10 °C/min under nitrogen. The degradation temperature (T_{deg}) was recorded at the 1% mass loss of the sample.

2.2.2 Differential scanning calorimetry (DSC)

DSC is the most used thermal technique that allows us to make qualitative and quantitative measurements. DSC determines the heat flow and the temperature related to calorimetric transitions as a function of temperature and time. DSC provides information about physical and chemical changes including endothermic (sample absorbs energy) and exothermic (sample releases energy) processes of materials during physical transitions which are caused by phase changes, cold crystallization, melting, crystallization, oxidation, and other heat-related changes [9]. Two kinds of DSC exist, so called heat-flux DSC and power-compensated DSC. In this thesis, the calorimetric investigations were performed with a heat-flux calorimeter from Thermal Analysis Instruments (DSC Q100 TA Instruments). The fundamental principle of this DSC lies in the difference between the amount of heat required to increase the temperature of a sample and that of a reference. The measurements of the heat-flux DSC T_{zero}^{TM} technology is based on the difference of heat flow between sample, reference, and furnace. In this type of DSC, the sample pan and reference pan are placed in a unique furnace (Fig.2.6).

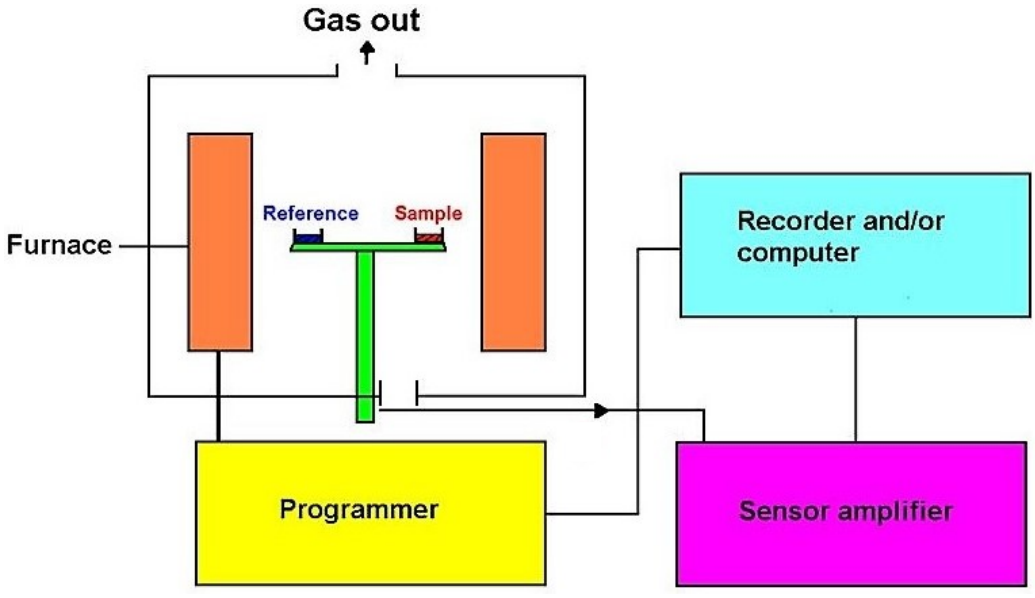

Figure 2. 6. Schematic representation of heat-flux DSC.

The furnace is subjected to the *T* changes and heat is transferred to the sample and reference. The temperature is measured continuously, and a differential technique is utilized to detect the heat flow into the sample and to equalize random heat gains and losses between reference and sample. DSC does not allow a direct determination of the heat content. In conventional DSC, the applied temperature ramp is linear:

$$T = T_i + \beta t \tag{2.1}$$

where *T* is the temperature at the time *t*, T_i is the initial temperature and β is the scanning rate. The resulting heat flow Φ in the heat transfer Q is determined as follows:

$$\Phi = \frac{dQ}{dt} \tag{2.2}$$

At the beginning of the measurement, the two thermocouples, i.e. sample and reference, are at the same temperature $T_0 = T_s = T_r$, where T_0 is temperature of the location of measurements, T_s is temperature of sample pan, and T_r is temperature of the reference pan. During heating, the temperature variation occurs between the sample pan and the reference pan due to the additional weight of sample. Therefore, the variation of heat transfer onto sample (Q_s) and reference (Q_r) is observed, which is related to the endothermic or exothermic events of the sample. The relation between heat transfer and the variation of temperature can be expressed by a thermal equivalent of the Ohm's law [10]:

$$\Phi = Q_s - Q_r = \frac{\Delta T}{R} \tag{2.3}$$

where *R* is the thermal resistance. This variation in temperature is associated to the specific heat capacity of the sample [11]:

$$\Phi = \frac{dQ}{dt} = C\frac{dT}{dt} = c.m.\beta \tag{2.4}$$

where *C* is the heat capacity, c = *C*/*m* is the specific heat capacity, *m* is the sample mass, and β is the scan rate (heating or cooling rate).

Since, DSC Q100 is based on the T_{zero}^{TM} technology and as such technology uses more complex equations of the heat flow, the relations between thermal resistance R_{SCP} and R_{RCP},

and heat capacities C_{scp} and C_{RCP} of the sample and reference cell platforms, respectively, are taken into account in the heat flow equation. Therefore, the temperatures T_s and T_r monitored as a function of a location temperature T_0 can be expressed as follows [12]:

$$\Phi = -\frac{T_s - T_r}{R} + (T_0 - T_s)\left(\frac{1}{R_{SCP}} - \frac{1}{R_{RCP}}\right) + (C_{RCP} - C_{SCP})\frac{dT_s}{dt} - C\frac{d\Delta T}{dt} \quad (2.5)$$

As the result of this complex function, a specific calibration procedure should be used. The calibration procedure has two identic constant heating rate measurements; first experiment should be performed without sample and pan (with empty furnace), and second experiment is carried out with sapphire disks which are placed on the sample and reference positions without pans and lids. Such experiments compute the resistance R_{SCP} and R_{RCP}, and capacitance C_{scp} and C_{RCP} of the cell. Then, the temperature and energy calibrations are carried out using indium standard (T_m = 156.6 °C and ΔH_m = 28.6 J.g^{-1}). Benzophenone can also be used as a second standard for the cell calibration in temperature ($T_{m,\ benzophenone}$ = 48.0 °C). The calibrations of temperature and energy have to be repeated according to the experimental scanning rate. In order to provide a good signal-to-noise ratio, the sample masses of 5-10 mg were used. Scanning rate was selected as 10 K.min^{-1} to ensure the good resolution of examined thermal events. All experiments were carried out under a nitrogen atmosphere.

2.2.3 Modulated temperature DSC (MT-DSC)

In standard DSC, sample undergoes the thermal events which affect its physical and/or chemical properties during the measurements. These thermal events consist of the glass transition, crystallization, and melting, as well as curing and evaporation. The “reversing” and “non-reversing” events may occur at the same time or in the same range of temperature. Thus, the average heat flows are overlapped and cannot be differentiated using standard DSC curves. In 1993, Reading et al. [13] proposed to express the heat flow measured from standard DSC as follows:

$$\Phi = \frac{dQ}{dt} = C^*\beta + f(t,T) \quad (2.6)$$

where f (*t, T*) corresponds to the part of the heat flow related to the kinetic or non-reversing events, so called non-reversing heat flow Φ_{NR}. The reversing heat flow Φ_R linked to the

thermodynamic events corresponds to the complex heat capacity and the scanning rate $C^*\beta$. The main difference of MT-DSC from standard DSC is the control of the sample temperature and the data treatment method. In addition to the linear temperature ramp as in standard DSC, MT-DSC includes a temperature modulation program in which the sample temperature follows a periodic wave pattern (such as a sinusoidal wave, shown in Fig. 2.7.). Reading et al. [14] proposed to super-impose sinusoidal oscillation with the linear temperature ramp in order to separate the reversing and non-reversing events:

$$T = T_i + \beta t + A\,sin\,(\omega t) \tag{2.7}$$

where A is the modulation amplitude and ω is the angular frequency of the temperature modulation with the period of oscillation $P = 2\pi/\omega$.

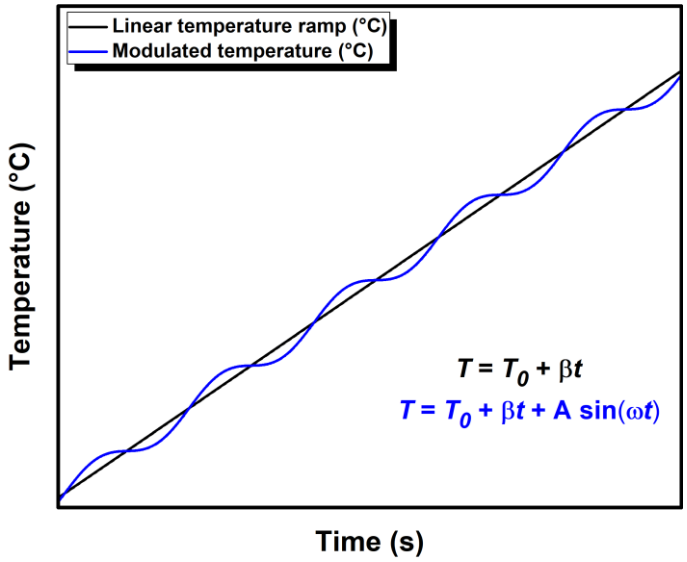

Figure 2. 7. Illustration of heating ramp in the MT-DSC experiment on PDLA sample with a modulation amplitude A = ± 0.318 K, a period of modulation P = 60 s ($\omega = 2\pi/P$) and underlying heating rate β_h = 2 K.min^{-1}. These experimental parameters correspond to a "heat-cool" mode.

The derivative of a sinusoidal temperature with respect to time gives the modulated heat flow Φ as follows:

$$\Phi = \frac{dQ}{dT} = C^*\,(\beta + A\omega\cos(\omega t)) \tag{2.8}$$

and the complex heat capacity C^* is defined as:

$$C^* = \frac{A_{HF}}{A_\beta} = \frac{\omega A C^*}{\omega A} \quad (2.9)$$

where A_{HF} and A_β are the amplitude of the heat flow modulation and of the heating rate modulation, respectively.

The thermodynamic events linked to the vibrational and translational motions of molecules can be investigated from the reversing heat flow Φ_R. Such motions are very rapid and can instantaneously follow any sample temperature modulation. On the contrary, the non-reversing heat flow Φ_{NR} cannot follow the modulation and contribute to the modulated part of the heat flow [15]. Thus, the total DSC signal simultaneously measured by MT-DSC corresponds to the signal measured by standard DSC and the reversing DSC. In that case, the reversing heat flow Φ_R and the non-reversing heat flow Φ_{NR} can be summarized according to:

$$\Phi_R = C^* \beta = \frac{A_{HF}}{A_\beta} \beta \quad (2.10)$$

$$\Phi_{NR} = \frac{dQ}{dt} - C^* \beta \quad (2.11)$$

A phase lag φ consists of the total heat flow and the heating modulation. In this situation, two evident heat capacity components considered as the in-phase component related to Φ_R C' and the out-of-phase component related to Φ_{NR} C'' can be determined by following equations:

$$C' = |C^*| \cos(\Phi) \quad (2.12)$$

$$C'' = |C^*| \sin(\Phi) \quad (2.13)$$

The MT-DSC measurements were carried out with the Q100 DSC from Thermal Analysis Instruments (DSC Q100 TA Instruments). All experiments were performed under a nitrogen atmosphere and the calibration of MT-DSC was carried out in three different steps:

1. the heat flow, the temperature and the baseline were calibrated by using T_{zero}^{TM} technology;
2. the temperature and the energy calibration were performed by using indium;

3. the specific heat capacity calibration was carried out using sapphire as a standard as it did not undergo any transition in the studied temperature range.

The heat capacity of sapphire as a function of temperature is known exactly and is very stable [16]. The third calibration step has to be repeated if the amplitude and period of oscillation, the average heating or cooling rate are changed. In the end, a calibration factor K_{CP} is calculated from the ratio of the experimental and theoretical specific heat capacity values of sapphire:

$$K_{C_P}(T) = \frac{C_{P_{Sapphire,theoretical}}(T)}{C_{P_{Sapphire,experimental}}(T)} \quad (2.14)$$

This factor is averaged on the temperature range of measurements and can be then used to correct the apparent heat capacity of sample.

In this work, MT-DSC analysis was performed in heat-cool mode to investigate the glass transition evolution of molecular dynamics in terms of free volume and CRR as well as to perform crystallinity degree calculation. The measurements were carried out with a modulation amplitude of ± 0.318 K, a period of 60 s and a scanning rate of 2 $K.min^{-1}$.

2.2.4 Fast scanning calorimetry (FSC)

Some thermal events or reactions may take place simultaneously during heating. While MT-DSC analysis allows us to dissociate the reversing and non-reversing events, Schick and Mathot proposed to apply very high scanning rates in order to avoid or prevent thermal reactions, as well as to observe very fast thermal events and/or crystallization processes [17]. In this case fast scanning calorimetry (FSC) is used. The fundamental principle of FSC is based on the measurement of the difference in amount of required heat to increase the temperature of a sample and a reference. The investigated sample and the reference are placed in separated furnaces. Then, both furnaces are heated and heat is transferred to the sample and the reference. The difference in thermal power which required to maintain the sample and the reference at the same temperature is monitored. In this work, FSC analysis was performed by fast scanning calorimeter Flash DSC 1 from Mettler Toledo with the power compensation twin-type calorimetric chip sensor, based on micro-electro-mechanical systems (MEMS)

technology. As shown in Fig. 2. 8, the twin-type chip sensor has two independent furnaces – one for a sample and the other one for reference. The MEMS chip sensor is made by a stable ceramic and the applied temperature is transferred by electrical thermocouples.

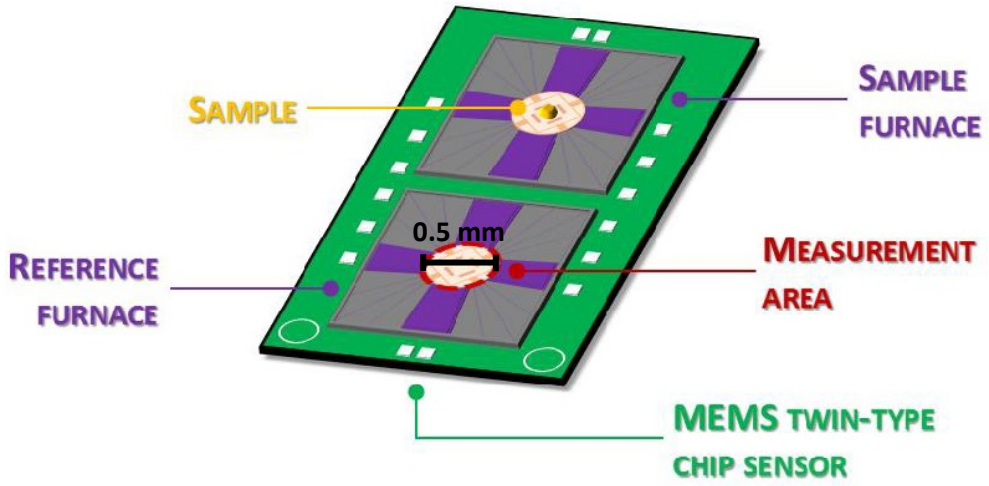

Figure 2. 8. Illustration of the twin-type chip sensor based on MEMS technology [18].

Both sides of the chip sensor contain two thermal resistance heaters in order to apply desired temperature and the temperature resolution is calculated by the time constant of the sensor (about 1 millisecond, i.e. thousand times less than in case of standard DSC). The heat flow is controlled through eight thermocouples at each side (totally sixteen thermocouples). The measurement area of the chip is fabricated of a silicon nitride and silicon dioxide coated with a thin layer of aluminum to provide homogenous temperature distribution. Before each use the chip sensor is conditioned and corrected according to Mettler Toledo procedures. The conditioning procedure allows verify the proper behavior of the sensor and its potential memory effects are erased by sensor heating to the maximum temperature (400 °C). The correction procedure is carried out in order to correct the thermocouple signal with respect to the sensor support temperature. The correction procedure is performed by comparing the signal of thermocouples with the temperature behavior of the heating resistance. In this work, small piece of sample was cut and placed directly in the center of the measurement area of a MultiSTAR UFS 1 MEMS chip sensor. A Huber TC100 intra cooler was used to cool the system down to -90 °C and carry out high cooling rates. The calorimeter was operated under nitrogen

gas flow of 20 mL.min^{-1} to avoid water condensation from the environment and to optimize the applied program temperature [19]. The mass of samples was estimated from the amplitude of the heat capacity step at the glass transition by comparing the value of the heat capacity step (ΔC_P) obtained by standard DSC at $|\beta_c| = \beta_h$ = 0.78 K.s^{-1} and the value of ΔC_P obtained by FSC at $|\beta_c| = \beta_h$ = 1500 K.s^{-1} [18]. The heat flow curves hereby were normalized to the mass and the scanning rate, and the spectra curves were then plotted in equivalent C_P unit, i.e. J.g^{-1}.K^{-1}.

2.2.4.1 Glass transition temperature determination by the fictive temperature concept

The respective glass transitions have been investigated in terms of fictive temperature and as a function of cooling rate. Thermal history of homopolymers and sc PLA samples was erased at 220 °C and 270 °C, respectively, by isotherms during 0.5 s before any investigations. Samples were then studied at temperatures from -50 °C to 270 °C at scanning rate $|\beta_c| = \beta_h$ ranging from 300 K.s^{-1} to 4000 K.s^{-1} to promote the resolution of investigated thermal events. Fig 2.9 presents the normalized heat flow of amorphous sc PLA sample as a function of temperature in the glass transition region.

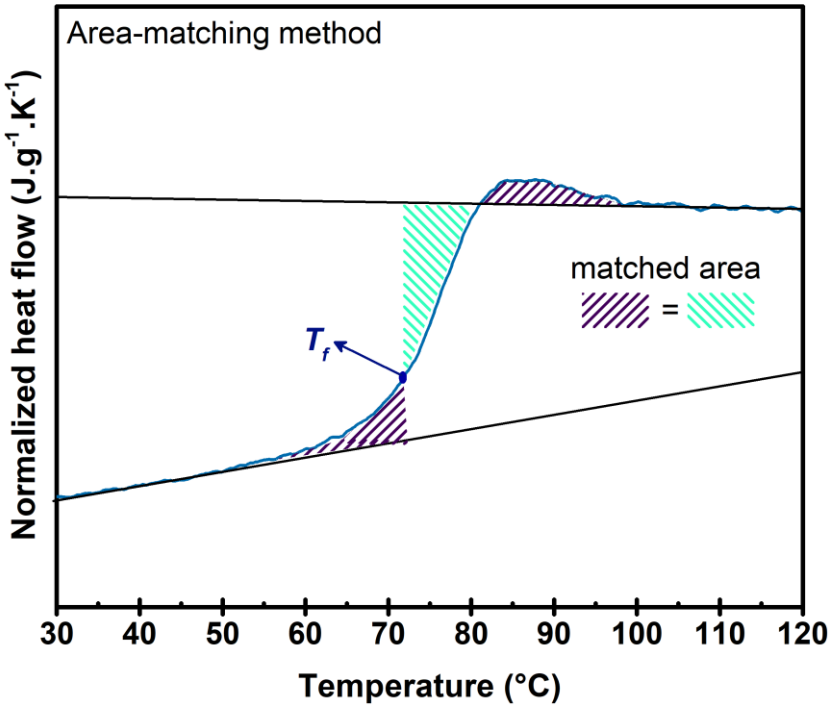

Figure 2. 9. FSC normalized heat flow curve of wholly amorphous sc PLA sample as a function of temperature upon heating at scanning rate $|\beta_c| = \beta_h$ = 1500 K.s^{-1}.

The values of the glass transition temperature were then calculated as the fictive temperatures by using area matching method that was proposed by Moynihan et al. [20], as shown in Fig 2.9. Since the heat capacity step at the glass transition is independent on the scanning rate, special attention is paid to the sensitivity, i.e. signal-to-noise ratio, of the heat flows during FSC experiments because of its dependence on the sample mass and scanning rate [21]. The cooling rate dependence of the fictive temperature is extensively presented in literature [22]. When applied cooling rate increases both the glass transition temperature and fictive temperature will increase according to the non-Arrhenius behavior. Such cooling rate dependence of the fictive temperature can be fitted by the Vogel-Fulcher-Tamman-Hesse (VFTH) equation [23]:

$$\log(|\beta_c|) = A_\beta - \frac{B}{T_f - T_V} \tag{2.15}$$

where A_β is a constant, B is a fitting parameter and T_V is a Vogel temperature which is the extrapolated temperature when relaxation time τ approaches infinite. In the concept of the fictive temperature, the VFTH equation can be modified to the Vogel-Fulcher-Tamman (VFT) equation to determine the dynamic fragility index m as follows [24, 25]:

$$m = \left[\frac{d(\log|\beta_c|)}{d\left(\frac{T_g}{T}\right)}\right]_{T = T_g} \tag{2.16}$$

Taking into account the VFTH behavior for the cooling rate dependence of the fictive temperature, m can also be expressed as follows:

$$m = \frac{B.T_g}{(T_g - T_V)^2} \tag{2.17}$$

The fictive temperatures as a function of cooling rate were determined by area-matching method for all the samples and the experimental data were fitted by the VFTH function to calculate the fragility index m.

2.2.4.2 Thermal lag corrections

In order to improve the accuracy of the fictive temperatures investigation by FSC, the thermal lag correction is required [17]. Thermal lag (δT_L) is defined as a shift in temperature due to the sample thickness and the high scanning rate, which provokes the heat transfer delay between heater and sample [26]. The thermal lags can be corrected by the melting of indium piece placed on the top of the sample [26-29]. As proposed by Schawe [27] two corrections of thermal lag may be applied: the static (δT_S) and the dynamic (δT_D) thermal lag. The static thermal lag (δT_S) corresponds to a third of the difference between the onsets melting point of an indium piece placed on the sample specimen and another one placed directly on the reference chip sensor, when extrapolated to heating rate zero. The dynamic thermal lag (δT_D) corresponds to a half of the difference between the fictive temperatures determined from measurements upon heating and cooling. A total thermal lag values were then calculated for all samples by following equation:

$$\delta T_L = \delta T_S + \delta T_D \tag{2.18}$$

2.2.4.3 Physical aging in a scanning rate range more than six decades

Physical aging was carried out at different aging temperatures (T_{ag} = T_g – 18 °C) calculated according to the corrected T_g for different aging time t_{ag} = 1 min; 10 min; 100 min at the scanning rate $|\beta_c|$ = β_h ranging from 300 K.s^{-1} to 4000 K.s^{-1}. Fig 2. 10a displays the normalized heat flows of aged and rejuvenated sample. Fig 2. 10b shows the scheme of enthalpy recovery determination of a glass, aged at a temperature T_{ag} during an aging time t_{ag} by the equations 1.23 and 1.24 [30].

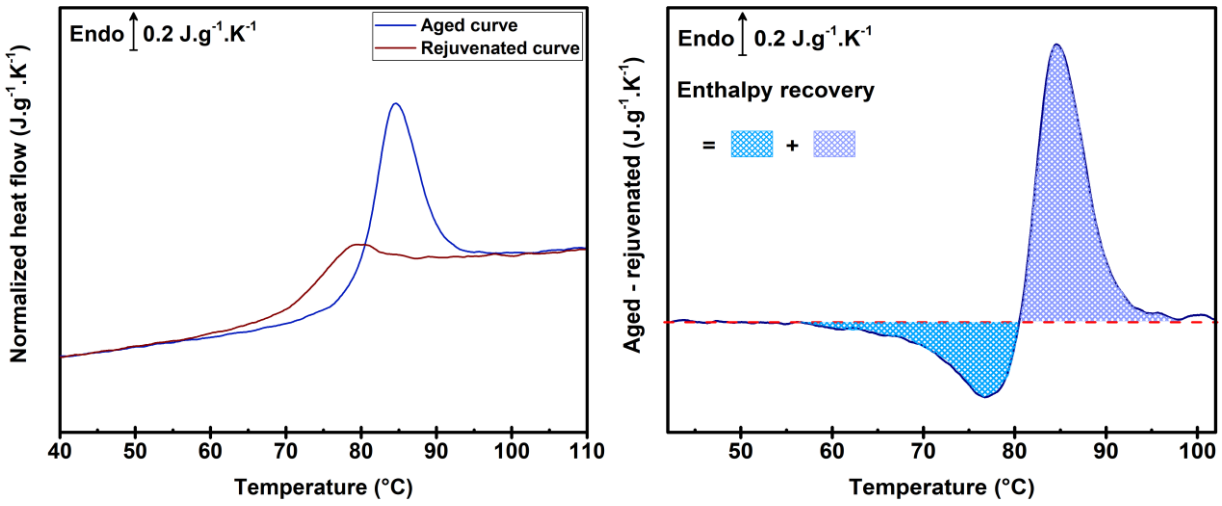

(a) (b)

Figure 2. 10. (a) Heat flows of aged and rejuvenated (non-aged) curves of amorphous sc PLA sample. (b) Schematic illustration of the enthalpy recovery calculation.

2.2.5 Dielectric relaxation spectroscopy (DRS)

DRS is a powerful technique to investigate molecular dynamic and relaxation phenomena of materials, especially polymers. The advantage of DRS is that measurements can be carried out at 9 decades of frequency or time, and this range can be extended up to 12 decades [31]. DRS analysis is based on the study of the motion of permanent dipoles present in a material as an impact of applied alternating electric field E(ω). In case of polymer, the net dipole moment per unit volume is linked to the total vector of all molecule dipoles that exist in the repeating unit, the polymer chain and overall structure in polymer chain. The electric field stimulates the electronic cell according to the atomic nucleus (so called electronic polarization) and composes induced dipole moment in atoms (so called atomic polarization). Such phenomenon in polymers is due to the rotational mobility of permanent dipole moments (μ), which are defined as dipole moments of chemical groups in the polymer chains. This reorientation of the permanent dipoles of the molecules allows us to determine the sample properties, i.e. permittivity, energy storage, resistivity and dissipation, and, thus, to investigate molecular motions occur within the polymers as a function of frequency and temperature.

Therefore, dielectric relaxation spectroscopy technique is usually used to investigate the molecular mobility [32-35]. In the frequency range of 10^{-6} to 10^{7} Hz, the sample can be studied as a circuit that is composed of an ideal capacitor and an ohmic resistor combined in parallel or serial. The complex impedance Z* (ω) of the circuit is measured by the spectrometer and may be defined in terms of energy dissipation or resistance R (ω), and energy storage or capacitance C (ω), in which ω the angular frequency is determined from the frequency *f* by the following equation:

$$\omega = 2\pi f \tag{2.19}$$

The derivation of the complex electrical impedance Z* (ω) gives other properties, such as electrical modulus M* (ω), electrical conductivity σ* (ω), resistivity R* (ω), and especially complex dielectric permittivity ε* (ω). To measure complex impedance Z* (ω), a sinusoidal voltage U*(ω) at a constant frequency is applied to the sample:

$$\mathrm{U}^{*}(\omega) = \mathrm{U}_0 \exp(j(\omega t)) \tag{2.20}$$

then, the current $\mathrm{I_S}^{*}$ (ω) is measured as follows:

$$\mathrm{I}_S^{*}(\omega) = \mathrm{I}_0 \exp(j\,(\omega t + \varphi)) \tag{2.21}$$

where φ is the phase shift between the applied voltage and measured current. The complex impedance Z* (ω) is then calculated by following ratio [36]:

$$\mathrm{Z}^{*}(\omega) = \frac{\mathrm{U}^{*}(\omega)}{\mathrm{I}^{*}(\omega)} \tag{2.22}$$

As shown in Fig.2.11, the impedance is determined from the measurements of two voltages corresponding to the generated voltage applied to the sample and the voltage-converted sample current $\mathrm{I_S}$ (ω). These voltages are analyzed by the Fourier transform technique to obtain information on their phases and amplitudes. The complex dielectric permittivity (ε*) of a capacitor C* filled with studied sample is expressed as:

$$\varepsilon^{*}(\omega) = \frac{C^{*}(\omega)}{C_0} \tag{2.23}$$

where C_0 is the capacitance of the empty capacitor. The capacitance of the empty capacitor can be defined as [36]:

$$C_0 = \frac{\varepsilon_0}{d} A \tag{2.24}$$

where ε_0 is the permittivity of vacuum, *A* is the area of the electrode and d is the thickness of the sample (distance between the plates as shown in Fig. 2.11). The complex dielectric permittivity (ε^*) can be derived by measuring the complex impedance $Z^*(\omega)$ of the sample:

$$\varepsilon^*(\omega) = \frac{1}{i\omega Z^*(\omega) C_0} \tag{2.25}$$

$$\varepsilon^*(\omega) = \varepsilon'(\omega) - i\varepsilon''(\omega) \tag{2.26}$$

where $\varepsilon'(\omega)$ is the real part (related to the stored energy) and $\varepsilon''(\omega)$ is the imaginary part (related to the dissipation of energy) of the complex dielectric permittivity (ε^*).

Permittivity allows us to investigate the ability of charges in a material to be reoriented or displaced in the presence of an external electric field in order to obtain information about the capacity of dipoles in a material mobility. In this study, DRS measurements were carried out with a Novocontrol Alpha analyzer. The temperature was controlled by a Quatro Novocontrol Cryosystem with temperature stability better than ± 0.2 K. Nonmetalized samples were placed between parallel 30 mm diameter inox plated electrodes. The broadband dielectric converter (Alpha analyzer interface) allows the measurement of the complex dielectric permittivity (real and imaginary parts) in a frequency range from 10^{-1} Hz to 10^6 Hz. The temperature was changed between -150 °C and 150 °C with increasing step of 10 °C for the range from -150 °C to 50 °C, and 1 °C for the range from 50 °C to 150 °C. During the whole measurements, the samples were kept in a pure nitrogen atmosphere.

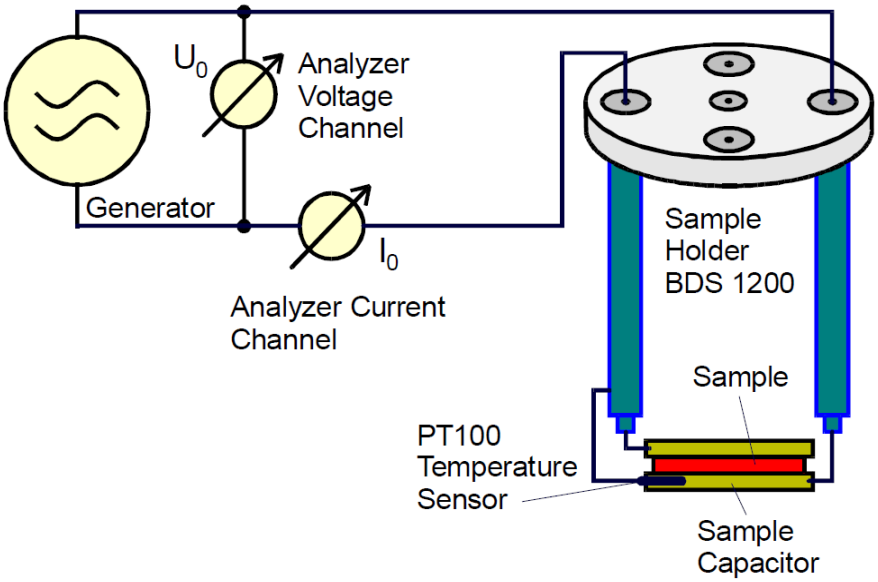

Figure 2. 11. Schematic representation of the spectrometer analyzer [37].

2.2.6 X-ray diffraction (XRD)

XRD is an analytical technique used for phase identification of crystalline phases. This analysis is based on a constructive interference of monochromatic X-rays and a crystalline sample and provides information on unit cell dimensions. X-rays are generated in a cathode ray tube by heating a filament to produce electrons, accelerating electrons towards a target material by applying a voltage, and bombarding the target material with electrons. When electrons have sufficient energy to dislodge inner shell electrons of the target material, characteristic X-ray spectra are obtained. As shown in Fig. 2.12, the basic principle of X-ray diffraction is based on the bombarding of a sample with an X-ray beam and the recording the intensity of the reflected X-rays. Constructive interference and peak intensity occur when the geometry of the loaded X-rays impinging the sample follows the Bragg's law [38]:

$$n\lambda = 2d\sin(\theta) \tag{2.27}$$

where d is the spacing between diffracting planes in the crystalline lattice, θ is the incident angle, n is any integer, and λ is the wavelength of the beam (depicted in Fig 2.13).

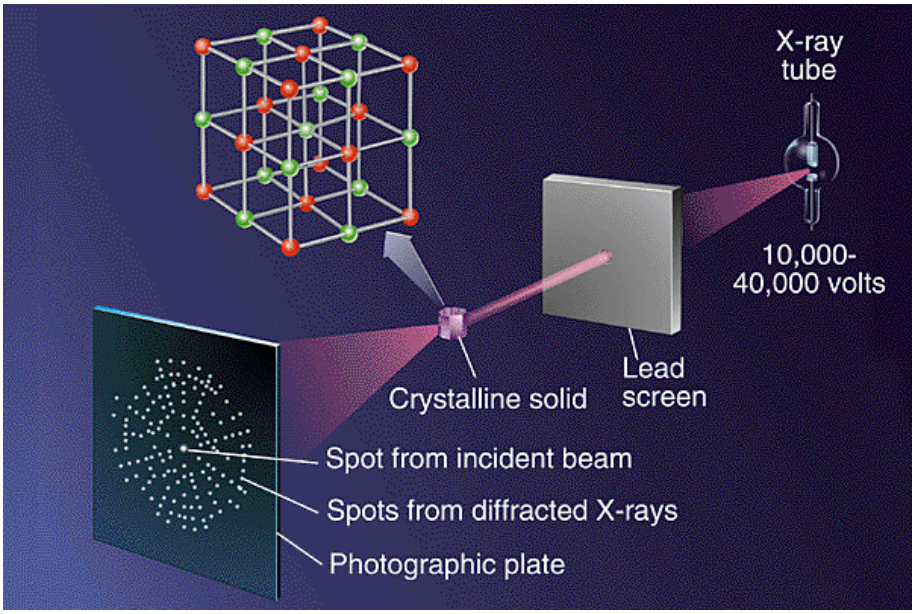

Figure 2. 12. Schematic representation of the basic principle of X-ray diffraction [39].

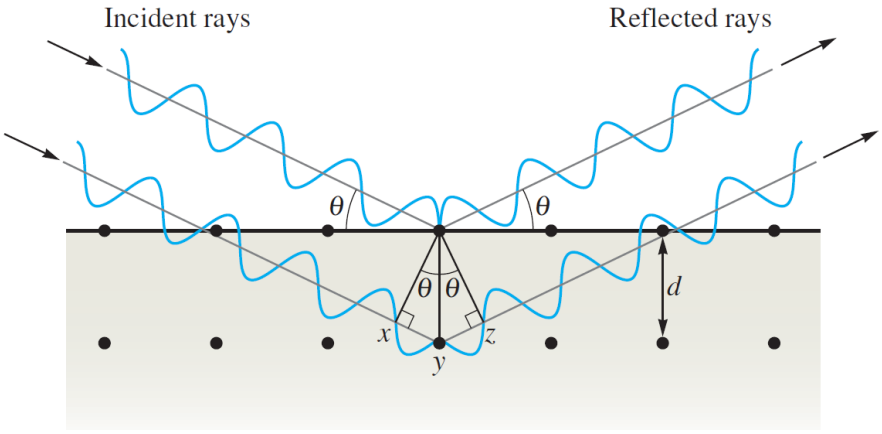

Figure 2. 13. Illustration of the Bragg's law [39].

X-ray diffraction technique is widely used for:

- characterization of crystalline materials;
- determination of unit cell dimensions;
- measurement of sample impurity;
- characterization of thin films by:
    - determining lattice mismatch between film and substrate;
    - determining dislocation density and quality of film;
    - determining the thickness, roughness and density.

In this work, XRD measurements were performed on Bruker's X-ray Diffraction D8-Discover instrument. The generator was set up at 35 kV and 40 mA and the target material copper for single-crystal diffraction with CuK_α radiation (λ = 1.54 Å) was selected. The measurements were run at room temperature (T= 25 ± 2 °C) from 5° to 40° at 0.04° increment with 1s/step scan speed. All X-ray patterns were corrected by background scattering.

2.2.7 Polarized optical microscopy (POM)

POM is a basic and sensitive technique used for both quantitative and qualitative studies of a wide range of anisotropic specimens. POM analysis is designed to observe and photograph specimens that are visible primarily due to their optically anisotropic character. In order to accomplish this task, POM uses polarized light. Therefore, in experiment two additional polarizing filters are associated to a conventional optical microscope:

- polarizer, positioned in the light path before the specimen;
- analyzer, placed in the optical pathway between the objective rear aperture and the observation tubes or camera port.

Such filters are used to restrict electro-magnetic field vectors constituting visible light to a single plane, as shown in Fig. 2. 14. As a consequence, all electro-magnetic field vectors are vibrating in the same plane and the light is then polarized.

In cross polarization mode, the analyzer is oriented perpendicularly to the first polarizer. This position leads to block remaining electro-magnetic field vectors. As a result, while no sample is placed on the light field, the light polarized by the polarizer is blocked by the analyzer, resulting in no visible light in the eyepiece. However, when birefringent sample, such as anisotropic material, is placed on the polarized light field, the restricted electro-magnetic field vectors coming through the sample are produced in many different perpendicular planes due to the refractive index depending on the polarization. Then, electro-magnetic field vectors which are parallel to the polarization direction of the analyzer can pass through and are visualized in the eyepiece.

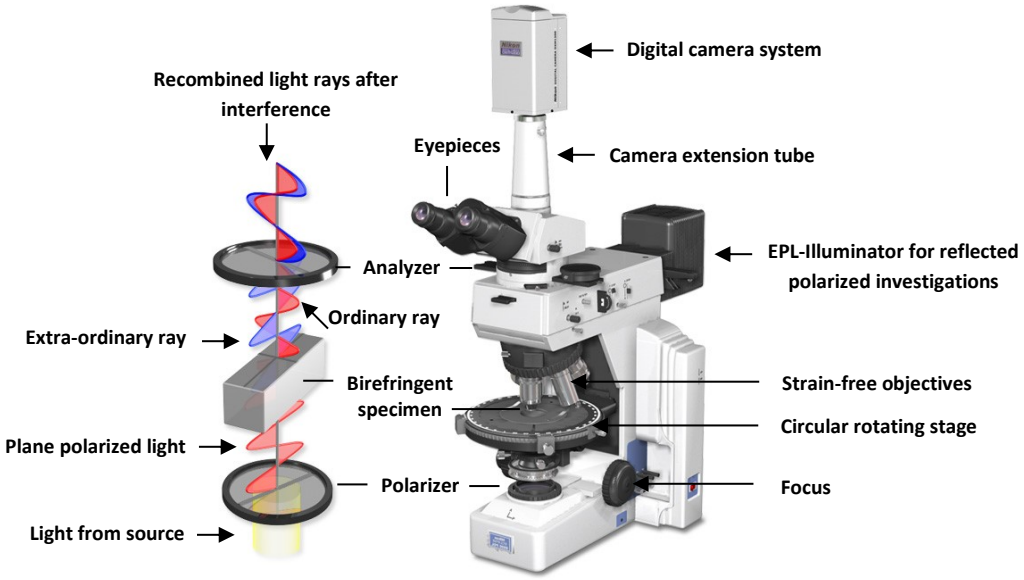

Figure 2. 14. Schematic representation of polarized optical microscopy configuration [40].

In this work, POM observations were carried out by using a universal Nikon EPI-illuminator with Nikon M Plan x2.5 / x5 / x10 lenses connected with a digital sight camera system from Nikon Corporation, either transmission or reflection mode. A Mettler FP82HT hot stage connected to a Mettler FP90 central processor was combined with POM as a temperature controller system during the crystallization observations.

2.2.8 Scanning electron microscopy (SEM)

During SEM analysis a sample is placed in a vacuum chamber and its surface is scanned by a focused beam of electrons. Due to the particle-wave duality of electrons, the electron beam is accelerated and focused on a sample in the path of anode, condenser and magnetic lenses, as shown in Fig 2. 15. These electrons interact with atoms in the sample as well as the sample surface. The primary beam focused on the sample area leads to the ejection of other electrons including secondary electrons, back-scattered electrons or X-rays. Specific detectors are used according to the materials nature and the signals measured involve information about the surface topography and the composition of the sample. In this work, SEM analysis was carried out by a Dual-BEAM LEO1530-ZEISS scanning electron microscopy to observe the surface morphology of semi-crystalline homopolymers PLLA and PDLA, and sc PLA.

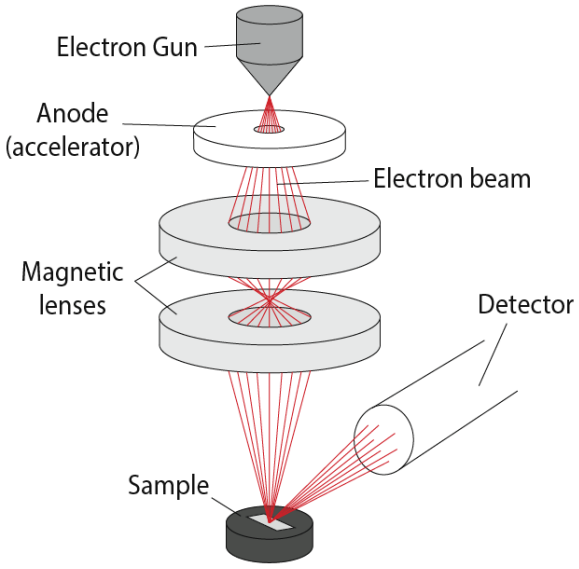

Figure 2. 15. Schematic representation of scanning electron microscopy analysis in a vacuum chamber.

2.2.9 Permeation measurements

2.2.9.1 Water permeation measurements

The permeation process includes several steps (shown in Fig 2.16) such as sorption, diffusion and desorption while maintaining the concentration of the permeant as a constant at the upstream interface of the film (*C'*). The concentration of the permeant at the downstream interface of the film (*C''*) is negligible compared to *C'* (*C'* >> *C''*). In case of this concentration difference, a transfer of matter is observed and follows the two laws of Fick [41]. The dissolution-diffusion process results from the association of two phenomena:

- the dissolution of permeant molecules within the material which is characterized thermodynamically by a solubility coefficient (*S*);
- the diffusion of permeant molecules through the material (kinetic order) and characterizes by diffusion coefficient (*D*).

The first law of Fick explains the dependence of the flux *J* (*x, t*) on the perpendicular position to the plane of the film (*x*) and the time (*t*) with the gradient of the local concentration *C* (*x, t*):

$$J\,(x,t) = -D\,\frac{\partial\, J\,(x,t)}{\partial x} \tag{2.28}$$

where *D* is the local diffusion coefficient of permeant. According to the observed Fickien mechanism [42] two types of diffusion can be present. The type I is observed when *D* is constant and the type II occurs when *D* depends on the concentration of the permeant. According to Fick's second law, the evolution of the local concentration with the divergence of the flux can be expressed as follows:

$$\frac{\partial C(x,t)}{\partial t} = \frac{\partial J(x,t)}{\partial x} \tag{2.29}$$

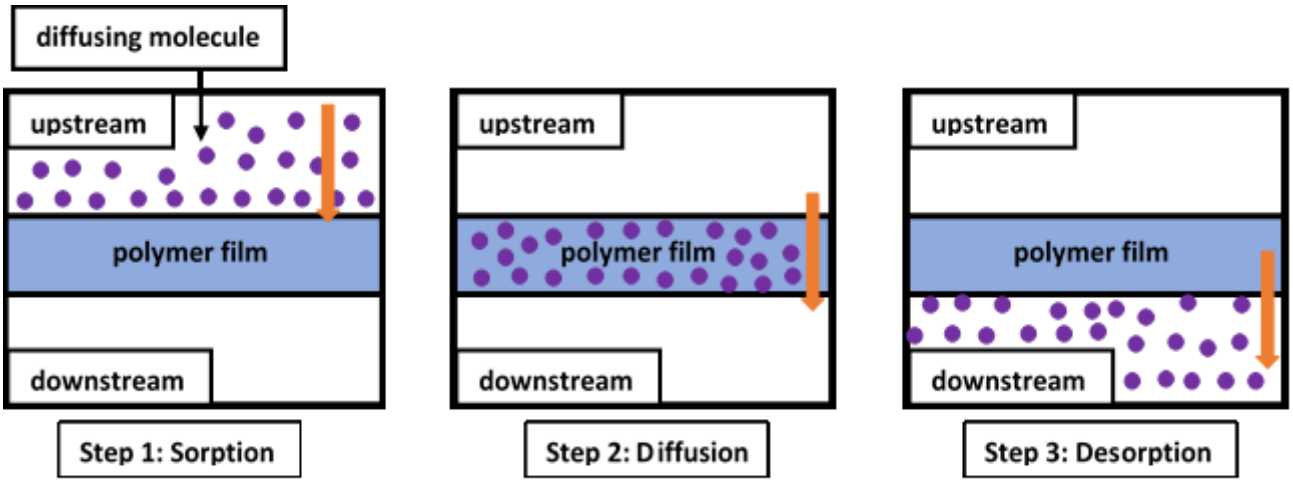

Figure 2. 16. Schematic representation of the principle of permeation measurements in 3 steps.

The interfaces of the film can be defined as $x = 0$ for upstream and $x = L$ for downstream, where *L* corresponds to the film thickness. Several hypotheses must be made in order to apply these diffusion models: (1) the sample is homogenous and initially no trace of permeant is present, (2) the impact of swelling during measurements is negligible, and (3) the sorption at the film surface reaches equilibrium in a quasi-instantaneous manner. The initial and limiting conditions are expressed by following functions and the permeant concentration profiles are depicted schematically in Fig 2.17.

when $t = 0$ $\quad 0 < x < L$ $\quad C(x, 0)$ (2.30)

when $t > 0$ $\quad x = 0$ $\quad C(0, t) = C' = C_{eq}$ (2.31)

when $t > 0$ $\quad x = L$ $\quad C(L, t) = C'' \approx 0$ (2.32)

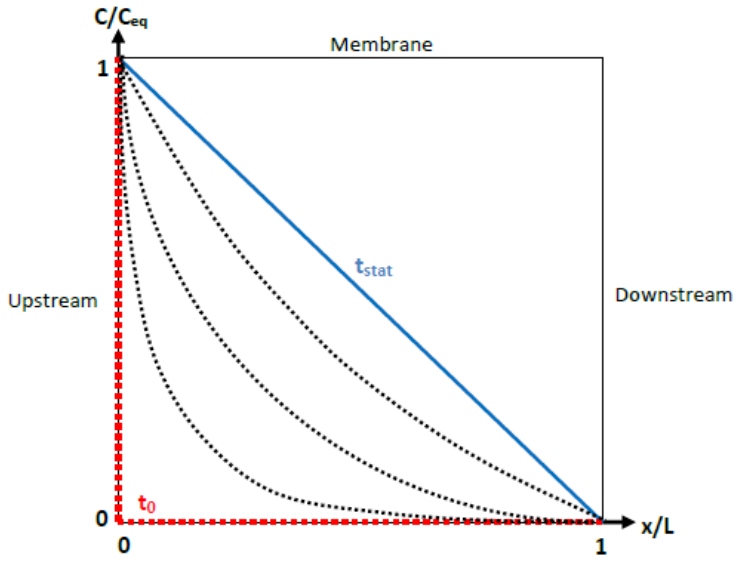

Figure 2. 17. Schematic representation of the profiles of permeant concentration in reduced scales at t = 0 up to steady state where $t = t_{stat}$ for constant D.

The transport properties of the samples (semi-crystalline PLLA, PDLA, and sc PLA) towards water at 25 °C, 45 °C and 65 °C were studied to investigate the influence of stereocomplexation on film barrier properties. The water permeation measurements were carried out by the device designed by MPBM team of PBS laboratory (Fig 2.18). The permeation cell, in which the sample is installed, is placed in a thermoregulated chamber (oven at T= 25 °C, 45 °C and 65 °C). Before measurement, a purge step is carried out with a flow of dry gas (Technical Nitrogen upstream and BIP downstream, Air Products®) applied for a certain time (generally 18h). The downstream gas arrives to a mirror hygrometer (General Eastern, USA) and the dew point temperature T_R (Dew point) is measured. When this temperature is sufficiently low (around -70 °C at atmospheric pressure), the flow of dry gas in upstream is stopped and liquid distillated water is added in the upstream compartment at a time t = 0. Due to the difference in the concentration of the permeant between the two compartments, the water molecules' transfer will result in a rise in the amount of water in the downstream compartment and so in a T_R increase over time, as shown in Fig. 2. 19. The measurements were repeated between 3 and 5 times for each sample and each temperature for better accuracy.

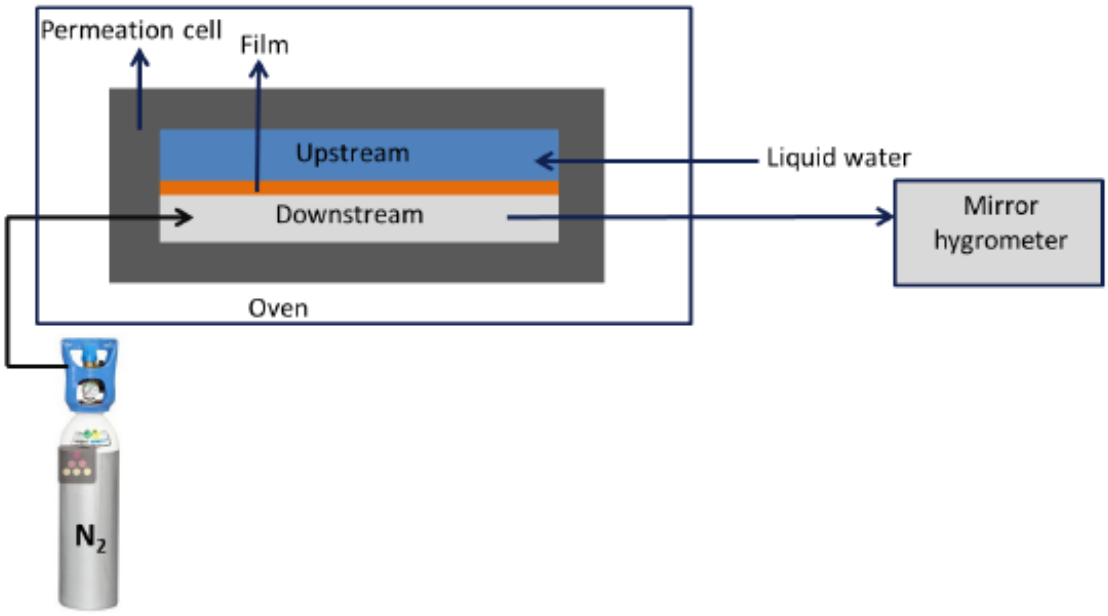

Figure 2. 18. Schematic illustration of the water permeation measurements.

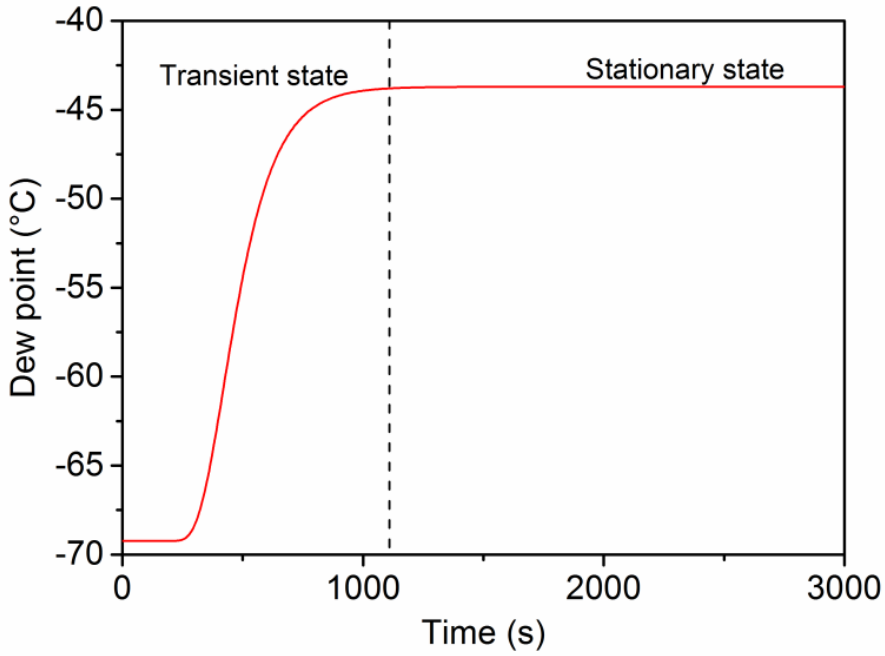

Figure 2. 19. Example of the evolution of dew point T_R over time during the water permeation measurement.

2.2.9.2 Gas permeation measurements (N_2, O_2, and CO_2)

Gas permeability was measured by the so called "time-lag" method [43] by using the experimental device reported by Joly et al. [44] (shown in Fig. 2. 20). The gases used are: nitrogen N_2 (Air Products®, purity 99.99%), oxygen O_2 (Air Liquide®, purity 99.99%) and carbon dioxide CO_2 (Air Products®, purity 99.5%).

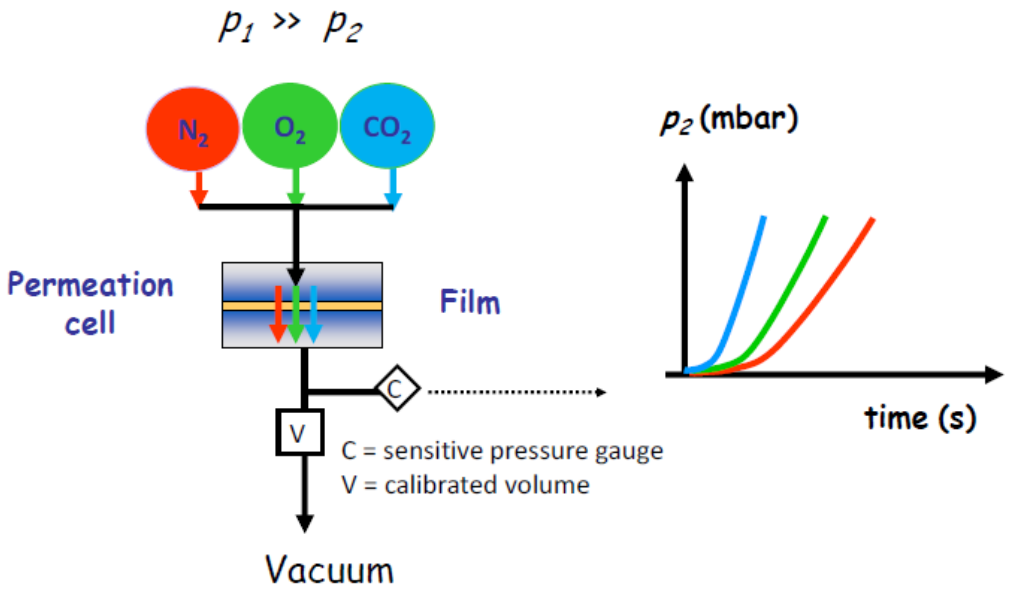

Figure 2. 20. Illustration of gas permeation apparatus.

Nitrogen, oxygen and carbon dioxide permeation properties of semi-crystalline PLLA, PDLA and sc PLA films at room temperature T= 25 ± 2 °C were determined using the permeation apparatus shown in Fig. 2. 20. Before measurements, the permeation cell (XX45047 Millipore filtration cell adapted for gas permeation) was completely evacuated by applying a vacuum on both sides of the film. Then, the upstream side was provided with the gas under test at pressure p_1 (3 bar). The increase of pressure in the calibrated downstream volume p_2 ($p_1 >> p_2$) was measured using a sensitive pressure gauge (0 – 10 mbar, Effa AW – 10 – T4) linked to a data acquisition system. The measurements of each gas were repeated between 3 and 5 times for each sample for better accuracy.

References

1. Zhang, J.; Tashiro, K.; Tsuji, H.; Domb, A. J. Disorder-to-Order Phase Transition and Multiple Melting Behavior of Poly(l-lactide) Investigated by Simultaneous Measurements of WAXD and DSC. *Macromolecules* **2008,** 41 (4), 1352-1357 DOI: 10.1021/ma0706071.
2. Zhang, J.; Duan, Y.; Sato, H.; Tsuji, H.; Noda, I.; Yan, S.; Ozaki, Y. Crystal Modifications and Thermal Behavior of Poly(l-lactic acid) Revealed by Infrared Spectroscopy. *Macromolecules* **2005,** 38 (19), 8012-8021 DOI: 10.1021/ma051232r.
3. Garlotta, D. A Literature Review of Poly(Lactic Acid). *Journal of Polymers and the Environment* **2001,** 9 (2), 63-84 DOI: 10.1023/a:1020200822435.
4. Woo, E. M.; Chang, L. Crystallization and morphology of stereocomplexes in nonequimolar mixtures of poly(l-lactic acid) with excess poly(d-lactic acid). *Polymer* **2011,** 52 (26), 6080-6089 DOI: https://doi.org/10.1016/j.polymer.2011.11.002.
5. Coats, A. W.; Redfern, J. P. Thermogravimetric analysis. A review. *Analyst* **1963,** 88 (1053), 906-924 DOI: 10.1039/AN9638800906.
6. Reyes-Labarta, J. A.; Marcilla, A. Thermal Treatment and Degradation of Cross-Linked Ethylene Vinyl Acetate–Polyethylene–Azodicarbonamide–ZnO Foams. Complete Kinetic Modeling and Analysis. *Industrial & Engineering Chemistry Research* **2012,** 51 (28), 9515-9530 DOI: 10.1021/ie3006935.
7. Reyes-Labarta, J. A.; Marcilla, A. Kinetic study of the decompositions involved in the thermal degradation of commercial azodicarbonamide. *Journal of Applied Polymer Science* **2008,** 107 (1), 339-346 DOI: doi:10.1002/app.26922.
8. Marcilla, A.; Gómez, A.; Reyes-Labarta, J. A. MCM-41 catalytic pyrolysis of ethylene–vinyl acetate copolymers: kinetic model. *Polymer* **2001,** 42 (19), 8103-8111 DOI: https://doi.org/10.1016/S0032-3861(01)00277-4.
9. Wunderlich, B., *Thermal Analysis of Polymeric Materials*. Springer, Berlin, Heidelberg: 2005.
10. G. W. H. Höhne; W. F. Hemminger; Flammersheim, H.-J., *Differential Scanning Calorimetry*. Springer-Verlag Berlin Heidelberg: Springer, Berlin, Heidelberg, 2003.
11. Schick, C. Differential scanning calorimetry (DSC) of semicrystalline polymers. *Anal Bioanal Chem* **2009,** 395 (6), 1589-1611 DOI: 10.1007/s00216-009-3169-y.
12. Danley, R. L. New heat flux DSC measurement technique. *Thermochimica Acta* **2002,** 395 (1), 201-208 DOI: https://doi.org/10.1016/S0040-6031(02)00212-5.
13. Reading, M.; Hahn, B. K.; Crowe, B. S. Method and apparatus for modulated differential analysis. 1994.
14. Lacey, A. A.; Price, D. M.; Reading, M., Theory and practice of modulated temperature differential scanning calorimetry. In *Modulated Temperature Differential Scanning Calorimetry*, Springer: 2006; pp 1-81.
15. Hutchinson, J. M.; Montserrat, S. The application of temperature-modulated DSC to the glass transition region: II. Effect of a distribution of relaxation times. *Thermochimica Acta* **2001,** 377 (1), 63-84 DOI: https://doi.org/10.1016/S0040-6031(01)00542-1.
16. Reading, M.; Hourston, D. J., *Modulated Temperature Differential Scanning Calorimetry*. Springer, Dordrecht: 2006.
17. Schick, C.; Mathot, V., *Fast Scanning Calorimetry*. Springer International Publishing: Switzerland, 2016.
18. Monnier, X.; Saiter, A.; Dargent, E. Physical aging in PLA through standard DSC and fast scanning calorimetry investigations. *Thermochimica Acta* **2017,** 648, 13-22 DOI: https://doi.org/10.1016/j.tca.2016.12.006.
19. Mathot, V.; Pyda, M.; Pijpers, T.; Vanden Poel, G.; van de Kerkhof, E.; van Herwaarden, S.; van Herwaarden, F.; Leenaers, A. The Flash DSC 1, a power compensation twin-type, chip-based fast scanning calorimeter (FSC): First findings on polymers. *Thermochimica Acta* **2011,** 522 (1), 36-45 DOI: https://doi.org/10.1016/j.tca.2011.02.031.

20. Moynihan, C. T.; Macedo, P. B.; Montrose, C. J.; Gupta, P. K.; DeBolt, M. A.; Dill, J. F.; Dom, B. E.; Drake, P. W.; Easteal, A. J.; Elterman, P. B.; Moeller, R. P.; Sasabe, H.; Wilder, J. A. Structural relaxation in vitreous materials. *Annals of the New York Academy of Sciences* **1976,** 279 (1), 15-35 DOI: doi:10.1111/j.1749-6632.1976.tb39688.x.

21. Verdonck, E.; Schaap, K.; Thomas, L. C. A discussion of the principles and applications of Modulated Temperature DSC (MTDSC). *International Journal of Pharmaceutics* **1999,** 192 (1), 3-20 DOI: https://doi.org/10.1016/S0378-5173(99)00267-7.

22. Gao, S.; Simon, S. L. Measurement of the limiting fictive temperature over five decades of cooling and heating rates. *Thermochimica Acta* **2015,** 603, 123-127 DOI: https://doi.org/10.1016/j.tca.2014.08.019.

23. Tammann, V. G.; Hesse, W. Die Abhängigkeit der Viscosität von der Temperatur bie unterkühlten Flüssigkeiten. *Zeitschrift für anorganische und allgemeine Chemie* **1926,** 156 (1), 245-257 DOI: doi:10.1002/zaac.19261560121.

24. Fulcher, G. S. ANALYSIS OF RECENT MEASUREMENTS OF THE VISCOSITY OF GLASSES. *Journal of the American Ceramic Society* **1925,** 8 (6), 339-355 DOI: doi:10.1111/j.1151-2916.1925.tb16731.x.

25. Schawe, J. E. K. Vitrification in a wide cooling rate range: The relations between cooling rate, relaxation time, transition width, and fragility. *The Journal of Chemical Physics* **2014,** 141 (18), 184905 DOI: 10.1063/1.4900961.

26. Poel, G. V.; Istrate, D.; Magon, A.; Mathot, V. Performance and calibration of the Flash DSC 1, a new, MEMS-based fast scanning calorimeter. *Journal of Thermal Analysis and Calorimetry* **2012,** 110 (3), 1533-1546 DOI: 10.1007/s10973-012-2722-7.

27. Schawe, J. E. K. Measurement of the thermal glass transition of polystyrene in a cooling rate range of more than six decades. *Thermochimica Acta* **2015,** 603, 128-134 DOI: https://doi.org/10.1016/j.tca.2014.05.025.

28. Gao, S.; Koh, Y. P.; Simon, S. L. Calorimetric Glass Transition of Single Polystyrene Ultrathin Films. *Macromolecules* **2013,** 46 (2), 562-570 DOI: 10.1021/ma3020036.

29. Shamim, N.; Koh, Y. P.; Simon, S. L.; McKenna, G. B. Glass transition temperature of thin polycarbonate films measured by flash differential scanning calorimetry. *Journal of Polymer Science Part B: Polymer Physics* **2014,** 52 (22), 1462-1468 DOI: doi:10.1002/polb.23583.

30. Hodge, I. M. Enthalpy relaxation and recovery in amorphous materials. *Journal of Non-Crystalline Solids* **1994,** 169 (3), 211-266 DOI: https://doi.org/10.1016/0022-3093(94)90321-2.

31. Lunkenheimer, P.; Loidl, A. Dielectric spectroscopy of glass-forming materials: α-relaxation and excess wing. *Chemical Physics* **2002,** 284 (1), 205-219 DOI: https://doi.org/10.1016/S0301-0104(02)00549-9.

32. Yin, H.; Napolitano, S.; Schönhals, A. Molecular Mobility and Glass Transition of Thin Films of Poly(bisphenol A carbonate). *Macromolecules* **2012,** 45 (3), 1652-1662 DOI: 10.1021/ma202127p.

33. Lukichev, A. A. Graphical method for the Debye-like relaxation spectra analysis. *Journal of Non-Crystalline Solids* **2012,** 358 (3), 447-453 DOI: https://doi.org/10.1016/j.jnoncrysol.2011.10.022.

34. Nobukawa, S.; Urakawa, O.; Shikata, T.; Inoue, T. Dynamics of a Probe Molecule Dissolved in Several Polymer Matrices with Different Side-Chain Structures: Determination of Correlation Length Relevant to Glass Transition. *Macromolecules* **2013,** 46 (6), 2206-2215 DOI: 10.1021/ma302567j.

35. Brás, A. R.; Fonseca, I. M.; Dionísio, M.; Schönhals, A.; Affouard, F.; Correia, N. T. Influence of Nanoscale Confinement on the Molecular Mobility of Ibuprofen. *The Journal of Physical Chemistry C* **2014,** 118 (25), 13857-13868 DOI: 10.1021/jp500630m.

36. Kremer F, S. A., *Broadband dielectric spectroscopy*. New York: Springer, 2003.

37. Novocontrol Technologies GmbH & Co. KG.- Alpha-A High Resolution Dielectric, Conductivity, Impedance and Gain Phase Modular Measurement System - User's Manual. **2010,** (9), 14.

38. Bragg, W. H.; Bragg, W. L. The reflection of X-rays by crystals. *Proceedings of the Royal Society of London. Series A* **1913,** 88 (605), 428-438 DOI: 10.1098/rspa.1913.0040.

39. Zumdahl, S. S.; Zumdahl, S. A., *Chemistry Seventh Edition*. Houghton Mifflin Company: Boston, 2007.

40. Robinson, P. C.; Davidson, M. W. Polarized Light Microscopy. https://www.microscopyu.com/techniques/polarized-light/polarized-light-microscopy (21 October 2018),

41. Fick, A. A. W. H., [Hermann von], *Uber Diffusion*. Johann Ambrosius Barth, Leipzig, 1855 Vol. Poggendorff's Annalen der Physik und Chemie, 94, 1855.

42. Frisch, H. L. The Time Lag in Diffusion. *The Journal of Physical Chemistry* **1957,** 61 (1), 93-95 DOI: 10.1021/j150547a018.

43. Barrer, R. M.; Rideal, E. K. Permeation, diffusion and solution of gases in organic polymers. *Transactions of the Faraday Society* **1939,** 35 (0), 628-643 DOI: 10.1039/TF9393500628.

44. Joly, C.; Le Cerf, D.; Chappey, C.; Langevin, D.; Muller, G. Residual solvent effect on the permeation properties of fluorinated polyimide films. *Separation and Purification Technology* **1999,** 16 (1), 47-54 DOI: https://doi.org/10.1016/S1383-5866(98)00118-X.

CHAPTER 3. INFLUENCE OF ELABORATION METHODS ON STEREOCOMPLEXATION REACTION

In order to study the stereocomplexation reaction, two different methods were used, i.e. the solvent casting and the extrusion. The experimental conditions (polymer concentration and homopolymer ratio in case of solution casting; and temperature and mixing time in case of extrusion) were optimized in terms of film microstructure and thermal properties.

3.1 Homopolymers

3.1.1 Homopolymer pellets

Dried PLLA and PDLA pellets were analyzed in order to investigate their thermal properties before further characterization.

3.1.1.1 Thermal stability of pellets

Fig 3.1 presents thermograms and derivative curves of thermograms for PLLA and PDLA pellets as a function of temperature. Thermal degradation temperature (T_{deg}) was determined as the temperature at which the mass loss was observed as shown in Table 3.1. PLLA pellets degrade about 25 °C lower than PDLA pellets (T_{deg} = 296 °C and T_{deg} = 321 °C, respectively) (Fig 3.1.a), while the maximum of derivative curves shows much less temperature variation between the homopolymers, i.e. about 5 °C (shown in Fig 3.1.b). In any case, T_{deg} of homopolymer pellets is sufficiently high for the stereocomplex formation.

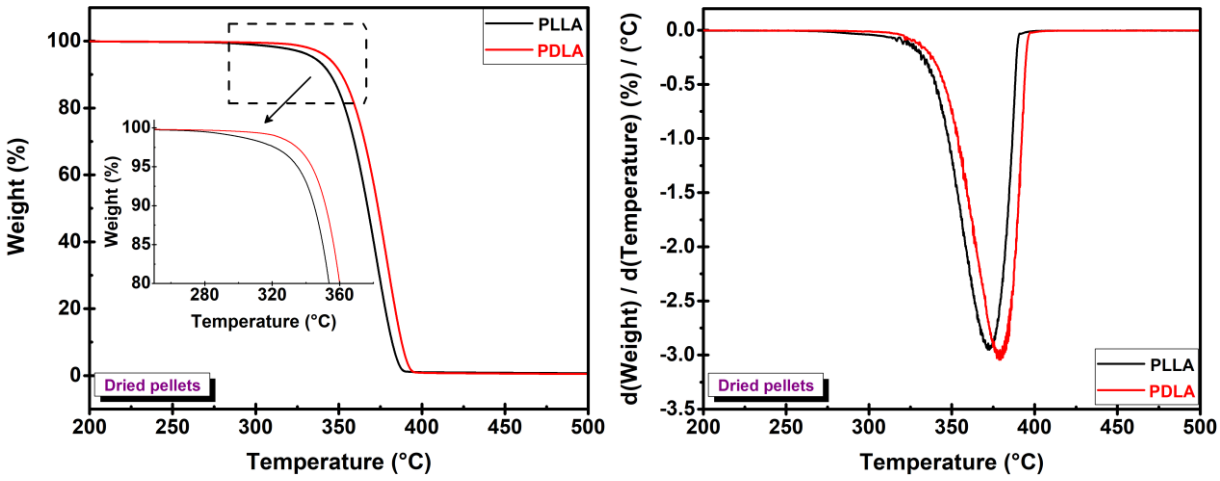

(a) (b)

Figure 3. 1. TGA curves of pure PLLA and PDLA pellets: (a) thermograms and (b) derivative curves as a function of temperature.

Sample	*T* of 1% weight loss (°C)	*T* of 50% weight loss (°C)	*Maximum of derivative curve* (°C)
PLLA pellet	296	367	373
PDLA pellet	321	373	378

Table 3. 1. Degradation temperature (T_{deg}) of pure PLLA and PDLA pellets at 1% and 50% weight loss and the maximum of derivative curves.

3.1.1.2 Thermal properties of pellets

DSC analysis was performed in order to examine the thermal properties of homopolymer pellets, i.e. glass transition temperature T_g, and melting temperature T_m. The DSC curves of homopolymer pellets are shown in Fig 3.2. The endothermic peaks at T_g (~ 60 °C) are due to the structural relaxation imposed by T_g. The endothermic peaks at ~ 175 °C correspond to the melting of homo-crystals $T_{m,\alpha}$ obtained by the cold-crystallization T_{cc} which is confirmed by the exothermic peaks at 104 °C and 90 °C for PLLA and PDLA, respectively.

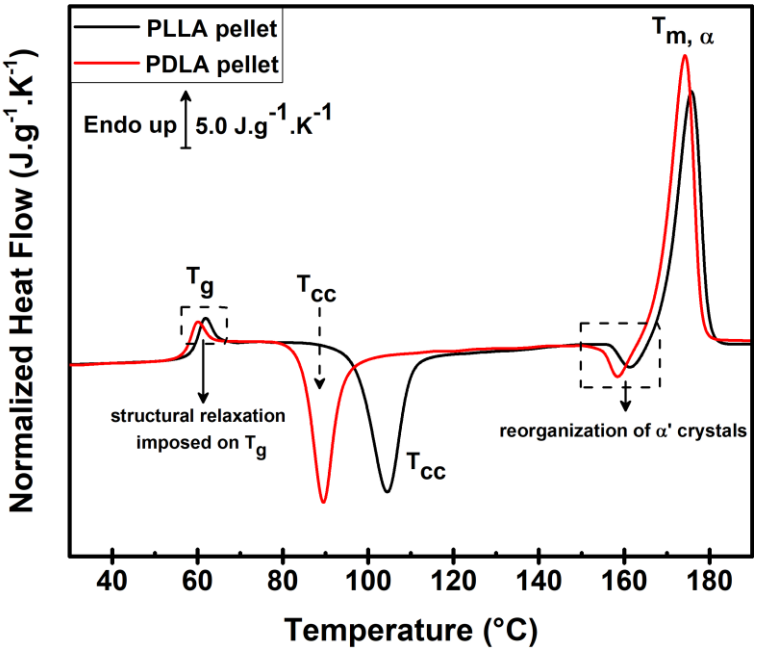

Figure 3. 2. DSC curves of PLLA and PDLA pellets.

The cold-crystallization at temperature $T < 120$ °C leads to α' crystals form formation, i.e. disordered crystals with hexagonal packing [1, 2]. The reorganization of α' imperfect crystals into α form crystals is noticed by the exothermic peak before melting at temperature

$T \approx 160$ °C. The values of the thermal parameters are presented in Table 3.2 and the crystallinity degree of α crystals is estimated by following equation [3]:

$$X_c = \frac{[\Delta H_m - \sum \Delta H_{cc}]}{\Delta H_m^0} \quad (3.1)$$

where ΔH_m is the measured melting enthalpy, $\Sigma \Delta H_{cc}$ is sum of cold crystallization enthalpy, ΔH_m^0 is the melting enthalpy of 100 % crystalline sample, which equals 93 J/g for α crystals of PLA [4]. The equal value of melting and cold-crystallization enthalpies reveals that homopolymer pellets are amorphous.

Sample	T_g (°C)	T_{cc} (°C)	ΔH_{cc} (J/g)	T_m (°C)	ΔH_m (J/g)	X_c (%)
PLLA pellet	60	104	47	176	48	1
PDLA pellet	59	90	51	174	53	2

Table 3. 2. The values of the glass transition temperature T_g, the cold-crystallization T_{cc}, and the melting T_m and the enthalpy of the cold-crystallization (ΔH_{cc}) and the melting (ΔH_m) for PLLA and PDLA pellets.

3.1.2 Homopolymer film samples

Homopolymer films were obtained by thermo-molded and solution casting methods (presented in chapter 2). The influence of the elaboration methods on homopolymers properties was investigated by DSC, MT-DSC and XRD analysis.

3.1.2.1 Amorphous homopolymers' film

Amorphous PLLA and PDLA films obtained by thermo-molding method were analyzed by DSC in order to examine thermal characteristics of homopolymers' films. Obtained DSC curves are presented in Fig 3.3. The values of the thermal parameters (T_g, T_{cc} and T_m) are presented in Table 3.3 and the crystallinity degree of α crystals is estimated by Eq 3.1. DSC curves of the thermo-molded homopolymer films reveal the formation of α' crystals that confirmed by the exothermic peaks at 90 °C and around 158 °C. The T_m of homopolymer crystals is observed at 174 °C for both PLLA and PDLA films. The close values of melting and cold-crystallization enthalpies reveal that the thermo-molded homopolymer films are amorphous.

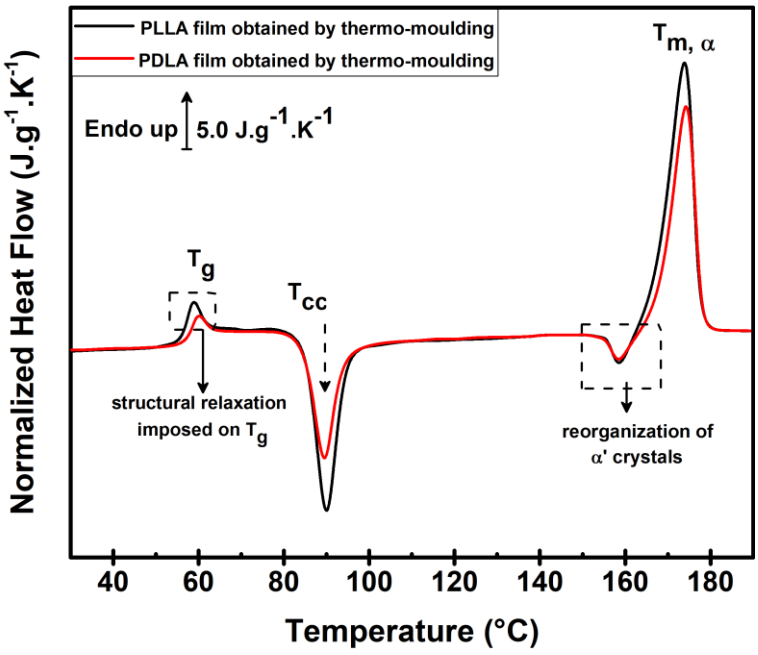

Figure 3. 3. DSC curves of thermo-molded PLLA and PDLA films.

Sample	T_g (°C)	T_{cc} (°C)	ΔH_{cc} (J/g)	T_m (°C)	ΔH_m (J/g)	X_c (%)
PLLA film	58	90	51	174	53	2
PDLA film	59	90	43	174	45	2

Table 3. 3. The values of the thermal properties of thermo-molded homopolymer films.

3.1.2.2 Semicrystalline homopolymers' film

Semicrystalline homopolymers' films were obtained by solution casting and characterized by DSC, MT-DSC and XRD analysis in order to investigate their thermal properties and microstructure. The DSC curves and thermal characteristics values of homopolymers film are presented in Fig 3.4 and Table 3.4, respectively. The 1st heating DSC curves show only endothermic peaks at 176 °C which correspond to the melting peaks of α homo-crystals of PLLA and PDLA obtained during solvent evaporation.

The obtained homopolymers films are semicrystalline with the X_c values equal 47 and 41 % for PLLA and PDLA, respectively. In order to study the stability of the homo-crystals 2nd heating scan was carried out (Fig 3.4b). Although, there is a α' crystals formation (~ 85 – 95 °C), the reformation of α crystals is confirmed by the melting peak at 176°C. The X_c values measured during 2nd heat are lower than the values obtained at 1st heat (Table 3.4). This result

testifies that the cooling at 10°C.min^{-1} is not enough to obtain wholly amorphous sample. Therefore, one can say that the α crystals obtained by solution casting method are rather stable.

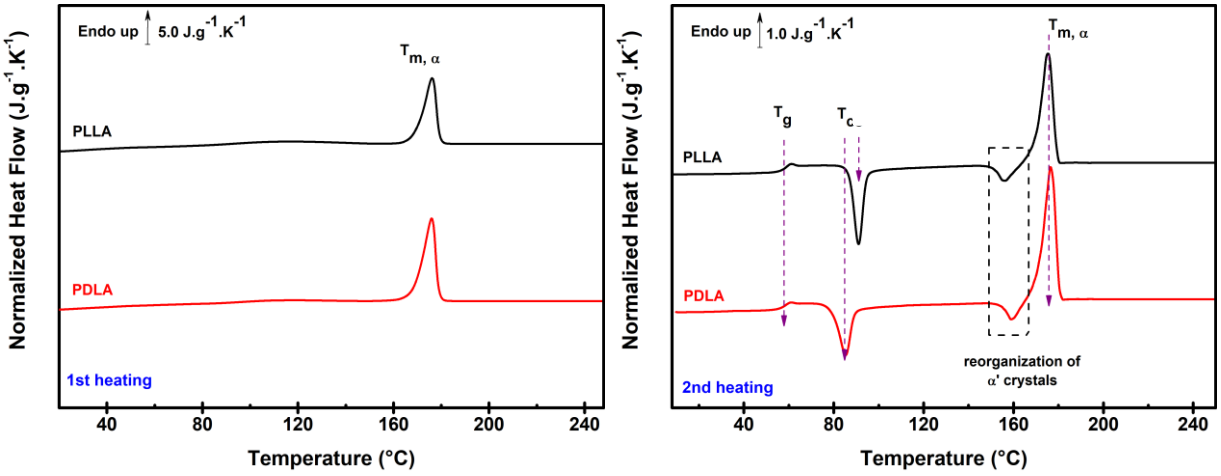

(a) (b)

Figure 3. 4. DSC curves of PLLA and PDLA films obtained by solution casting: (a) 1st and (b) 2nd heating.

Samples	ΔH_m (J/g)		ΔH_{cc} (J/g)		X_c (%)		T_m (°C)	
	1st heat	2nd heat	1st heat	2nd heat	1st heat	2nd heat	1st heat	2nd heat
PLLA film	44	47	-	26	47	23	176	176
PDLA film	38	40	-	31	41	10	176	176

Table 3. 4. The values of the thermal properties of homopolymer films obtained by solution casting.

The properties of the amorphous phase of semicrystalline homopolymers' films were analyzed by MT-DSC to estimate the T_g and the heat capacity step (ΔC_p). After *in-situ* melting, homopolymer films were quenched at cooling rate 0.78 K.s^{-1} and the MT-DSC curves are presented in Fig 3.5. The T_g and ΔC_p values were determined as explained in section 1.8.1. The values of T_g and ΔC_p shows that homopolymers exhibit the similar glass transition properties as the T_g values are 59.3 and 60.5 °C for PLLA and PDLA, respectively, and the ΔC_p values are 0.46 J.g^{-1}.K^{-1} for both homopolymers.

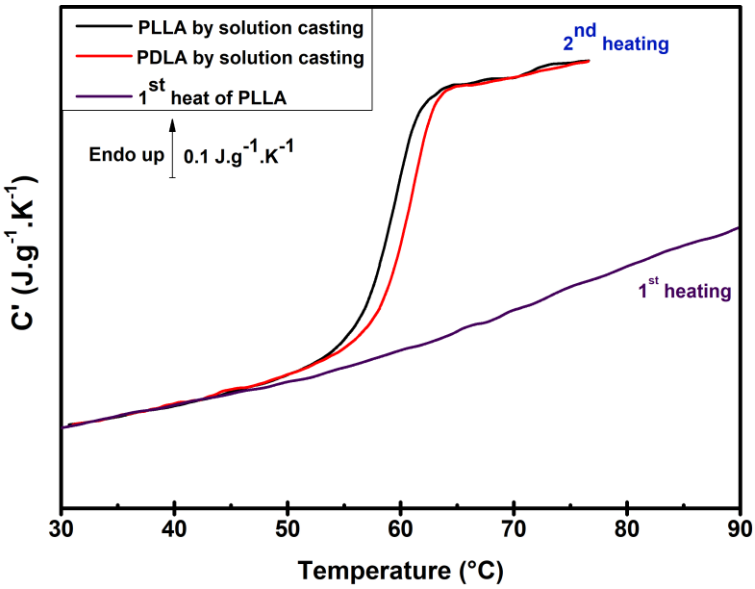

Figure 3. 5. Real component (C') of the complex heat capacity after phase lag correction as a function of temperature for PLLA and PDLA films obtained by solution casting.

The microstructure investigation for homopolymer films obtained by solution casting was carried out by XRD measurements. Homopolymers films have diffractions peaks at 2θ = 16.7°, 17.6°, 19.5°, 22° and 26° as shown in Fig 3.6. The results of XRD spectra for homopolymer films are in good agreement with the literature as homo-crystals show the reflection at similar 2θ values [5].

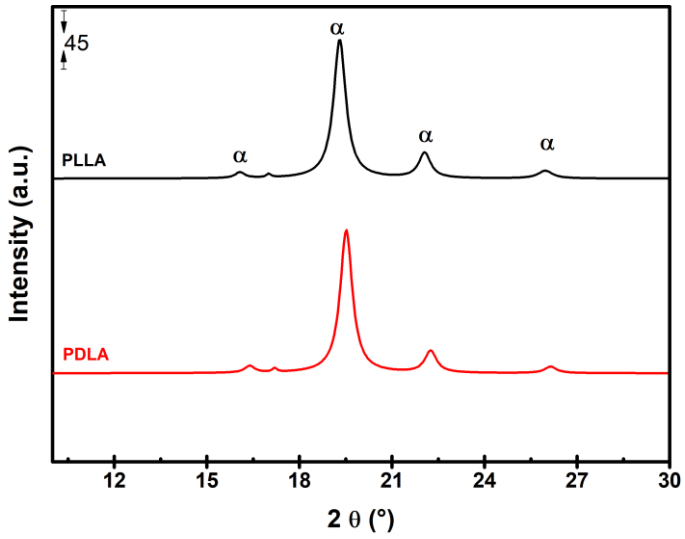

Figure 3. 6. XRD patterns for homopolymers films obtained by solution casting.

3.2 Stereocomplex PLA

The sc PLA films obtained by extrusion process and solution casting were characterized in order to investigate the influence of the elaboration methods on stereocomplex formation.

3.2.1 Semicrystalline sc PLA by extrusion

Sc PLA samples were analyzed to examine the influence of the extrusion temperature (T_{ext}) and extrusion time (t_{ext}) on the thermal properties and microstructure of sc PLA.

3.2.1.1 Thermal stability

Thermogravimetric analysis was performed in order to determine the T_{deg} of sc PLA obtained by extrusion process (Table 3.5). It is shown that the extrusion process has the influence on the T_{deg} as depicted in Fig 3.7. The degradation of sc PLA obtained by extrusion process is initiated below 300 °C while homopolymers (PLLA and PDLA) start to degrade above 300 °C. In addition, thermal treatment and its time duration decreases the T_{deg} of sc PLA from 317 °C to 273 °C.

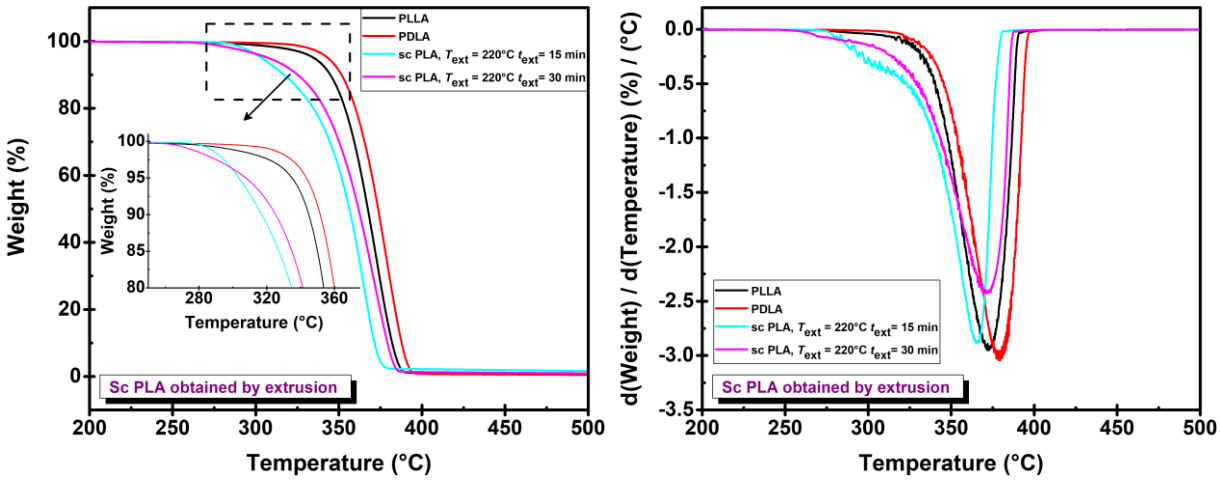

Figure 3. 7. TGA curves of sc PLA obtained by extrusion (T_{ext} = 220°C, t_{ext} = 15 and 30 min): (a) thermograms and (b) derivative curves as a function of temperature.

Elaboration conditions	*T* of 1% weight loss (°C)	*T* of 50% weight loss (°C)	*Maximum of derivative curve* (°C)
T_{ext} = 220 °C, t_{ext} = 15 min	286	356	365
T_{ext} = 220 °C, t_{ext} = 30 min	273	362	372

Table 3. 5. Degradation temperature (T_{deg}) of sc PLA obtained by extrusion process.

Such results are supported by the work of Bao et al. [6] on stereocomplex formation by extrusion process. Bao et al. reported that elaboration methods had influence on the thermal degradation temperature of sc PLA as degradation temperature decreased with increasing of extrusion temperature and time. Such diminution of the temperature can be explained by a partial degradation of the polymer chain during the extrusion process.

3.2.1.2 Influence of the extrusion temperature (T_{ext})

Calorimetric investigations were carried out also for sc PLA obtained by extrusion process in order to study the influence of the extrusion temperature T_{ext} on the sc PLA formation. As one can see, the increase of the extrusion temperature from 180 °C to 220 °C provokes the formation of sc PLA with different thermal behavior (Fig 3.8). For the blends extruded at T_{ext} = 180, 200 and 220 °C, the pure sc crystals formation was confirmed by the endothermic melting peaks at $T_{m,\,sc}$ = 220 – 238 °C. In the case of T_{ext} = 190 °C, the cold crystallization of α crystals $T_{cc,\,\alpha}$ = 103 °C, the melting of α crystals $T_{m,\,\alpha}$ = 170 °C, and the melting of sc crystals $T_{m,\,sc}$ = 224 °C are observed during the 1st heating step. In case of T_{ext} = 210°C, the melting of α and sc crystals is observed. The melting enthalpy and the crystallinity degree (Eq 3.1, where the melting enthalpy of 100 % crystalline sc sample is 146 J/g) of extruded samples were determined and presented in Table 3.6. The higher yield of the stereocomplex formation was observed at the extrusion temperature T_{ext} = 220 °C with the crystallinity degree $X_{c,\,sc}$ of 55 % and the melting enthalpy sc crystals $\Delta H_{m,\,sc}$ of 80 J/g.

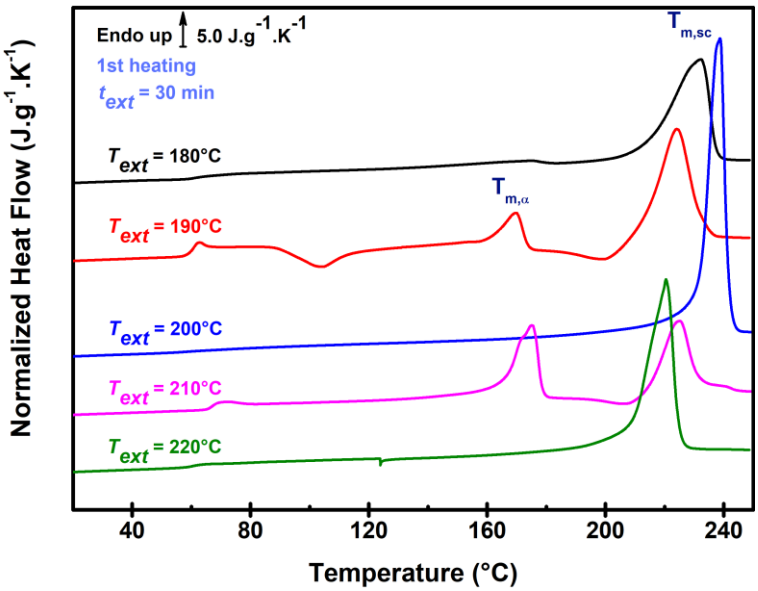

Figure 3. 8. The 1st heating DSC curves of sc PLA obtained by extrusion process at the extrusion temperature T_{ext} = 180 – 220 °C and the extrusion time t_{ext} = 30 min.

Samples 1st heating	ΔH_m (J/g)		X_c (%)	
	α	sc	α	sc
Sc PLA, T_{ext} = 180 °C	–	65	–	45
Sc PLA, T_{ext} = 190 °C	13	57	14	39
Sc PLA, T_{ext} = 200 °C	–	30	–	21
Sc PLA, T_{ext} = 210 °C	33	34	35	23
Sc PLA, T_{ext} = 220 °C	–	80	–	55

Table 3. 6. The values of the melting enthalpy (ΔH_m) and the crystallinity degree (X_c) determined from 1st heating for sc PLA obtained by extrusion at different extrusion temperature.

In order to study the crystallization process of α and sc crystals, the analysis of cooling DSC curves was performed. Fig 3.9 presents the DSC cooling curves at $|\beta_c|$ = 10 K.min^{-1} for all samples obtained by extrusion process. In the case of T_{ext} = 180 °C, the crystallization of pure α crystals was observed at $T_{c,\alpha}$ = 107 °C during the cooling step. For the T_{ext} = 190, 200, and 210 °C, the crystallization of both α and sc crystals takes place as the exothermic peak is revealed at $T_{c,\alpha}$ = 112 – 130 °C and $T_{c,sc}$ = 150 – 162 °C, respectively (Fig 3.7). In addition, in the case of T_{ext} = 220 °C, the crystallization of sc crystals takes place at $T_{c,sc}$ = 169 °C and no crystallization of α crystals can be revealed.

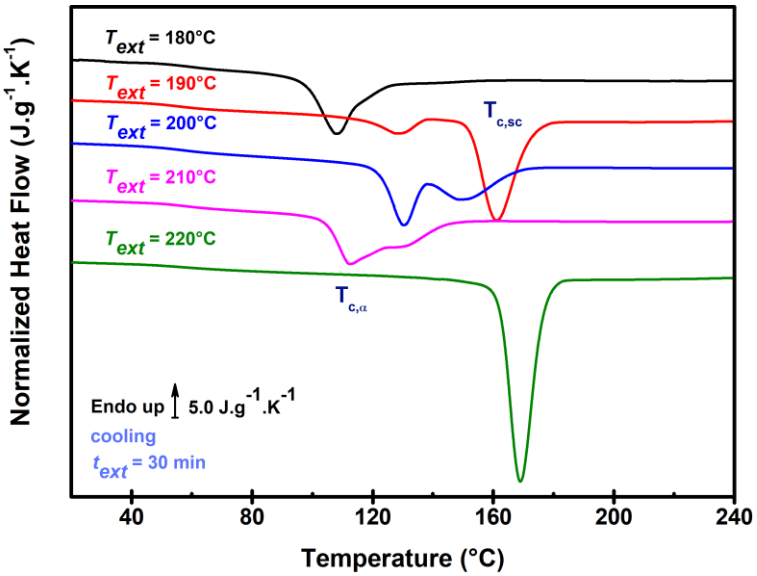

Figure 3. 9. DSC curves of cooling after 1st heating for sc PLA obtained by extrusion at T_{ext}= 180 – 220 °C, t_{ext} = 30 min.

During the 2nd heating step for T_{ext} < 220 °C (presented in Fig 3.10), the formation of α crystals during cooling is confirmed by the intense melting peak at $T_{m,\alpha}$ = 176 °C, whereas the sc crystals melting is observed at $T_{m,sc}$ = 220 °C. The decrease in the melting temperature of the sc crystals for T_{ext} = 180 °C (i.e. from 232 °C to 220 °C) may be caused by the change in the crystal size reduced by the thermal protocol. It is interesting to note that with the increasing T_{ext} from 190 °C to 210 °C, the formation of α crystals is increased while stereocomplex formation decreases. This inverse relation can be revealed by the intensity of melting peak of both α and sc crystals as presented in Table 3.7. These results could be explained by "a low temperature approach" proposed by Bao et al. [6]. The authors reported that blending of the low molecular weight PLLA and PDLA at low temperature ($T \approx$ 160 – 170 °C) could lead to the formation of sc crystals in the blends. On the other hand, Bao et al. also noted that stereocomplexation from high molecular weight polymer ($MW > 10^5$ kDa) by extrusion should be carried out at high extrusion temperature, i.e. above 220 °C. However, the higher temperature can cause the thermal degradation of homopolymers during the process, thus a special attention should be paid on the extrusion temperature. In our case, the temperature impact on low molecular weight ($MW < 10^5$ kDa) PLLA and PDLA homopolymers was observed as the quantity of sc crystals decreased with the increasing temperature. In case of T_{ext} = 220 °C,

the pure sc crystals crystallization during cooling was confirmed by the melting peak at $T_{m,\,sc}$ = 218 °C with the same melting enthalpy and crystallinity degree as during 1st heating step (Fig 3.10 and Table 3.7).

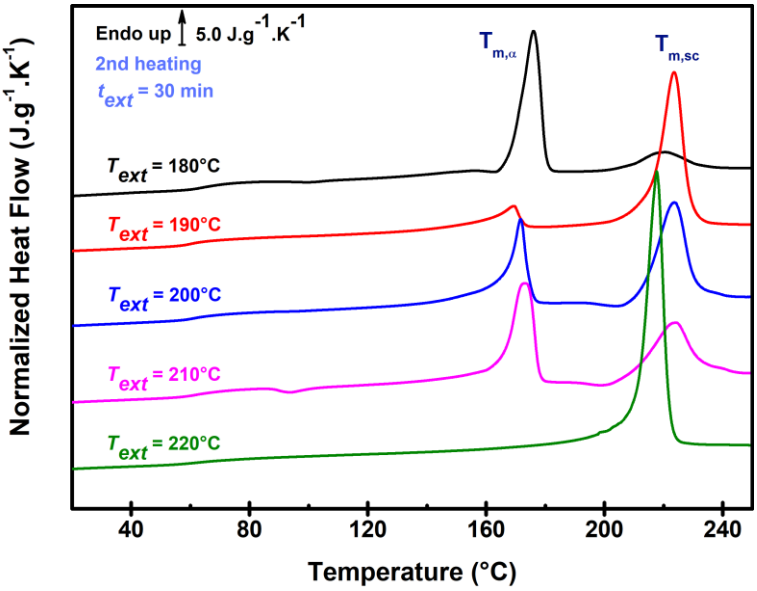

Figure 3. 10. The 2nd heating DSC curves of sc PLA obtained by extrusion process at T_{ext}= 180 – 220 °C and t_{ext} = 30 min.

Samples 2nd heating	ΔH_m (J/g)		X_c (%)	
	α	sc	α	sc
Sc PLA, T_{ext} = 180 °C	37	11	40	8
Sc PLA, T_{ext} = 190 °C	8	55	9	38
Sc PLA, T_{ext} = 200 °C	26	41	28	28
Sc PLA, T_{ext} = 210 °C	36	31	39	22
Sc PLA, T_{ext} = 220 °C	–	80	–	55

Table 3. 7. The values of the melting enthalpy (ΔH_m) and the crystallinity degree (X_c) determined from 2nd heating for the sc PLA obtained by extrusion at different extrusion temperature.

As one can note from the results in Table 3.7, the highest crystallinity degree of the sc crystals is observed for the sc PLA obtained at T_{ext} = 220 °C, t_{ext} = 30 min on the contrary to "a low temperature approach". Moreover, the only presence of melting of sc crystals at $T_{m,\,sc}$ = 218 °C during the 2nd heating step testifies to the highest stability of sc crystals obtained at T_{ext} = 220 °C during t_{ext} = 30 min. The higher the temperature, the more stable the sc crystals. This

fact can be explained by the nucleation agent exerting distinct effects of stereocomplexation on homocrystallization [7].

3.2.1.3 Influence of the extrusion time (t_{ext})

In order to study the influence of the extrusion time on the stability of the sc crystals, sc PLA was also elaborated at T_{ext} = 220 °C during t_{ext} = 15 min. As for the sc PLA elaborated during t_{ext} = 30 min, pure sc PLA crystals were obtained during the extrusion process as shown in Fig 3.11.

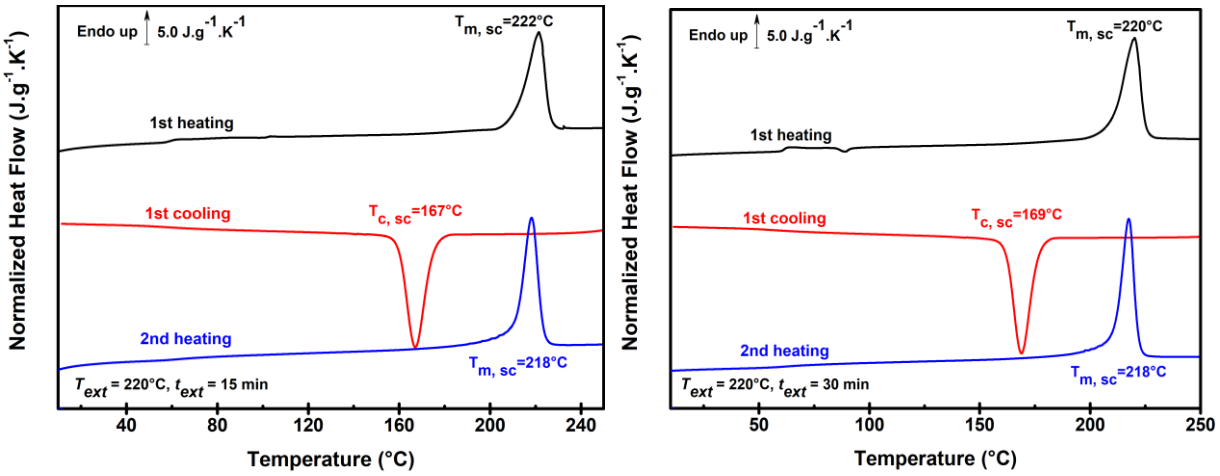

(a) (b)

Figure 3. 11. DSC curves of sc PLA obtained by extrusion process at T_{ext}= 220 °C during the extrusion time (a) t_{ext} = 15 min and (b) t_{ext} = 30 min.

No formation of α crystals is observed during the cooling as the curve of the 2nd heating step is characterized by only melting peak of sc crystals at $T_{m,\,sc}$ = 218 °C for both studied extrusion time. The sc PLA elaborated at t_{ext} = 15 min has the same values of melting enthalpy (ΔH_m = 80 J/g) and the crystallinity degree (X_c = 55%) as the one elaborated at t_{ext} = 30 min. Therefore, one can conclude that the optimum extrusion conditions of pure sc crystals formation are T_{ext} = 220 °C and t_{ext} = 15 min.

3.2.1.4 Stability of sc crystals obtained by extrusion

Isothermal step during t_{iso} = 120 min at T_{iso} = 260 °C was performed between the 1st heating and 1st cooling step. After this isothermal step, the samples were cooled down to 0 °C

and heated one more time to 260 °C (10 K.min^{-1}). As shown in Fig 3.10, sc crystals in the sc PLA are thermally stable. In sc PLA extruded during 15 and 30 min, the presence of pure sc PLA is confirmed by the melting peak at $T_{m,\,sc}$ = 221 °C during 1st heating step. During the cooling step, the sc crystal crystallization is observed at $T_{m,\,sc}$ = 137 °C and 149 °C for the blend extruded at 220 °C during 15 min and 30 min, respectively, (Fig 3.12a and 3.12b, respectively).

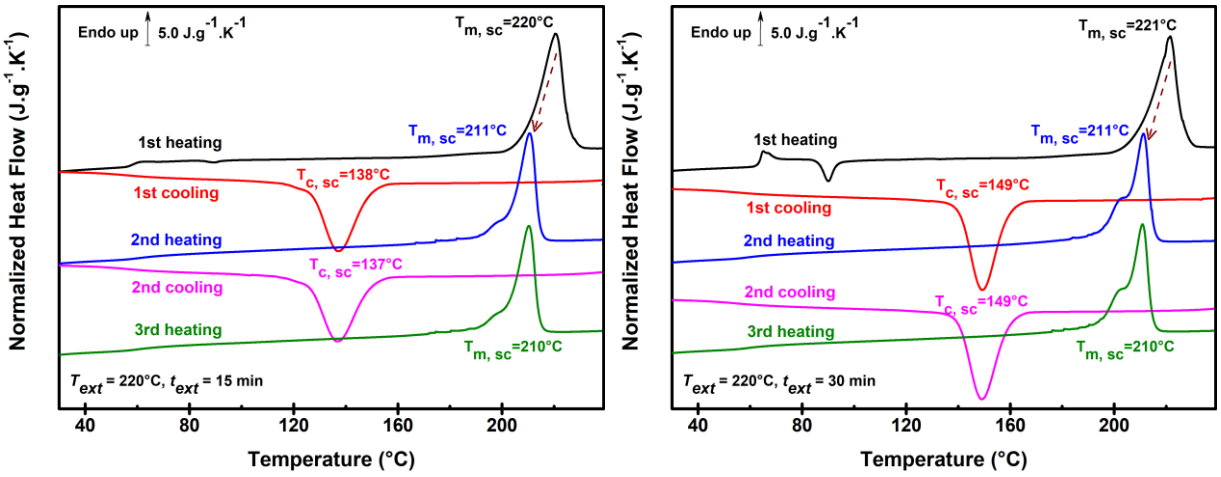

(a) (b)

Figure 3. 12. DSC curves of sc PLA obtained by extrusion process at T_{ext}= 220 °C during (a) t_{ext} = 15 min and (b) t_{ext} = 30 min. Isothermal step was applied at T_{iso} = 260 °C during 120 min between the 1st heating step and the 1st cooling step.

The heating and cooling cycles were carried out for several times in order to confirm the thermal stability and thermal characteristics of sc PLA. The decrease of 10 °C in the melting temperature can be explained by the change in the crystal size of sc crystals during the heat-cool processes.

3.2.2 Semicrystalline sc PLA by solution casting

Sc PLA obtained by solution casting was analyzed to investigate the influence of the polymer concentration and the ratio of the homopolymers (PLLA and PDLA) on the sc PLA formation.

3.2.2.1 Thermal stability

TGA was performed to determine the T_{deg} in order to examine the influence of solution casting method on thermal degradation. The solution casting method has no significant influence on the T_{deg} as one can see from Fig 3.13 and Table 3.8. Sc PLA obtained by solution casting starts to degrade above 300 °C as well as homopolymers (PLLA and PDLA), while the degradation of sc PLA obtained by extrusion process is initiated below 300 °C (section 3.2.1.1). Thus, the thermal degradation of sc PLA depends strongly on the elaboration method used.

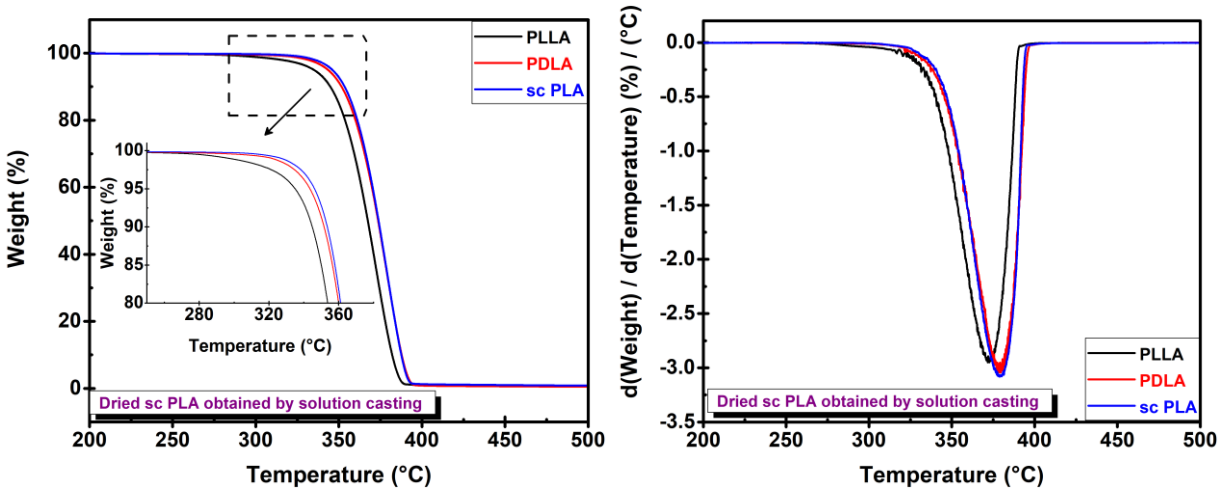

(a) (b)

Figure 3. 13. TGA curves of pure PLLA and PDLA pellets and sc PLA obtained by solution casting: (a) thermograms and (b) derivative curves as a function of temperature.

Elaboration conditions	*T* of 1% weight loss (°C)	*T* of 50% weight loss (°C)	*Maximum of derivative curve* (°C)
PLLA pellet	296	367	373
PDLA pellet	321	373	378
PLLA:PDLA = 50:50, d = 3 g/dL	317	362	379

Table 3. 8. Degradation temperature (T_{deg}) of sc PLA (PLLA:PDLA = 50:50) obtained by solution casting.

3.2.2.2 Influence of the polymer concentration

The influence of polymer concentration was investigated by DSC and XRD analysis to define the optimum conditions for the sc crystals elaboration. During DSC analysis the

stereocomplexation is characterized by means of the melting peaks of sc, α and α' crystals. Fig 3.14 presents the normalized heat flow curves of sc PLA films obtained by solution casting at 50:50 ratio of PLLA:PDLA with the concentration of 1, 2 and 3 g/dL. The curves of pure homopolymers (PLLA and PDLA) are given for comparison. The endothermic peaks at temperature of 176 °C and 233 °C correspond to the melting of α crystals and sc crystals, respectively. It should be noted that the shape of sc PLA melting peaks show different behavior compared to homopolymers melting peaks. The doubled melting peak testifies to the not homogenous distribution of the crystals size in sc PLA samples.

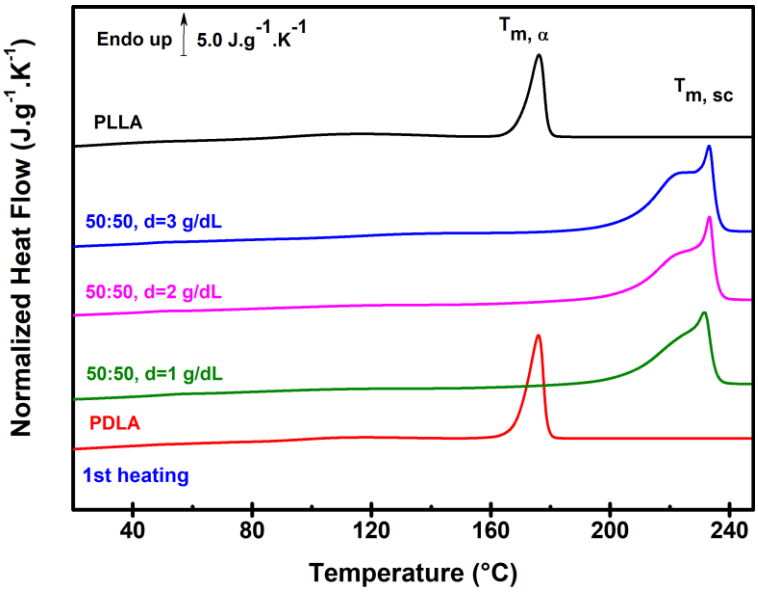

Figure 3. 14. DSC curves of sc PLA film obtained by solution casting (PLLA:PDLA = 50:50) as a function of polymer concentration.

Table 3.9 presents the crystallinity degree values. In the sc PLA film at 50:50 ratio of PLLA:PDLA, the pure sc crystallites were obtained whatever the polymer concentration. As shown in Fig 3.14 and Table 3.9, the polymer concentration has no significant influence on the stereocomplexation.

Samples	ΔH_m (J/g)		X_c (%)	
	α	sc	α	sc
PLLA	44	–	47	–
PLLA:PDLA = 50:50, d = 1 g/dL	–	75	–	53
PLLA:PDLA = 50:50, d = 2 g/dL	–	80	–	56
PLLA:PDLA = 50:50, d = 3 g/dL	–	77	–	54
PDLA	38	–	41	–

Table 3. 9. The values of the melting enthalpy (ΔH_m) and the crystallinity degree (X_c) as a function of polymer concentration.

In addition, the microstructure of sc PLA films obtained at the ratio of 50:50 PLLA:PDLA with the concentration of 1, 2 and 3 g/dL was investigated and XRD spectra are presented in Fig 3.15. Sc PLA shows diffraction peaks at 2θ = 14°, 24° and 28° while homopolymers PLLA and PDLA have peaks at 2θ = 19.5°, 22° and 26°.

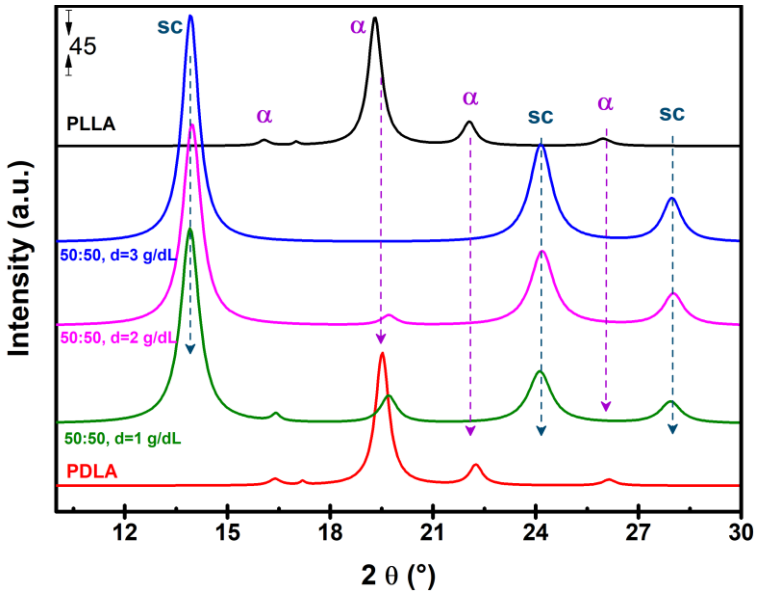

Figure 3. 15. XRD patterns of the sc PLA film obtained by solution casting at the ratio of 50:50 PLLA:PDLA with the concentration of 1, 2, and 3 g/dL.

Although, the α crystals presence in the film of 50:50 ratio of PLLA:PDLA with the concentration of 1 and 2 g/dL was not confirmed by DSC measurements, the XRD spectra of these samples show the α crystal existence confirmed by small intensive peaks at 17° and 19°.

Therefore, one may noticed that the polymer concentration has slight influence on the homocrystals presence in the obtained film of sc PLA.

3.2.2.3 Influence of the ratio of homopolymers

In order to study the influence of the homopolymers' ratio on the stereocomplexation reaction, the films with different ratio of homopolymers (PLLA:PDLA) were elaborated. The results of 1st heating scan are presented in Fig 3.16. The presence of α crystals was confirmed by the endothermic melting peak at $T_{m,\alpha}$ = 176 °C. At the same time, the peak at $T_{m,sc}$ = 225 - 235 °C testifies to the sc crystals presence. Thermal analysis results show that the homocrystallization occurs simultaneously due to the unpaired homopolymers chain when deviating from equimolar ratio of PLLA and PDLA. According to the obtained stereocomplex crystalline structure, PLLA and PDLA chains are paired in each units with the equilateral triangles structure. Therefore, equimolar blending ratio (50:50) is found to be the optimum condition for stereocomplex crystals formation. The result of pure stereocomplex formation at 50:50 ratio of homopolymers was also reported by Ikada et al. [8].

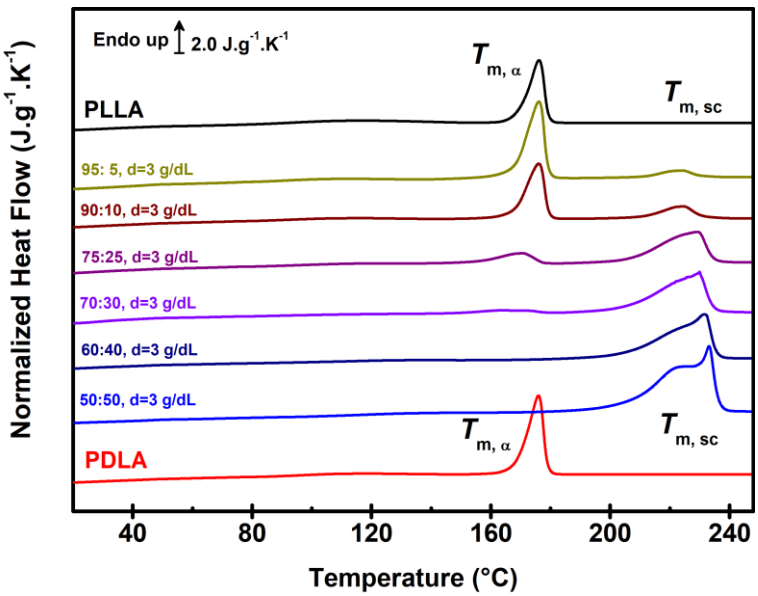

Figure 3. 16. DSC curves of sc PLA film obtained by solution casting at constant polymer concentration (d= 3 g/dL) as a function of homopolymer ratio.

The crystallinity degree of α and sc crystals was calculated by Eq 3.1 and the obtained values are gathered in Table 3.10. As shown in Fig 3.16 and Table 3.10, the ratio of

homopolymers has significant influence on the stereocomplex formation. The decrease in the melting enthalpy and the crystallinity degree of sc crystals was observed with the decreasing of the PDLA content in the racemic mixture of PLLA and PDLA. Tsuji et al. [9-11] indicated that the melting peaks of both homo crystals and sc crystals were observed when PDLA fraction (X_D) was between 0.1 to 0.3 and 0.7 to 0.9, while the pure stereocomplex was detected for X_D between 0.4 and 0.6 with maximum of the melting enthalpy (ΔH_m) at X_D = 0.5. The pure homocrystallization occurred near X_D = 0 and 1. In our case, the optimum blending ratio of homopolymers for pure stereocomplex formation was found to be 60:40 and 50:50 (Table 3.10).

Samples	ΔH_m (J/g)		X_c (%)	
	α	sc	α	sc
PLLA	44	–	47	–
PLLA:PDLA = 95:05, d = 3 g/dL	42	7	45	5
PLLA:PDLA = 90:10, d = 3 g/dL	33	13	35	9
PLLA:PDLA = 75:25, d = 3 g/dL	11	41	12	29
PLLA:PDLA = 70:30, d = 3 g/dL	4	48	4	34
PLLA:PDLA = 60:40, d = 3 g/dL	–	64	–	45
PLLA:PDLA = 50:50, d = 3 g/dL	–	75	–	53
PDLA	38	–	41	–

Table 3. 10. The melting enthalpy (ΔH_m) and crystallinity degree (X_c) values as a function of homopolymer ratio determined from 1st heating scan.

The XRD patterns of films with different ratio of PLLA:PDLA (i.e. from 50:50 up to 95:5) are presented in Fig 3.17. As one can see, when deviating from the equivalent ratio of homopolymers, the formation of homocrystals is observed. The existence of sc crystals and α crystals is revealed by the reflection peaks of α crystals (2θ = 19.5°, 22° and 26°) and sc crystals (2θ = 14°, 24° and 28°). The results of XRD spectra are in good accordance with the literature, as the α crystals show the reflection at 2θ = 16.6°, 19.1° and 17°, 19° [5] and the sc crystals show the reflection at 2θ = 12°, 21°, 24° [5] and 12°, 20.9°, 24° [12].

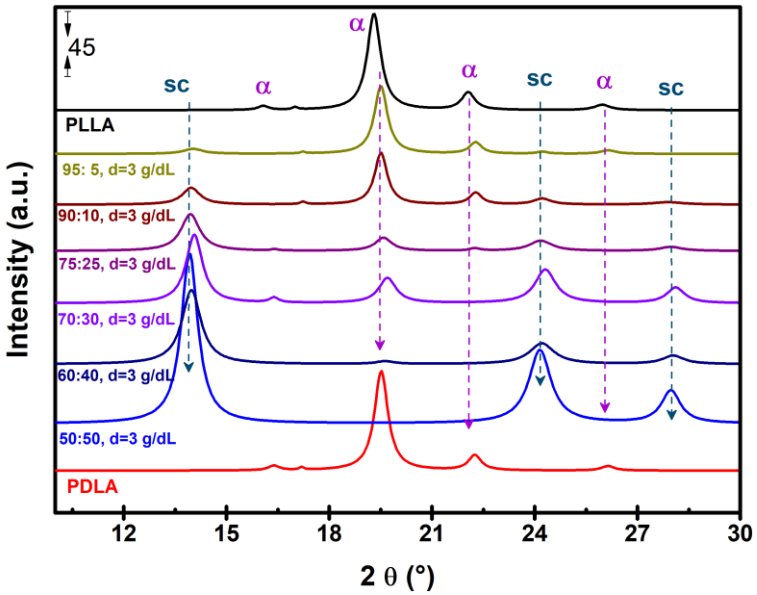

Figure 3. 17. XRD patterns of the PLLA/PDLA film obtained by solution casting at the different ratio of PLLA:PDLA.

The stability of the sc PLA was investigated during 2nd heating scan of DSC measurements (Fig 3.18). It was found that the sc PLA crystals obtained by solution casting were not stable, as already during the 2nd heating up to 250 °C the crystallization and melting of α crystals was visible and confirmed by cold-crystallization and melting peak. Moreover, the intensity of melting peak $T_{m,\ sc}$ at 223 °C, which corresponds to the sc crystals melting, decreases significantly after heating (Fig 3.18). The values of the melting enthalpy and crystallinity degree drastically reduce for sc crystals. The crystallinity degree of sc crystals decreases from 54 % to 10 % even for the sample with 50:50 and 60:40 ratio of PLLA:PDLA during the 2nd heating scan, as shown in Table 3.11. In addition, the α' crystals formation is observed with cold-crystallization at ≈ 85 °C (the cold-crystallization at temperature T < 100 °C leads to the formation of α' crystals form consisting in disordered crystals with hexagonal packing [1, 2]). The reorganization of α' imperfect crystals into α form crystals was observed by the exothermic peak before melting at temperature T ≈ 160 °C. The presence of sc PLA crystals in PLLA/PDLA films was confirmed by T_m value found between 223 °C and 233 °C, depending on the homopolymers' ratio (Fig 3.16 and 3.18).

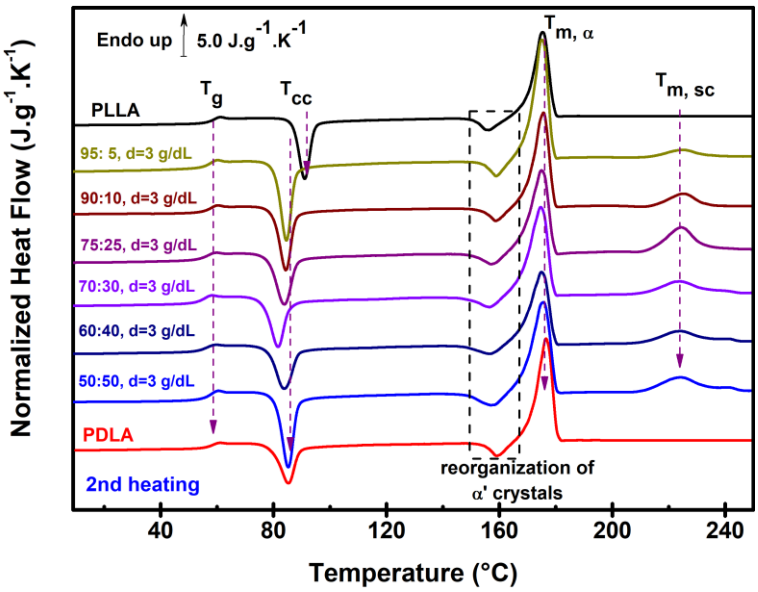

Figure 3. 18. The 2nd heating DSC curves of sc PLA film obtained by solution casting at different ratio of PLLA:PDLA.

The DSC results confirm that the heating of the blends leads to homopolymer crystallization whatever the ratio of homopolymers. Only under certain experimental conditions the pure sc PLA crystals were obtained (i.e. without α and α' crystals) by solution casting, namely at 50:50 and 60:40 ratio of PLLA:PDLA. Moreover, it can be pointed out that sc material is not stable, as the α' crystals could appear during cooling and 2nd heating (after 1st melting, Fig 3.18).

Samples 2nd heating	ΔH_{cc} (J/g)		ΔH_m (J/g)		X_c (%)	
	α	sc	α	sc	α	sc
PLLA	26	–	47	–	23	–
PLLA:PDLA = 60:40, d = 3 g/dL	28	–	39	14	12	10
PLLA:PDLA = 50:50, d = 1 g/dL	31	–	37	16	6	11
PLLA:PDLA = 50:50, d = 2 g/dL	31	–	37	14	6	10
PLLA:PDLA = 50:50, d = 3 g/dL	31	–	37	15	6	11
PDLA	31	–	40	–	10	–

Table 3. 11. The melting enthalpy (ΔH_m) and the crystallinity degree (X_c) values determined from 2nd heating scan as a function of PLLA:PDLA ratio.

3.3 Amorphous phase of stereocomplex PLA

MT-DSC analysis was performed to investigate the amorphous character and to determine the calorimetric glass transition temperature of the samples elaborated by solution casting and extrusion process. Since the material barrier properties are linked with the molecular mobility and free volume, the Donth's approach [13] was applied in order to investigate the free volume and the CRR size (as detailed in section 1.8.2). MT-DSC measurements were carried out in heat-cool mode, and obtained curves showed the real (C') and the imaginary (C") parts of the complex heat capacity as a function of temperature (detailed in section 2.2.3)

3.3.1 MT-DSC analysis of sc PLA obtained by extrusion process

It was found by the conventional DSC analysis that the optimum conditions of the stereocomplex formation by extrusion process were the extrusion temperature T_{ext} = 220 °C and the extrusion time t_{ext} = 15 min. Therefore, MT-DSC measurements were carried out for this sc PLA blend. MT-DSC curves of sc PLA are presented in Fig 3.19. The values of glass transition temperature estimated from the 1st and 2nd heating step of MT-DSC measurements are presented in Table 3.12. The CRR size of semicrystalline sc PLA films is estimated by Eq 1.20 to be 1.6 nm and 1.3 nm (from 1st heating and 2nd heating), respectively, and is discussed later. Sc PLA obtained by extrusion process has similar glass transition temperature T_g (60 – 62 °C) as amorphous neat PLA and homopolymers, but it has different heat capacity step: 0.24 $J.g^{-1}.K^{-1}$ compared to 0.15 $J.g^{-1}.K^{-1}$ for homopolymers. The results show that the amorphous phase of sc PLA is not interlocked by the sc crystallites during the stereocomplexation by extrusion process. The DSC curves reveal that sc PLA obtained by extrusion process is not quenched to obtained wholly amorphous sc PLA by the cooling rate of $|\beta_c|$ = 0.78 $K.min^{-1}$ which is the maximum cooling rate for the used apparatus (Q100 TA Instruments). Therefore, sc PLA sample is semicrystalline during the 2nd heating step. Therefore, the minimum required cooling rate for quenching of sc PLA obtained by extrusion was investigated by FSC. It was found that sc PLA obtained by extrusion process should be vitrified at the scanning rate $|\beta_c|$ higher than 200 $K.min^{-1}$.

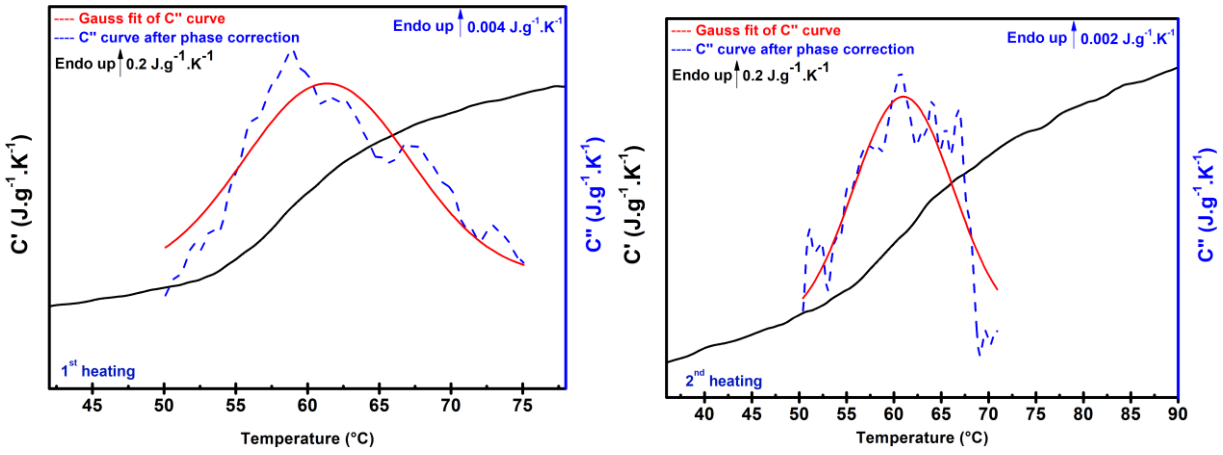

(a) (b)

Figure 3. 19. C' and C" curves of sc PLA obtained by extrusion: (a) the 1st heating and (b) 2nd heating scan.

PLLA/PDLA blend by extrusion	T_g (°C)	ΔC_p (J.g^{-1}.K^{-1})	T_{max} of Gaussian fit	ξ (nm)	X_c (%)
1st heating step	60	0.24	61	1.6	55
2nd heating step	62	0.15	61	1.3	55

Table 3.12. Glass transition parameters of sc PLA obtained by extrusion process.

3.3.2 MT-DSC analysis of sc PLA obtained by solution casting

Since the presence of pure sc crystals was observed in PLLA/PDLA film at the ratio of 50:50 and 60:40 of PLLA:PDLA, the glass transition investigations were carried out for these samples. The 1st heating ramp of MT-DSC measurements of sc PLA film obtained by solution casting exhibits low heat capacity step due to high X_c (Fig 3.20). Therefore, only the 2nd heating step after quenching at $|\beta_c|$ = 0.78 K.min^{-1} will be presented. Fig 3.21a presents the real (C') and the imaginary (C") parts of complex heat capacity of sc PLA film (PLLA:PDLA = 50:50). Fig 3.21b reveals the glass transition and the heat capacity step of amorphous sc PLA film with PLLA:PDLA ratio of 50:50 and 60:40. The determined values of the glass transition and the CRR size are presented in Table 3.13. The CRR size of semicrystalline (from 1st heating) and fully amorphous (from 2nd heating) sc PLA films was estimated by Eq 1.20 to be 0.8 nm and 2.9 nm, respectively. The number of structural units in CRR (N_α) was determined for the semicrystalline and totally amorphous PLLA/PDLA films (Table 3.13) according to Eq 1.21.

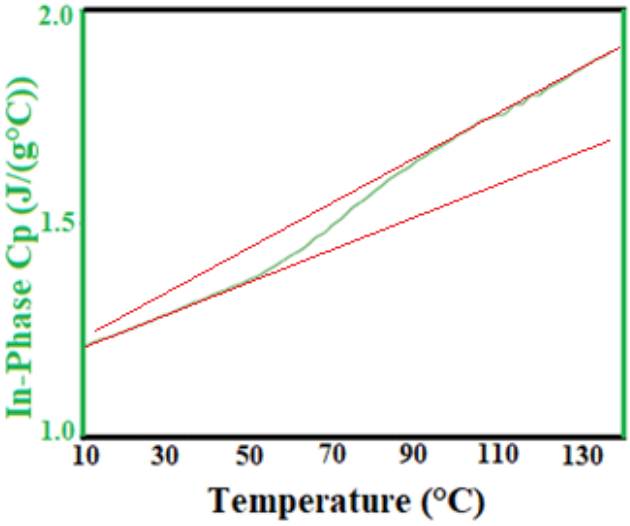

Figure 3. 20. C' curve of semicrystalline sc PLA film (PLLA:PDLA = 50:50) obtained by solution casting during the 1st heating scan of MT-DSC measurement.

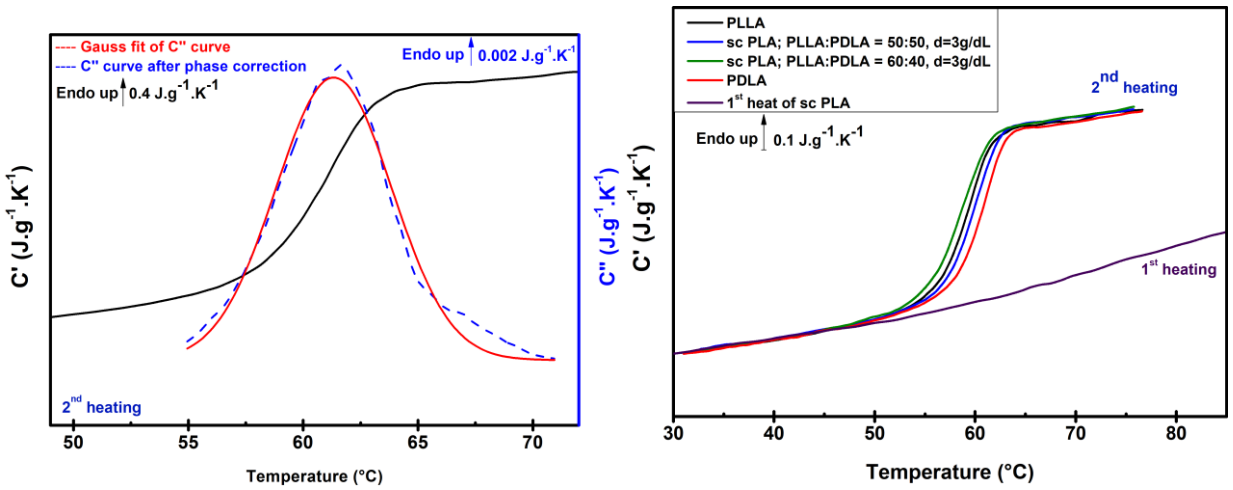

(a) (b)

Figure 3. 21. MT-DSC curves of sc PLA obtained by solution casting: (a) the real (C') and the imaginary (C") parts of the complex heat capacity as a function of temperature, (b) the glass transition of the amorphous sc PLA films.

Wholly amorphous sc PLA has the similar heat capacity step as amorphous neat PLA [14], PLLA and PDLA. Wholly amorphous sc PLA has the glass transition temperature T_g at 61 °C and the heat capacity step of 0.54 $J.g^{-1}.K^{-1}$, whereas neat PLA and homopolymers (PLLA, PDLA) have

the glass transition temperature T_g at 60 °C, the heat capacity step of neat PLA and homopolymers are 0.51 $J.g^{-1}.K^{-1}$ and 0.46 $J.g^{-1}.K^{-1}$, respectively. It should be noted that the glass transition of semicrystalline sc PLA film obtained by solution casting is rather wide and the temperature transition range (δT > 10 °C) is out of the limits of Donth's approach (shown in Fig 3.20), thus the N_α value of semicrystalline sc PLA film is too small (N_α = 5).

PLLA/PDLA film by solution casting	T_g (°C)	ΔC_p ($J.g^{-1}.K^{-1}$)	T_{max} of Gaussian fit (°C)	δT	ξ (nm)	N_α
semicrystalline	69	0.12	58	16.9	0.8	5
amorphous	61	0.54	61	2.5	2.9	262

Table 3. 13. Glass transition parameters of sc PLA obtained by solution casting method determined from MT-DSC measurements.

3.3.3 Comparing the amorphous phase species of sc PLA by "A 3-phase model"

During the crystallization of polymer, the amorphous region volume is regularly diminished and the decoupling between crystalline and amorphous phases remains generally incomplete due to the macromolecular length [15]. Such incomplete coupling leads to decrease in chain mobility of amorphous phase. It is suggested to describe the semicrystalline polymers by a 3-phase model including the crystalline phase, the mobile amorphous phase (MAP) and the rigid amorphous fraction (RAF) [16, 17]. According to Androsch and Wünderlich [18], the RAF amount corresponds to a number of the coupling between the crystalline and the amorphous phase. Whereas the MAP remains inside the lamella stack, the RAF is obtained as an interfacial nanolayer between the lamellae and MAP [19]. The in-phase components C' are obtained and depicted in Fig 3.19 and 3.20 for the semicrystalline sc PLA obtained by extrusion and solution casting, respectively. Typically, the MAP degree X_{MAP} from the ΔC_p step at T_g can be calculated as [14]:

$$X_{MAP} = \frac{\Delta C_p}{\Delta C_p^0} \quad (3.2)$$

where $\Delta C_p = C'_{liquid} - C'_{solid}$ is the thermal heat capacity step at T_g for semicrystalline sc PLA samples and ΔC_p^0 is that of the wholly amorphous sample. As shown in Table 3.14, and Fig. 3.22, the total of the X_{MAP} and X_c is far from the equation line $X_{MAP} + X_c = 1$. Therefore, the RAF

must be taken into account in a 3-phase model. In this case $X_{MAP} + X_c + X_{RAF} = 1$, where X_{RAF} corresponds to the RAF content.

Sc PLA samples	ΔC_p (J.g^{-1}.K^{-1})		X_{MAP} (%)		X_{RAF} (%)		X_c (%)	
	1st heat	2nd heat	1st heat	2nd heat	1st heat	2nd heat	1st heat	2nd heat
Solution casting	0.12	0.54	22	100	24	-	54	-
Extrusion	0.24	0.15	44	28	1	17	55	55

Table 3. 14. The values of the degree of mobile amorphous phase X_{MAP}, rigid amorphous fraction X_{RAF}, and the crystallinity X_c of sc PLA obtained by solution casting and extrusion.

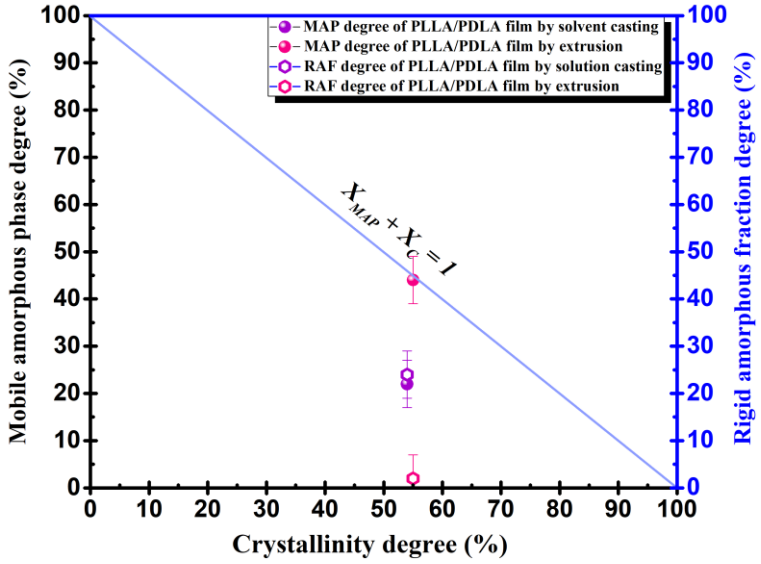

Figure 3. 22. The evolution of the degree of mobile amorphous phase (X_{MAP}) and rigid amorphous fraction (X_{RAF}) as a function of crystallinity degree (X_c) of sc PLA obtained by solution casting (purple symbols) and by extrusion (pink symbols).

On the other hand, such results show that the mobile amorphous phase of sc PLA obtained by extrusion is higher than that obtained by solution casting, whereas the rigid amorphous phase of sc PLA obtained by extrusion is negligible and lower than the one of sc PLA obtained by solution casting. In order to examine the relaxation of amorphous phase of semicrystalline sc PLA obtained by both solution casting and extrusion, the heat capacity step was normalized to be in 0 to 1 scale (Fig 3.23). As seen in Fig 3.23, the amorphous phase of sc PLA obtained by extrusion (T_{ext} = 220°C, t_{ext} = 30 min) relaxes independently from the existence of stereocomplex crystalline structure, while the amorphous phase of sc PLA obtained by

solution casting relaxes at higher temperature due to crystalline structure hindrance. It is found that the mechanical and thermal impact during the extrusion process lead to a better decoupling between the crystalline and the amorphous phase. Such difference can be explained by the crystallization process which is obtained from the molten state during the extrusion when is occurred at room temperature during the solution casting method.

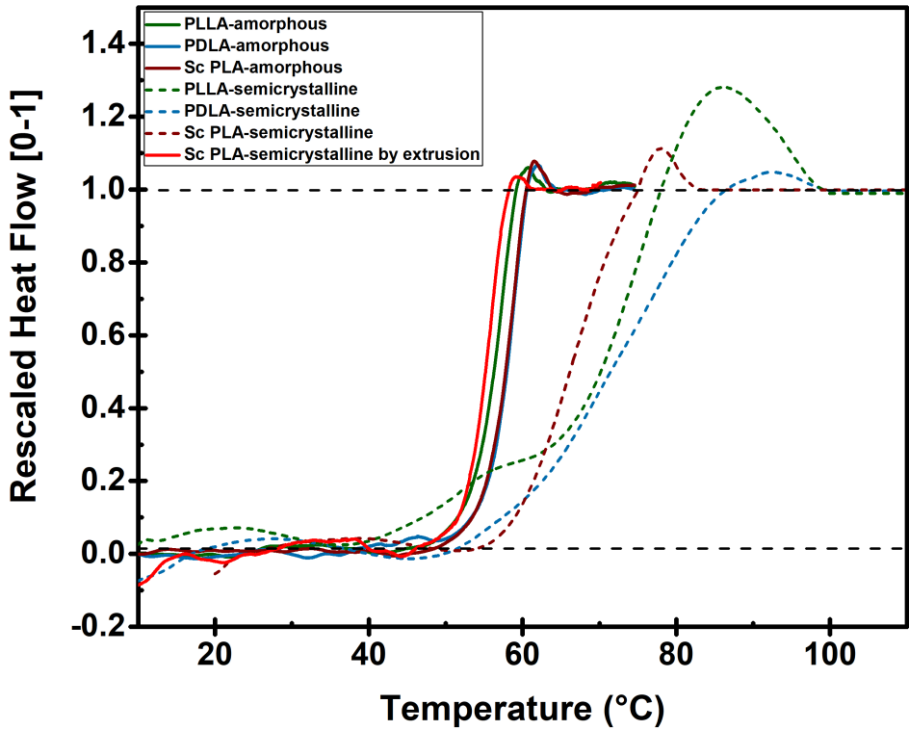

Figure 3. 23. Rescaled heat flow curves of amorphous and semicrystalline homopolymers and sc PLA obtained by solution casting and extrusion process.

Conclusion

Stereocomplex PLAs were successfully elaborated by both solution casting and extrusion process. The new crystalline structure revealed by microstructural investigation enhances the thermal properties of PLLA/PDLA film. It was found that the extrusion process had the influence on the thermal degradation temperature. Thermal treatment during the extrusion process probably leads to the polymer partial degradation. Therefore, a decrease of the degradation temperature is observed. The extrusion temperature has significant influence on the stereocomplexation, as the pure and stable sc PLA crystals were obtained at T_{ext} = 220 °C and t_{ext} = 15 min. In addition, the amorphous phase of sc PLA obtained by extrusion

process relaxes independently from sc crystalline structure. However, the obtained samples were extremely mechanically fragile for further analysis.

The influence of the ratio of homopolymers was studied resulting in the pure sc PLA crystals formation in some cases. The optimum conditions of solution casting method were established as the pure sc PLA crystals were obtained only at ratio of 50:50 and 60:40 with the polymer concentration of 3 g/dL. It was found that solution casting has no influence on the thermal degradation temperature. However, the obtained pure sc PLA crystals were not stable as the appearance of the α crystals was observed during 2^{nd} heating scan.

In order to understand the properties of sc PLA, the further advance analysis will be carried out for the sc PLA sample obtained by solution casting (50:50 ratio of PLLA:PDLA, d= 3 g/dL). The amorphous phase species of sc PLA (obtained by solution casting and thermally molded-quenched according to the section 2.1.2.2.) will be detailed and discussed in the next chapter.

References

1. Kawai, T.; Rahman, N.; Matsuba, G.; Nishida, K.; Kanaya, T.; Nakano, M.; Okamoto, H.; Kawada, J.; Usuki, A.; Honma, N.; Nakajima, K.; Matsuda, M. Crystallization and Melting Behavior of Poly (l-lactic Acid). *Macromolecules* **2007,** 40 (26), 9463-9469 DOI: 10.1021/ma070082c.
2. Zhang, J.; Tashiro, K.; Tsuji, H.; Domb, A. J. Disorder-to-Order Phase Transition and Multiple Melting Behavior of Poly(l-lactide) Investigated by Simultaneous Measurements of WAXD and DSC. *Macromolecules* **2008,** 41 (4), 1352-1357 DOI: 10.1021/ma0706071.
3. Li, B.; Dong, F.-X.; Wang, X.-L.; Yang, J.; Wang, D.-Y.; Wang, Y.-Z. Organically modified rectorite toughened poly(lactic acid): Nanostructures, crystallization and mechanical properties. *European Polymer Journal* **2009,** 45 (11), 2996-3003 DOI: https://doi.org/10.1016/j.eurpolymj.2009.08.015.
4. Fischer, E. W.; Sterzel, H. J.; Wegner, G. Investigation of the structure of solution grown crystals of lactide copolymers by means of chemical reactions. *Kolloid-Zeitschrift und Zeitschrift für Polymere* **1973,** 251 (11), 980-990 DOI: 10.1007/bf01498927.
5. Tsuji, H.; Sugiyama, H.; Sato, Y. Photodegradation of Poly(lactic acid) Stereocomplex by UV-Irradiation. *Journal of Polymers and the Environment* **2012,** 20 (3), 706-712 DOI: 10.1007/s10924-012-0424-7.
6. Bao, R.-Y.; Yang, W.; Jiang, W.-R.; Liu, Z.-Y.; Xie, B.-H.; Yang, M.-B.; Fu, Q. Stereocomplex formation of high-molecular-weight polylactide: A low temperature approach. *Polymer* **2012,** 53 (24), 5449-5454 DOI: https://doi.org/10.1016/j.polymer.2012.09.043.
7. Sun, J.; Yu, H.; Zhuang, X.; Chen, X.; Jing, X. Crystallization Behavior of Asymmetric PLLA/PDLA Blends. *The Journal of Physical Chemistry B* **2011,** 115 (12), 2864-2869 DOI: 10.1021/jp111894m.
8. Ikada, Y.; Jamshidi, K.; Tsuji, H.; Hyon, S. H. Stereocomplex formation between enantiomeric poly(lactides). *Macromolecules* **1987,** 20 (4), 904-906 DOI: 10.1021/ma00170a034.
9. Tsuji, H.; Horii, F.; Hyon, S. H.; Ikada, Y. Stereocomplex formation between enantiomeric poly(lactic acid)s. 2. Stereocomplex formation in concentrated solutions. *Macromolecules* **1991,** 24 (10), 2719-2724 DOI: 10.1021/ma00010a013.
10. Tsuji, H.; Hyon, S. H.; Ikada, Y. Stereocomplex formation between enantiomeric poly(lactic acid)s. 3. Calorimetric studies on blend films cast from dilute solution. *Macromolecules* **1991,** 24 (20), 5651-5656 DOI: 10.1021/ma00020a026.
11. Tsuji, H.; Hyon, S. H.; Ikada, Y. Stereocomplex formation between enantiomeric poly(lactic acid)s. 4. Differential scanning calorimetric studies on precipitates from mixed solutions of poly(D-lactic acid) and poly(L-lactic acid). *Macromolecules* **1991,** 24 (20), 5657-5662 DOI: 10.1021/ma00020a027.
12. Quynh, T. M.; Mai, H. H.; Lan, P. N. Stereocomplexation of low molecular weight poly(L-lactic acid) and high molecular weight poly(D-lactic acid), radiation crosslinking PLLA/PDLA stereocomplexes and their characterization. *Radiation Physics and Chemistry* **2013,** 83, 105-110 DOI: https://doi.org/10.1016/j.radphyschem.2012.10.002.
13. Donth, E. The size of cooperatively rearranging regions at the glass transition. *Journal of Non-Crystalline Solids* **1982,** 53 (3), 325-330 DOI: https://doi.org/10.1016/0022-3093(82)90089-8.
14. Delpouve, N.; Saiter, A.; Dargent, E. Cooperativity length evolution during crystallization of poly(lactic acid). *European Polymer Journal* **2011,** 47 (12), 2414-2423 DOI: https://doi.org/10.1016/j.eurpolymj.2011.09.027.
15. Righetti, M. C.; Tombari, E.; Lorenzo, M. L. D. Crystalline, mobile amorphous and rigid amorphous fractions in isotactic polystyrene. *European Polymer Journal* **2008,** 44 (8), 2659-2667 DOI: https://doi.org/10.1016/j.eurpolymj.2008.05.026.
16. Bartolotta, A.; Di Marco, G.; Farsaci, F.; Lanza, M.; Pieruccini, M. DSC and DMTA study of annealed cold-drawn PET: a three phase model interpretation. *Polymer* **2003,** 44 (19), 5771-5777 DOI: https://doi.org/10.1016/S0032-3861(03)00589-5.

17. Wunderlich, B. Reversible crystallization and the rigid–amorphous phase in semicrystalline macromolecules. *Progress in Polymer Science* **2003,** 28 (3), 383-450 DOI: https://doi.org/10.1016/S0079-6700(02)00085-0.
18. Androsch, R.; Wunderlich, B. The link between rigid amorphous fraction and crystal perfection in cold-crystallized poly(ethylene terephthalate). *Polymer* **2005,** 46 (26), 12556-12566 DOI: https://doi.org/10.1016/j.polymer.2005.10.099.
19. Chen, H.; Cebe, P. Investigation of the rigid amorphous fraction in Nylon-6. *Journal of Thermal Analysis and Calorimetry* **2007,** 89 (2), 417-425 DOI: 10.1007/s10973-007-8215-4.

CHAPTER 4. MOLECULAR DYNAMIC STUDY IN AMORPHOUS STEREOCOMPLEX POLYLACTIDE

In this chapter, the influence of the tacticity on molecular dynamics of sc PLA's amorphous phase will be presented. In order to study the molecular dynamics the results of Fast Scanning Calorimetry (FSC) and Dielectric Relaxation Spectroscopy (DRS) were correlated. The combination of these two techniques allowed us to investigate the primary and secondary segmental relaxations of sc PLA and to compare them with the relaxations of amorphous homopolymers, PLLA and PDLA. In addition, different approaches (namely, fictive temperature, aging process, free volume model) were used in order to determine the amorphous phase properties.

4.1 Investigation of the amorphous phase properties through FSC

The glass transition temperature (T_g) is the most important parameter for the structural relaxation analysis. Therefore, the evolution of T_g as a function of scanning rate was studied by means of the fictive temperature (T_f) concept (presented in section 2.2.4.1) [1]. During the measurements special attention is paid to the sensitivity of the heat flows of FSC curves because of its dependence on the sample mass and scanning rate [2]. The obtained sample mass is equal to 45 ± 3 ng according to the ΔC_P = 0.46 $Jg^{-1}K^{-1}$ and 0.54 $Jg^{-1}K^{-1}$ for homopolymers and sc PLA, respectively, measured by DSC (Fig 4.1), by comparing the value of the heat capacity step (ΔC_P) of wholly amorphous samples [3].

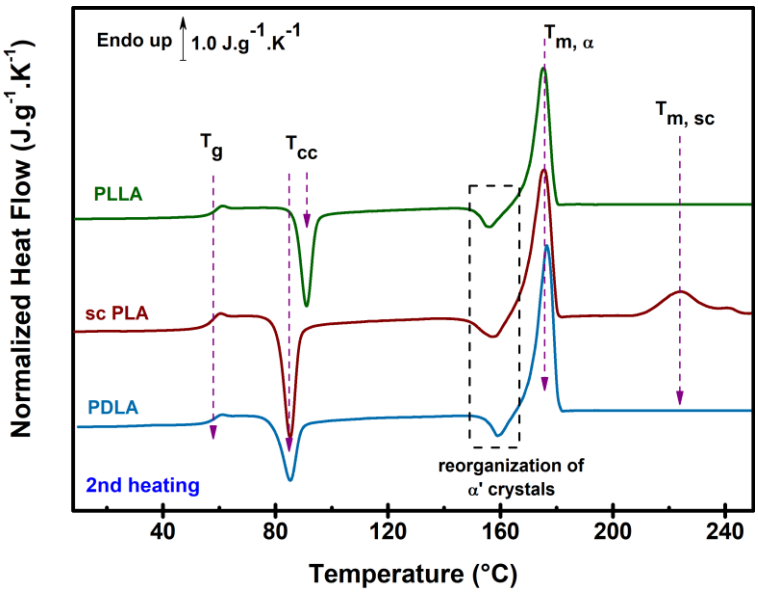

Figure. 4. 1. DSC normalized heat flow of the wholly amorphous PLLA, PDLA and sc PLA samples.

At the beginning samples were studied at temperatures from -50 °C to 270 °C with scanning rate $|\beta_c| = \beta_h$ ranging from 300 Ks^{-1} up to 4000 Ks^{-1} to determine the glass transition temperature. The normalized heat flows curves obtained by FSC are presented in Fig 4.2. The sensitivity of the signal becomes too low when decreasing the scanning rate from 4000 $K.s^{-1}$ to 300 $K.s^{-1}$ (Fig 4.2). Nevertheless, no enthalpy relaxation and thermal lag are observed during cooling. However, there are endothermic peaks which correspond to the enthalpy relaxation. Besides, shifts of the glass transition associated to the thermal lag can be observed during heating for each scanning rate.

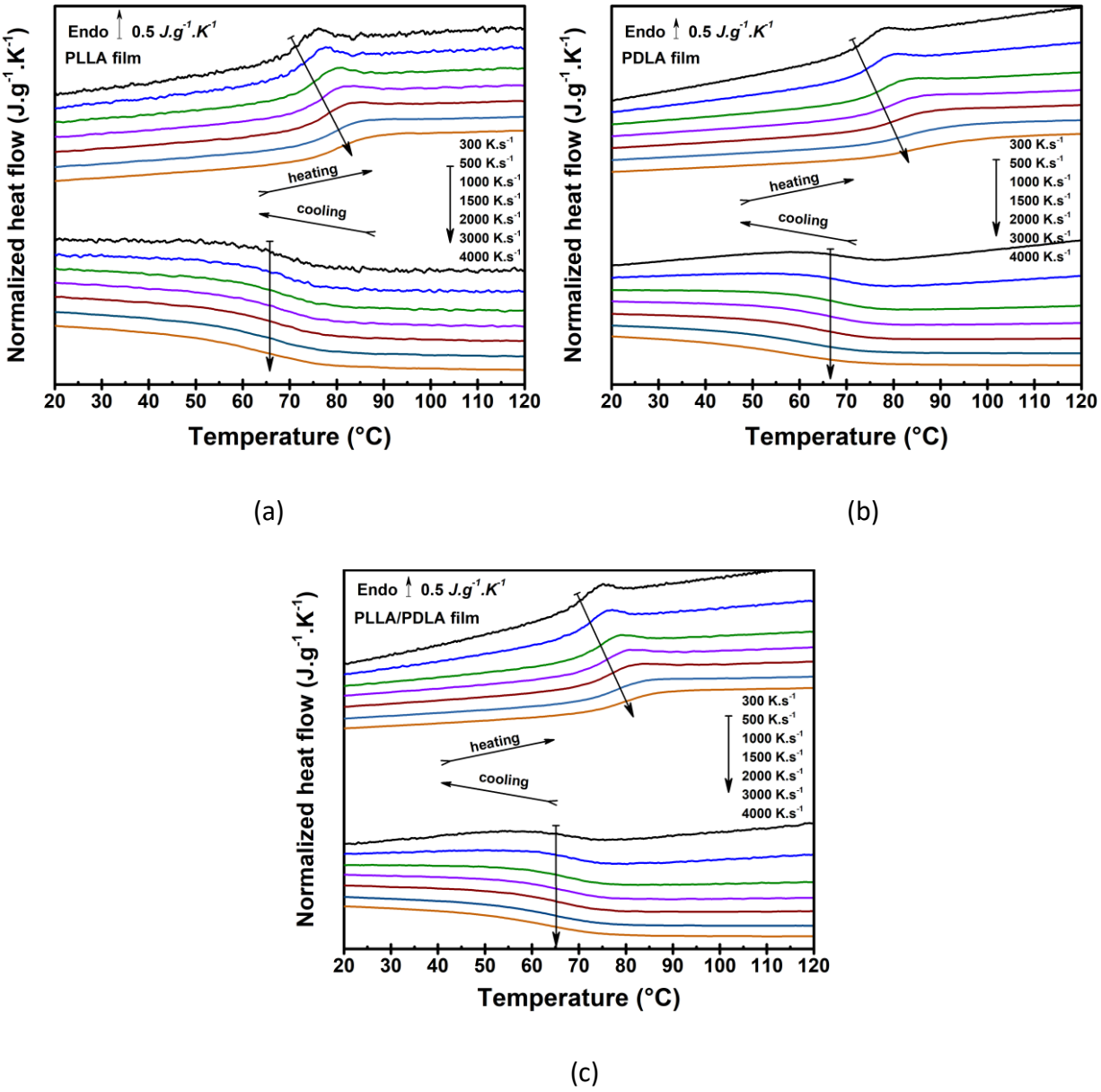

Figure. 4. 2. FSC normalized heat flow of the wholly amorphous samples as a function of temperature upon heating and cooling at equivalent scanning rate $|\beta_c| = \beta_h$ ranging from 300 K.s^{-1} up to 4000 K.s^{-1}: (a) PLLA, (b) PDLA, (c) sc PLA film samples. Arrows are given to follow the glass transition region.

4.1.1 The glass transition temperature and thermal lag corrections

The thermal lag obtained from FSC curves between heating and cooling is shown in Fig 4.2. Therefore, the thermal lag correction was carried out in order to improve the accuracy of the T_f investigation as detailed in section 2.2.4.2. The temperature corrections are done as proposed by Schawe [4] (values are presented in Appendix Chap 4 (A. 4.1)). The T_f and total

thermal lag were determined for wholly amorphous samples at scanning rate of seven decades – from 300 K.s^{-1} up to 4000 K.s^{-1}. At the rate of $|\beta_c| = \beta_h$ = 300 K.s^{-1}, no dynamic thermal lag δT_D was observed for PLLA and PDLA, while it was 0.6 °C for sc PLA. The δT_D increases with the scanning rate increase, and it reaches nearly 3 °C for $|\beta_c| = \beta_h$ = 4000 K.s^{-1} for all samples. On the contrary, a static thermal lag δT_S exists even at the lower scanning rates due to the sample thickness, and it increases with the increase of scanning rate. The calculated T_f upon heating increases with the scanning rate, while the calculated T_f upon cooling remains equal 65 $\pm$ 1 °C for PLLA and sc PLA, and 66 $\pm$ 1 °C for PDLA. The difference between the lowest and the highest values of the fictive temperature measured from heating is observed from 5 °C up to 10 °C. The average values of the T_f measured during cooling should match well with the average values of the corrected T_f from heating. Taking into account advantages of the δT_D and δT_S calibrations, the measured fictive temperatures from heating are corrected for each scanning rate (detailed in A. 4.1 and A. 4.2). The corrected T_f shows independent behavior from the scanning rate, and the average values are 65 $\pm$ 2, 66 $\pm$ 2, 65 $\pm$ 2 °C for PLLA, PDLA and sc PLA, respectively. In addition, Schawe purposed that the static effect can be prevented by the sample thickness of 10 µm or lower and, thus, the thermal lag occurs only due to the dynamic temperature gradient in case of the relatively lower scanning rates, i.e. < 100 K.s^{-1} [4]. However, in this research high scanning rates were investigated in order to measure T_f during heating and cooling, thus δT_S might also be considered for samples with thickness lower than 10 µm. Therefore, the estimation of the T_f was carried out one more time for the same cooling rate and different heating rates. Since the T_f and/or T_g depend on the applied cooling rate, the same cooling rate (0.78 K.s^{-1}) is applied to all samples to vitrify, thus the unique T_f is measured during heating [5]. As the results of the vitrification, the calculated and corrected T_f by FSC must be equal the T_f measured upon cooling at 0.78 K.s^{-1} by DSC. The evolution of the measured T_f shows that when the heating rate increases, the heat transfer delay is observed in the samples and the T_f of the samples increases in the temperature range from 54 °C up to 69 °C (Fig 4.3). The T_f measured by FSC upon heating without correction, T_f corrected from δT_D and T_f corrected from δT_L are plotted in Fig 4.3. The T_f of wholly amorphous samples measured upon cooling by conventional DSC is also depicted by dark red sphere. Due to the straight line

signal upon cooling on FSC, the T_f upon cooling was determined from the signal on conventional DSC as 56 ± 1 °C for PLLA and PDLA, 54 ± 1 °C for sc PLA as shown in Fig 4.3.

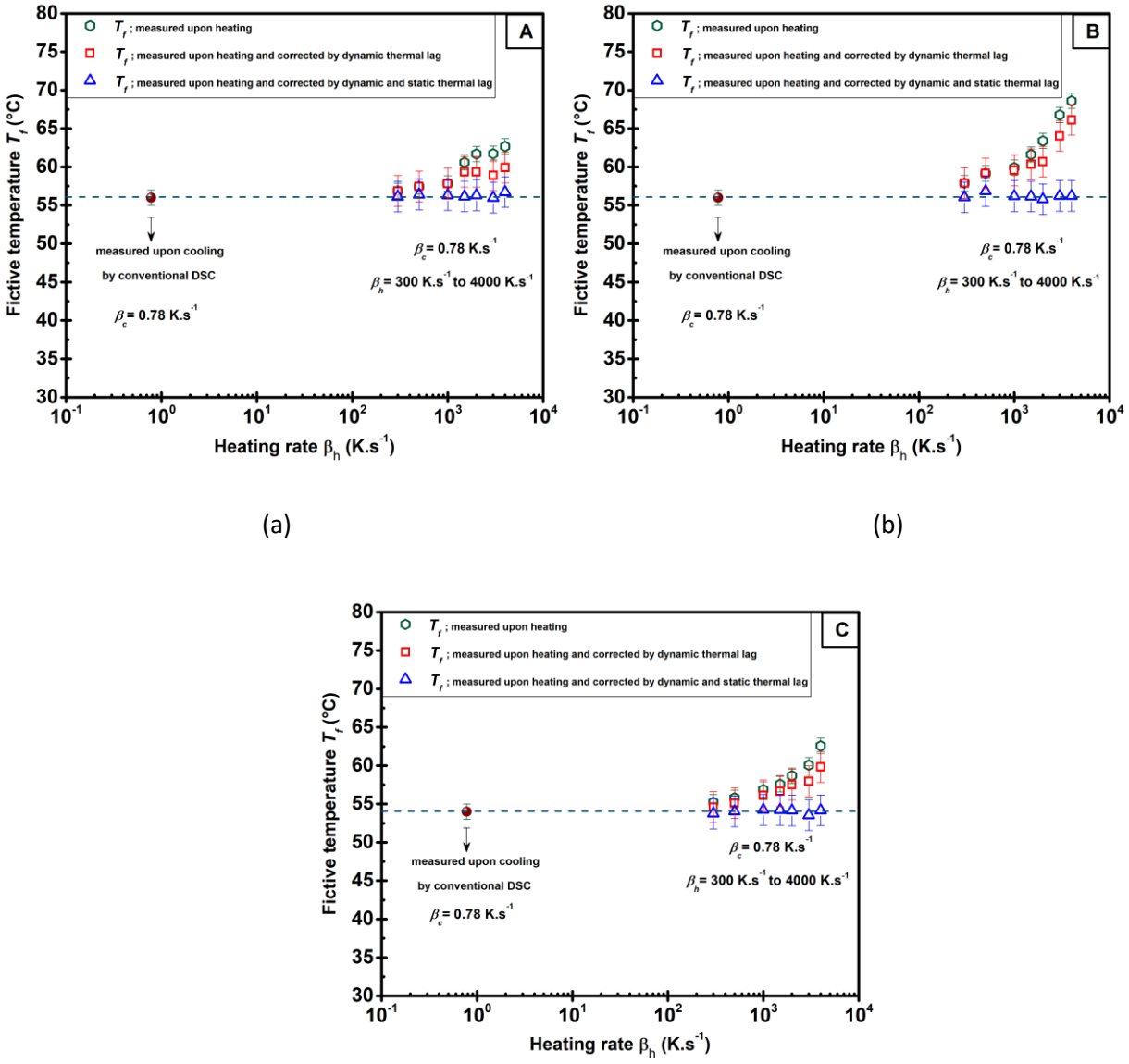

(a) (b)

(c)

Figure 4. 3. Evolution of the T_f as a function of the heating rate β_h from 300 Ks^{-1} to 4000 Ks^{-1} investigated after vitrified the samples at $|\beta_c|$ = 0.78 K s^{-1}: (a) PLLA, (b) PDLA and (c) sc PLA. Dash line is average from blue empty up triangle (FSC) and dark red sphere (DSC).

Then, the values of T_f obtained by DSC were compared with the values of the corrected T_f from FSC. Only the δT_D was applied to the T_f to observe the necessity of the δT_S correction. As one can see, the T_f is still dependent on the heating rate after δT_D subtraction (Fig 4.3).

Therefore, the δT_D is not convenient to complete δT_L correction in case of high scanning rates. When δT_S was subtracted from the measured T_f as well as δT_D, the non-dependency of the T_f on heating rate and the matching between the corrected T_f from heating and the T_f measured upon cooling were observed (Fig 4.3).

Consequently, from the results of the thermal lag corrections, it may be noted that when the same cooling rate is applied, the same T_g and/or T_f is measured. It should be also mentioned that no significant difference of the T_f could be noted between the three polymers. On the other hand, the same values of the T_f were determined whatever the high cooling rates. Similar results were found for PLA-based polymers and its derivatives [3]. However, the difference between the T_f measured after cooling at $|\beta_c|$ = 0.78 K.s^{-1} and $|\beta_c|$ = 1500 K.s^{-1} is observed. Thus, this fact means that there is a critical cooling rate to obtain the unique glasses. Due to such difference between the values of T_f upon cooling at $|\beta_c|$ = 0.78 K.s^{-1} and $|\beta_c|$ = 1500 K.s^{-1}, the cooling rate dependency of T_f is well defined. Therefore, a lack of the applied cooling rate dependence of the fictive temperature can be observed in glass-forming systems above certain and/or critical scanning rate during FSC measurements [6, 7].

4.1.2 The fragility index m

The cooling rate dependence of the T_f was studied and it was fitted by the VFTH equation (Eq 2.15) (Appendix Chap 4 (A. 4.3)) to determine the dynamic fragility index *m* by VFT equation (Eq 2.16 and Eq 2.17) [5, 8-10]. In the *m* calculation, T_g is taken as the T_f determined at a cooling rate of 0.78 K.s^{-1} as 329 K and 327 K for homopolymers and sc PLA, respectively. According to the obtained results (Table 4.1), the calculated values of the dynamic fragility *m* for studied films are rather close taking into account the measurement precision. These values are in the range of the fragility values defined by Angell: $16 \leq m \leq 200$. The higher the value of *m*, the more fragile the system. So, all the samples can be defined as "fragile".

Sample	*B (K)*	T_V *(K)*	*M*
PLLA	36 ± 11	48 ± 3	185 ± 17
PDLA	37 ± 8	48 ± 3	190 ± 11
Sc PLA	73 ± 22	41 ± 4	142 ± 44

Table 4. 1. The VFTH fitting parameters and the dynamic fragility index of studied samples.

4.2 Structural relaxation dynamics through physical aging

The measured and corrected T_f values were determined to estimate the aging temperature (T_{ag}). The determined constant values of T_f at all scanning rates exhibit unique glass formation. Due to the estimation of unique glass obtained by higher cooling rate, the scanning rate dependence of the physical aging was investigated.

4.2.1 Influence of the scanning rate on physical aging

Physical aging was carried out at the T_{ag} calculated according to the corrected T_g which are 66 °C for PDLA and 65 °C for PLLA and sc PLA after a cooling at 1500 K.s^{-1}, as shown in section 2.2.4.3. The recovery enthalpy values were calculated and compared for each scanning rate and aging time (t_{ag}) for all the samples (detailed in section 2.2.4.3) [11]. The enthalpy recovery for each samples (PLLA, PDLA and sc PLA) at the scanning rate range for t_{ag} = 1 min, 10 min and 100 min has similar behavior. Therefore, only the results of aging at the scanning rate $|\beta_c| = \beta_h$ ranging from 300 K.s^{-1} up to 4000 K.s^{-1} are shown as an example (Fig 4.4).

As one can see from Fig 4.4a, the peaks are shifted towards higher temperatures with the increase of the scanning rate due to the smearing effects. In addition, as shown in Fig 4.4b, the values of enthalpy recovery are independent on the scanning rate, but dependent on the t_{ag}, as average values of 5.5 ± 0.4 J/g, 7.8 ± 0.3 J/g, and 9.7 ± 0.4 J/g for 1 min, 10 min, and 100 min, respectively, are obtained. Thus, not only the fictive temperature shows independence on the scanning rate, but also the enthalpy recovery is independent from scanning rate above the critical cooling rate. Therefore, for further physical aging analysis to compare the structural relaxation of amorphous PLLA, PDLA and sc PLA, the scanning rate of $|\beta_c| = \beta_h$ = 1500 K.s^{-1} was chosen due to the less signal-noise ratio.

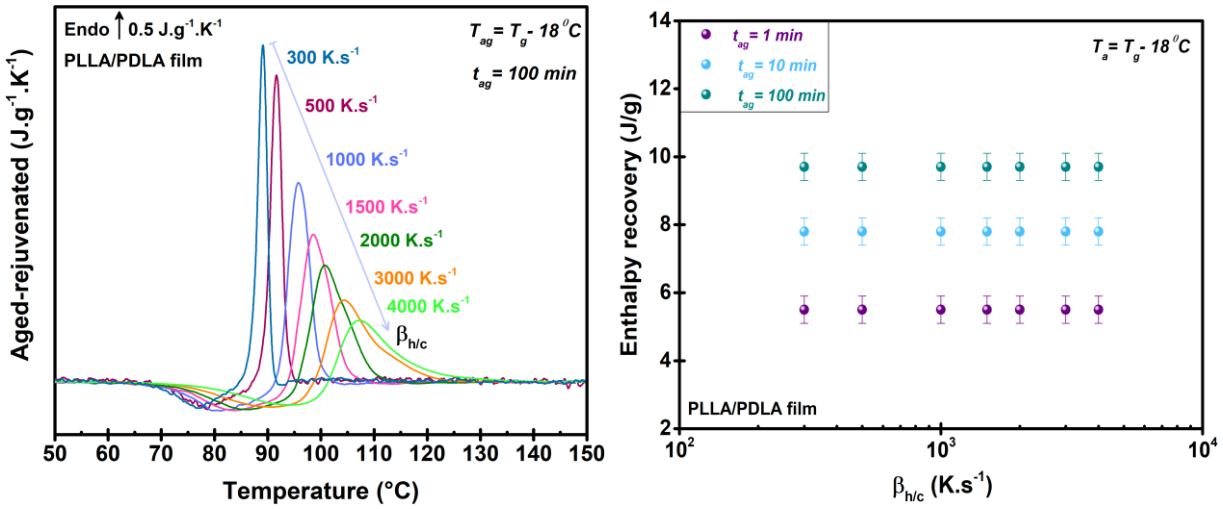

(a) (b)

Figure 4. 4. Aging of sc PLA at $T_{ag} = T_g - 18$ °C at the scanning rate range $|\beta_c| = \beta_h$ from 300 K.s^{-1} up to 4000 K.s^{-1}. (a) Normalized heat flow subtraction for t_{ag} = 100 min. (b) Values of the enthalpy recovery as a function of $\beta_{h/c}$ for t_{ag} = 1 min; 10 min; 100 min.

4.2.2 Physical aging at four different aging temperature

The physical aging was carried out at the T_{ag} chosen as $T_{ag} = T_f - 5$ °C, $T_{ag} = T_f - 8$ °C, $T_{ag} = T_f - 13$ °C and $T_{ag} = T_f - 18$ °C with the t_{ag} ranging from 0.001 min to 100 min for all the samples. The enthalpy recovery of the structural relaxation of amorphous samples was investigated to define the chirality impacts on the relaxation. Physical aging of polymers was widely studied and it was reported that quenching or higher cooling rates allowed us to accelerate the aging and the enthalpy recovery of materials to reach equilibrium on laboratory scale [3, 12-15]. Fig 4.5 presents the normalized heat flows of all the aged samples from 0.001 min up to 100 min obtained by FSC at $|\beta_c| = \beta_h$ = 1500 K.s^{-1} for the T_{ag} below the respective glass transition temperature. The red dash line corresponds to the rejuvenated curve. For all the curves, endothermic relaxation peaks are superimposed to the glass transition and shift towards higher temperature with the increasing t_{ag}, as usually observed for physical aging [3, 12-15]. The endothermic peaks are intense and broadened, thus, the lower the T_{ag}, the higher the enthalpy recovery. Fig 4.6 shows the decline of the enthalpy during the physical aging for all studied T_{ag}.

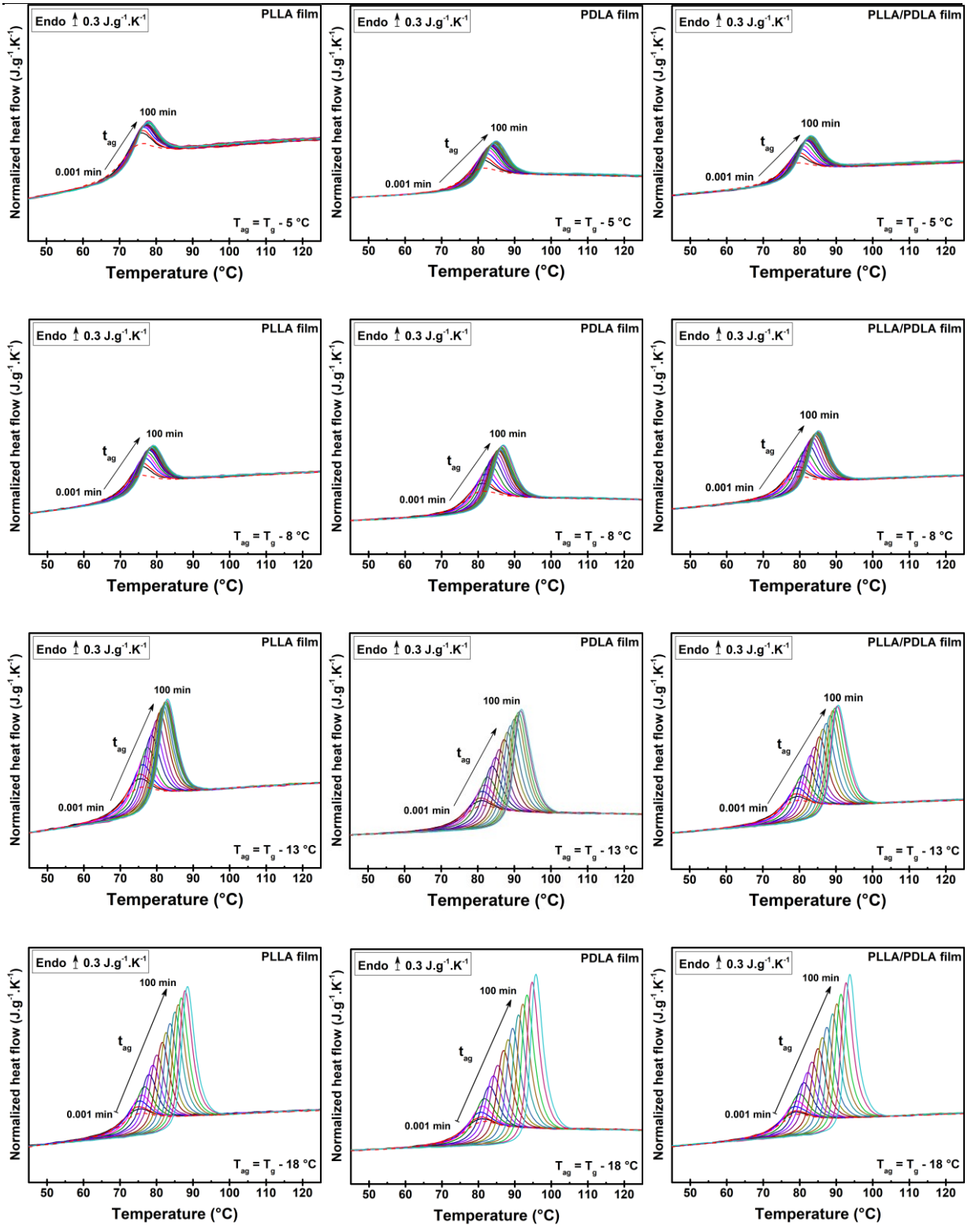

Figure 4. 5. Aged amorphous (a) PLLA, (b) PDLA and (c) sc PLA films examined by FSC. Graphs on the same line represent the same T_{ag}.

The difference between the total enthalpy loss ΔH_∞ and the enthalpy recovery at a given aging time ΔH_{tag} shows different behaviors according to the T_{ag}. Despite the different structure of samples, similarities are observed for the same T_{ag} and t_{ag}. The kinetic decay of the enthalpy recovery during the physical aging is similar for different samples. A rapid kinetics of physical aging was observed as the equilibrium was reached after 1 min at 5 °C below T_g. Besides the rapid kinetics, FSC also allows us to analyze few ng sample as a reference of the bulk sample in shorter aging time such as 0.001 min due to the formation of glass with high fictive temperature with very short relaxation time [16]. The enthalpy recovery is guided by a single step decay and the classical stretched tendency is observed similar to other glassy polymers [16-18].

As depicted in Fig 4.6, the enthalpy recovery exhibits a single step decay towards equilibrium and the glass completely releases its excess of energy in the range of aging time at the highest aging temperature. Such result is opposite to the assumption proposed by Gomez Ribelles et al. [19, 20] based on DSC measurements. The authors assumed that thermodynamic equilibrium cannot be reached because of the steric hindrance and molecular mobility induced during structural relaxation. In addition, Hutchinson et al. [21] reported that a certain fraction of the glass-forming liquid was vitrified towards the glass transition. Therefore, the slow-process (i.e. the vitrified fraction) and the fast-process (i.e. the non-vitrified fraction inhibit) to reach the thermodynamic equilibrium. FSC allows obtaining glasses with high enthalpy and reaching the thermodynamic equilibrium. The lowest aging temperatures exhibits also single step decay, but does not allow reaching the equilibrium at the investigated aging time.

Although all the samples have the similar behavior (i.e. a single step decay), in order to compare the relaxation kinetics of all the amorphous samples, the enthalpy recovery and the master curves of normalized enthalpies are investigated and presented in Fig 4.7.

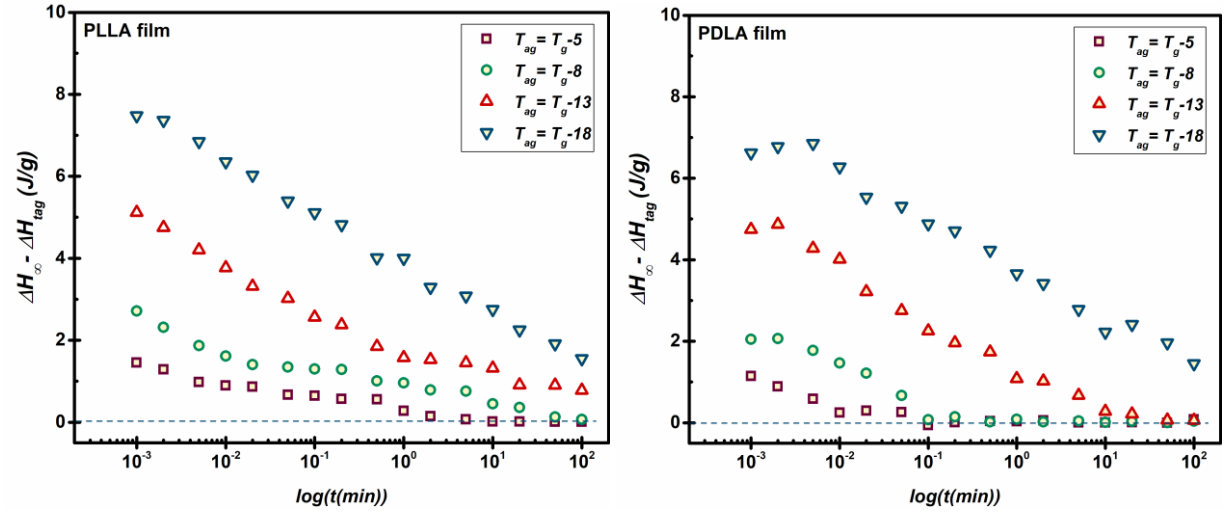

(a) (b)

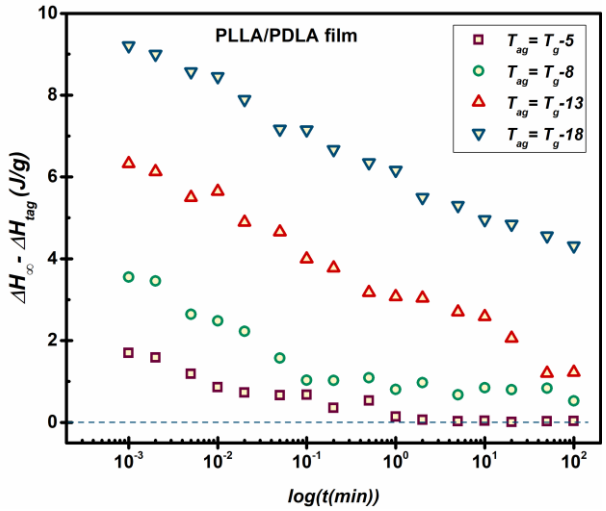

(c)

Figure 4. 6. Time evolution of the difference between the ΔH_∞ and the ΔH_{tag} for the aged amorphous (a) PLLA, (b) PDLA and (c) sc PLA as a function of T_{ag} with the aging time ranging from 0.001 min to 100 min at $|\beta_c| = \beta_h = 1500$ K.s^{-1}.

The difference in the calculated total enthalpy loss ΔH_∞ is caused by the amplitude of the heat capacity step of the samples (0.46 and 0.54 J.g^{-1}.K^{-1} for homopolymers and sc PLA, respectively). As shown in Fig 4.7a, the physical properties are dependent on the logarithm of the t_{ag}. Therefore, the aging rate can be determined as the slope of the linear fit and corresponds to the enthalpy change towards equilibrium. One can noticed from the Fig 4.7a that all the samples have the similar rate of enthalpy recovery (1.36 $\pm$ 0.06 J/decade). Fig 4.7b presents superimposition of the master curve of normalized enthalpy recovery as a function

of the logarithm of the t_{ag}. The enthalpy recoveries are normalized by the infinite enthalpy loss as follows:

$$\Delta H_{normalized} = \frac{\Delta H_{\infty} - \Delta H_{recovery}}{\Delta H_{\infty}} \quad (4.1)$$

where $\Delta H_{normalized}$ is the normalized enthalpy recovery, $\Delta H_{recovery}$ is the measured enthalpy recovery of the aged samples, and ΔH_{∞} is the total enthalpy loss.

In addition, the Tool-Narayanaswamy-Moynihan (TNM) model is used to explain the evolution of the glass transition temperature related to the relaxation enthalpy and aging temperature (T_{ag}) for an aging time (t_{ag}) [11, 22]. The TNM model is used to fit master curves by assuming a specific expression for the temperature and structure dependence of the relaxation time τ (T, T_g) [23] as follows:

$$\tau\left(T_f, T\right) = A \exp\left\{\frac{x\,\Delta H}{RT} + \frac{(1-x)\Delta H}{RT_f}\right\} \quad (4.2)$$

where T is a reference temperature well above the glass transition temperature, x is the nonexponential parameter determining the broadness of the relaxation spectrum. When these parameters are obtained by DSC analysis, so the shape of parameters corresponds to the behavior of the system in the out-of-equilibrium state. However, some inconsistencies were reported concerning the equilibrium behavior if the relaxation expressed for τ (T, T_f) was not fitted correctly. On the contrary to the complexity of TNM model, in our case, the master curves of enthalpy recovery of all the samples can be fitted using a simplified approach, i.e. the Kohlrausch-Williams-Watts (KWW) function [24], as follows:

$$\phi\,(t) = e^{-(t/\,\tau_{KWW})^{\beta_{KWW}}} \quad (4.3)$$

where $\Phi(t)$ is the correlation function, β_{KWW} ($0 < \beta_{KWW} < 1$) is a stretch exponent, and τ_{KWW} is the relaxation time for $\beta_{KWW} = 1$. As shown in Fig 4.7, the master curves of $T_{ag} = T_g - 8$ °C were taken as a reference temperature to impose all the master curves and the other curves were shifted over the reference curve with the shift factor $x = 0.4$ for $T_{ag} = T_g - 5$ °C and $x = -0.2$ for $T_{ag} = T_g - 13$ °C and $T_{ag} = T_g - 18$ °C. In this case, KWW function is sufficient to fit all the curves

within the single relaxation time τ which is determined as 0.04 s according to the reference temperature. The kinetics of decays of the enthalpy recovery of all the samples during the physical aging is exactly the same. No influence of the tacticity on the structural relaxation is observed as a result of kinetic investigation.

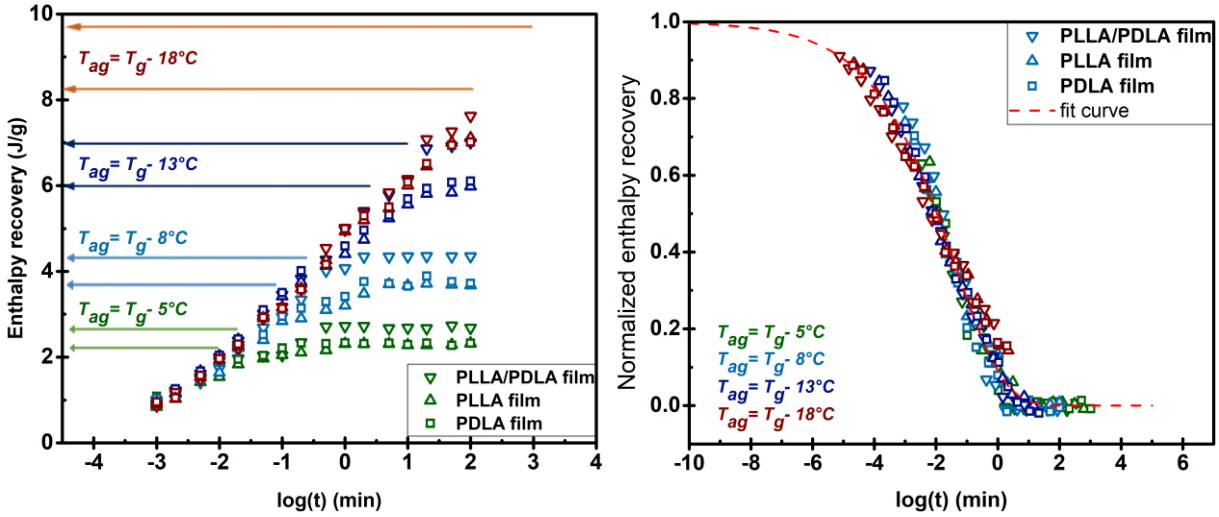

(a) (b)

Figure 4. 7. (a) Time evolution of the enthalpy recovery ΔH_t for aged amorphous PLLA (up triangle), PDLA (square) and sc PLA (down triangle) films at different T_{ag}. The arrows show the values of ΔH_∞ for homopolymers and sc PLA. (b) Master curves of the enthalpy recovery normalized by the infinite enthalpy loss. Red dash line corresponds to the KWW fitting (Eq 4.3).

4.3 Segmental relaxation investigations by DRS

The molecular dynamics of all the amorphous samples was investigated by means of dielectric relaxation spectroscopy (DRS). The α-relaxation parameters like the dielectric strength, the relaxation time and the fragility index of all samples were examined to combine the results with the results of FSC. The cooperativity of molecular mobility is presented in the notion of the dynamically correlated number N_C and the cooperativity degree N_α.

4.3.1 The α-relaxation process

The experimental raw data obtained from dielectric relaxation spectroscopy measurements are presented in 3-D illustration in Fig 4.8. The dielectric loss ε'' is measured as a function of temperature and frequency. The dielectric spectra of all samples display

similar characteristics in the same temperature range towards the glass transition. The α-relaxation peak which is the dielectric response of the glass transition, broadens and shifts towards higher temperature as the frequency increases. The conductivity phenomenon which is related to the charge transport is also observed at high temperature and low frequency. The dielectric relaxation spectra can be characterized by a "step-like" decrease of ε' and a peak of ε" in the frequency range at an isothermal temperature. The main parameters to characterize dielectric properties can be determined from both ε' and ε" versus frequency plot. As an example, the relaxation time τ_{max} can be determined from the maximum value of frequency f_{max} where ε" reaches its maximum value at a certain temperature *T*. The measured complex permittivity signals (ε*) associated with the primary (α-relaxation) and secondary (β-relaxation) relaxation were fitted by the empirical Havriliak-Negami (HN) function (Eq 4.4) to complete quantitative analysis of the dielectric spectra in the frequency domain [25]:

$$\varepsilon^*(\omega) = \varepsilon_\infty + \frac{\Delta\varepsilon}{[1+(i\omega\tau_{HN})^{\alpha_{HN}}]^{\beta_{HN}}} \tag{4.4}$$

The HN function allows to fit the real (ε' (ω)) and the imaginary (ε" (ω)) components of the complex dielectric permittivity (ε* (ω)) by the following equations:

$$\varepsilon'(\omega) = \varepsilon_\infty + \Delta H_{HN} \frac{\cos(\beta_{HN}\varphi_{HN})}{\left[1+2\sin\left(\frac{\pi(1-\alpha_{HN})}{2}\right)(\omega\tau_{HN})^{\alpha_{HN}}+(\omega\tau_{HN})^{2\alpha_{HN}}\right]^{\beta_{HN}/2}} \tag{4.5}$$

$$\varepsilon''(\omega) = \Delta H_{HN} \frac{\sin(\beta_{HN}\varphi_{HN})}{\left[1+2\sin\left(\frac{\pi(1-\alpha_{HN})}{2}\right)(\omega\tau_{HN})^{\alpha_{HN}}+(\omega\tau_{HN})^{2\alpha_{HN}}\right]^{\beta_{HN}/2}} \tag{4.6}$$

where ω is the angular position (ω = 2π*f*), ε_∞ is the unrelaxed dielectric permittivity, $\Delta\varepsilon_{HN}$ is the relaxation strength, τ_{HN} is a characteristic relaxation time and α_{HN} and β_{HN} are shape parameters describing the symmetric and asymmetric broadening factor of the dielectric spectra, respectively. In order to improve the consistency of the fit results, the fitting has been carried out for both real and imaginary parts of the complex signals.

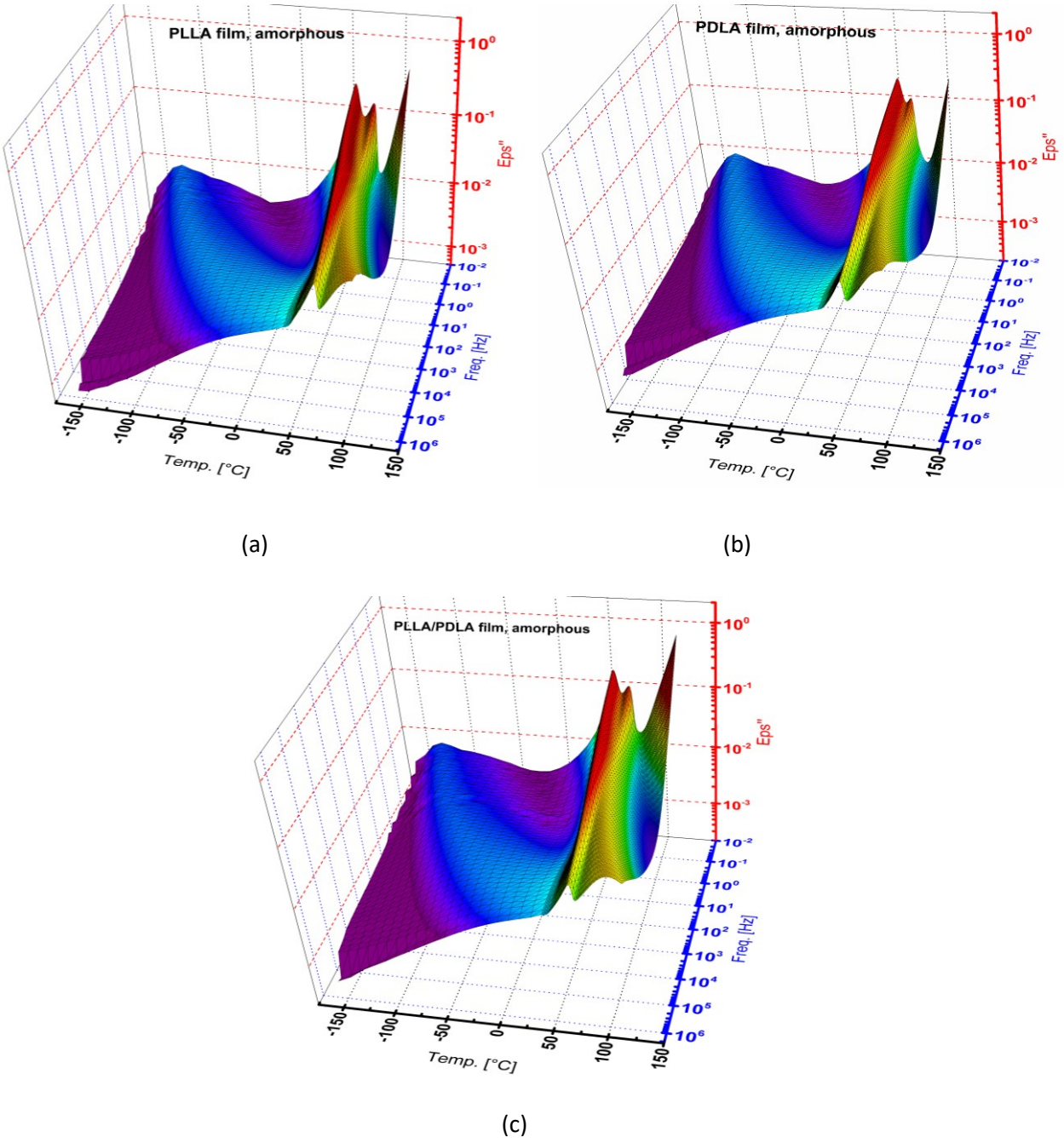

Figure 4. 8. Dielectric loss (ε”) versus frequency and temperature for all studied amorphous samples: (a) PLLA, (b) PDLA and (c) sc PLA.

The isothermal dielectric spectra of amorphous sc PLA are shown as a function of frequency for different temperatures in Fig 4.9A and Fig 4.9C as an example of DRS analysis. All the amorphous samples show similar variations during relaxation investigations. It should be noted that all samples show two complex relaxation processes. The first one is the

secondary relaxation (β-process) observed at low frequencies and temperatures (Fig 4.9A). This relaxation shifts towards higher frequency range as the temperature increases. The second one is the primary relaxation (α-process) which can be clearly seen in higher temperature range (Fig 4.9C).

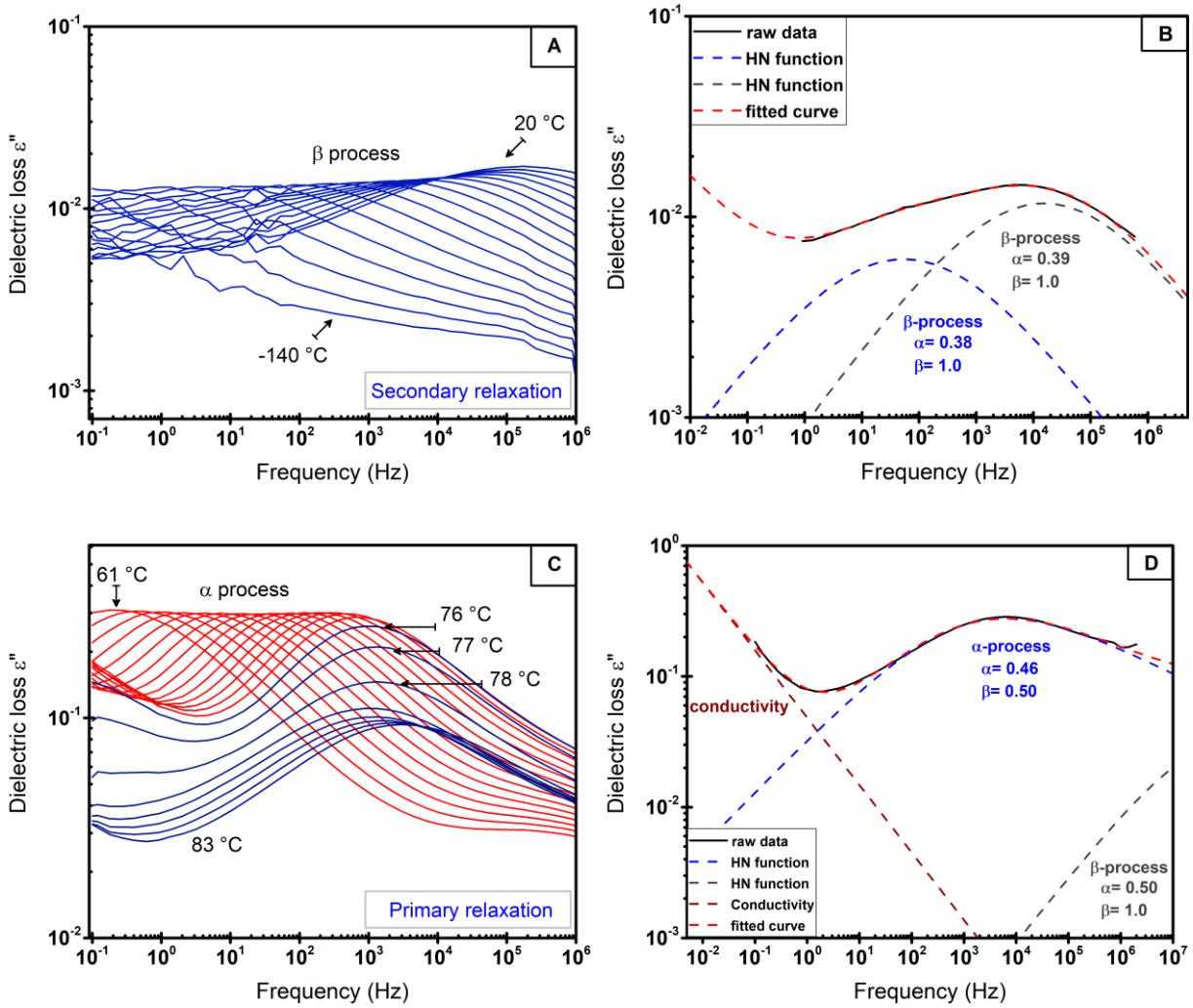

Figure 4. 9. Imaginary parts of the complex dielectric permittivity (ε'') versus frequency of amorphous sc PLA film: (A) in the glassy state at temperature $T < T_g$, (B) clarification of dielectric spectra fitting for secondary relaxation (β-process), (C) in the liquid state at temperature $T > T_g$, and (D) clarification of dielectric spectra fitting for primary relaxation (α-process) by HN complex functions.

The two HN complex functions are used to fit isothermal dielectric loss spectra with a conductivity contribution to investigate the relaxation phenomena. The HN shape parameters of both relaxations in amorphous sc PLA were shown in Fig 4.9B and 4.9D. All amorphous

samples have the same temperature dependence for the main relaxation processes, in which both α and β relaxations shift to higher frequencies but keep the same amplitude as the temperature increases until the cold crystallization temperatures of amorphous samples. As shown in Fig 4.9C, there is a strong reduction in the amplitude of dielectric loss above *T* = 75 °C due to the cold crystallization during the measurements. Therefore, the analytical procedure of fitting was carried out until the first crystallization appeared. The demonstration of complex secondary relaxation with two contributions is supported by the results obtained for the other polyesters, such as poly(ethylene terephthalate) (PET) [26, 27], PLA [28] and poly(hydroxyalkanoates) (PHAs) [29]. In addition, Soccio et al. [30] reported that such a broad β relaxation phenomenon is caused by interactions between ester functional groups and the main polymer chain as well as stereocomplexation between homopolymers (PLLA and PDLA). In the case of poly(butylene 2,5-furanoate), the β relaxation has two processes which are a faster β_1 relaxation due to the association of the mobile subunit with the C − O of the ester group and a slower β_2 relaxation correlated to the connection between the aromatic ring and C = O of the ester group. In the case of stereocomplexation, such a classical broad β relaxation of polyesters maybe caused by similar interactions between the mobile subunit and the C − O of the ester group and/or the main chain and C = O of the ester group due to the stereoselective van der Waals forces. Therefore, the isothermal spectra of β relaxation were analyzed by two symmetrical HN functions, called Cole-Cole functions at different temperatures.

4.3.1.1 The master curves and shape parameters: α and β

The shape parameters determined by the HN fits of the α-relaxation process are used to define the symmetric and asymmetric broadening of the complex dielectric function [31]. The values of the shape parameters determined for all the samples are found to be less than 1 in accordance with literature [31]. By using the estimated values of τ_{HN}, α_{HN}, β_{HN} parameters, the relaxation time, $\tau_{max} = (2\pi f_{max})^{-1}$ was calculated as [31]:

$$\tau_{max} = \tau_{HN} \times \left[\frac{\sin\left(\frac{\alpha_{HN}\beta_{HN}\pi}{2+2\,\beta_{HN}}\right)}{\sin\left(\frac{\alpha_{HN}\pi}{2+2\beta_{HN}}\right)}\right]^{1/\alpha_{HN}} \quad (4.7)$$

The correlation function can be calculated using the HN relationship [32]:

$$f(\tau) = \frac{1}{\pi} \frac{\left(\frac{\tau}{\tau_{HN}}\right)^{\beta_{HN}\alpha_{HN}} \sin(\beta_{HN}\varphi)}{\left[1+\left(\frac{\tau}{\tau_{HN}}\right)^{2\alpha_{HN}}+2\left(\frac{\tau}{\tau_{HN}}\right)^{\alpha_{HN}}\cos(\pi\alpha_{HN})\right]^{\beta_{HN}/_2}} \quad (4.8)$$

with

$$\varphi = \frac{\pi}{2} - tan^{-1}\left[\frac{\left(\frac{\tau_{HN}}{\tau}\right)^{\alpha_{HN}}+\cos(\pi\alpha_{HN})}{\sin(\pi\alpha_{HN})}\right] \quad (4.9)$$

where $f(\tau)$ is the distribution function, τ_{HN} is the HN relaxation time, α_{HN} and β_{HN} are the HN shape parameters. Therefore, in term of the distribution of relaxation time, the correlation function Φ (t) is expressed by [32]:

$$\Phi(t) = \int_0^\infty f(\tau) exp^{-t/\tau} dt \quad (4.10)$$

In a certain time domain, the correlation function can be well described by the KWW stretch exponential function as presented in Eq 4.3 [33]. To express the time-scale required for molecular units to relax or move, the master plots of the dielectric loss for each isothermal spectrum are reported in Fig 4.10. The results show very good overlap of all the curves forming a single master curve. On the other hand, systematic deviation from the master curve is observed in the high frequency range for the α relaxation. This kind of deviation can be explained by the contribution of noncooperative localized molecular mobility, such as β relaxation process, combined with the molecular mobility of localized molecules. Furthermore, such an interdependence of α and β relaxations was reported also by Johari and Goldstein [34] and was investigated in glass-forming systems [35, 36]. While the temperature of measurement is increased, the impact of the β relaxation increases on the master curves. The non-Debye relaxation in the time range (t) is empirically explained by the KWW function [24]. Each master curve was fitted by the KWW relationship (Eq 4.3) in order to calculate KWW stretching parameter β_{KWW}. The stretching parameter β_{KWW} allows comparing any asymmetrical broadening behavior of the relaxation process at high frequencies with the exponential decay which corresponds to a Debye relaxation with β_{KWW} = 1.

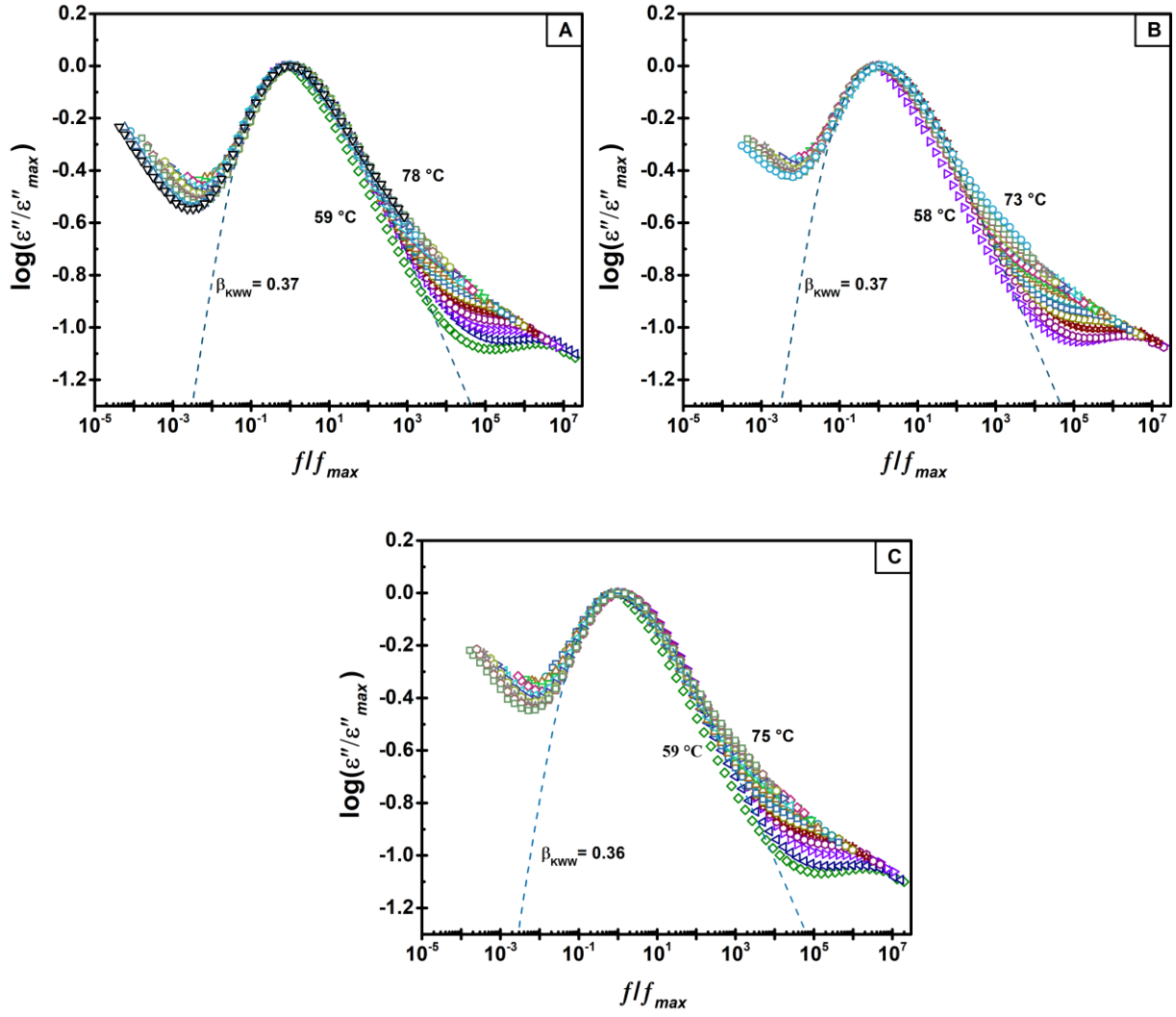

Figure 4. 10. Log-log plot of the master curves of amorphous (A) PLLA, (B) PDLA and (C) sc PLA samples. Light blue dash lines correspond to the KWW fits.

The HN parameters are correlated with the stretching parameter β_{KWW} as follows [31]

$$\beta_{KWW} = (\alpha_{HN}\beta_{HN})^{0.813} \tag{4.11}$$

The master curves were obtained by normalization of the spectra with the maximum of ε" and its counterpart frequency at the different temperatures (from 58 °C to 78 °C with a step of 1 °C) and fitted by KWW function to graphically visualize the stretching parameter β_{KWW}. These master plots lead to show whether temperature has influenced on the shape of the structural relaxation process, which would represent different distributions of the relaxation times at different temperatures. As shown in Fig 4.11, the values of β_{KWW} are experimentally found to be 0.37 ± 0.02 for PLLA and PDLA, and 0.36 ± 0.02 for sc PLA. These values have a

good compliance with the values calculated by Eq 4.16: 0.40 ± 0.01 for PLLA, 0.39 ± 0.01 for PDLA and 0.39 ± 0.01 for sc PLA. In addition, This result is in good agreement with the value reported in literature for PLA from DSC measurements, $\beta_{KWW} \approx 0.35$ [37].

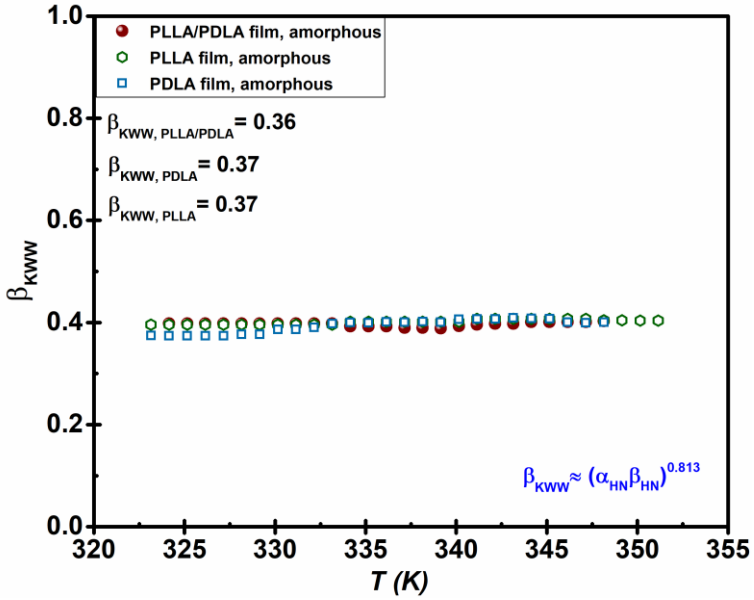

Figure 4. 11. Variation of the β_{KWW} parameter as a function of temperature for studied samples.

4.3.1.2 Dielectric relaxation strength $\Delta\varepsilon_\alpha$

The dielectric relaxation strength $\Delta\varepsilon_\alpha$ of α relaxation recorded for all the isothermal measurements is obtained by fitting the experimental data with the HN function. In addition, as reported by Onsager, Fröhlich, and Kirkwood [31], the values of $\Delta\varepsilon_\alpha$ depend on several parameters and are also calculated by the generalized form of the Debye's theory as follows:

$$\Delta\varepsilon_\alpha = \frac{1}{3\varepsilon_0} g_K \frac{\mu^2}{k_B T} \frac{N}{V} \tag{4.12}$$

where ε_0 is the dielectric permittivity of vacuum, g_K is the Kirkwood correlation factor which corresponds to the short-range intermolecular interactions leading to specific static dipole-dipole orientations, μ^2 is the time-correlation function of the total dipole moment, k_B is the Boltzmann's constant, T is the temperature, and N/V is the volume density of dipoles involved in the relaxation process. Fig 4.12 presents the temperature dependence of the $\Delta\varepsilon_\alpha$ of α-relaxation for PLLA, PDLA and sc PLA.

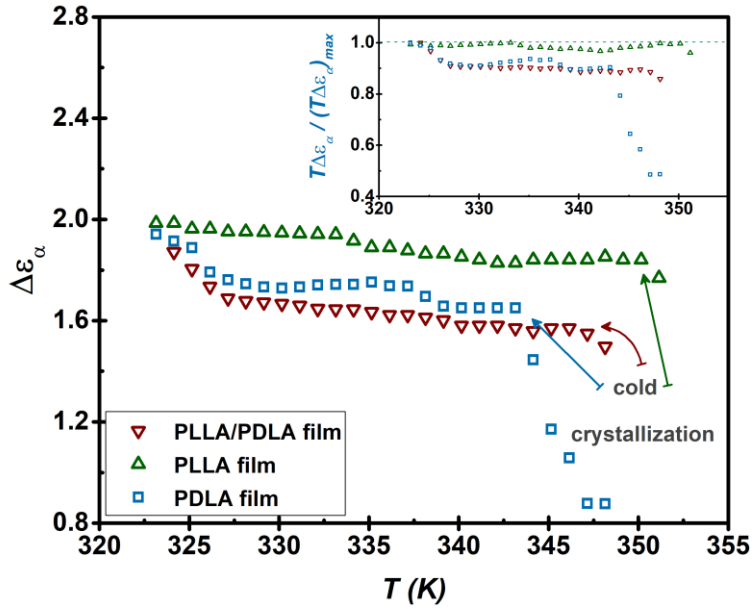

Figure 4. 12. Temperature dependence of the dielectric strength $\Delta\varepsilon_\alpha$ of α-relaxation for amorphous PLLA, PDLA and sc PLA.

In general, the dielectric relaxation strength $\Delta\varepsilon_\alpha$ decreases with temperature increasing [31, 37, 38]. Such a temperature dependence of $\Delta\varepsilon_\alpha$ was also reported in literature for other kinds of glass-forming systems, i.e. polymers and thin polymer films [31, 38, 39]. The obtained results indicate the same behavior of the dielectric strength $\Delta\varepsilon_\alpha$ for all the samples (Fig 4.12). In addition, the dielectric strength $\Delta\varepsilon_\alpha$ of sc PLA is close to the $\Delta\varepsilon_\alpha$ values of homopolymers. The maximum values of $\Delta\varepsilon_\alpha$ were reported at the lowest measurement temperature for each sample. The maximum of $\Delta\varepsilon_\alpha$ value (2.0 ± 0.5) is close to the previously reported results of Pluta et al. [40] for PLA (~ 2.5). The inset in Fig 4.12 presents the normalized $\Delta\varepsilon_\alpha$ by temperature ($T\,\Delta\varepsilon_\alpha$ normalized to the maximum value at lowest measured temperature) as a function of temperature for all the samples. Inset plot shows that $T\Delta\varepsilon_\alpha$ decreases with increasing temperature for each studied sample. As reported by Schönhals [41], such temperature dependence caused by an increasing influence of intermolecular interactions between dipoles with decreasing temperature. Therefore, the stronger the temperature dependence of $\Delta\varepsilon_\alpha$, the stronger the intermolecular interactions with decreasing temperature. Thus, such characteristics of the α-relaxation can be defined by cooperativity character of the fundamental molecular motion responsible for the molecular dynamics. The size of the

cooperative rearranging region increases with decreasing the temperature and, therefore, effective dipole moment increases [41].

4.3.1.3 Relaxation map for α- and β-relaxation

The relaxation map in Fig 4.13 shows the relaxation times τ_{max} as a function of the inverse temperature for both α and β processes. The temperature dependence of the relaxation time, i.e. the recorded τ_{max} values, could be fitted and well described by the Arrhenius law as follows:

$$\tau = \tau_{0,A} exp\left(\frac{E_a}{RT}\right) \quad (4.13)$$

where E_a is the activation energy of the β_1 relaxation, R is the gas constant, and $\tau_{0,A}$ is a pre-exponential factor.

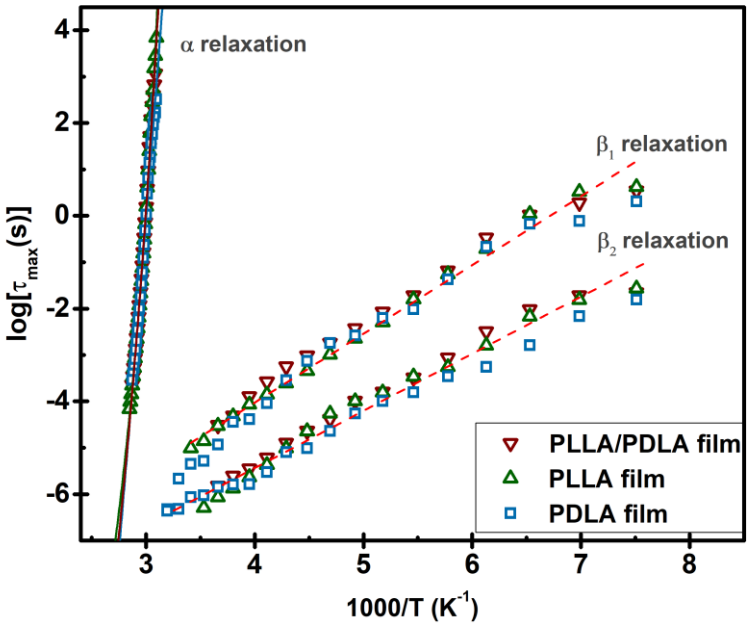

Figure 4. 13. Temperature dependence of structural α and β relaxation times as a function of the inverse of temperature for amorphous PLLA, PDLA and sc PLA films.

The values of activation energy E_a are calculated as 64 ± 10 kJ/mol for PLLA, 57 ± 12 kJ/mol for PDLA, and 65 ± 10 kJ/mol for sc PLA. Such results are in good agreement with the results for the other polyesters – 79 ± 10 kJ/mol for PET [42] and 36 - 46 kJ/mol for PLA [28].

The values of E_a correspond to the local motions of the polar subunits of all the samples. In addition, the E_a value obtained for sc PLA is the same that the value obtained for PLLA and PDLA. Such results can be at the origin of the similarity in the chemical structure of the repeating units of homopolymers and sc PLA (Fig 2.1).

4.3.1.4 Angell's and Stickel's plot of α relaxation

To investigate molecular dynamics in α relaxation process, Angell's and Arrhenius plots are studied and presented in Fig 4.14. The symbols correspond to the experimental data and the red lines represent the VFT fits. T_g corresponds to τ = 100 s and ν_{max}^{α} is a relaxation rate, which is equivalent to $1/\tau_{max}$, where $\tau_{max} = 1/2\pi f_{max}$ [43].

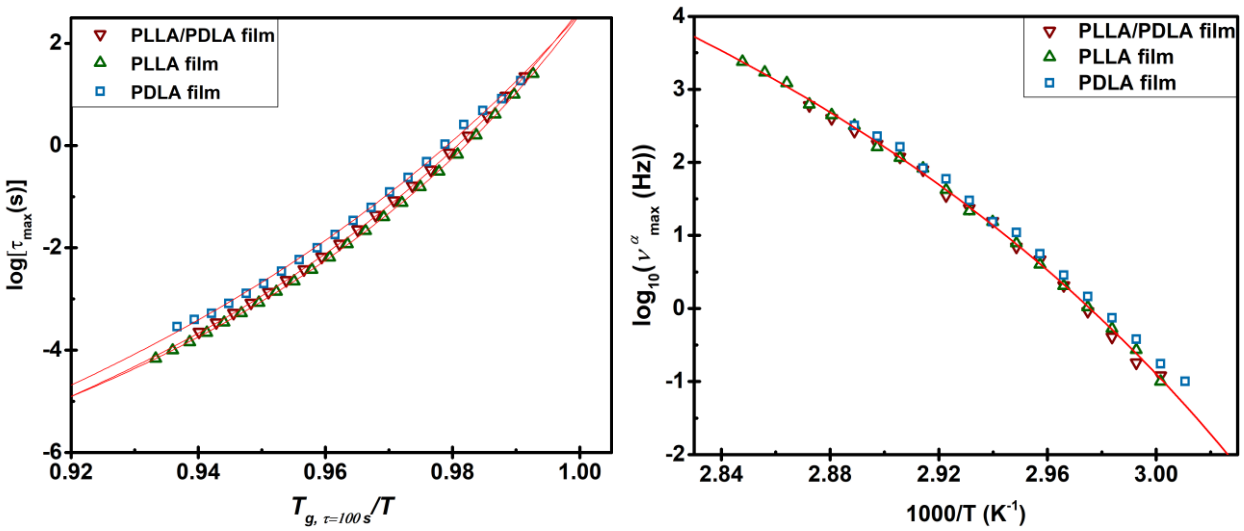

(a) (b)

Figure 4. 14. (a) Relaxation time τ_{max} as a function of normalized temperature $T_{g,\ \tau=100s}/T$ (the Angell's plot), (b) Arrhenius plot of the amorphous PLLA, PDLA and sc PLA films for the α relaxation process.

The temperature dependence of the relaxation time of the α-relaxation can be fitted by a Vogel-Fulcher-Tamman law (VFT) by the following equation:

$$\tau_{max} = \tau_0 exp\left(\frac{DT_0}{T-T_0}\right) \quad (4.14)$$

where τ_{max} is the relaxation time at the maximum of the α relaxation, D is the dimensionless parameter defined as the steepness strength, T_0 is a reference temperature - so called Vogel

temperature, and τ_0 is a pre-exponential factor. The Angell's plots in Fig 4.14 are all practically superimposed. Furthermore, the temperature dependence of the relaxation frequency corresponding to the dielectric α relaxation peak ν_{max}^{α} is superimposed. Such a similarity can be explained by the similar dynamic glass transition temperature as shown in Table 4.2. The dielectric value of the glass transition temperature is usually selected as a temperature at a relaxation time equal to 100 s. The temperatures obtained by DRS at relaxation time equal 10 s match better with the calorimetric glass transition temperatures obtained by MT-DSC with a period of 60 s [44]. In literature, there are several studies of dielectric values of the glass transition temperature showing good deal with the values observed by thermal techniques, such as DSC and MT-DSC [45, 46]. For better fit of relaxation data in the relaxation temperature range, a second VFT law is required to define the temperature dependence of the relaxation time depending on the material [47, 48].

Samples	T_g(τ=100 s) (K)	T_g(τ=10 s) (K)	T_g (K)	*D*	T_0 (K)	log(τ_0) (s)	E_a (kJ mol^{-1})
PLLA	328	331	332	3.5	296	-13	64.4
PDLA	328	330	331	5.7	299	-15	57.3
Sc PLA	329	332	332	4.3	299	-14	64.7
PLA [49]	327	327		5	292	-14	

Table 4. 2. Results obtained by DRS: the glass transition temperature at τ= 100 and 10 s; dimensionless parameter of the VFT equation *D*; reference temperature T_0; the relaxation time extrapolated at an infinite temperature τ_0; the activation energy of the β_1-relaxation E_a. The values of T_g are obtained by MT-DSC measurements.

The temperature dependence of the relaxation time of α-process is investigated by analyzing the derivative method as proposed by Stickel et al. [50]. Stickel et al. presented the VFT description in glassy liquids which is associated with the linearity of Φ_T as a function of *T*:

$$\Phi_T = \left[\left(\frac{dlog_{10}\tau_{max}}{d(1000/T)}\right)\right]^{-1/2} \quad (4.15)$$

Stickel's plot is important key tool to determine the dynamic crossover temperature between two dynamic domains [47, 51]. Fig 4.15 depicts the derivative analysis of the dielectric relaxation time for all the samples. As shown, a single linear fit is sufficient to examine the behavior on the entire temperature range. For quantitative analysis, the VFT parameters *B* (*B*

= $D_T \times T_0$) and the temperature T_0 (Φ_T = 0) were estimated from derivative-based analysis by linear regression as follows [38]:

$$\left[\left(\frac{d\log_{10}1/\tau_{max}}{dT}\right)\right]^{-1/2} = \left(\frac{D_T}{2.303}\right)^{-1/2}(T - T_0) \quad (4.16)$$

The value of T_0 and D_T are determined to be 293 ± 5 K and 4.12 ± 1 (as an average for three samples), respectively, so the parameter B is calculated to be 1207 ± 100 K. The parameters obtained from the Stickel's analysis have good agreement and are similar for all the samples. This result is in good agreement with previous work on neat PLA presented by Rijal et al. [49]. All these parameters correspond to the fragility index values of the glass-forming liquids. By taking into account VFT fits and the derivative-based (Stickel's) analysis, uncertainty for the parameter B can be taken in the range of ± 100, so Stickel's analysis can be also used to export VFT parameter for fragility investigation.

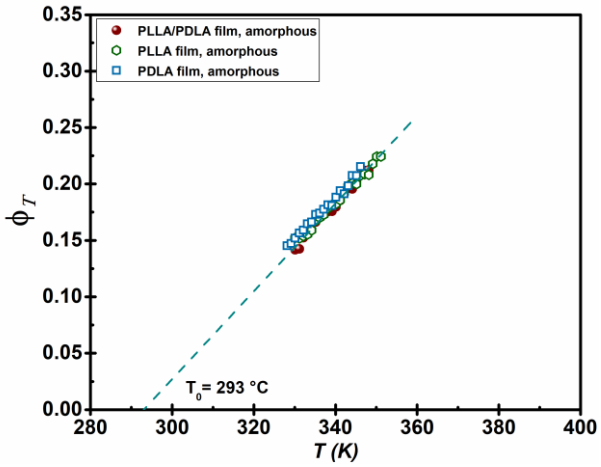

Figure 4. 15. The derivative-based analysis of the temperature evolution of dielectric relaxation data, so called Stickel's plot. Light blue dash line corresponds to the linear fit of the relaxation data. T_0 is the Vogel temperature.

4.3.2 The fragility index *m* by DRS

The next step of analysis for glassy polymers is calculating the fragility index m to extend quantitative comparison. High values of the fragility index m demonstrate "fragile" materials with a non-Arrhenius temperature dependence of the relaxation time τ_α approaches to T_g. The systems called "strong" supercooled liquids represent linear Arrhenius-like

temperature dependence of the relaxation time on the Arrhenius diagram. As defined, for *m* > 30 liquids are considered as "fragile", whereas for *m* < 30 they are defined as "strong". The degree of deviation from Arrhenius-type temperature dependence near T_g allows a classification of glass-formers on the basis of the structural relaxation, so called "fragility concept" by Angell et al. [52, 53] as follows:

$$m = \left. \frac{d\ log(\tau_{max})}{d\left(\frac{T_g}{T}\right)} \right|_{T = T_g} \tag{4.17}$$

where T_g / T is the temperature normalized with respect to the glass transition temperature T_g. All parameters which are necessary to calculate the fragility index are gathered in Table 4.2.

The calculated values of *m* for homopolymers and sc PLA are 146 and 150, respectively. Therefore, such results correspond to "fragile" glass-formers. Such behavior depends on the molecular structure with extended van der Waals interactions and/or hydrogen bonds between polymer chains [52, 54]. In previous works, the fragility index *m* of PLAs was reported as 144 [49], 155 [55], 149 [56]. According to the accuracy of $\pm$ 10 % for the fragility index calculation, we can assume that amorphous sc PLA has practically the same fragility index as neat PLA and homopolymers. Furthermore, the values of the fragility index *m* determined from DRS analysis match well with the values of fragility index *m* calculated from FSC measurements by VFT fitting.

4.3.3 Molecular mobility and dynamic heterogeneity

Previously, Schick et al. [57] combined DRS, MT-DSC and Ac-chip calorimetry in order to study molecular mobility of different polymers, such as polystyrene (PS) and poly(methyl methacrylate) (PMMA). They found that the different experimental techniques show consistent results of cooperativity length obviously correlated with the structural relaxation temperature and time dependence.

4.3.3.1 Method of extraction the parameters for cooperativity size calculation

Typical length scale of cooperativity ranging from 1 to 3.5 nm was provided at the glass transition temperature for different glassy polymers. Besides, the relationship between the cooperativity, the glass transition temperature and the fragility index has been purposed [58]. It is found that the CRR size increases with increasing fragility. Fig 4.16 represents isochronal spectra of the dielectric loss in the frequency range of 2.10^6 Hz down to 0.1 Hz combined with the heat capacity curves from MT-DSC as a function of the temperature for sc PLA (same calculation was applied for all the amorphous samples). The dielectric spectra were plotted by subtracting the contribution of the conductivity and the secondary β relaxation. The observed relaxation peak corresponds to the segmental (α-) relaxation process. The CRR length can be estimated by using the temperature fluctuation of the amorphous phase by Eq 1.20 as Donth proposed [59]. All the quantities used in Donth's approach [59] were determined from DRS and MT-DSC investigation.

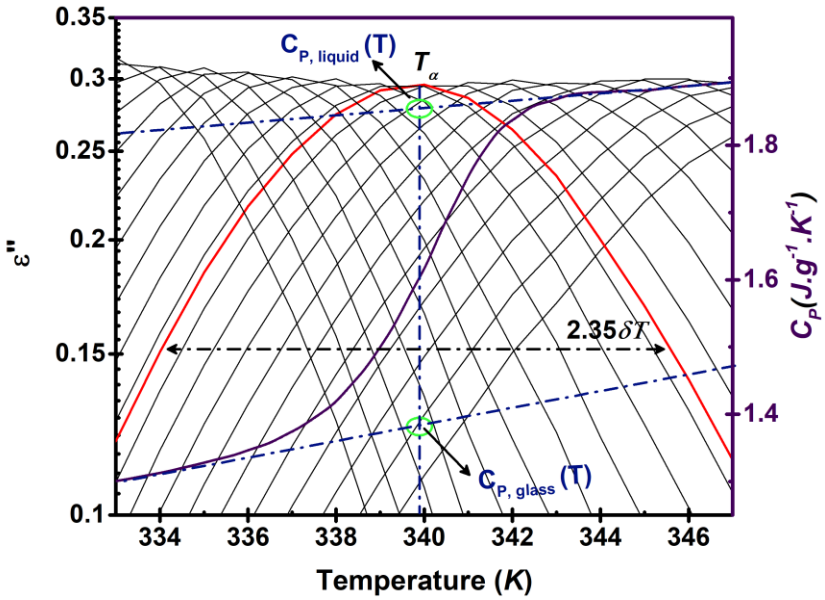

Figure 4. 16. Dielectric loss (without conductivity) from DRS measurements and heat capacity from MT-DSC measurement as a function of temperature. The blue dash lines present the heat capacity in the glassy and liquid states. The red line corresponds to the Gaussian fit of a dielectric loss spectra.

As shown in Fig 4.16, the temperature fluctuation δT (related to the standard deviation σ_T of the Gaussian peak function) is calculated as δT = FWMH / 2.35 and the dynamic glass

transition temperature T_α (corresponds to the maximum of the Gaussian peak) is exported from Gaussian fit of the imaginary part of MT-DSC and DRS spectra by following equation:

$$C''(T) \ or \ \varepsilon''(T) = \frac{A}{\sigma_T\sqrt{(2\pi)}}\exp\left(\frac{T-T_\alpha}{\sigma_T}\right)^2 \quad (4.18)$$

where *A* corresponds to the peak area, σ_T is the standard deviation and T_α is the dynamic glass transition temperature. The value ΔC_P^{-1} is the difference in the inverse of the isobaric heat capacity between the glass and the liquid at T_α and exported from the calorimetric investigation, as shown in Fig 4.16.

Therefore, combination of MT-DSC and DRS allows us to calculate the temperature dependence of the cooperativity length ξ_α (by Eq 1.20) and the cooperativity number of relaxing entities N_α (by Eq 1.21) as well as the number of dynamically correlated units N_C (by Eq 1.15) in a wide temperature and relaxation time range from the onset of cooperativity in the crossover region to the calorimetric glass transition temperature T_g.

4.3.3.2 The cooperativity length ξ_α and cooperativity degree N_α

The cooperativity length ξ_α and the cooperativity degree N_α were estimated in a wide range of temperature and relaxation time for each investigated sample. The cooperativity length ξ_α associated with the α-relaxation as a function of temperature and relaxation time determined from MT-DSC and DRS measurements is presented in Fig 4.17. The results shows that the cooperativity length ξ_α depends on the relaxation time and the glass transition temperature. In addition, the cooperativity degree N_α is presented in Fig 4.18 to investigate the temperature dependence of N_α and compare it with other systems. A non-linear increase of the cooperativity length ξ_α and the cooperativity degree N_α with decreasing temperature and increasing relaxation time is observed for each sample. All studied samples have similar behavior regarding temperature dependence of the cooperativity parameters. In addition, the similarity in the cooperativity length of homopolymers and sc PLA could also be correlated with the results of similar fragility index *m* of samples. It should be noted that the extrapolation of the cooperativity length ξ_α estimated from DRS over a wide range of relaxation time and temperature fits very well with the values estimated by MT-DSC (star

shape symbols) at calorimetric glass transition T_α at $\tau \approx 10$ s as well as the cooperativity number N_α. However, such a non-linear temperature dependence of ξ_α and N_α can be related to the temperature dependence of the relaxation time. The cooperativity length ξ_α at the calorimetric T_g for all the samples is quite similar, i.e. 2.9 ± 0.2 nm for PLLA and sc PLA, and 2.8 ± 0.2 nm for PDLA, independently from the intermolecular interactions obtained through stereocomplexation.

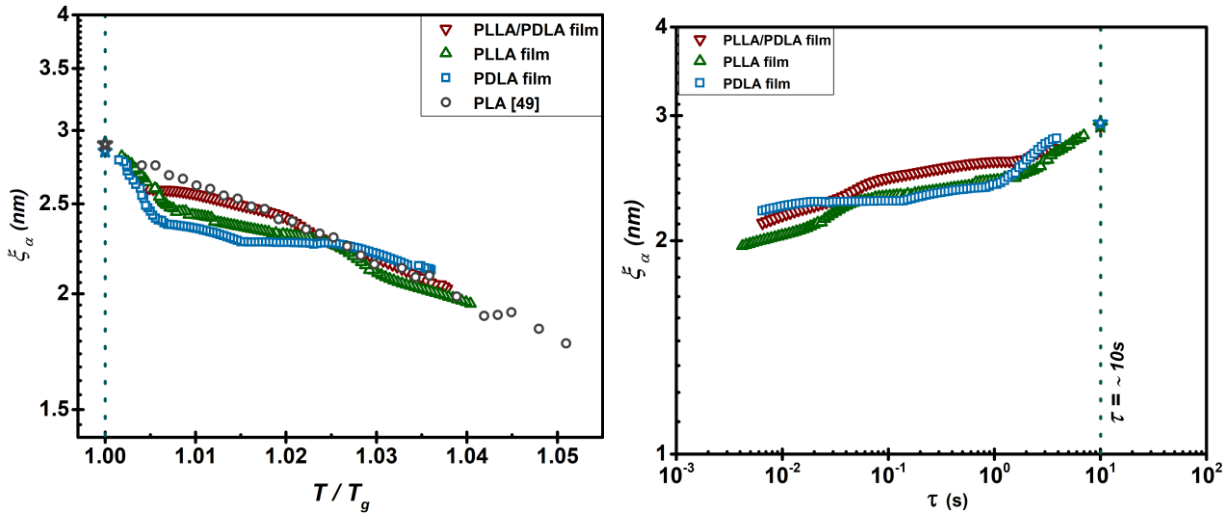

(a) (b)

Figure 4. 17. The cooperativity length ξ_α as a function of (a) normalized temperature at T_g and (b) relaxation time for each sample obtained from DRS measurements by estimated the calorimetric glass transition temperature at period 60 s, $\tau \sim 10$ s. The star shaped symbols at $T / T_g = 1$ correspond to the results derived from MT-DSC analysis at T_α at $\tau \approx 10$ s.

Furthermore, as depicted in Fig 4.17, the values are rather similar to the results obtained by Rijal et al. [49] for commercial PLA. It is interesting to compare the results of our systems with the results of Hamonic et al. [60] obtained for another polyester, PET with different microstructure, i.e. wholly amorphous and isotropic PET, and semi-crystalline PET drawn at two different draw ratio (λ) (Fig 4.18). Hamonic et al. have shown a huge impact of the microstructure on the temperature dependence of the cooperativity.

As a consequence, if the amorphous phase is anisotropic and constraint by crystallites (i.e. highly drawn PET [60]), the CRR size and N_α are drastically smaller. These results reveal that cooperativity could vary a lot in the amorphous part of the polymer, but in the case of amorphous PLA, stereocomplexation has no significant influence.

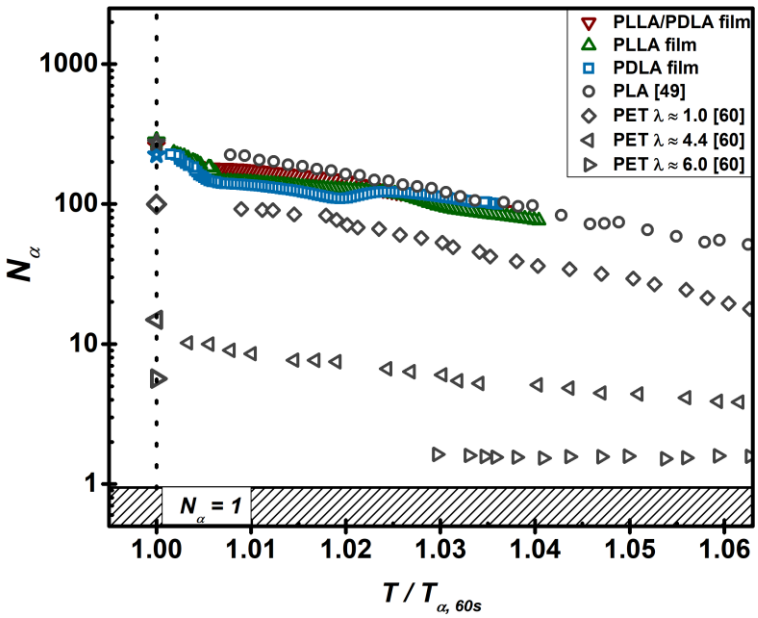

Figure 4. 18. The cooperativity degree N_α as a function of normalized temperature. The star shaped symbols at $T / T_{\alpha, 60\,s} = 1$ correspond to the results obtained from MT-DSC analysis at T_α at $\tau \approx 10$ s.

4.3.3.3 Dynamic heterogeneity and comparison of N_C and N_α

The number of dynamically correlated segments N_C of all the samples is calculated by Eq 1.15 and is depicted in Fig 4.19 as a function of temperature normalized to T_g. The calculated values of N_C for each sample exhibit similar temperature dependence. The slight increase of the number of dynamically correlated segments N_C with decreasing temperature towards the glass transition temperature is observed in Fig 4.19. These results show good relevance with the tendency for all the amorphous samples. Furthermore, the increase of N_C with decreasing temperature is independent from the chemical structure of the glass-forming liquid samples. Therefore, such increase can be explained by two regimes: the first fast regime is observed at short relaxation times and the second one, much slower, is noted for relaxation times towards the glass transition. Thus, the extent of spatial correlation in the molecular dynamics so grows as temperature approaches the glass transition. This result is supported by

several works [49, 61, 62] and can be predicted also by the mode coupling theory [63]. These results support the common evolution of N_C during the relaxation for a large family of glass-forming liquids.

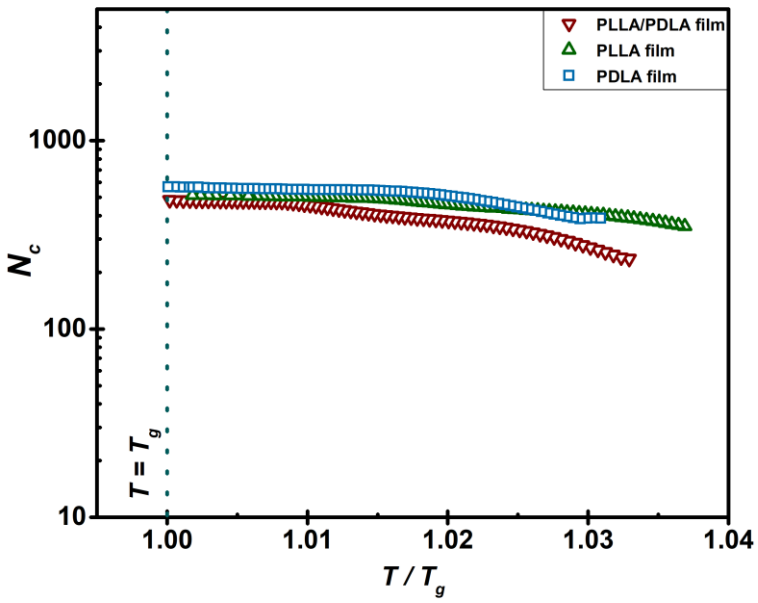

Figure 4. 19. The number of dynamically correlated segments N_C as a function of temperature normalized at T_g for all the samples.

Although the direct comparison of N_C and N_α is insignificant due to the shift in absolute values, similar behavior can be observed for all the samples. The increase of N_α with increasing relaxation time can be also described by a short relaxation time, a single power law and a long relaxation times up to T_g (τ = 100 s), as the variations of N_C. In order to compare more precisely the number of dynamically correlated segments N_C with the cooperativity degree N_α calculated from the Donth's approach, the ratio N_C / N_α is presented in Fig 4.20 as a function of the relaxation time. When close to the T_g (in the range of $\tau_{Tg} \approx$10 s – 100 s), the values of N_C and N_α are rather similar (N_C / N_α ~ 1). However, these values start to deviate with the relaxation time decrease. Therefore, we may suppose that such similarities can be found in the physical definition of N_α and N_C. The number of dynamically correlated segments N_C is calculated based on the 4-point correlation approach, different from the Donth's approach, since it allows us to calculate the number of molecules whose dynamics are correlated depending on the temperature fluctuations. However, with a relaxation time decrease, the

ratio of N_C / N_α slightly increases and remains constant. For these two approaches, the temperature or the relaxation time associated with the value N_C or N_α = 1 corresponds to the limit of the cooperativity, and defines a "cross-over" point in Arrhenius diagram. From the results of N_C and N_α as a function of relaxation time, the "cross-over" point is observed at the relaxation time $\tau \sim 10^{-13}$ s depending on the N_C = 1, but it is at the range of $\tau \sim 10^{-11}$ s according to N_α = 1 for all the samples (as an average of three samples). Results show that N_α decreases faster than N_C with a decreasing relaxation time. According to the relaxation time investigation, the different asymptotic behaviors are observed in these two models. These new and original results of sc PLA compared to the homopolymers indicate that the origin of the cooperative molecular motions for both N_C and N_α of sc PLA is independent from stereocomplexation. Therefore, the different values of the relaxation time and the different definitions between correlated and cooperative motions (especially for very short relaxation times) resulting in the correlated motions appear at a time scale lower than the cooperative motions.

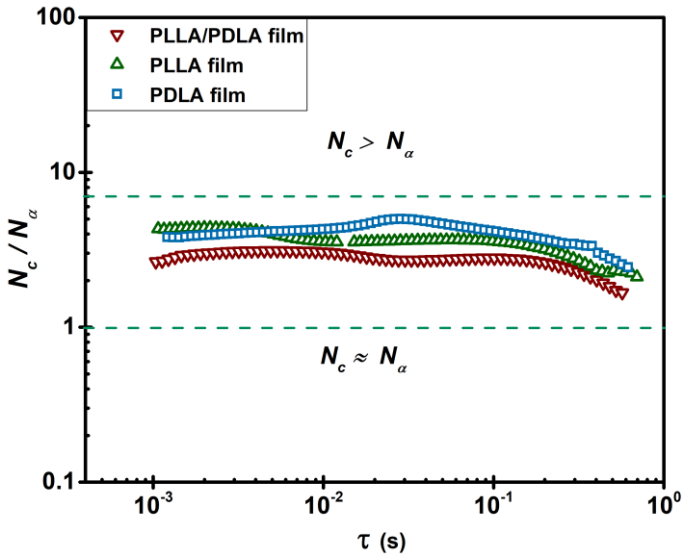

Figure 4. 20. The ratio of N_C / N_α as a function of the relaxation time.

Conclusion

In this chapter, the influence of the tacticity on the molecular dynamic of poly(lactides) has been investigated in terms of the segmental (α-process) relaxation by FSC and DRS measurements. It is found that fictive temperatures and glass transition values determined by different techniques (by FSC, DSC, MT-DSC or DRS) have same values for PLLA, PDLA and sc PLA. The kinetics of enthalpy recovery of amorphous sc PLA and homopolymers (PLLA and PDLA) was investigated by FSC measurements. The results show that the enthalpy recovery has a single step decay towards equilibrium and glasses are allowed to completely relax in the range of aging time. It is found that the relaxation kinetics of the glass towards the enthalpy recovery of the supercooled liquid is independent on the tacticity in the stereocomplex structure.

Furthermore, the structural relaxation investigation was carried out by DRS analysis for wholly amorphous samples. The α- and β-processes of wholly amorphous samples were examined to observe the dielectric properties such as relaxation time, dielectric strength, and fragility. All the samples have the similar dielectric properties independently on the tacticity existence. The cooperativity length ξ_α estimated from Donth's approach for the all samples was studied and found to be very similar at the glass transition (≈ 2.9 nm) and in a wide temperature range. It is shown that the cooperativity length ξ_α has no dependence on the chemical structure, while the cooperativity number N_α has the strong dependence on the microstructure. Moreover, no effect of stereocomplexation on the origin of the cooperative molecular motions is observed. The correlated motions appear at a time scale lower than the cooperative motions for all the samples. It is found that the kinetics of the segmental relaxation of wholly amorphous sc PLA and the amorphous phases of PLAs are the same. In addition, the results of β-process testifies that the local movements of polymer chain are independent from the stereocomplexation impacts on the local interactions in case of amorphous samples, although stereocomplexation led to generate different crystalline phase.

References

1. Moynihan, C. T.; Macedo, P. B.; Montrose, C. J.; Gupta, P. K.; DeBolt, M. A.; Dill, J. F.; Dom, B. E.; Drake, P. W.; Easteal, A. J.; Elterman, P. B.; Moeller, R. P.; Sasabe, H.; Wilder, J. A. Structural relaxation in vitreous materials. *Annals of the New York Academy of Sciences* **1976,** 279 (1), 15-35 DOI: doi:10.1111/j.1749-6632.1976.tb39688.x.
2. Verdonck, E.; Schaap, K.; Thomas, L. C. A discussion of the principles and applications of Modulated Temperature DSC (MTDSC). *International Journal of Pharmaceutics* **1999,** 192 (1), 3-20 DOI: https://doi.org/10.1016/S0378-5173(99)00267-7.
3. Monnier, X.; Saiter, A.; Dargent, E. Physical aging in PLA through standard DSC and fast scanning calorimetry investigations. *Thermochimica Acta* **2017,** 648, 13-22 DOI: https://doi.org/10.1016/j.tca.2016.12.006.
4. Schawe, J. E. K. Measurement of the thermal glass transition of polystyrene in a cooling rate range of more than six decades. *Thermochimica Acta* **2015,** 603, 128-134 DOI: https://doi.org/10.1016/j.tca.2014.05.025.
5. Gao, S.; Simon, S. L. Measurement of the limiting fictive temperature over five decades of cooling and heating rates. *Thermochimica Acta* **2015,** 603, 123-127 DOI: https://doi.org/10.1016/j.tca.2014.08.019.
6. Monnier, X.; Saiter, A.; Dargent, E. Vitrification of PLA by fast scanning calorimetry: Towards unique glass above critical cooling rate? *Thermochimica Acta* **2017,** 658, 47-54 DOI: https://doi.org/10.1016/j.tca.2017.10.019.
7. Dhotel, A.; Rijal, B.; Delbreilh, L.; Dargent, E.; Saiter, A. Combining Flash DSC, DSC and broadband dielectric spectroscopy to determine fragility. *Journal of Thermal Analysis and Calorimetry* **2015,** 121 (1), 453-461 DOI: 10.1007/s10973-015-4650-9.
8. Fulcher, G. S. ANALYSIS OF RECENT MEASUREMENTS OF THE VISCOSITY OF GLASSES. *Journal of the American Ceramic Society* **1925,** 8 (6), 339-355 DOI: doi:10.1111/j.1151-2916.1925.tb16731.x.
9. Schawe, J. E. K. Vitrification in a wide cooling rate range: The relations between cooling rate, relaxation time, transition width, and fragility. *The Journal of Chemical Physics* **2014,** 141 (18), 184905 DOI: 10.1063/1.4900961.
10. Tammann, V. G.; Hesse, W. Die Abhängigkeit der Viscosität von der Temperatur bie unterkühlten Flüssigkeiten. *Zeitschrift für anorganische und allgemeine Chemie* **1926,** 156 (1), 245-257 DOI: doi:10.1002/zaac.19261560121.
11. Hodge, I. M. Enthalpy relaxation and recovery in amorphous materials. *Journal of Non-Crystalline Solids* **1994,** 169 (3), 211-266 DOI: https://doi.org/10.1016/0022-3093(94)90321-2.
12. Dobircau, L.; Delpouve, N.; Herbinet, R.; Domenek, S.; Pluart, L.; Laurent, D.; Ducruet, V.; Dargent, E. Molecular mobility and physical ageing of plasticized poly(lactide). *Polymer Engineering & Science* **2015,** 55 (4), 858-865 DOI: doi:10.1002/pen.23952.
13. Pan, P.; Zhu, B.; Inoue, Y. Enthalpy Relaxation and Embrittlement of Poly(l-lactide) during Physical Aging. *Macromolecules* **2007,** 40 (26), 9664-9671 DOI: 10.1021/ma071737c.
14. Celli, A.; Scandola, M. Thermal properties and physical ageing of poly (l-lactic acid). *Polymer* **1992,** 33 (13), 2699-2703 DOI: https://doi.org/10.1016/0032-3861(92)90440-8.
15. Hutchinson, J. M. Physical aging of polymers. *Progress in Polymer Science* **1995,** 20 (4), 703-760 DOI: https://doi.org/10.1016/0079-6700(94)00001-I.
16. Koh, Y. P.; Grassia, L.; Simon, S. L. Structural recovery of a single polystyrene thin film using nanocalorimetry to extend the aging time and temperature range. *Thermochimica Acta* **2015,** 603, 135-141 DOI: https://doi.org/10.1016/j.tca.2014.08.025.
17. Koh, Y. P.; Gao, S.; Simon, S. L. Structural recovery of a single polystyrene thin film using Flash DSC at low aging temperatures. *Polymer* **2016,** 96, 182-187 DOI: https://doi.org/10.1016/j.polymer.2016.04.047.

18. Boucher, V. M.; Cangialosi, D.; Alegría, A.; Colmenero, J. Complex nonequilibrium dynamics of stacked polystyrene films deep in the glassy state. *The Journal of Chemical Physics* **2017,** 146 (20), 203312 DOI: 10.1063/1.4977207.
19. Gomez Ribelles, J. L.; Monleon Pradas, M. Structural Relaxation of Glass-Forming Polymers Based on an Equation for Configurational Entropy. 1. DSC Experiments on Polycarbonate. *Macromolecules* **1995,** 28 (17), 5867-5877 DOI: 10.1021/ma00121a025.
20. Salmerón Sánchez, M.; Touzé, Y.; Saiter, A.; Saiter, J. M.; Gómez Ribelles, J. L. Influence of the chemical structure on the kinetics of the structural relaxation process of acrylate and methacrylate polymer networks. *Colloid and Polymer Science* **2005,** 283 (7), 711-720 DOI: 10.1007/s00396-004-1207-z.
21. Hutchinson, J. M.; Montserrat, S.; Calventus, Y.; Cortés, P. Application of the Adam–Gibbs Equation to the Non-Equilibrium Glassy State. *Macromolecules* **2000,** 33 (14), 5252-5262 DOI: 10.1021/ma992015r.
22. Andreozzi, L.; Faetti, M.; Zulli, F.; Giordano, M. Connecting Shear Stress Relaxation and Enthalpy Recovery in Polymers through a Modified TNM Approach. *Macromolecules* **2004,** 37 (21), 8010-8016 DOI: 10.1021/ma049334p.
23. NARAYANASWAMY, O. S. A Model of Structural Relaxation in Glass. *Journal of the American Ceramic Society* **1971,** 54 (10), 491-498 DOI: doi:10.1111/j.1151-2916.1971.tb12186.x.
24. Williams, G.; Watts, D. C. Non-symmetrical dielectric relaxation behaviour arising from a simple empirical decay function. *Transactions of the Faraday Society* **1970,** 66 (0), 80-85 DOI: 10.1039/TF9706600080.
25. Havriliak, S.; Negami, S. A complex plane representation of dielectric and mechanical relaxation processes in some polymers. *Polymer* **1967,** 8, 161-210 DOI: https://doi.org/10.1016/0032-3861(67)90021-3.
26. Sperling, L. H., *Introduction to Physical Poymer Science*. John Wiley & Sonc, Inc.: 2005; p 687-756.
27. Iwao, O.; Bernhard, W. Reversible local melting in polymer crystals. *Macromolecular Rapid Communications* **1997,** 18 (4), 313-318 DOI: doi:10.1002/marc.1997.030180407.
28. Starkweather, H. W.; Avakian, P.; Fontanella, J. J.; Wintersgill, M. C. Internal motions in polylactide and related polymers. *Macromolecules* **1993,** 26 (19), 5084-5087 DOI: 10.1021/ma00071a016.
29. Crétois, R.; Delbreilh, L.; Dargent, E.; Follain, N.; Lebrun, L.; Saiter, J. M. Dielectric relaxations in polyhydroxyalkanoates/organoclay nanocomposites. *European Polymer Journal* **2013,** 49 (11), 3434-3444 DOI: https://doi.org/10.1016/j.eurpolymj.2013.07.009.
30. Soccio, M.; Martínez-Tong, D. E.; Alegría, A.; Munari, A.; Lotti, N. Molecular dynamics of fully biobased poly(butylene 2,5-furanoate) as revealed by broadband dielectric spectroscopy. *Polymer* **2017,** 128, 24-30 DOI: https://doi.org/10.1016/j.polymer.2017.09.007.
31. Kremer F, S. A., *Broadband dielectric spectroscopy*. New York: Springer, 2003.
32. Bello, A.; Laredo, E.; Grimau, M.; Nogales, A.; Ezquerra, T. A. Relaxation time distribution from time and frequency domain dielectric spectroscopy in poly(aryl ether ether ketone). *The Journal of Chemical Physics* **2000,** 113 (2), 863-868 DOI: 10.1063/1.481862.
33. Dhotel, A.; Chen, Z.; Sun, J.; Youssef, B.; Saiter, J.-M.; Schönhals, A.; Tan, L.; Delbreilh, L. From monomers to self-assembled monolayers: the evolution of molecular mobility with structural confinements. *Soft Matter* **2015,** 11 (4), 719-731 DOI: 10.1039/C4SM01893A.
34. Johari, G. P.; Goldstein, M. Viscous Liquids and the Glass Transition. II. Secondary Relaxations in Glasses of Rigid Molecules. *The Journal of Chemical Physics* **1970,** 53 (6), 2372-2388 DOI: 10.1063/1.1674335.
35. Kessairi, K.; Capaccioli, S.; Prevosto, D.; Lucchesi, M.; Sharifi, S.; Rolla, P. A. Interdependence of Primary and Johari−Goldstein Secondary Relaxations in Glass-Forming Systems. *The Journal of Physical Chemistry B* **2008,** 112 (15), 4470-4473 DOI: 10.1021/jp800764w.

36. Hachenberg, J.; Bedorf, D.; Samwer, K.; Richert, R.; Kahl, A.; Demetriou, M. D.; Johnson, W. L. Merging of the α and β relaxations and aging via the Johari–Goldstein modes in rapidly quenched metallic glasses. *Applied Physics Letters* **2008,** 92 (13), 131911 DOI: 10.1063/1.2903697.
37. Mano, J. F.; Gómez Ribelles, J. L.; Alves, N. M.; Salmerón Sanchez, M. Glass transition dynamics and structural relaxation of PLLA studied by DSC: Influence of crystallinity. *Polymer* **2005,** 46 (19), 8258-8265 DOI: https://doi.org/10.1016/j.polymer.2005.06.096.
38. Yin, H.; Napolitano, S.; Schönhals, A. Molecular Mobility and Glass Transition of Thin Films of Poly(bisphenol A carbonate). *Macromolecules* **2012,** 45 (3), 1652-1662 DOI: 10.1021/ma202127p.
39. Rotella, C.; Napolitano, S.; De Cremer, L.; Koeckelberghs, G.; Wübbenhorst, M. Distribution of Segmental Mobility in Ultrathin Polymer Films. *Macromolecules* **2010,** 43 (20), 8686-8691 DOI: 10.1021/ma101695y.
40. Pluta, M.; Jeszka, J. K.; Boiteux, G. Polylactide/montmorillonite nanocomposites: Structure, dielectric, viscoelastic and thermal properties. *European Polymer Journal* **2007,** 43 (7), 2819-2835 DOI: https://doi.org/10.1016/j.eurpolymj.2007.04.009.
41. Schönhals, A. Evidence for a universal crossover behaviour of the dynamic glass transition. *EPL (Europhysics Letters)* **2001,** 56 (6), 815.
42. Mackintosh, A. R.; Liggat, J. J. Dynamic mechanical analysis of poly(trimethylene terephthalate)—A comparison with poly(ethylene terephthalate) and poly(ethylene naphthalate). *Journal of Applied Polymer Science* **2004,** 92 (5), 2791-2796 DOI: doi:10.1002/app.20290.
43. Saiter, A.; Prevosto, D.; Passaglia, E.; Couderc, H.; Delbreilh, L.; Saiter, J. M. Cooperativity length scale in nanocomposites: Interfacial and confinement effects. *Physical Review E* **2013,** 88 (4), 042605 DOI: 10.1103/PhysRevE.88.042605.
44. Saiter, J. M.; Grenet, J.; Dargent, E.; Saiter, A.; Delbreilh, L. Glass Transition Temperature and Value of the Relaxation Time at Tg in Vitreous Polymers. *Macromolecular Symposia* **2007,** 258 (1), 152-161 DOI: doi:10.1002/masy.200751217.
45. Puente, J. A. S.; Rijal, B.; Delbreilh, L.; Fatyeyeva, K.; Saiter, A.; Dargent, E. Segmental mobility and glass transition of poly(ethylene-vinyl acetate) copolymers: Is there a continuum in the dynamic glass transitions from PVAc to PE? *Polymer* **2015,** 76, 213-219 DOI: https://doi.org/10.1016/j.polymer.2015.09.007.
46. Leonardi, A.; Dantras, E.; Dandurand, J.; Lacabanne, C. Dielectric relaxations in PEEK by combined dynamic dielectric spectroscopy and thermally stimulated current. *Journal of Thermal Analysis and Calorimetry* **2013,** 111 (1), 807-814 DOI: 10.1007/s10973-012-2548-3.
47. Martinez-Garcia, J. C.; Martinez-Garcia, J.; Rzoska, S. J.; Hulliger, J. The new insight into dynamic crossover in glass forming liquids from the apparent enthalpy analysis. *The Journal of Chemical Physics* **2012,** 137 (6), 064501 DOI: 10.1063/1.4739750.
48. Novikov, V. N.; Sokolov, A. P. Universality of the dynamic crossover in glass-forming liquids: A ``magic'' relaxation time. *Physical Review E* **2003,** 67 (3), 031507 DOI: 10.1103/PhysRevE.67.031507.
49. Rijal, B.; Delbreilh, L.; Saiter, A. Dynamic Heterogeneity and Cooperative Length Scale at Dynamic Glass Transition in Glass Forming Liquids. *Macromolecules* **2015,** 48 (22), 8219-8231 DOI: 10.1021/acs.macromol.5b01152.
50. Stickel, F.; Fischer, E. W.; Richert, R. Dynamics of glass-forming liquids. I. Temperature-derivative analysis of dielectric relaxation data. *The Journal of Chemical Physics* **1995,** 102 (15), 6251-6257 DOI: 10.1063/1.469071.
51. Casalini, R.; Roland, C. M. Viscosity at the Dynamic Crossover in o-Terphenyl and Salol under High Pressure. *Physical Review Letters* **2004,** 92 (24), 245702 DOI: 10.1103/PhysRevLett.92.245702.
52. Angell, C. A. Spectroscopy simulation and scattering, and the medium range order problem in glass. *Journal of Non-Crystalline Solids* **1985,** 73 (1), 1-17 DOI: https://doi.org/10.1016/0022-3093(85)90334-5.
53. Angell, C. A. Formation of Glasses from Liquids and Biopolymers. *Science* **1995,** 267 (5206), 1924-1935 DOI: 10.1126/science.267.5206.1924.

54. Bouthegourd, E.; Esposito, A.; Lourdin, D.; Saiter, A.; Saiter, J. M. Size of the cooperative rearranging regions vs. fragility in complex glassy systems: Influence of the structure and the molecular interactions. *Physica B: Condensed Matter* **2013,** 425, 83-89 DOI: https://doi.org/10.1016/j.physb.2013.05.029.

55. Delpouve, N.; Delbreilh, L.; Stoclet, G.; Saiter, A.; Dargent, E. Structural Dependence of the Molecular Mobility in the Amorphous Fractions of Polylactide. *Macromolecules* **2014,** 47 (15), 5186-5197 DOI: 10.1021/ma500839p.

56. Zuza, E.; Ugartemendia, J. M.; Lopez, A.; Meaurio, E.; Lejardi, A.; Sarasua, J.-R. Glass transition behavior and dynamic fragility in polylactides containing mobile and rigid amorphous fractions. *Polymer* **2008,** 49 (20), 4427-4432 DOI: https://doi.org/10.1016/j.polymer.2008.08.012.

57. Chua, Y.; Schulz, G.; Shoifet, E.; Huth, H.; Zorn, R.; Scmelzer, J. P.; Schick, C., *Glass transition cooperativity from broad band heat capacity spectroscopy*. 2014; Vol. 292, p 1-12.

58. Sasaki, T.; Ichimura, M.; Irie, S. Correlation between fragility and cooperativity in segmental dynamics of glass-forming para-substituted polystyrenes. *Polymer Journal* **2015,** 47, 687 DOI: 10.1038/pj.2015.50.

59. Donth, E. The size of cooperatively rearranging regions at the glass transition. *Journal of Non-Crystalline Solids* **1982,** 53 (3), 325-330 DOI: https://doi.org/10.1016/0022-3093(82)90089-8.

60. Hamonic, F.; Prevosto, D.; Dargent, E.; Saiter, A. Contribution of chain alignment and crystallization in the evolution of cooperativity in drawn polymers. *Polymer* **2014,** 55 (12), 2882-2889 DOI: https://doi.org/10.1016/j.polymer.2014.04.030.

61. Dalle-Ferrier, C.; Thibierge, C.; Alba-Simionesco, C.; Berthier, L.; Biroli, G.; Bouchaud, J. P.; Ladieu, F.; L'Hôte, D.; Tarjus, G. Spatial correlations in the dynamics of glassforming liquids: Experimental determination of their temperature dependence. *Physical Review E* **2007,** 76 (4), 041510 DOI: 10.1103/PhysRevE.76.041510.

62. Capaccioli, S.; Ruocco, G.; Zamponi, F. Dynamically Correlated Regions and Configurational Entropy in Supercooled Liquids. *The Journal of Physical Chemistry B* **2008,** 112 (34), 10652-10658 DOI: 10.1021/jp802097u.

63. Götze, W., *Complex Dynamics of Glass-Forming Liquids: A Mode-Coupling Theory*. OUP Oxford: 2008.

CHAPTER 5. MICROSTRUCTURE INFLUENCE ON MECHANICAL AND BARRIER PROPERTIES OF STEREOCOMPLEX PLA

The influence of the stereocomplexation on the barrier properties of PLA-based materials towards water and gases (N_2, O_2 and CO_2) is discussed in the present chapter. Special attention is paid on the water permeability as a function of temperature. Transport properties towards water were investigated for both the amorphous and semicrystalline samples. In addition, gas permeation measurements were carried out to investigate the barrier properties of semicrystalline samples. The transport properties were correlated with the microstructure investigations.

5.1 Microstructure investigations

DSC and XRD measurements were carried out to study the microstructure of the crystalline phases of polymer films. As depicted in Fig 5.1, the sc PLA crystal has higher melting temperature (about 50 °C) than α crystals.

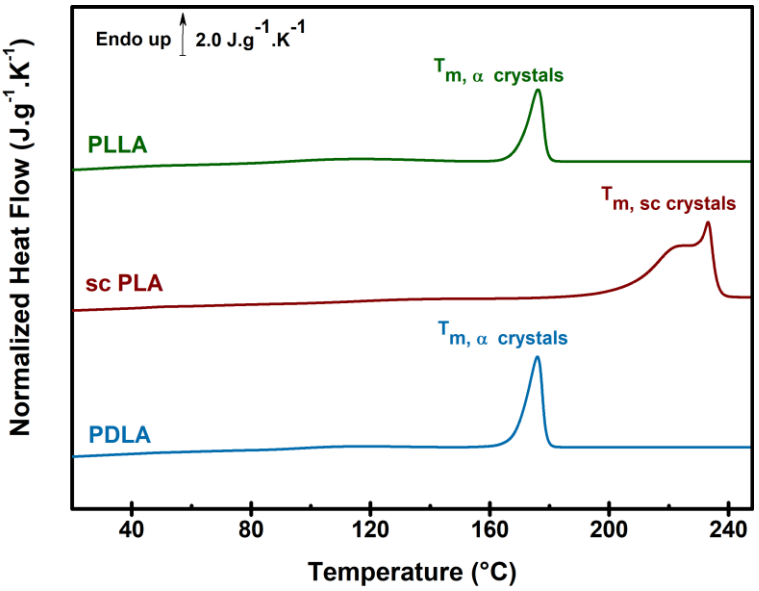

Figure 5. 1. Normalized heat flow curves of PLLA, PDLA, and sc PLA films.

The values of thermal characteristics (i.e. glass transition temperature T_g, heat capacity step ΔC_p, crystallinity degree X_c) calculated from DSC measurements are presented in Table 5.1 for homopolymers and sc PLA. The T_g values of semicrystalline PLAs are higher than those of amorphous PLAs due to the strong coupling between the phases caused by the low crystallization temperature (Table 5.1) (it is also discussed previously in Chap. 3 (Fig 3.23)). The X_c value of sc PLA is slightly higher than that of homopolymers. Also, semicrystalline sc PLA has smaller heat capacity step which is closed to the limit of detection as compared to homopolymers. Therefore, we observed broad glass transition range. The crystalline structure was also confirmed by XRD analysis as presented in Fig 5.2. The presence of only one crystalline phase was revealed by the reflection peaks at 2θ = 19° and 22° for α crystals and 2θ = 14°, 24° and 28° for sc crystals.

Samples	T_g (°C)		ΔC_p (J.g^{-1}.K^{-1})		3-phases of semicrystalline samples		
	amorphous	semicrystalline	amorphous	semicrystalline	X_c (%)	X_{MAP} (%)	X_{RAF} (%)
PLLA	59	75	0.46	0.16	48	35	17
PDLA	61	76	0.46	0.19	48	41	11
Sc PLA	59	69	0.54	0.12	54	22	24

Table 5. 1. Thermal properties of studied amorphous and semicrystalline samples.

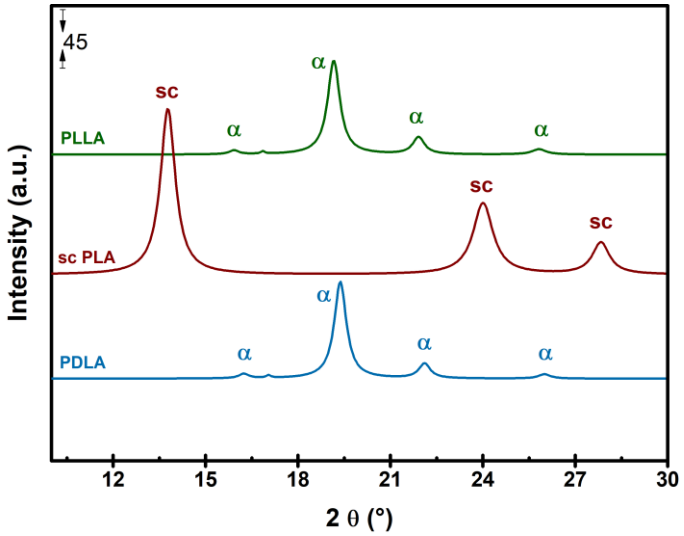

Figure 5. 2. XRD spectra of PLLA, PDLA and sc PLA films.

In addition, surface morphology of PLLA, PDLA and sc PLA films was examined by SEM (Fig 5.3). As one can see from Fig 5.3, homopolymers films are characterized by a granular structure (Fig 5.3a and b) while sc PLA film has a smooth compact structure (Fig 5.3c). Besides, no porosity is observed for all film samples. Such difference in surface morphology can be caused by the formation of the different crystallites types (i.e. pseudoorthorhombic which contains 10_3 helices for homo-crystals and triclinic in which *L*- and *D*-lactide are packed as parallel taking 3_1 helical conformation for sc crystals [1]) during the crystallization through solvent evaporation.

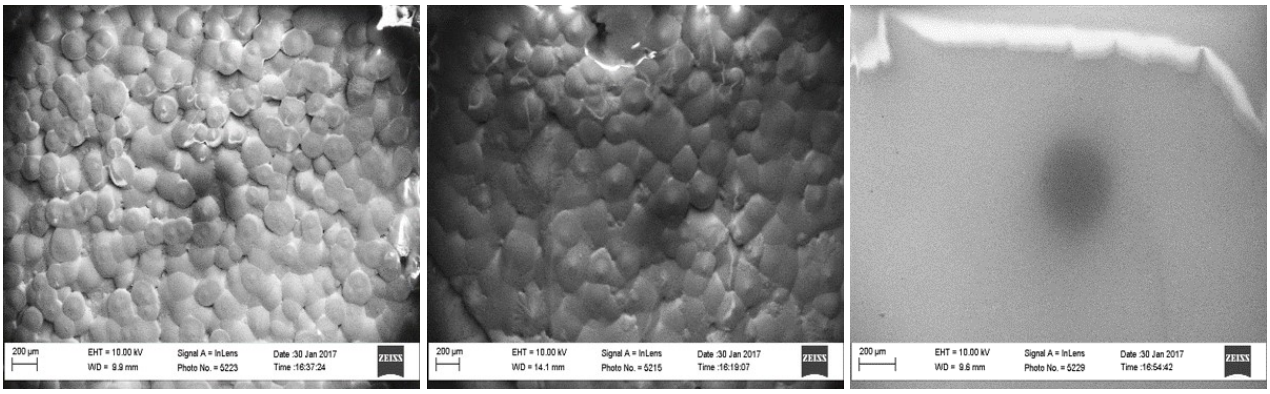

(a) (b) (c)

Figure 5. 3. SEM images of (a) PLLA, (b) PDLA, and (c) sc PLA film.

5.2 Barrier Properties

Several works can be already found in the literature dealing with the improvement of the barrier properties of PLA-based membrane in order to fulfill the industrial packaging requirements. Tenn et al. [2] found that the incorporation of nanoparticles (Cloisite 30B (C30B)) in the PLA matrix decreased the water permeability with the increase of the nanoclay content. It is also shown that the transport properties depend strongly on the dispersion state of the nanoclay platelets and their orientation in the PLA matrix. Tenn et al. [3] also found that despite the fact that the surface modification of PLA films by hydrophobic plasma treatments improved the water barrier properties, no influence was observed on the transport properties towards oxygen. Besides the nanocharges [4-6], the transport properties can be improved by modifying the morphology of the polymer films [7-10]. For example, Messin et al. [11] revealed that the use of semicrystalline poly(butylene succinate-*co*-butylene adipate (PBSA) polymer improved the barrier properties of PLA in the case of multilayer PLA/PBSA film. In addition, Delpouve et al. [12] confirmed that the presence of α' crystals had no influence on the PLA water permeability, but the drawing processes allowed improving the PLA barrier properties due to the crystals shape and increase in crystallinity degree. Therefore, it was shown that the crystalline and amorphous phase organizations are the main parameter of the barrier properties improvement in the case of PLA [12]. Furthermore, Bai et al. [13] reported

that the shape of crystals had influence on the barrier properties. The oxygen barrier performance of PLA was improved through constructing parallel-aligned shish-kebab-like crystals with well-interlocked boundaries.

In our work, the transport properties of PLA-based materials obtained by stereocomplexation are investigated and compared to those of homopolymers. The permeation measurements for homopolymers (PLLA, PDLA) and sc PLA are performed towards water and gases (N_2, O_2 and CO_2) and are correlated with the molecular mobility study (i.e. the CRR volume and size).

5.2.1 Water barrier properties

The water permeation measurements were carried out at controlled temperature 25 °C, 45 °C and 65 °C by using a home-made apparatus (as detailed in chapter 2). The water permeation flux *J* was recorded at the dry interface of the investigated sample. To annihilate the influence of the film thickness, the water permeation kinetics curves were analyzed by using the reduced scale $JL = f\ (t/L^2)$. Each permeation curve may be divided into three parts [14]. At the beginning of the measurement no water flux is determined, i.e. $JL = 0$. Then, after a while, water molecules start to pass through the film and the strong increase of the water flux is observed. Such increase corresponds to the transient step, from which the diffusion coefficient *D* can be estimated. After transient step, the steady state (stationary state, during which the water flux remains constant J_{stat}) is reached and the permeability coefficient *P* can be calculated as the amplitude of the curve. Therefore, the reduced water permeation flux was plotted as a function of the reduced time, and the values of the water permeability coefficient *P* were determined from the flux at stationary state J_{stat} by using the following equation:

$$P = \frac{J_{stat}L}{\Delta a} \tag{5.1}$$

where *L* is the thickness of the film sample and Δa is the activity difference between the two faces of the sample, $\Delta a = 1$ in case of liquid water, i.e. liquid water on the upstream and dry

gas on the downstream face of the film. The permeability coefficient *P* is usually expressed in Barrer units as:

$$1\ Barrer = \ 10^{-10}\ \frac{cm^3\ (STP)cm}{cm^2\ s\ cmHg} \tag{5.2}$$

The materials often used such as epoxy resins or polyesters, may suffer from plasticization, local strain and chemical modifications/degradations over a long period of time [15]. In order to examine the possible plasticization effect induced by the water molecules in the studied samples, the dimensionless curve $j = f(\tau)$ calculated from Fick's equations was defined by Follain et al [16], where $j = \frac{J}{J_{stat}}$, $\tau = \frac{D.t}{L^2}$ and *D* is the diffusion coefficient assumed as a constant value. The diffusion coefficient *D* was calculated from the transient regime of the water permeation flux according to the Fickian behavior. The two distinct diffusion coefficient noted as $D_{0.24}$ and $D_{0.62}$ can be distinguished:

$$D_{0.24} = \ \frac{L^2 \times 0.091}{t_{0.24}} \tag{5.3}$$

and

$$D_{0.62} = \ \frac{L^2}{t_{0.62}} \tag{5.4}$$

$D_{0.24}$ and $D_{0.62}$ were calculated at two different times of the permeation process (assumed as t_I and t_L) that corresponds to the inflection point I (j_I = 0.24, τ = 0.091) and to the time-lag point *L* (j_L = 0.62, τ = 1/6) of the theoretical flux curve, respectively, as detailed in Fig 5.4 [17].

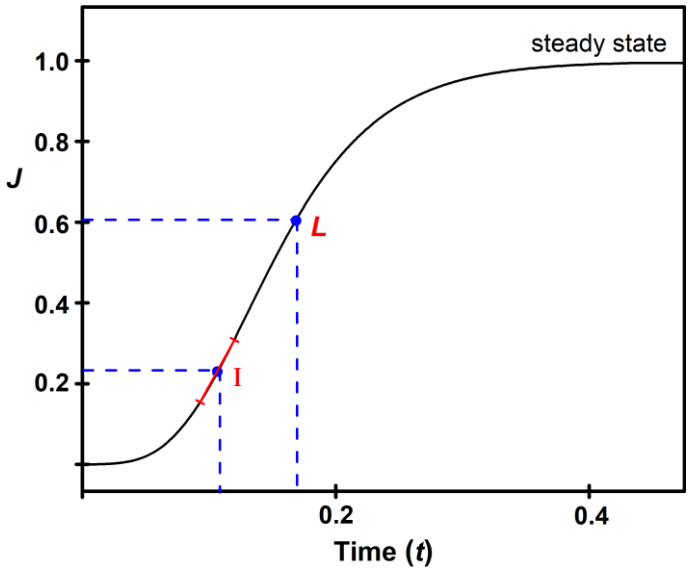

Figure 5. 4. Representation of the flux (*J*) as a function of time (*t*) to determine the *P* and *D* coefficient.

The plasticization effect induced by water molecules maybe described by an exponential dependence of diffusion coefficient with water concentration by:

$$D = D_0 e^{\gamma . C} \tag{5.5}$$

where D_0 is the diffusion coefficient when the water concentration tends to 0, γ is the plasticization factor and *C* is the local permeant concentration in the membrane. Therefore, the maximum diffusion coefficient D_M can be determined as follows [15]:

$$D_M = D_0 e^{\gamma\, C_{eq}} \tag{5.6}$$

where C_{eq} is the water concentration within the studied sample at the stationary state. Therefore, the mean integral diffusion coefficient <*D*> can be calculated as follows:

$$< D > = \frac{1}{\Delta C} \int_{C_1}^{C_2} D\,(C).dC \tag{5.7}$$

5.2.1.1 Water permeability of amorphous samples

The water permeation tests of amorphous samples towards water were carried out at 25°C to examine the stereocomplexation impact on the barrier properties. The water permeation coefficient was calculated from the $J^*L = f(t/L^2)$ curves (Fig 5.5a) and the values are presented in Fig 5.5b. Sc PLA reveals lower value of *P* as compared to homopolymers.

Therefore, one can say that stereocomplexation improves the water barrier properties due to the intermolecular stereoselective interactions; although, the glass transition properties (T_g, CRR volume and size) and molecular dynamics of amorphous samples are the same (presented in Chap. 4). As seen in Fig 5.5a and c, an increase in the delay time in diffusion on the normalized curve of flux for sc PLA is observed compared to the homopolymers. The calculated values of D_0 (C=0) and D_M (C=C_{eq}) are shown in Table 5.2. As one can see, the increase of the D values with the water concentration and the plasticizing factor $\gamma > 0$ confirm the existence of plasticizing effect. According to the values of water concentration (C_{eq}) at steady state, sc PLA films are characterized by lower value of C_{eq} compared to homopolymers. It can be also noted the higher affinity between water molecules and homopolymers was revealed. This affinity can be at the origin of the differences in barrier properties of the studied samples taking into account that intermolecular stereoselective interactions limit the water concentration in the film in case of sc PLA.

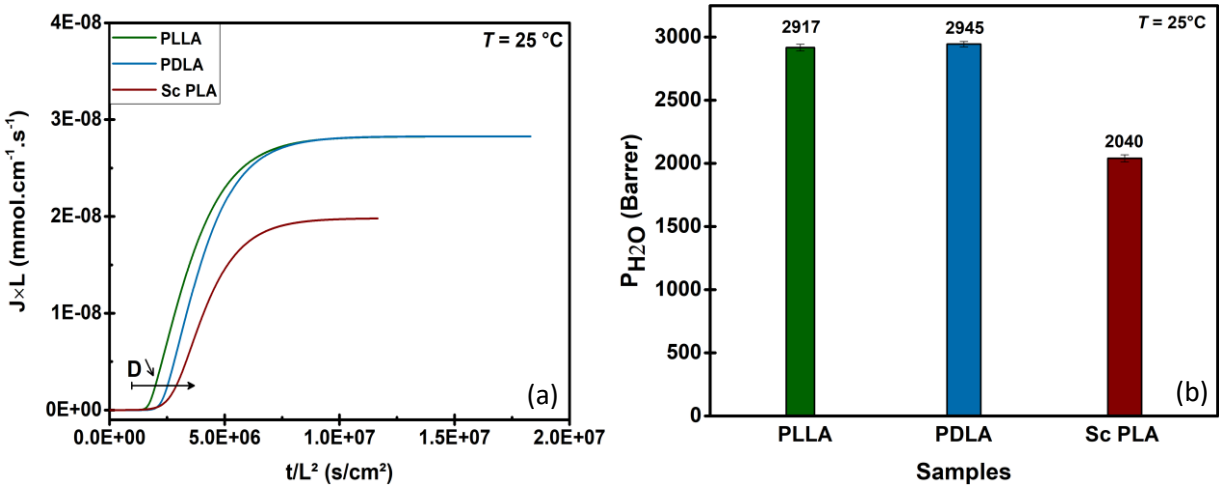

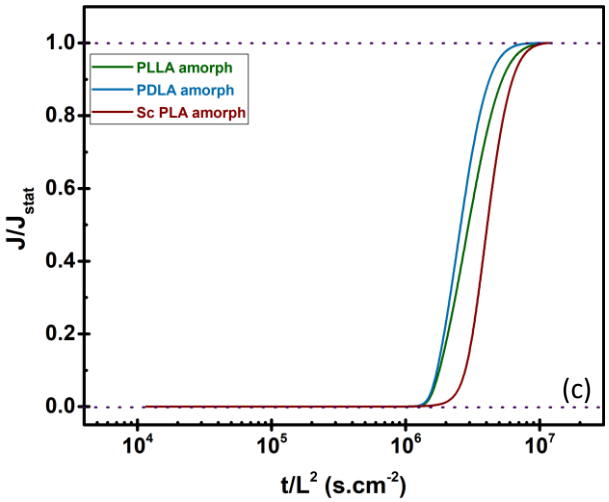

Figure 5. 5. (a) Evolution of the reduced flux of water permeation (*J*L*) as a function of reduced time (t^*L^2), (b) water permeability coefficient *P* and (c) normalized water permeation curves as a function of the reduced time for amorphous PLLA, PDLA and sc PLA.

Samples	P (Barrer)	$D_0 . 10^8$ ($cm^2.s^{-1}$)	$D_M . 10^8$ ($cm^2.s^{-1}$)	γC_{eq}	γ ($cm^3.mmol^{-1}$)	C_{eq} ($mmol.cm^{-3}$)
PLLA	2917 ±26	2.4 ± 0.3	14.6 ± 2.7	1.8 ± 0.2	4.3 ± 0.1	0.42 ± 0.03
PDLA	2945 ± 21	1.6 ± 0.4	18.0 ± 2.9	2.4 ± 0.1	5.8 ± 0.4	0.42 ± 0.04
Sc PLA	2040 ± 28	1.3 ± 0.1	18.7 ± 2.7	2.7 ± 0.2	8.8 ± 1.8	0.30 ± 0.05

Table 5. 2. Water permeametric coefficients of amorphous PLLA, PDLA and sc PLA at 25 ± 1°C.

5.3.1.2 Water permeability of semicrystalline samples

The water barrier properties of semicrystalline samples were studied at temperature of 25 °C, 45 °C and 65 °C. The results are presented for each measurements' temperature separately. According to the obtained results, the permeation flux through the sc PLA film is lower than that in the case of two homopolymers whatever the studied temperature. Such results obviously demonstrate an improvement of the barrier properties of PLA by the stereocomplexation and/or crystallization. Besides, it should be noted that while the permeability coefficient of sc PLA increases with *T*, the permeability of homopolymers decreases by increasing the temperature.

- **$T_{permeation}$ = 25°C**

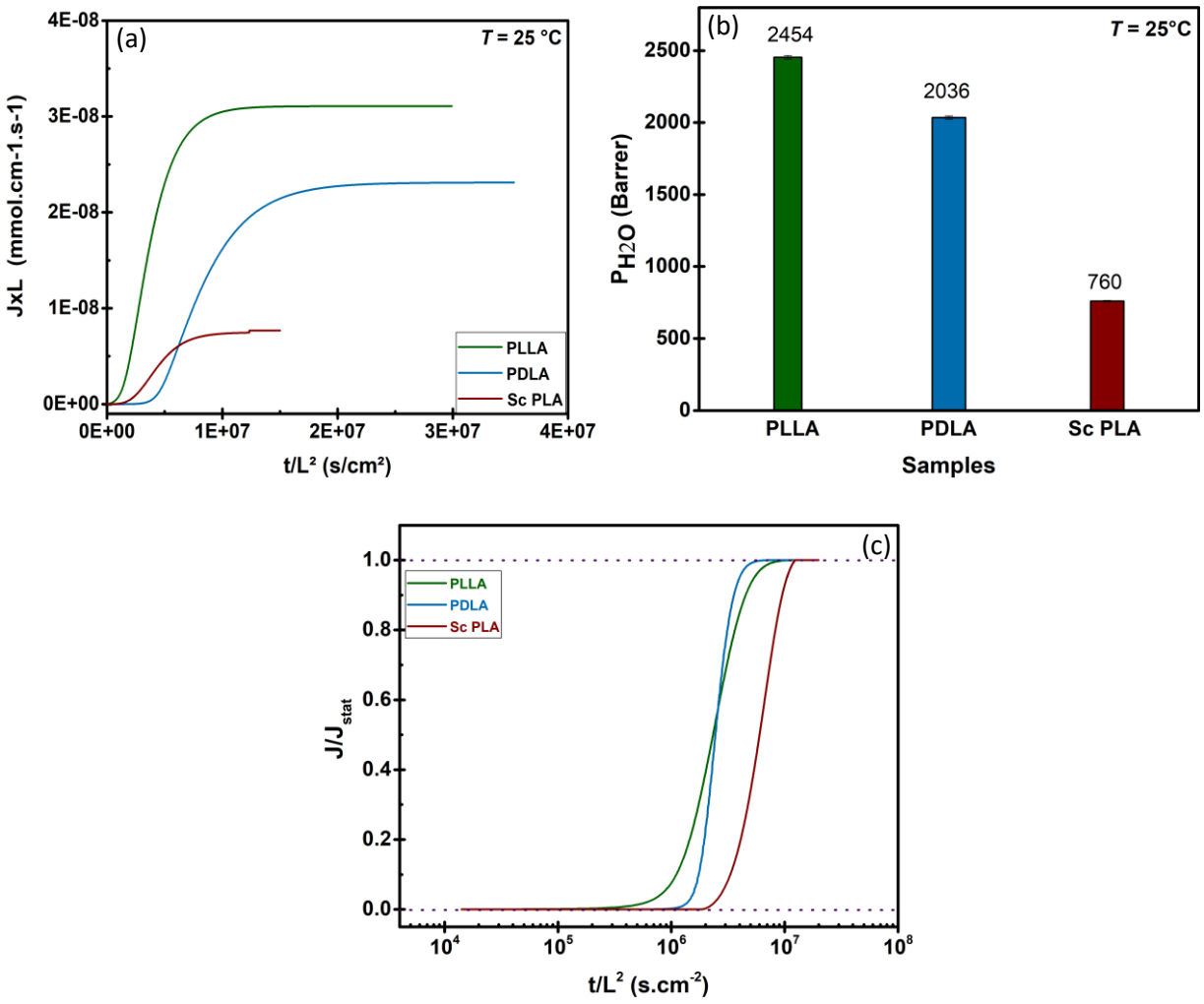

Figure 5. 6. (a) Evolution of the reduced flux of water permeation (J^*L) as a function of reduced time (t^*L^2), (b) water permeability coefficient P, and (c) normalized water permeation curves as a function of the reduced time for semicrystalline PLLA, PDLA and sc PLA at $T_{permeation}$ = 25 °C.

25°C Samples	P (Barrer)	$D_0 . 10^8$ ($cm^2.s^{-1}$)	$D_M . 10^8$ ($cm^2.s^{-1}$)	γC_{eq}	γ ($cm^3.mmol^{-1}$)	C_{eq} ($mmol.cm^{-3}$)
PLLA	2454 ± 13	1.26 ± 0.34	8.7 ± 8.7	2.17 ± 1.22	2.29 ± 0.18	0.83 ± 0.03
PDLA	2036 ± 11	0.92 ± 0.56	7.01 ± 1.9	2.04 ± 0.05	2.64 ± 0.62	0.77 ± 0.08
Sc PLA	760 ± 5	1.76 ± 0.05	4.74 ± 1.7	0.99 ± 0.02	4.00 ± 1.23	0.25 ± 0.02

Table 5. 3. Water permeametric coefficients of semicrystalline PLLA, PDLA and sc PLA at 25 ± 1°C.

- **$T_{permeation}$ = 45°C**

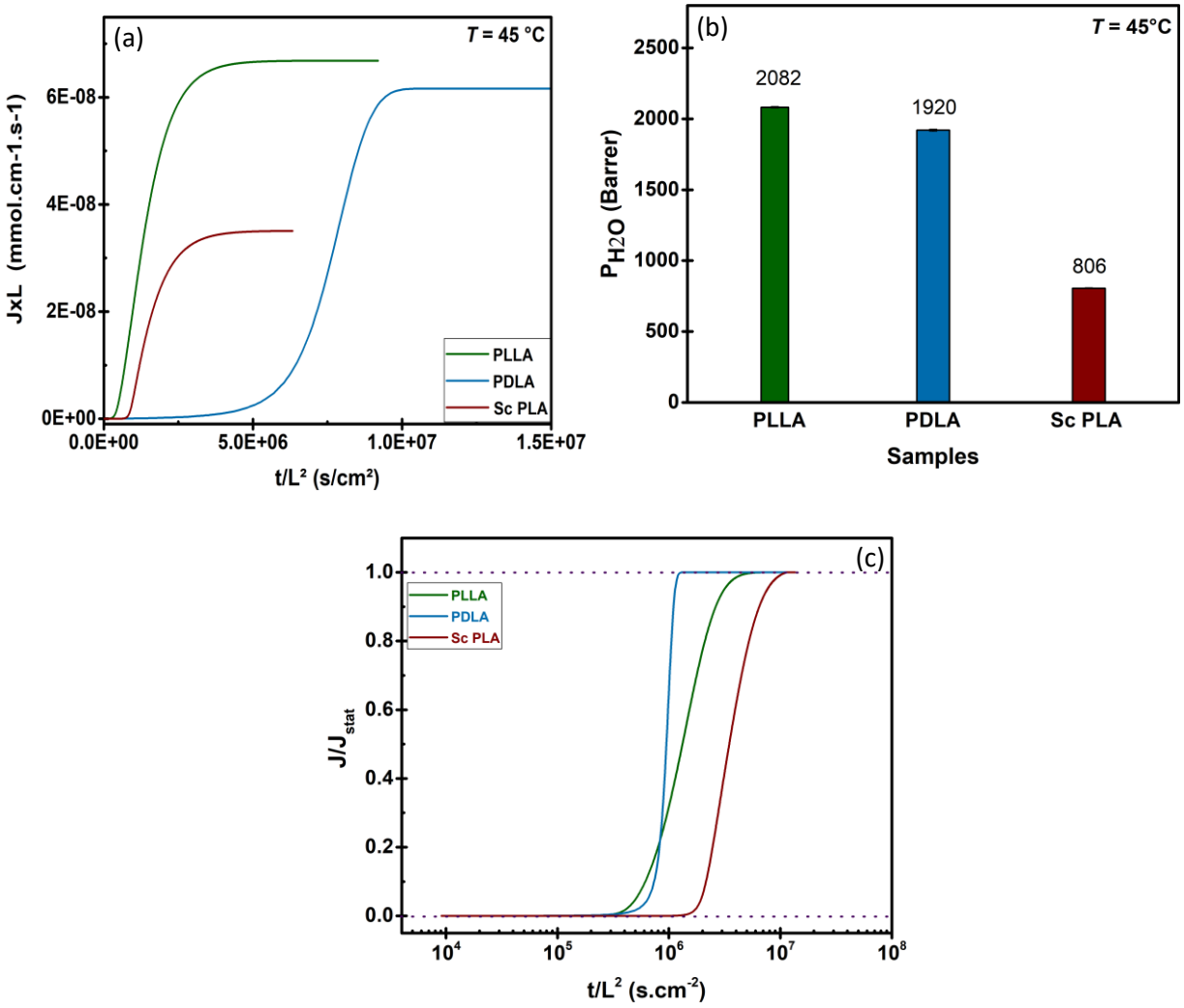

Figure 5. 7. (a) Evolution of the reduced flux of water permeation (J^*L) as a function of reduced time (t^*L^2), (b) water permeability coefficient P, and (c) normalized water permeation curves as a function of the reduced time for semicrystalline PLLA, PDLA and sc PLA at $T_{permeation}$ = 45 °C.

45°C Samples	P (Barrer)	$D_0 . 10^8$ ($cm^2.s^{-1}$)	$D_M . 10^8$ ($cm^2.s^{-1}$)	γC_{eq}	γ ($cm^3.mmol^{-1}$)	C_{eq} ($mmol.cm^{-3}$)
PLLA	2082 ± 6	1.13 ± 0.57	16.13 ± 1.6	4.78 ± 0.37	2.59 ± 0.32	0,79 ± 0.07
PDLA	1920 ± 9	1.40 ± 0.36	14.15 ± 4.9	3.57 ± 0.05	2.23 ± 0.67	0.42 ± 0.04
Sc PLA	806 ± 4	2.14 ± 0.09	16.3 ± 3.2	2.03 ± 0.22	8.79 ± 1.77	0.24 ± 0.08

Table 5. 4. Water permeametric coefficients of semicrystalline PLLA, PDLA and sc PLA at 45 ± 1°C.

- **$T_{permeation}$ = 65°C**

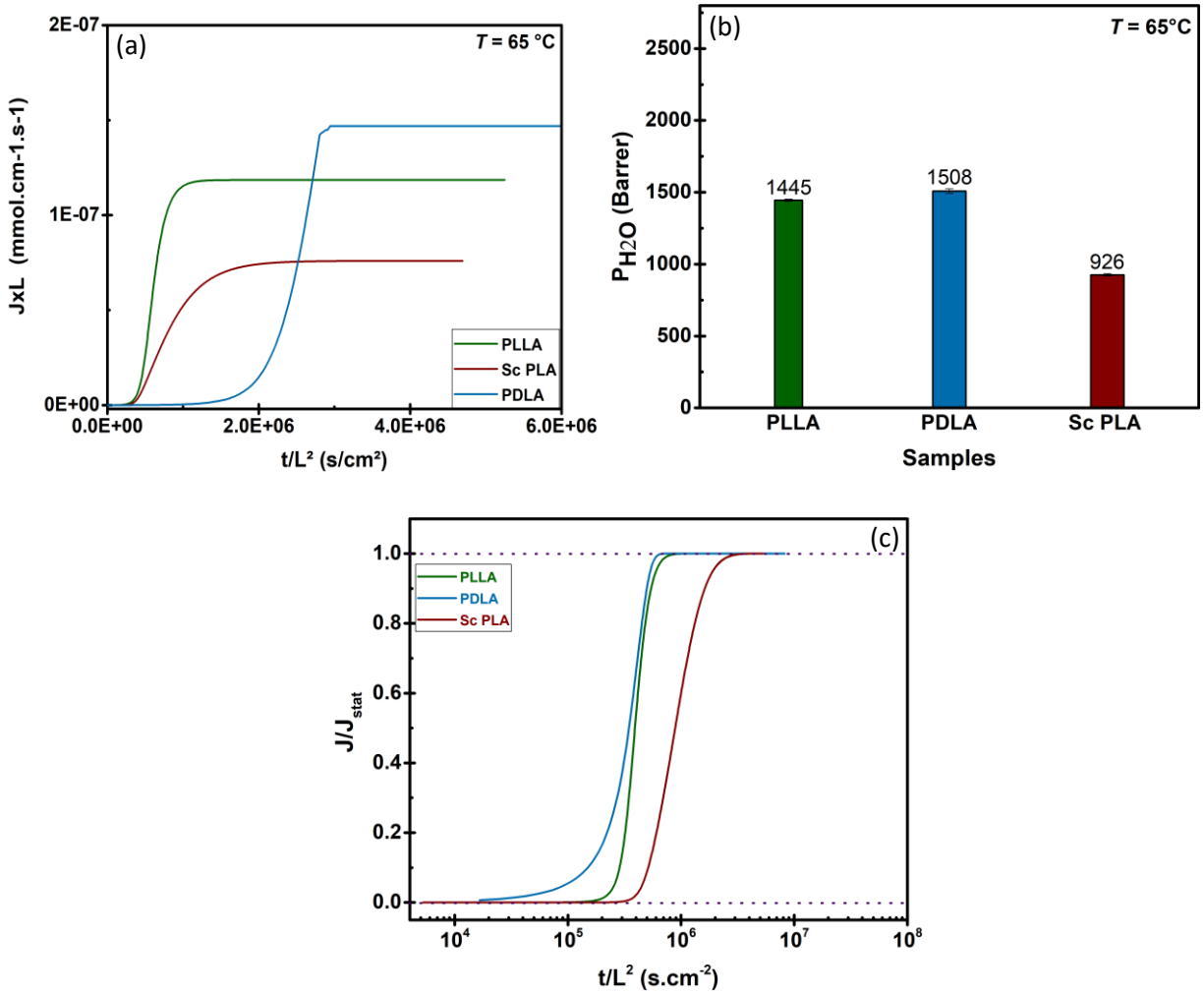

Figure 5. 8. (a) Evolution of the reduced flux of water permeation (J^*L) as a function of reduced time (t^*L^2), (b) water permeability coefficient P, and (c) normalized water permeation curves as a function of the reduced time for semicrystalline PLLA, PDLA and sc PLA at $T_{permeation}$ = 65 °C.

65°C Samples	P (Barrer)	$D_0 . 10^8$ ($cm^2.s^{-1}$)	$D_M . 10^8$ ($cm^2.s^{-1}$)	γC_{eq}	γ ($cm^3.mmol^{-1}$)	C_{eq} ($mmol.cm^{-3}$)
PLLA	1445 ± 8	6.79 ± 0.47	15.4 ± 2.7	3.12 ± 0.26	1.24 ± 0.14	0,45 ± 0.07
PDLA	1508 ± 16	4.05 ± 0.36	12.2 ± 2.9	1.22 ± 0.08	1.08 ± 0.34	0.35 ± 0.06
Sc PLA	926 ± 8	1.2 ± 0.03	5.1 ± 1.3	1.48 ± 0.47	5.20 ± 0.87	0.28 ± 0.03

Table 5. 5. Water permeametric coefficients of semicrystalline PLLA, PDLA and sc PLA at 65 ± 1°C.

The normalized water permeation curves as a function of the reduced time are plotted to compare the kinetics of diffusion for all the samples at each $T_{permeation}$. An increase in the delay time for the sc PLA is observed compared to the homopolymers at all studied temperatures. In addition, one can note a decrease in the delay time observed in case of diffusion through homopolymers with T increasing, while the delay time remains practically constant in case of sc PLA (Fig 5.6 - 5.8). It is known that water can cause a plasticization effect in the polymer samples [16]. The comparison of D_I and D_L coefficients exhibits that the value of D_L is higher than the value of D_I for homopolymers (Table 5.5). Considering that the former value is related to a final period of the transient state (J/J_{st} = 0.62), the smaller D_I value corresponds to an increase in the water diffusion during the permeation test. In general, such diffusion increase is associated with the plasticization effect of the water which leads to an increase of the material free volume [16, 18].

Temperature ($T_{permeation}$) (°C)	**<D> ($cm^2.s^{-1}$).10^{10}**			**$D_{0.24}$ ($cm^2.s^{-1}$).10^{10}**			**$D_{0.62}$ ($cm^2.s^{-1}$).10^{10}**		
	PLLA	**PDLA**	**Sc PLA**	**PLLA**	**PDLA**	**Sc PLA**	**PLLA**	**PDLA**	**sc PLA**
25	371	300	301	384	151	210	400	184	245
45	844	385	698	105	135	352	160	209	416
65	4712	4250	2666	1810	4110	1590	2580	4437	1820

Table 5. 6. The diffusion coefficient of PLLA, PDLA and sc PLA as a function of temperature.

Although according to the D_I and D_L coefficients the plasticization effect is observed. The aging phenomenon should be also taken into account in the amorphous phase organizations in case of homopolymers. Such result is totally different from the results for homopolymers found in literature. It was previously reported that thermal disturbance within the material caused an increase in the mobility of the polymer chain and, therefore, the transport phenomena were impacted by the variation of free volume resulting in increase of permeability [19, 20]. On the other hand, the aging effect could occur due to the temperature effect during the measurements. The samples were kept for purge step (drying step) under the nitrogen atmosphere at $T_{permeation}$ = 45 °C and 65 °C during more than 18 hours. Considering

the decrease in permeability coefficient, DSC analysis was performed for the studied samples in order to observe the aging effect in case of homopolymers. The DSC results (e.g. Fig 5.9) reveal that there is an endothermic peak superimposed with the glass transition which corresponds to the structural relaxation caused by aging (further results are shown in Appendix Chap 5 (A. 5.1 and 5.2)). The physical aging causes the structural relaxation towards equilibrium and results in a reduction in free volume causing lower permeability [21-25].

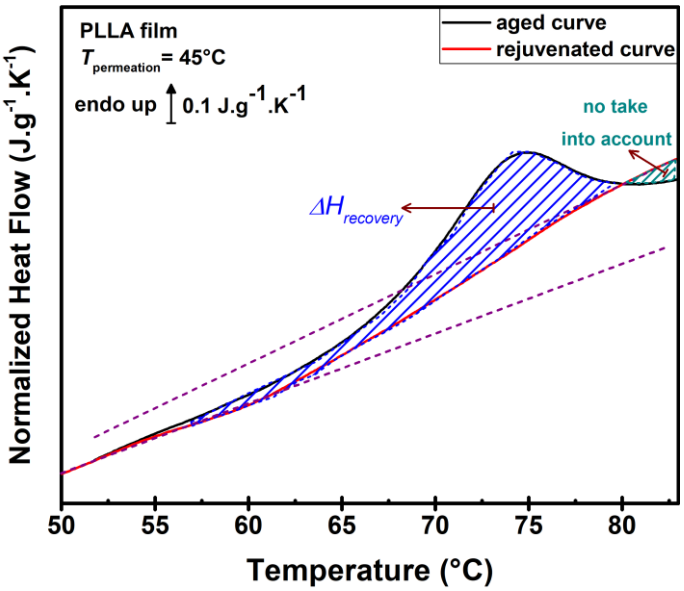

Figure 5. 9. DSC curves of studied semicrystalline PLLA after the permeation test at 45 ± 1°C.

The enthalpy recovery of the structural relaxation of studied PLLA and PDLA samples were approximatively calculated (shown in Fig 5.9) and results are presented in Table 5.7. The results for PLLA and PDLA were found to be 1.7 and 1.8 J/g (g of polymer) for measurement performed at 45 °C and 2.0 and 2.9 J/g (g of polymer) for measurement performed at 65 °C, respectively. Very small endothermic peak superimposed with the glass transition is observed in case of sc PLA whereas the value of the enthalpy recovery is negligible (Table 5.7) (curves are shown in Appendix Chap 5 (A. 5.1 and 5.2)). The enthalpy recovery of studied samples is normalized by the MAP content to compare with the infinite enthalpy recovery (ΔH_∞) of wholly amorphous samples (Table 5.7). From this approximation, the enthalpy recovery values ($\Delta H_{recovery}$ and ΔH_∞) were compared, and, it was revealed that the MAP probably relaxed completely during the measurement performed at 65°C whereas the complete relaxation is

not observed during the measurement performed at 45 °C. In case of measurement at 45 and 65 °C (the closest T to T_g), the aging effect eliminates the excess free volume and increases the barrier properties. As seen from Fig 5.10 (red circles) and well known in literature, the closer to T_g, the system is quicker to reach equilibrium. So, the strong effect of aging, which is confirmed by DSC analysis, is revealed by a decrease in the permeation coefficient values during the measurements at 25 °C and up to 65 °C (Table 5.3 – 5.5).

Temperature	**25 °C**		**45 °C**			**65 °C**	
Samples		$\Delta H_{recovery}$ **(J/(g polymer))**	$\Delta H_{recovery}$ **(J/(g MAP))**	ΔH_{∞}	$\Delta H_{recovery}$ **(J/(g polymer))**	$\Delta H_{recovery}$ **(J/(g MAP))**	ΔH_{∞}
PLLA	ND	1.7	5	14	2	6	5
PDLA	ND	1.8	4	14	2.9	7	5
Sc PLA	ND	0.2	1	13	0.08	0.4	2

Table 5. 7. The enthalpy recovery values of semicrystalline PLLA, PDLA and sc PLA as a function of temperature after permeation measurements. ND: non-detected.

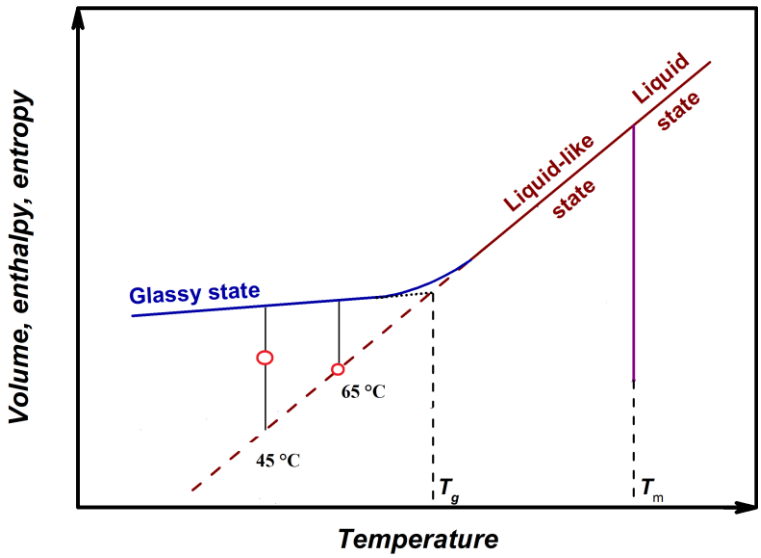

Figure 5. 10. Schematic illustration of the temperature dependence of the thermodynamic properties of the systems. Red circles present the studied samples towards equilibrium.

5.3.2 Gas barrier properties

The packaging materials should have high performances to be impermeable at dry state to protect the foods from the oxidation and moisture. On the other hand, fresh fruits and vegetables are the sources of biochemical reactions which consume oxygen (O_2) and produce carbon dioxide (CO_2) and water. Therefore, the barrier properties and selectivity of packaging materials are important for industrial applications. In this thesis, the effect of stereocomplexation on the nitrogen (N_2), O_2 and CO_2 barrier properties of semicrystalline PLLA, PDLA and sc PLA films was investigated using the permeation apparatus shown in Chap. 2. The permeation and selectivity values for films were determined. Before measurement, the permeation cell was completely evacuated by applying a vacuum on both sides of the film. Then, the upstream side was provided with the gas with a pressure *p1* (3 bar). The increase of pressure *p2* in the calibrated downstream volume was measured using a sensitive pressure gauge linked to a data acquisition system.

The permeability can be described using Fick's first law, resulting in the permeability coefficient as follows:

$$P_i = D_i S_i \tag{5.8}$$

where D_i is the average effective diffusion coefficient (cm^2/s) and S_i is the solubility coefficient (cm^3 (STP)/(cm^3 cmHg)) of component *i*. In addition, from the flux transient, the diffusion coefficient can be derived as follows:

$$D = \frac{L^2}{6 \times t_l} \tag{5.9}$$

where *L* is the sample thickness, *D* is the diffusion coefficient at the response time t_l called "time-lag", which corresponds to intercept of the asymptotic straight line of stationary flux with time axis.

When the permeation flux and the diffusion coefficient are determined, the permeability *P* and the solubility *S* coefficients can be calculated using the variable pressure method by assuming *p1 >> p2* as follows [26, 27]:

$$P = \frac{J_{stat}\, L}{\Delta P} \tag{5.10}$$

where J_{stat} is the stationary flux, and ΔP is the pressure difference between the upstream and downstream chambers of the permeation cell, and:

$$S = \frac{P}{D} \tag{5.11}$$

The ideal separation factor (selectivity coefficient α (*A, B*)) of a polymer film for gas A over gas B is given by the ratio of the gas permeability coefficients determined for gases *A* and *B*, respectively. Consequently this selectivity is the product of diffusivity and solubility selectivity:

$$\alpha\,(A,B) = \frac{P_A}{P_B} = \frac{D_A}{D_B}\,\frac{S_A}{S_B} \tag{5.12}$$

where D_A/D_B is the diffusivity selectivity and S_A/S_B is the solubility selectivity. Generally, gas diffusivity is enhanced by decreasing penetrant size, increasing polymer chain flexibility, increasing polymer fractional free volume and decreasing polymer-penetrant interactions. On the other hand, penetrant solubility is increased by increasing the condensability of the penetrant (which increases with increasing critical temperature of the gas) and increasing polymer-penetrant interactions. Therefore, the nature of the penetrant has a key role to investigate the barrier properties of studied film. Indeed, the polarizability, solubility, kinetic diameter, Van der Waals volume and critical temperature of the penetrant govern the transport properties. The characteristic parameters of used gases are presented in Table 5.8. In this thesis, the effect of the stereocomplexation on both the permeation and selectivity values for PLA-based films was investigated. The change in permeability and selectivity as a function of crystalline structure variations, free volume effects, glass transition temperature and MAP and RAF content is discussed.

Gas	Kinetic diameter (Å)	Polarizability ($cm^3 \times 10^{25}$)	Van der Waals volume ($cm^3.mol^{-1}$)	Critical temperature (°C)
N_2	3.64	17.6	39.1	-147
O_2	3.46	15.9	31.8	-118
CO_2	3.30	26.5	42.7	31

Table 5. 8. Physical properties of gas [28, 29].

Due to the high permeability of homopolymers, a mechanical support, i.e. silicone film (s) is placed above the sample in order to delay the gas diffusion. The silicone film used in this study is a commercial silicone referenced as pure silicone with thickness *L*s of 0.100 $\pm$ 0.005 cm (purchased from Solutions Elastomères Cie, St Etienne, France). This silicone is very permeable [30]. In this case, the permeability coefficient of studied sample was calculated according to:

$$\frac{L}{P} = \sum \frac{L_i}{P_i} \tag{5.13}$$

where *L* and *P* are the total thickness and the total permeability coefficient of the multilayer sample, L_i and P_i are the thickness and the permeability coefficient of each layer of the multilayer system, respectively. The quantity $R = L/P$ is the resistance of the sample to gas permeation. In the case of a multilayer sample, the total resistance is the sum of the resistance ($R_i = L_i/P_i$) of each layer [31]. The resistance $R_s = L_s/P_s$ of the silicone sample and the resistance of the multilayer sample ($R_{su} = L_{su}/P_{su}$ silicone/unknown sample) can be determined. The resistance L_u/P_u of the unknown film can be deduced from the global resistance by:

$$L_{SU}/P_{SU} = L_S/P_S + L_U/P_U \tag{5.14}$$

$$P_U = L_U/(L_{SU}/P_{SU} - L_S/P_S) \tag{5.15}$$

The gas permeation measurements were carried out firstly for pure silicone films. The results are presented in Appendix Chap 5 (A. 5.3, A. 5.4 and A. 5.5). The increase of the pressure *p2* as a function of time is presented for all tested gases (N_2, O_2 and CO_2). Considering the gas permeability dependence on the nature and size of the penetrant, and also on the nature of the polymer, D.W. Van Krevelen [32] proposed the permeability coefficients of N_2, O_2 and CO_2

gases follow the order according to their kinetic diameter as: *P* (N_2) < *P* (O_2) < *P* (CO_2). The same order was observed in case of the silicone film. Permeability coefficients and the values of selectivity (α) of the silicone film towards N_2, O_2 and CO_2 were calculated and results are presented in Table A. 5.4 and Table A. 5.5. After silicone film, the silicone-PDLA bilayer system was studied to calculate the permeability coefficient of PDLA film. The pressure curves (Fig 5.11) reveal that the permeability coefficients follow the same order as proposed depending on the kinetic diameters of penetrants (*P* (N_2) < *P* (O_2) < *P* (CO_2)). Furthermore, the experimental pressure curves for each gas are practically all superimposed (Fig 5.11) that indicates an excellent reproducibility of the measurements.

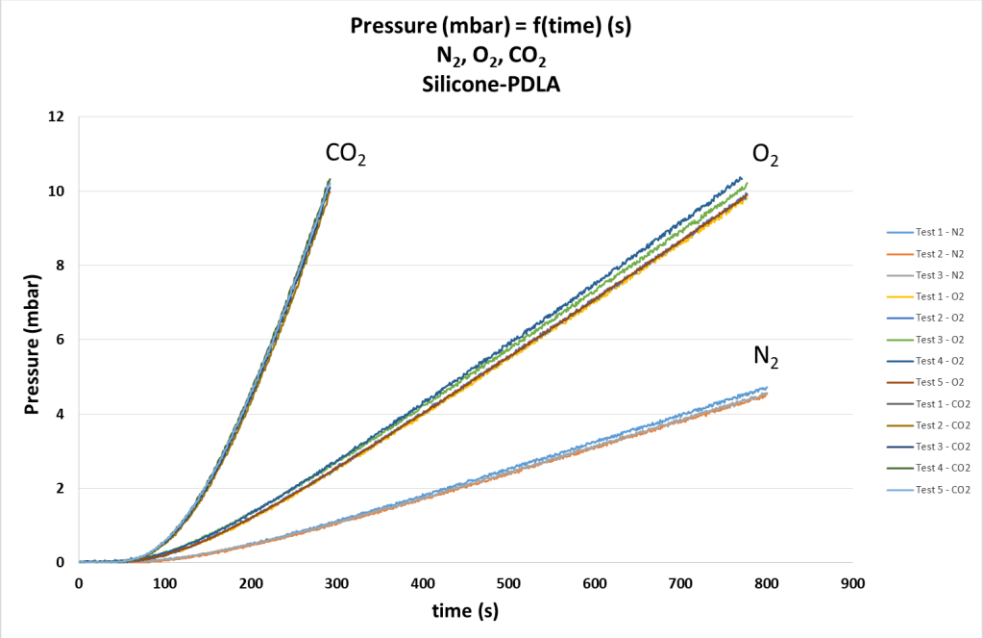

Figure 5. 11. Pressure as a function of time for silicone-PDLA system.

The permeation coefficient and the selectivity of PDLA film can be calculated by applying the law of series of resistance to diffusion (Eq 5.15) (Table 5.9). The same technique was applied also for PLLA film to calculate the permeability parameters towards N_2, O_2 and CO_2. The experimental curves for each gas are practically all superimposable (Fig 5.12), nevertheless we can note that the results with the nitrogen gas are more dispersed. Such behavior can be explained by the densification of the polymer film caused by specific interactions between the polymer film and N_2. Indeed, permeation of larger penetrants

molecules (i.e. N_2) is more affected by changes in free volume than permeation of small molecule (i.e. CO_2) [33]. The permeation parameters of PLLA film can be also calculated by the law of series of resistance to diffusion (Eq 5.15) (Table 5.9).

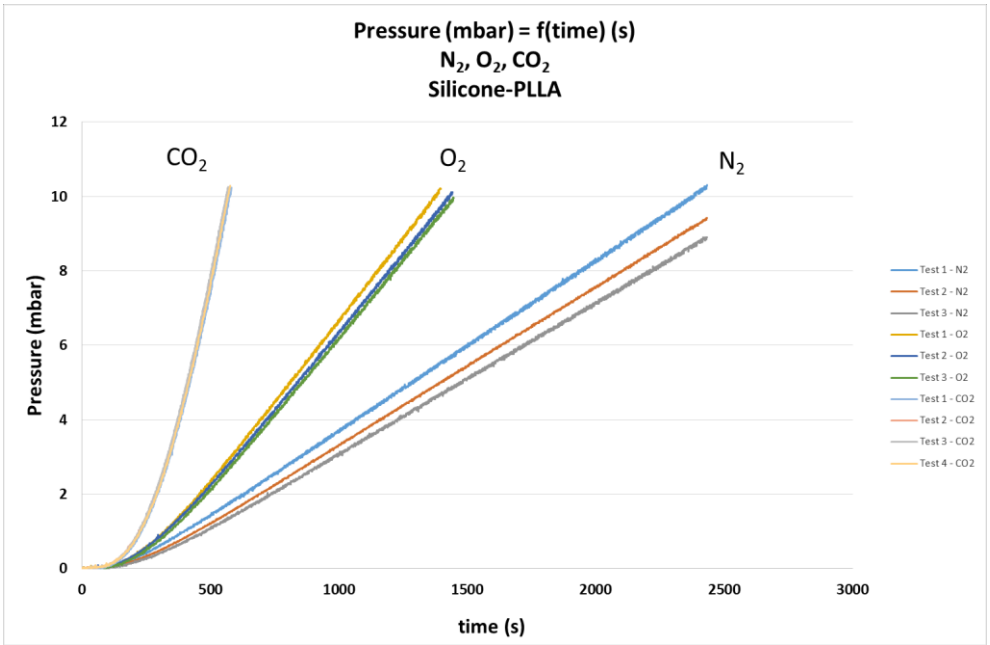

Figure 5. 12. Pressure as a function of time for silicone-PLLA system.

The use of silicone film was not necessary for sc PLA. However, the high mechanical fragility of sc PLA was a problem because of the film crack caused by the vacuum. The experimental curves (Fig 5.13) reveal that the results are not perfectly superimposable. It was impossible to study CO_2 permeation with the same sc PLA sample, because of the sample cracking during the drying step. The permeation tests with CO_2 have been realized with another sc PLA sample, and we supposed that the sample was cracked between the 3rd and 4th test (Fig 5.14). And, really the photo of sc PLA samples indicates that the samples are damaged during the measurements. Therefore, only the results of first tests were taken into account.

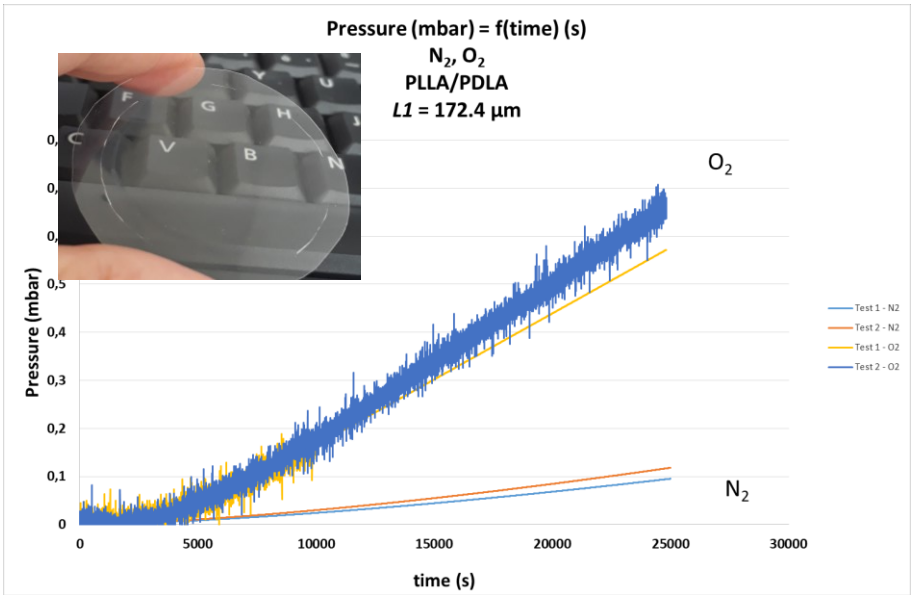

Figure 5. 13. Pressure as a function of time for sc PLA film towards N_2 and O_2.

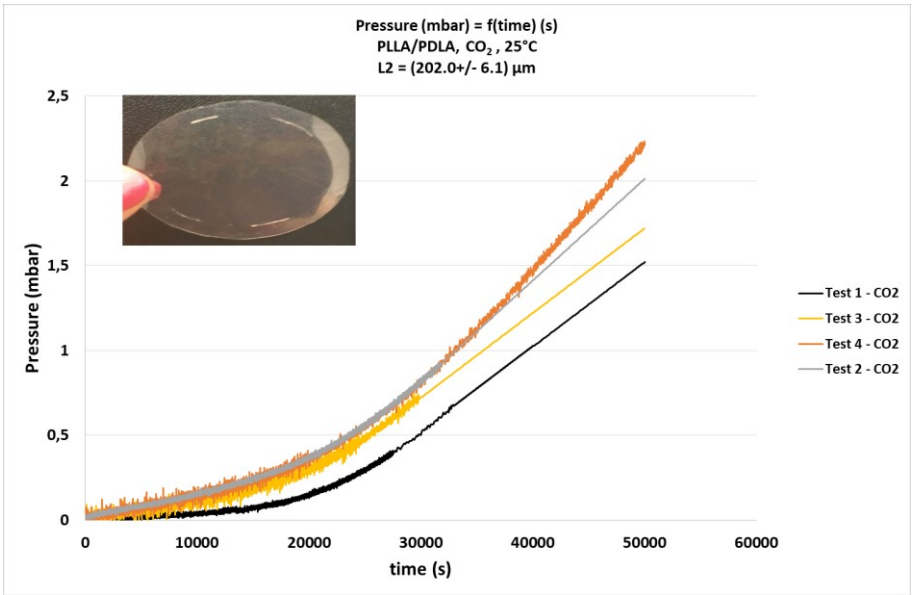

Figure 5. 14. Pressure as a function of time for sc PLA film towards CO_2.

The permeability coefficient of all studied samples is presented in Table 5.9. As can be seen from the results, whatever the studied film, the same tendency is observed for the order of permeability coefficient ($P(CO_2) > P(O_2) > P(N_2)$), i.e. according to the gas kinetic diameter. Also whatever the penetrant gas, the sc PLA has lower permeability coefficient than that for homopolymers. Indeed, this result can be explained by the fact that the permeability

coefficient is a result of the diffusion coefficient (which corresponds to the mobility of the gas through the film) and the solubility coefficient (which reflects the capacity of a molecule to condense in the polymer). So, due to the lower kinetic diameter (3.30 Å) and highest critical temperature (31 °C), CO_2 has the highest permeability coefficient value among all gases studied. The presence of polar ester oxygens in the polymer chain favors the solubility of quadrupolar CO_2 over the other non-polar gases [34-36].

As reported in literature, the presence of crystals is a predominant factor to cause more tortuosity in the film and to make it less permeable. In our case, this factor was not taken into consideration due to the similar crystallinity degree of studied films (Table 5.1). Nassar et al. [37] reported that the RAF content in the semicrystalline samples has strong influence on the barrier properties. This is due to RAF insufficient decoupling from the crystalline phase that provides an accelerated pathway for diffusion and, thus increases permeability. Therefore, we focused our attention on the influence of the crystals type (α and sc) and the RAF content in the semicrystalline films. In our case, the higher RAF content is observed in case of sc PLA (Table 5.1).

Permeability coefficient *P* (Barrer)	**N_2**	**O_2**	**CO_2**
PDLA	138 ± 21	339 ± 44	2081 ± 187
PLLA	38 ± 12	71 ± 25	283 ± 22
Sc PLA	0.024 ± 0.004	0.14 ± 0.02	0.28 ± 0.04

Table 5. 9. The permeability coefficient of studied films towards N_2, O_2 and CO_2.

However, sc PLA is found to be more barrier than homopolymers films. Indeed, the measurement temperature ($T = 25 \pm 1$ °C) is below the glass transition temperature of studied samples (Table 5.1). Therefore, film samples are in the glassy state, so the polymer chains are rigid and less mobile. In addition, sc PLA has the lowest glass transition temperature (about > 5 °C), nevertheless sc PLA presents better barrier properties whatever the penetrant gases. To better understand the transport properties of the studied samples, the variations of the different permeametric coefficients (i.e. diffusion and solubility coefficients) were also investigated. The diffusion and solubility coefficient values are presented in Table 5.10 and

5.11, respectively. The diffusivity of a gas is related to the mobility of this gas within the polymer film. The value of the diffusion coefficient will therefore mainly depend on the size of the penetrating molecules. The smaller the volume of the gas molecule, the easier it will diffuse through the film (i.e. a molecule with a larger volume will be slowed down and, therefore, will have more difficulty to move through the polymer chains). So, according to the Van der Waals volumes of gases, i.e. V_{O_2}= 31.8 $cm^3.mol^{-1}$ < V_{N_2}= 39.1 $cm^3.mol^{-1}$ < V_{CO_2} = 42.7 $cm^3.mol^{-1}$ (Table 5.8) the values of the diffusion coefficient should have such tendency as $D(CO_2) > D(N_2) > D(O_2)$. As can be seen from Table 5. 10, only PDLA film has this tendency, whereas PLLA has tendency as $D(N_2) > D(O_2) > D(CO_2)$ which can be explained by the condensation effect of O_2 resulting in the decrease in diffusion. In addition, sc PLA presents inverse tendency with the Van der Waals volume as $D(CO_2) < D(N_2) < D(O_2)$. Due to the steric hindrance in sc PLA, the results show that the bigger the size of the penetrant molecule, the longer time will be required to cross the film, and the diffusion will be slowed down. The diffusion coefficients evolution exhibit that the transport of gases through these films is not done in the same way. This difference can be related to the different crystalline structure (sc and α) between sc PLA and homopolymers and, therefore, related to the free volume and RAF content.

Diffusion coefficient . 10^8 D ($cm^2.s^{-1}$)	**N_2**	**O_2**	**CO_2**
PDLA	1169 ± 32	1397 ± 55	1424 ± 27
PLLA	1025 ± 120	877 ± 34	796 ± 19
Sc PLA	0.57 ± 0.05	1.15 ± 0.13	0.34 ± 0.12

Table 5. 10. The diffusion coefficient of studied films towards N_2, O_2 and CO_2.

The different diffusion coefficients values were obtained for the studied samples, therefore, the lower permeability coefficient value in the case of sc PLA may be correlated with the solubility coefficients values. The obtained solubility coefficients of studied samples are presented in Table 5. 11. The solubility coefficient of polymers has an evolution according to the critical temperatures of the penetrant molecules as follows: $S(N_2) < S(O_2) < S(CO_2)$, ($T_C(N_2) < T_C(O_2) < T_C(CO_2)$) (Table 5.8) [38, 39]. As can be seen from Table 5.11, the solubility

coefficient values of studied films present good accordance with literature. In the case of sc PLA, the lowest solubility values are observed suggesting an improvement of the barrier properties, except for CO_2. The higher CO_2 solubility coefficient can be explained by the RAF content which effects the solubility coefficient by increasing the free volume.

Solubility coefficient . 10^2 *S* (cm^3(STP).cm^{-3}cmHg)	**N_2**	**O_2**	**CO_2**
PDLA	0.18 ± 0.01	0.32 ± 0.01	1.32 ± 0.04
PLLA	0.13 ± 0.01	0.29 ± 0.01	1.29 ± 0.06
Sc PLA	0.05 ± 0.01	0.12 ± 0.03	1.36 ± 0.31

Table 5. 11. The solubility coefficient of studied films towards N_2, O_2 and CO_2.

The efficiency of the studied films to separate the components in the penetrants mixture can be defined by the selectivity parameters presented in Table 5.12. Although the strong decrease in permeability is observed in the case of for sc PLA for both water and gases, the significant selectivity is observed only for systems containing water. Therefore, one can note that stereocomplexation causes more important decrease in gas barrier properties of film compare to the water barrier properties which must be taking into account for food packaging. In addition, due to the biochemical reaction products, decreasing the respiratory intensity is always aimed for the longer life-time, which can be obtained by the reduction of partial pressure of oxygen in the packaging materials. Moreover, the presence of H_2O and CO_2 leads to a bad taste and smell in the packed products. Therefore, high H_2O / O_2 permselectivity and the low O_2 permeability is an optimum condition to reduce the respiratory intensity and the anaerobic fermentation rate to have longer life-time. The result of permselectivity (Table 5.12) shows that stereocomplexation not only improves barrier properties, but also achieves the $\alpha_{H2O\ /\ O2}$ value of PLA-based materials for packaging applications. The trade-off between the H_2O and O_2 permeability and the ideal separation factor $\alpha_{H2O\ /\ O2}$ was found in case of sc PLA.

Selectivity ($\alpha_{A/B}$)	CO_2/O_2	CO_2/N_2	O_2/N_2	H_2O/O_2	H_2O/N_2	H_2O/CO_2
PDLA	6	15	2	6	15	1
PLLA	4	7	2	34	65	9
Sc PLA	2	12	6	5630	31667	2713

Table 5. 12. The selectivity parameters of studied films.

Moreover, the sc PLA results show better improvements and/or are in good accordance with previous works to achieve better barrier properties of PLA-based polymers. For example, Picard et al [40] reported that the barrier properties of PLA nanocomposites film can be improved by increasing the content of organo-modified montmorillonite (O-MMT). In that work, crystallinity degree was increased up to 35% by annealing time and temperature. For the maximum crystallinity degree value of annealed and charged (4 wt %) PLA samples (X_c = 46%), the O_2 permeability coefficient of PLA composite was calculated as 0.23 ± 0.03 Barrer. In another work, Pinto et al. [41] studied nanocomposite thin films of PLA which were produced by incorporating small amounts (0.2 to 1 wt%) of graphene oxide (GO) and graphene nanoplatelets (GNP). The permeabilities towards O_2 are decreased from 3.76 Barrer for PLA to 1.49 and 1.30 Barrer; and the N_2 permeability coefficients are decreased from 1.10 Barrer for PLA to 0.502 and 0.237 Barrer for nanocomposite film with increasing the percentage GO and GNP up to 0.6 wt%, respectively. Furthermore, Lehermeier et al. [42] investigated barrier properties of amorphous PLA and biaxially oriented semicrystalline PLA film. They proposed that polymer chain branching and small changes in L:D stereochemical content of PLA have no influence on the permeation properties and the most promoted influence is caused by the crystallinity degree. The sample prepared in that work [42] has the crystallinity degree X_c = 18 % and the permeability coefficients of N_2, O_2 and CO_2 were determined to be 1.3, 3.3 and 10.2 Barrer, respectively. So, one can say that the results of the sc PLA studied in this thesis show superior barrier properties of PLA-based material compare to the previous works. Furthermore, sc PLA possesses enhanced barrier properties compared to the petroleum-based polymers usually used in the food packaging (Table 5.13).

Samples	N_2	O_2	CO_2
Sc PLA	0.03	0.14	0.28
LDPE	1.9	6.9	28.0
PS	2.2	2.6	10.5
PET	0.008	0.04	0.2

Table 5. 13. The permeability coefficient of sc PLA compared to the petroleum-based polymers (LDPE: low-density polyethylene, PS: polystyrene, PET: polyethylene terephthalate) [42].

Conclusion

Nowadays, a market of packaging requires more eco-friendly materials with high performances, i.e. strong mechanical and barrier properties. In this thesis, we proposed facile method in order to improve the mechanical and transport properties of PLA, namely the stereocomplex formation between PLLA and PDLA. The water resistance of amorphous and semicrystalline PLA-based film and the permeation of nitrogen, oxygen and carbon dioxide in semicrystalline samples were studied to examine the influence of the stereocomplexation on transport properties. The presence of pure homo- or sc crystals was confirmed by XRD and DSC analysis. The morphology of the obtained films was investigated by SEM analysis. SEM results show that the homopolymers films exhibit granular structure, while sc PLA films reveal a smooth compact structure. Furthermore, no porosity is observed for all the film samples.

Superior mechanical properties have been achieved by stereocomplexation of homopolymers through formation of stereocomplex crystals which are formed by intermolecular crosslinking. The barrier properties of poly(lactide) were also enhanced by stereocomplexation.

One should note that although there is no difference on the glass transition properties of amorphous samples (i.e. the same glass transition, molecular mobility and CRR size), the water barrier properties of amorphous PLA-based sample can be improved by stereocomplexation. Furthermore, the value of water permeability coefficient of amorphous sc PLA at 25°C is close to the value of water permeability coefficient of semicrystalline (X_C = 48%) homopolymers.

CHAPTER 5. MICROSTRUCTURE INFLUENCE ON MECHANICAL AND BARRIER PROPERTIES OF STEREOCOMPLEX PLA

The transport properties of semicrystalline pure PLLA, PDLA and sc PLA were investigated by water permeation measurements as a function of the temperature. The water permeation results reveal an important barrier improvement for sc PLA - up to 70% as compared to the homopolymers. It is found that even if the molecular structure of samples is the same, the stereocomplexation creates the macromolecular reorganization in PLA-based films. Moreover, one can note that the type of crystals is the predominant factor on the barrier properties compared to the RAF content (i.e. although sc PLA has higher RAF content than homopolymers, it is still more barrier than homopolymers). It is also very interesting that the barrier properties of homopolymers are found to increase with the *T* increase due to the aging effect revealed in case of homopolymers.

The gas permeation results clearly show that stereocomplexation not only enhances the water barrier properties, but also improves the gas barrier properties. The results of sc PLA reveal that the proposed new method can be applied to the biobased homopolymers, which have different tacticity, to increase the competition with non-ecofriendly petroleum-based polymers used in food packaging applications. From that point, the investigation of the relation between the microstructure of PLA and the water and gas barrier performance is still a key in the improvement of the transport properties of PLA towards different permeants. Nevertheless, the improved barrier properties of sc PLA (PLLA/PDLA) films through enhanced stereocomplexation may comply with the requirement for high temperature engineering and packaging application.

References

1. Okihara, T.; Tsuji, M.; Kawaguchi, A.; Katayama, K.-I.; Tsuji, H.; Hyon, S.-H.; Ikada, Y. Crystal structure of stereocomplex of poly(L-lactide) and poly(D-lactide). *Journal of Macromolecular Science, Part B* **1991,** 30 (1-2), 119-140 DOI: 10.1080/00222349108245788.
2. Tenn, N.; Follain, N.; Soulestin, J.; Crétois, R.; Bourbigot, S.; Marais, S. Effect of Nanoclay Hydration on Barrier Properties of PLA/Montmorillonite Based Nanocomposites. *The Journal of Physical Chemistry C* **2013,** 117 (23), 12117-12135 DOI: 10.1021/jp401546t.
3. Tenn, N.; Follain, N.; Fatyeyeva, K.; Poncin-Epaillard, F.; Labrugere, C.; Marais, S. Impact of hydrophobic plasma treatments on the barrier properties of poly(lactic acid) films. *RSC Advances* **2014,** 4 (11), 5626-5637 DOI: 10.1039/C3RA45323E.
4. Thellen, C.; Orroth, C.; Froio, D.; Ziegler, D.; Lucciarini, J.; Farrell, R.; D'Souza, N. A.; Ratto, J. A. Influence of montmorillonite layered silicate on plasticized poly(l-lactide) blown films. *Polymer* **2005,** 46 (25), 11716-11727 DOI: https://doi.org/10.1016/j.polymer.2005.09.057.
5. Alexandre, B.; Langevin, D.; Médéric, P.; Aubry, T.; Couderc, H.; Nguyen, Q. T.; Saiter, A.; Marais, S. Water barrier properties of polyamide 12/montmorillonite nanocomposite membranes: Structure and volume fraction effects. *Journal of Membrane Science* **2009,** 328 (1), 186-204 DOI: https://doi.org/10.1016/j.memsci.2008.12.004.
6. Chivrac, F.; Angellier-Coussy, H.; Guillard, V.; Pollet, E.; Avérous, L. How does water diffuse in starch/montmorillonite nano-biocomposite materials? *Carbohydrate Polymers* **2010,** 82 (1), 128-135 DOI: https://doi.org/10.1016/j.carbpol.2010.04.036.
7. Wang, H.; Keum, J. K.; Hiltner, A.; Baer, E. Confined Crystallization of PEO in Nanolayered Films Impacting Structure and Oxygen Permeability. *Macromolecules* **2009,** 42 (18), 7055-7066 DOI: 10.1021/ma901379f.
8. Ponting, M.; Lin, Y.; Keum, J. K.; Hiltner, A.; Baer, E. Effect of Substrate on the Isothermal Crystallization Kinetics of Confined Poly(ε-caprolactone) Nanolayers. *Macromolecules* **2010,** 43 (20), 8619-8627 DOI: 10.1021/ma101625h.
9. Mackey, M.; Flandin, L.; Hiltner, A.; Baer, E. Confined crystallization of PVDF and a PVDF-TFE copolymer in nanolayered films. *Journal of Polymer Science Part B: Polymer Physics* **2011,** 49 (24), 1750-1761 DOI: 10.1002/polb.22375.
10. Wang, H.; Keum, J. K.; Hiltner, A.; Baer, E. Crystallization Kinetics of Poly(ethylene oxide) in Confined Nanolayers. *Macromolecules* **2010,** 43 (7), 3359-3364 DOI: 10.1021/ma902780p.
11. Messin, T.; Follain, N.; Guinault, A.; Sollogoub, C.; Gaucher, V.; Delpouve, N.; Marais, S. Structure and Barrier Properties of Multinanolayered Biodegradable PLA/PBSA Films: Confinement Effect via Forced Assembly Coextrusion. *ACS Applied Materials & Interfaces* **2017,** 9 (34), 29101-29112 DOI: 10.1021/acsami.7b08404.
12. Delpouve, N.; Stoclet, G.; Saiter, A.; Dargent, E.; Marais, S. Water Barrier Properties in Biaxially Drawn Poly(lactic acid) Films. *The Journal of Physical Chemistry B* **2012,** 116 (15), 4615-4625 DOI: 10.1021/jp211670g.
13. Bai, H.; Huang, C.; Xiu, H.; Zhang, Q.; Deng, H.; Wang, K.; Chen, F.; Fu, Q. Significantly Improving Oxygen Barrier Properties of Polylactide via Constructing Parallel-Aligned Shish-Kebab-Like Crystals with Well-Interlocked Boundaries. *Biomacromolecules* **2014,** 15 (4), 1507-1514 DOI: 10.1021/bm500167u.
14. Denny Kamaruddin, H.; Koros, W. J. Some observations about the application of Fick's first law for membrane separation of multicomponent mixtures. *Journal of Membrane Science* **1997,** 135 (2), 147-159 DOI: https://doi.org/10.1016/S0376-7388(97)00142-7.
15. Marais, S.; Métayer, M.; Nguyen, Q. T.; Labbé, M.; Langevin, D. New methods for the determination of the parameters of a concentration-dependent diffusion law for molecular penetrants

from transient permeation or sorption data. *Macromolecular Theory and Simulations* **2000,** 9 (4), 207-214 DOI: doi:10.1002/(SICI)1521-3919(20000401)9:4<207::AID-MATS207>3.0.CO;2-Q.

16. Follain, N.; Valleton, J.-M.; Lebrun, L.; Alexandre, B.; Schaetzel, P.; Metayer, M.; Marais, S. Simulation of kinetic curves in mass transfer phenomena for a concentration-dependent diffusion coefficient in polymer membranes. *Journal of Membrane Science* **2010,** 349 (1), 195-207 DOI: https://doi.org/10.1016/j.memsci.2009.11.044.

17. Crank, J.; Park, G. S., *Diffusion in Polymers*. London and New York, 1968 1st Edition.

18. Tenn, N.; Follain, N.; Fatyeyeva, K.; Valleton, J.-M.; Poncin-Epaillard, F.; Delpouve, N.; Marais, S. Improvement of Water Barrier Properties of Poly(ethylene-co-vinyl alcohol) Films by Hydrophobic Plasma Surface Treatments. *The Journal of Physical Chemistry C* **2012,** 116 (23), 12599-12612 DOI: 10.1021/jp302223j.

19. Kumins, C. A.; Roteman, J. Diffusion of gases and vapors through polyvinyl chloride-polyvinyl acetate copolymer films I. Glass transition effect. *Journal of Polymer Science* **1961,** 55 (162), 683-698 DOI: 10.1002/pol.1961.1205516222.

20. Yasuda, H.; Hirotsu, T. The effect of glass transition on gas permeabilities. *Journal of Applied Polymer Science* **1977,** 21 (1), 105-112 DOI: 10.1002/app.1977.070210109.

21. Kim, J. H.; Koros, W. J.; Paul, D. R. Physical aging of thin 6FDA-based polyimide membranes containing carboxyl acid groups. Part I. Transport properties. *Polymer* **2006,** 47 (9), 3094-3103 DOI: https://doi.org/10.1016/j.polymer.2006.02.083.

22. Tiemblo, P.; Guzmán, J.; Riande, E.; Mijangos, C.; Reinecke, H. Effect of physical aging on the gas transport properties of PVC and PVC modified with pyridine groups. *Polymer* **2001,** 42 (11), 4817-4823 DOI: https://doi.org/10.1016/S0032-3861(00)00922-8.

23. Pfromm, P. H.; Koros, W. J. Accelerated physical ageing of thin glassy polymer films: evidence from gas transport measurements. *Polymer* **1995,** 36 (12), 2379-2387 DOI: https://doi.org/10.1016/0032-3861(95)97336-E.

24. Rowe, B. W.; Freeman, B. D.; Paul, D. R. Physical aging of ultrathin glassy polymer films tracked by gas permeability. *Polymer* **2009,** 50 (23), 5565-5575 DOI: https://doi.org/10.1016/j.polymer.2009.09.037.

25. Langsam, M.; Robeson, L. M. Substituted propyne polymers—part II. Effects of aging on the gas permeability properties of poly[1-(trimethylsilyl)propyne] for gas separation membranes. *Polymer Engineering & Science* **1989,** 29 (1), 44-54 DOI: 10.1002/pen.760290109.

26. Glatz, F. P.; Mülhaupt, R.; Schultze, J. D.; Springer, J. Gas permeabilities and permselectivities of amorphous segmented 6F poly (arylene thioether imide)s and the corresponding poly(arylene sulfone imide)s. *Journal of Membrane Science* **1994,** 90 (1), 151-159 DOI: https://doi.org/10.1016/0376-7388(94)80042-1.

27. Joly, C.; Le Cerf, D.; Chappey, C.; Langevin, D.; Muller, G. Residual solvent effect on the permeation properties of fluorinated polyimide films. *Separation and Purification Technology* **1999,** 16 (1), 47-54 DOI: https://doi.org/10.1016/S1383-5866(98)00118-X.

28. Kim, J. H.; Ha, S. Y.; Lee, Y. M. Gas permeation of poly(amide-6-b-ethylene oxide) copolymer. *Journal of Membrane Science* **2001,** 190 (2), 179-193 DOI: https://doi.org/10.1016/S0376-7388(01)00444-6.

29. Paul, D., *Polymeric Gas Separation Membranes.* Boca Raton: CRC Press: 1994.

30. Merkel, T. C.; Bondar, V. I.; Nagai, K.; Freeman, B. D.; Pinnau, I. Gas sorption, diffusion, and permeation in poly(dimethylsiloxane). *Journal of Polymer Science Part B: Polymer Physics* **2000,** 38 (3), 415-434 DOI: doi:10.1002/(SICI)1099-0488(20000201)38:3<415::AID-POLB8>3.0.CO;2-Z.

31. Barrer, R. M. Diffusion and permeation in heterogeneous media. *Diffusion in Polymers* **1968**, 165-217.

32. Van Krevelen, D. W., *Properties determining mass transfer in polymeric systems // Chap. 18 in "Properties of polymers"*. Fourth completely revised edition ed.; Elsevier B.V 2009.

33. Wolinska-Grabczyk, A.; Kubica, P.; Jankowski, A. Effect of the acetate group content on gas permeation through membranes based on poly(ethylene-co-vinyl acetate) and its blends. *Journal of Membrane Science* **2013,** 443, 227-236 DOI: https://doi.org/10.1016/j.memsci.2013.04.057.

34. Bondar, V. I.; Freeman, B. D.; Pinnau, I. Gas sorption and characterization of poly(ether-b-amide) segmented block copolymers. *Journal of Polymer Science Part B: Polymer Physics* **1999,** 37 (17), 2463-2475 DOI: doi:10.1002/(SICI)1099-0488(19990901)37:17<2463::AID-POLB18>3.0.CO;2-H.

35. Bondar, V. I.; Freeman, B. D.; Pinnau, I. Gas transport properties of poly(ether-b-amide) segmented block copolymers. *Journal of Polymer Science Part B: Polymer Physics* **2000,** 38 (15), 2051-2062 DOI: doi:10.1002/1099-0488(20000801)38:15<2051::AID-POLB100>3.0.CO;2-D.

36. Lin, H.; Freeman, B. D. Materials selection guidelines for membranes that remove CO2 from gas mixtures. *Journal of Molecular Structure* **2005,** 739 (1), 57-74 DOI: https://doi.org/10.1016/j.molstruc.2004.07.045.

37. Fernandes Nassar, S.; Guinault, A.; Delpouve, N.; Divry, V.; Ducruet, V.; Sollogoub, C.; Domenek, S. Multi-scale analysis of the impact of polylactide morphology on gas barrier properties. *Polymer* **2017,** 108, 163-172 DOI: https://doi.org/10.1016/j.polymer.2016.11.047.

38. Barrer, R. M.; Skirrow, G. Transport and equilibrium phenomena in gas–elastomer systems. I. Kinetic phenomena. *Journal of Polymer Science* **1948,** 3 (4), 549-563 DOI: doi:10.1002/pol.1948.120030410.

39. Amerongen, G. J. v. Diffusion in Elastomers. *Rubber Chemistry and Technology* **1964,** 37 (5), 1065-1152 DOI: 10.5254/1.3540396.

40. Picard, E.; Espuche, E.; Fulchiron, R. Effect of an organo-modified montmorillonite on PLA crystallization and gas barrier properties. *Applied Clay Science* **2011,** 53 (1), 58-65 DOI: https://doi.org/10.1016/j.clay.2011.04.023.

41. Pinto, A. M.; Cabral, J.; Tanaka, D. A. P.; Mendes, A. M.; Magalhães, F. D. Effect of incorporation of graphene oxide and graphene nanoplatelets on mechanical and gas permeability properties of poly(lactic acid) films. *Polymer International* **2013,** 62 (1), 33-40 DOI: doi:10.1002/pi.4290.

42. Lehermeier, H. J.; Dorgan, J. R.; Way, J. D. Gas permeation properties of poly(lactic acid). *Journal of Membrane Science* **2001,** 190 (2), 243-251 DOI: https://doi.org/10.1016/S0376-7388(01)00446-X.

CONCLUSIONS & PROSPECTS

In recent years, PLA-based materials have attracted great interest as a biobased ecofriendly polyester to replace petroleum-based plastic used in many applications (i.e. biomedical devices, tissue engineering, and in packaging). Therefore, the new production strategy, called stereocomplexation, is developed to obtain a material with better physical properties. Moreover, the behavior of the amorphous phase and the transport properties of stereocomplex PLA was still enigmatic topic. In that concern, the goal of this thesis is to have better understanding and advanced investigation of the amorphous phase properties and the evolution of the barrier properties of stereocomplex PLA with the aim of improving the knowledge about sc PLA and stereocomplexation reactions.

The first part of this thesis was devoted to optimization of the elaboration method of stereocomplex PLA with pure stereocomplex crystals as a crystalline structure. For this purpose, stereocomplex PLA was elaborated by extrusion process (at different extrusion temperature and extrusion time) and by solution casting (with different polymer concentrations and homopolymers' ratio). The thermal and microstructural analyses of the obtained films reveal that:

- extrusion process allows decreasing the thermal degradation temperature of stereocomplex PLA with an increasing extrusion temperature and time, whereas the solution casting method has no influence on the thermal behavior of sc PLA;
- extrusion temperature (T_{ext}) is found to have influence on the stereocomplex formation as pure and stable stereocomplex crystals were obtained at T_{ext} = 220°C;
- the polymer concentration has slight influence on the stereocomplexation and the homopolymer presence. Besides, the obtained stereocomplex crystals by solution casting are not stable;
- the ratio of homopolymers has significant influence on the stereocomplex formation and the found optimum conditions of blending ratio are 60:40 and 50:50 for PLLA:PDLA;

- semicrystalline sc PLA obtained by extrusion process presents 2-phase model ($X_{MAP} + X_c = 1$), whereas semicrystalline sc PLA obtained by solution casting reveals 3-phase model ($X_{MAP} + X_c + X_{RAF} = 1$) due to the different crystallization temperature which is higher in the case of extrusion process.

In the second part of this study, the objective was to investigate the chirality/tacticity impact on the molecular dynamics of amorphous stereocomplex PLA. The physical aging study was carried out by FSC in order to examine the glass transition parameters and the structural relaxation of amorphous stereocomplex PLA. The dynamic parameters associated to the α relaxation process, i.e. the relaxation time, the dielectric strength, and the fragility, have been investigated by DRS. The dynamic heterogeneities and the cooperative length scales at the dynamic glass transition have been studied by combining DRS and MT-DSC techniques. According to the molecular dynamic investigation, one may conclude that:

- amorphous stereocomplex PLA has the same glass transition temperature as amorphous homopolymers;
- the enthalpy recovery has a single step decay towards equilibrium and the relaxation kinetics of the glass (PLLA, PDLA and sc PLA) is independent on the tacticity in stereocomplex structure;
- the dielectric properties are independent on the tacticity presence;
- the cooperativity length ξ_α and cooperativity number N_α have no dependence on the chemical structure (i.e. chirality) in the case of amorphous samples;
- through the β-process analysis it is found that the local movements of polymer chain are independent from the stereocomplexation in case of amorphous samples. However, different crystalline phase is obtained during stereocomplexation.

Our aim was also to investigate the influence of the stereocomplexation on the transport properties of PLA. Therefore, last part of this thesis is focused on the analysis of the barrier properties towards water and gases (N_2, O_2, and CO_2). Special attention was paid to the water permeation of semicrystalline stereocomplex PLA as a function of temperature.

According to the permeation measurements results, the improvements of barrier properties of PLA can be presented as follows:

- the glass transition properties and molecular dynamics of amorphous samples was found to be same for homopolymers and sc PLA and the stereocomplex presence improves the barrier properties of amorphous stereocomplex PLA;
- in case of semicrystalline samples, an important barrier improvement for stereocomplex PLA was observed; i.e. up to 70% as compared to the homopolymers;
- stereocomplex PLA shows better barrier properties with increasing the temperature of permeation measurements;
- the aging effect on the barrier properties of homopolymers was observed as decrease in the values of permeation coefficient with increasing measurement temperature;
- the gas barrier properties are also enhanced by stereocomplexation, thus stereocomplexation can be used as a new method to polymers synthesis for food packaging applications.

Future work can be directed towards the production optimization of stereocomplex PLA films through the extrusion process if it were to be targeted for packaging applications. From this optimization, different amorphous fractions could be obtained and analyzed (i.e. dielectric properties, barrier properties, etc.) for its barrier properties as the function of temperature. A complete gas permeation measurement as the function of temperature for both amorphous and semicrystalline samples can also be carried out to study stereocomplexation effect on the transport properties of PLA. Rheology analysis at high temperature can be also performed to investigate mechanical properties of stereocomplex PLA.

The study of molecular dynamics as a function of frequency and temperature for semicrystalline samples is also crucial to understand the chirality effect of stereocomplex PLA. High pressure DRS analysis could be utilized to reveal the piezoelectric properties of stereocomplex PLA. Over the last decade, there is an increase interest towards the piezo-

response of biobased polymers as compared to other synthetic piezo-materials (e.g. ceramics). Besides packaging applications, the understanding of piezoelectricity is useful in applications that involve separation membranes, pressure sensors, energy harvester and transparent nanogenerator, and ultrasound-based systems (microphones, echolocation).

APPENDIX

Chapter 4

$\lvert\beta_c\rvert=\beta_h$ (Ks^{-1})	δT_L			T_f from heating (°C)			T_f corrected from heating (°C)			T_f from cooling (°C)		
	(A)	(B)	(C)	(A)	(B)	(C)	(A)	(B)	(C)	(A)	(B)	(C)
300	0.8	1.8	1.5	64.0	67.6	66.8	63.2	65.8	65.4	65.0	65.6	65.6
500	1.0	2.3	1.8	64.2	68.1	67.1	63.2	65.8	65.3	64.2	66.1	65.7
1000	1.5	3.7	2.6	68.0	69.7	67.8	66.5	66.0	65.2	64.9	66.0	65.3
1500	4.4	5.5	3.3	69.4	71.2	68.9	64.9	65.7	65.6	65.9	65.7	65.1
2000	5.4	7.6	4.5	70.5	72.2	70.0	65.1	64.6	65.5	65.8	65.8	65.7
3000	5.7	10.6	6.5	71.1	75.1	72.1	65.4	64.5	65.6	64.5	66.6	64.9
4000	5.0	12.4	8.4	73.0	78.8	73.6	68.1	66.4	65.2	65.5	65.8	65.1

A. 4. 1. The measured and corrected values of the total thermal lag and the fictive temperatures for the different scanning rates for (A) PLLA, (B) PDLA, (C) sc PLA.

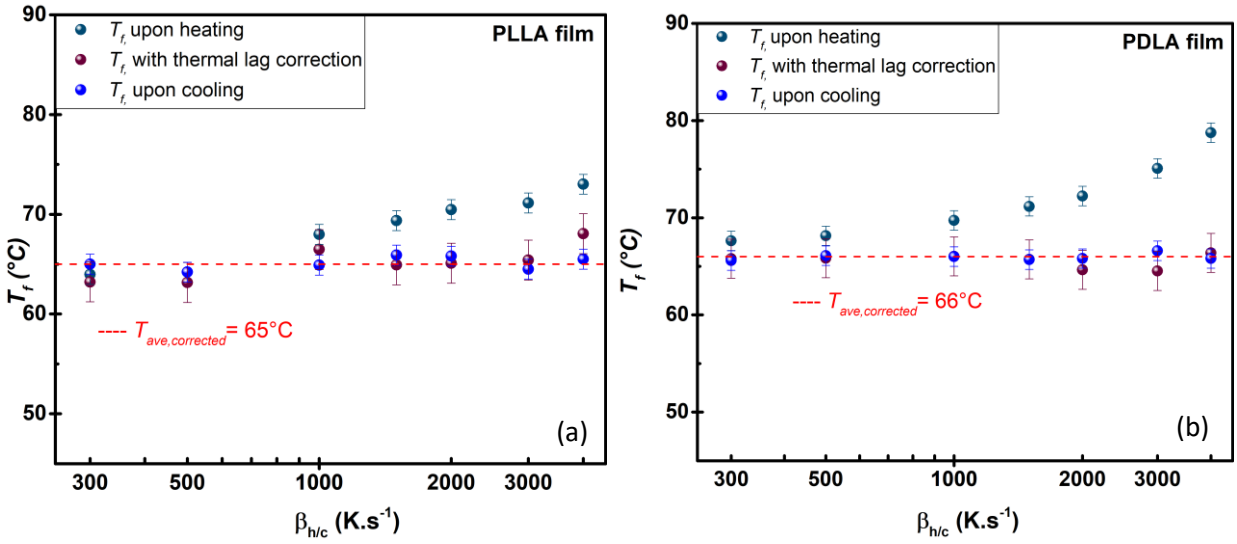

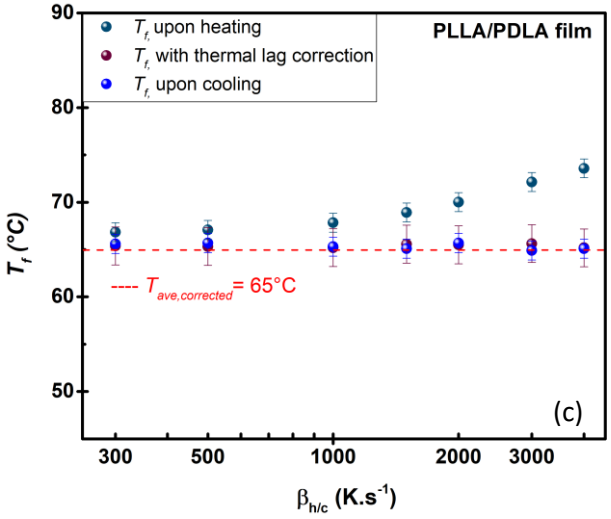

A. 4. 2. Evolution of the fictive temperature as a function of equivalent scanning rate for amorphous samples: (a) PLLA, (b) PDLA and (c) sc PLA.

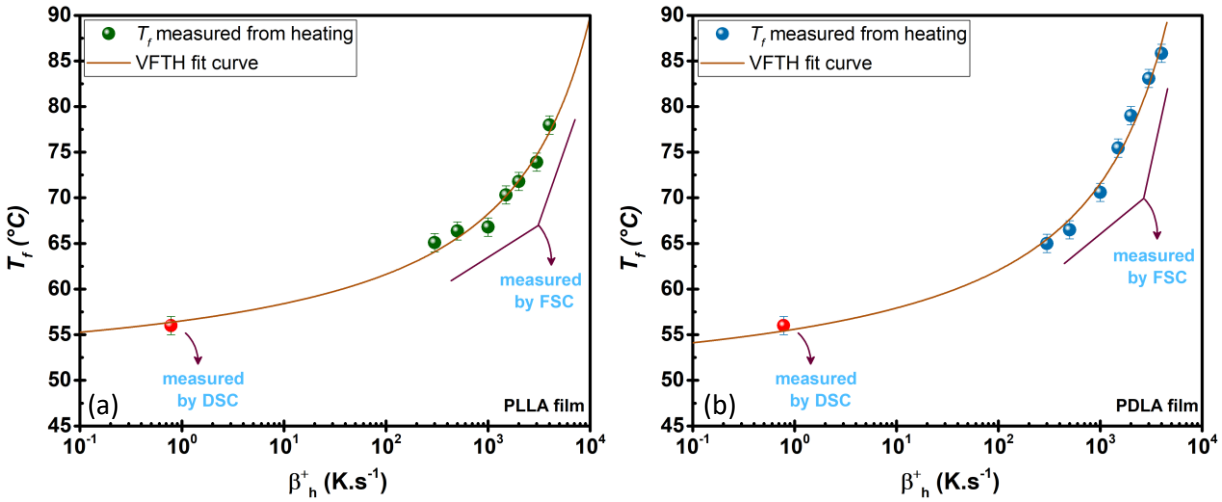

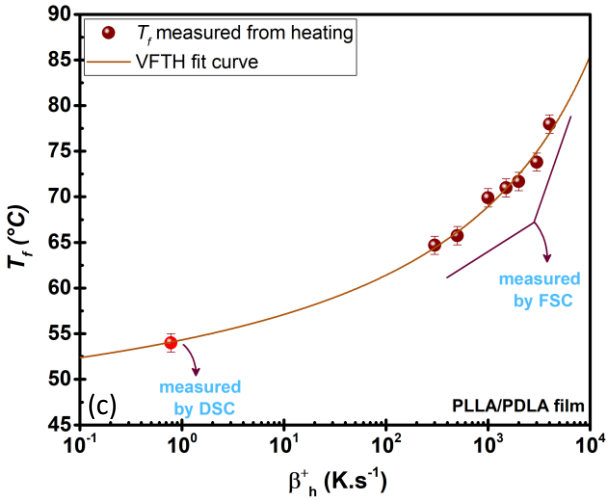

A. 4. 3. Evolution of the fictive temperature measured upon heating as a function of the scanning rate $|\beta_c| = \beta_h$ for (a) PLLA, (b) PDLA and (c) PLLA/PDLA. The red-colored symbols present the fictive temperature determined from DSC at $|\beta_c| = \beta_h = 0.78$ K.s^{-1}. The other results present the fictive temperature determined from FSC at $|\beta_c| = \beta_h$ ranging from 300 K.s^{-1} up to 4000 K.s^{-1}. The solid lines correspond to the VFTH fit.

Chapter 5

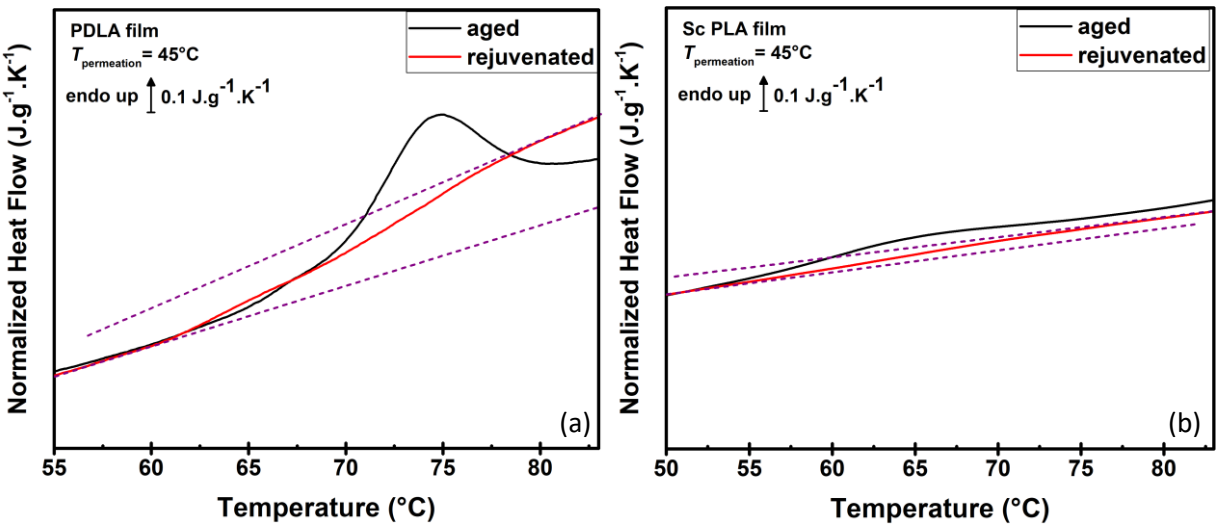

A. 5. 1. DSC curves of studied semicrystalline: (a) PDLA and (b) sc PLA after the permeation test at 45 ± 1°C.

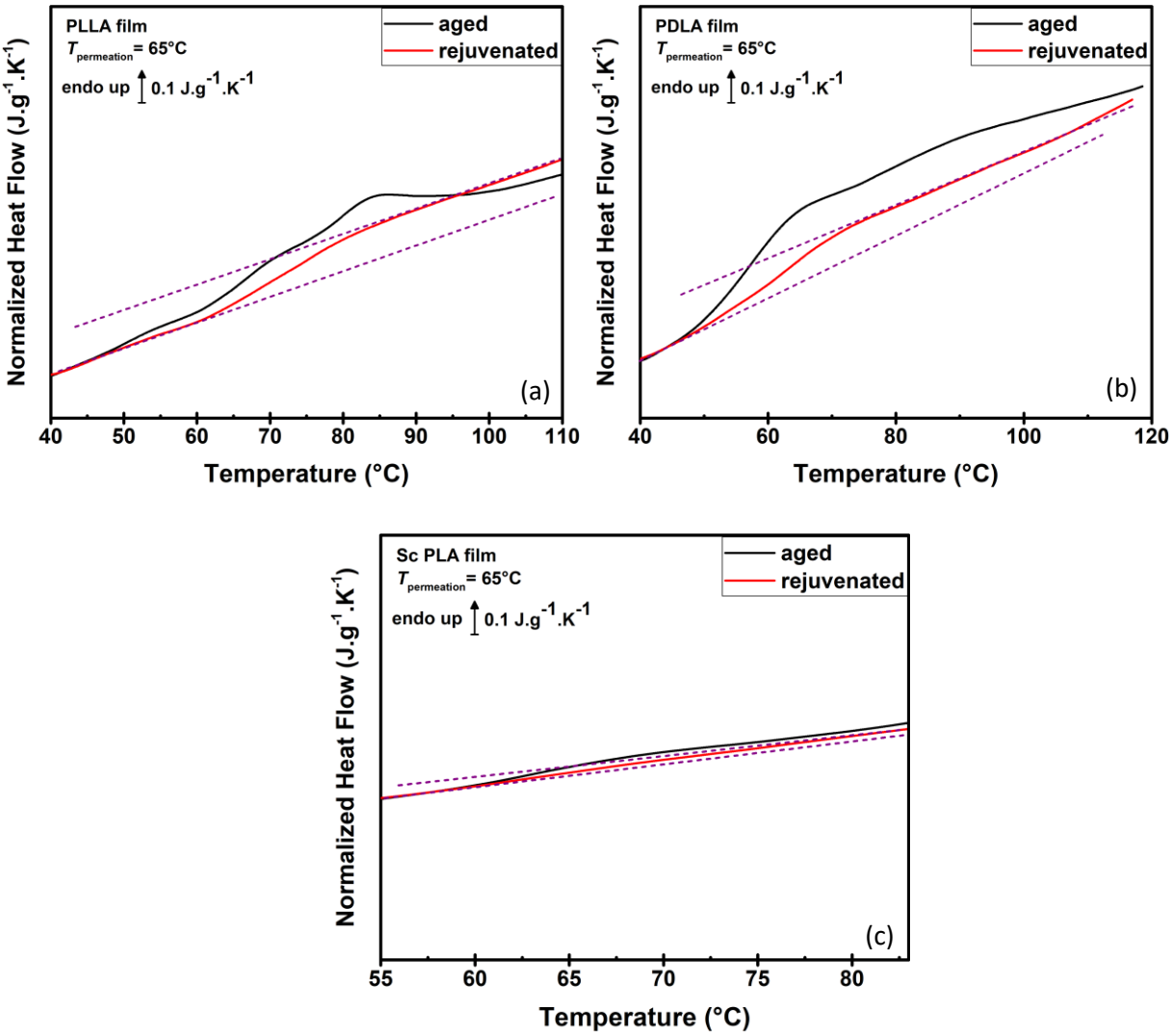

A. 5. 2. DSC curves of studied semicrystalline: (a) PLLA, (b) PDLA and (c) sc PLA after the permeation test at 65 ± 1°C.

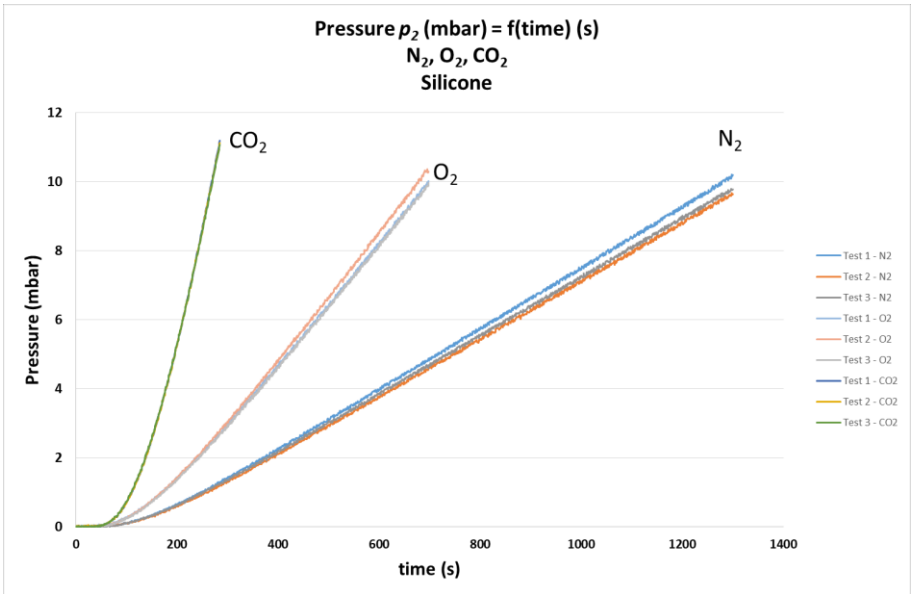

A. 5. 3. Pressure as a function of time for silicone film.

Permeability coefficient P (Barrer)	**N_2**	**O_2**	**CO_2**
Silicone	215 ± 1.7	460 ± 10	1853 ± 6

A. 5. 4. The permeability coefficient of silicone film towards N_2, O_2 and CO_2.

Selectivity	**O_2/N_2**	**CO_2/ N_2**	**CO_2/ O_2**
α	2.1	8.6	1.0

A. 5. 5. The selectivity of silicone film.

Analyse Thermique Avancée et Propriétés de Transport de Matériaux PolyLactide Stéréocomplexe

L'originalité de ce travail repose sur une approche physique et physico-chimique des propriétés de mélanges de polylactides de chiralité différentes (poly L-lactique acide et poly D-lactique acide) et sur l'influence de cette chiralité sur les propriétés des phases amorphes de ces matériaux. Les matériaux sont des mélanges élaborés à partir de deux homopolymères (PLLA et PDLA) selon deux méthodes ; coulée en solution ou par extrusion. Nous avons étudié des matériaux totalement amorphes et cristallisés de façon isotrope afin de générer une phase amorphe plus ou moins confinée. Il est montré que le mélange pouvant donner naissance à une phase cristalline stéréocomplexe ne peut être obtenu que dans certaines conditions. Les résultats des analyses thermiques et de perméation ont montré que le mélange PLLA/PDLA améliore certaines propriétés du matériau, notamment des propriétés barrières à l'eau et aux gaz plus élevées par rapport aux homopolymères parents. Afin d'étudier la mobilité moléculaire des phases amorphes, du vieillissement physique et de la relaxation structural (relaxation α et β), le concept de Région de Réarrangement Coopératif (CRR) a été appliqué. Il a été montré que les phases amorphes des homopolymères et du mélange ont exactement les mêmes propriétés à la transition vitreuse et dans l'état vitreux lorsque les matériaux sont totalement amorphes.

Mots-clés: stéréocomplexation, PLA stéréocomplexe, propriétés de transport, analyse thermique, dynamique moléculaire, relaxation structurale, vieillissement physique, Spectroscopie de Relaxation Diélectrique, Calorimétrie à Balayage Rapide, Perméation

Advanced Thermal Analysis and Transport Properties of Stereocomplex PolyLactide

The originality of this work is based on analysis of physical and physicochemical properties of polylactide mixtures of different chirality (poly L-lactic acid and poly D-lactic acid) and on the influence of the chirality on the amorphous phase's properties. The materials mixtures are elaborated from two homopolymers (PLLA and PDLA) according to two methods; solution casting or extrusion. Totally amorphous and isotropically crystallized materials with more or less confined amorphous phase were studied. It is shown that a stereocomplex crystalline phase can be obtained only under certain experimental conditions. The results of the thermal and permeation analyzes showed that the PLLA / PDLA mixture improved certain properties of the material, namely higher barrier properties towards liquid water and gases were obtained compared to parent homopolymers. In order to study the molecular mobility of amorphous phases, physical aging and structural relaxation (α and β relaxation), the Cooperative Rearrangement Region (CRR) concept has been applied. It has been shown that the amorphous phases of the homopolymers and the mixture have exactly the same properties at the glass transition and in the vitreous state when the materials are totally amorphous.

Keywords: stereocomplexation, stereocomplex PLA, transport properties, thermal analysis, molecular dynamic, structural relaxation, physical aging, Dielectric Relaxation Spectroscopy, Fast Scanning Calorimetry, Permeation